

Spring 1995

Locations and spectra of cosmic gamma-ray bursts

Richard Marc Kippen

University of New Hampshire, Durham

Follow this and additional works at: <https://scholars.unh.edu/dissertation>

Recommended Citation

Kippen, Richard Marc, "Locations and spectra of cosmic gamma-ray bursts" (1995). *Doctoral Dissertations*. 1844.
<https://scholars.unh.edu/dissertation/1844>

This Dissertation is brought to you for free and open access by the Student Scholarship at University of New Hampshire Scholars' Repository. It has been accepted for inclusion in Doctoral Dissertations by an authorized administrator of University of New Hampshire Scholars' Repository. For more information, please contact nicole.hentz@unh.edu.

INFORMATION TO USERS

This manuscript has been reproduced from the microfilm master. UMI films the text directly from the original or copy submitted. Thus, some thesis and dissertation copies are in typewriter face, while others may be from any type of computer printer.

The quality of this reproduction is dependent upon the quality of the copy submitted. Broken or indistinct print, colored or poor quality illustrations and photographs, print bleedthrough, substandard margins, and improper alignment can adversely affect reproduction.

In the unlikely event that the author did not send UMI a complete manuscript and there are missing pages, these will be noted. Also, if unauthorized copyright material had to be removed, a note will indicate the deletion.

Oversize materials (e.g., maps, drawings, charts) are reproduced by sectioning the original, beginning at the upper left-hand corner and continuing from left to right in equal sections with small overlaps. Each original is also photographed in one exposure and is included in reduced form at the back of the book.

Photographs included in the original manuscript have been reproduced xerographically in this copy. Higher quality 6" x 9" black and white photographic prints are available for any photographs or illustrations appearing in this copy for an additional charge. Contact UMI directly to order.

UMI

A Bell & Howell Information Company
300 North Zeeb Road, Ann Arbor, MI 48106-1346 USA
313/761-4700 800/521-0600

**LOCATIONS AND SPECTRA
OF
COSMIC GAMMA-RAY BURSTS**

BY

R. MARC KIPPEN
B.S., University of New Hampshire, 1988
M.S., University of New Hampshire, 1991

A DISSERTATION

Submitted to the University of New Hampshire
in Partial Fulfillment of
the Requirements for the Degree of

Doctor of Philosophy
in
Physics

May 1995

UMI Number: 9528766

UMI Microform 9528766

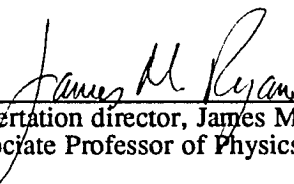
Copyright 1995, by UMI Company. All rights reserved.

**This microform edition is protected against unauthorized
copying under Title 17, United States Code.**

UMI

**300 North Zeeb Road
Ann Arbor, MI 48103**

This dissertation has been examined and approved.



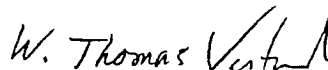
Dissertation director, James M. Ryan
Associate Professor of Physics



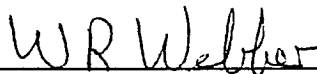
F. William Hersman
Associate Professor of Physics



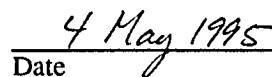
Eberhard Möbius
Associate Professor of Physics



W. Thomas Vestrand
Research Associate Professor of Physics



William R. Webber
Research Professor of Physics



Date

For Betsey

ACKNOWLEDGEMENTS

I wish to express my sincere gratitude to my advisor James Ryan for convincing me to continue in my graduate studies and for allowing me to participate in this research program. His knowledge, experience and humor have been a great source of inspiration and his guidance and support over the years have made a large contribution to this work. This dissertation could not have been completed without the groundwork and continued support of the COMPTEL instrument team led by Volker Schönfelder. I am particularly obliged to team members Alanna Connors, John Macri, Mark McConnell, Martin Varendorff, Lorraine Hanlon, Christoph Winkler, Rob van Dijk, Kevin Bennett and Lucien Kuiper for their help and insightful ideas on statistics, data analysis and the idiosyncrasies of the instrument. The COMPTEL operations team led by John Macri deserves special credit for their eager willingness to go beyond the call of duty in delivering data, as do Tom Milliman, John Labonte and Rita Freuder for helping me solve the mysteries of computers. I gratefully acknowledge the efforts of those collaborators who have been a part of this research, including the BATSE instrument team led by Gerald Fishman and Charles Meegan and the members of the optical and radio counterpart search program led by Bernie McNamara and Tom Harrison. I thank Kevin Hurley and Brenda Dingus for communicating their early IPN and EGRET results to me. Finally, I thank my fellow students and friends at the University of New Hampshire (especially Srinivas Kappadath, Doug Biesecker, Richard Miller, Carmen Gagne, Bill Peria, Vance Pomeroy and Raid Suleiman) for sharing in this experience and for helping me along the way. This work was supported by the National Aeronautics and Space Administration of the United States under NASA contract NAS5-26645.

TABLE OF CONTENTS

DEDICATION.....	iii
ACKNOWLEDGEMENTS.....	iv
LIST OF TABLES.....	viii
LIST OF FIGURES.....	ix
ABSTRACT.....	xii

CHAPTER	PAGE
I. INTRODUCTION.....	1
A. Cosmic Gamma-Ray Bursts.....	1
B. Observational Constraints.....	2
i. Temporal Characteristics.....	3
ii. Spectral Characteristics.....	6
iii. Burst Directions and Frequency.....	9
C. Theoretical Burst Source Scenarios.....	13
i. The Pre-BATSE Paradigm.....	13
ii. The Post-BATSE Dilemma.....	16
D. Present Work.....	18
II. INSTRUMENTATION AND ANALYSIS TECHNIQUES.....	20
A. COMPTEL: The Imaging Compton Telescope.....	20
i. Instrument Characteristics.....	21
ii. General Instrument Response.....	23
iii. In-Flight Performance and Background.....	25
iv. Burst Detection Capabilities.....	27
B. Fundamental Analysis Techniques.....	29

i.	Data Processing and Selection.....	29
ii.	Burst Source Localization.....	31
a.	Spatial Response Representation.....	31
b.	Maximum-Likelihood Imaging.....	34
c.	Background Determination.....	36
iii.	Burst Spectral Analysis.....	39
a.	Energy Response and Spectral Deconvolution.....	39
b.	Parameter Estimation and Model Testing.....	42
c.	Background Determination.....	43
III.	COMPTEL OBSERVATIONS OF GAMMA-RAY BURSTS.....	45
A.	Burst Search Strategy.....	45
B.	Observations.....	47
IV.	RESULTS OF SPATIAL ANALYSIS.....	49
A.	Burst Source Localization.....	49
i.	COMPTEL Localizations.....	49
ii.	Combined COMPTEL/IPN Localizations.....	53
B.	COMPTEL/IPN Burst Distance Constraints.....	55
C.	Large-Scale Angular Distribution.....	58
D.	Small-Scale Angular Distribution and Burst Recurrence.....	62
E.	Discussion.....	68
i.	Distance Constraints.....	68
ii.	Large-Scale Distribution.....	70
iii.	Small-Scale Distribution.....	72
V.	RESULTS OF SPECTRAL ANALYSIS.....	75
A.	COMPTEL Measurements of MeV Burst Emission.....	75
B.	Spectral Modeling.....	78
i.	Continuum Emission and Attenuation Mechanisms.....	79

ii. Modeling of COMPTEL Spectra.....	85
C. Wide-Band Gamma-Ray Burst Spectra.....	91
i. Spectral Breaks.....	97
ii. Extended High-Energy Emission.....	98
D. Pair Production and Relativistic Motion	101
E. Discussion	108
i. Overall Spectral Shape.....	109
ii. High-Energy Emission and Relativistic Motion.....	111
VI. FADING COUNTERPART SEARCH RESULTS	115
A. Past Counterpart Search Strategies and Results.....	116
B. Rapid Burst Response	120
C. Multiwavelength Burst Observations.....	124
i. Results From Individual Bursts.....	125
a. GRB 930131	125
b. GRB 930309	126
c. GRB 940217	127
d. GRB 940301	127
D. Discussion	129
VII. SUMMARY AND CONCLUSIONS.....	135
APPENDICES	138
A. COMPTEL GAMMA-RAY BURST CATALOG	139
B. SYSTEMATIC ERRORS	150
A. Systematic Burst Location Errors.....	150
B. Systematic Errors in Spectral Analysis	153
C. COMPTEL SKY EXPOSURE MATRIX	158
REFERENCES.....	162

LIST OF TABLES

TABLE	PAGE
3.1 COMPTEL Burst Detection Parameters.....	47
4.1 COMPTEL Burst Localization Parameters	51
4.2 Combined COMPTEL/IPN (BATSE/ <i>Ulysses</i>) Burst Localization Parameters.....	54
4.3 COMPTEL/IPN (BATSE/ <i>Ulysses</i>) Burst Distance Limits.....	57
4.4 Angular Distribution Moments for 18 COMPTEL Gamma-Ray Bursts	61
5.1 Spectral and Temporal Burst Parameters.....	76
5.2 Time-Averaged Spectral Fit Parameters	86
5.3 Advanced Model Spectral Fit Parameters.....	90
5.4 Multi-Instrument Spectral Comparisons.....	93
5.5 Limits on Burst Source Distance and Relativistic Bulk Motion	108
6.1 Rapid Burst Response Performance	124
6.2 Rapid Observations of GRB 940301 (First Five Days).....	128

LIST OF FIGURES

FIGURE	PAGE
2.1 Schematic diagram of the Compton Gamma Ray Observatory spacecraft showing its four scientific instruments	20
2.2 Schematic diagram of the Imaging Compton Telescope (COMPTEL) illustrating its principle of detection	22
2.3 Effective detection area of COMPTEL (as determined from simulation) as a function of energy for several different point-source incident angles.....	24
2.4 Simulated angular and energy response of COMPTEL to monoenergetic point sources at normal incidence with nominal data selections.....	25
2.5 Orbital variations of the telescope event-rate and earth horizon angle over a typical observing day.....	26
2.6 COMPTEL telescope burst sensitivity as a function of burst zenith angle for several different power law spectra.....	28
2.7 Illustration of the COMPTEL spatial response to a point-source	31
2.8 COMPTEL point spread function (determined from simulation) in two dimensions for an assumed $E^{-2.0}$ power law spectrum	33
2.9 Maximum likelihood ratio sky-maps of two simulated point sources	35
2.10 Typical background data-space distributions from isotropic model and direct measurement.....	36
2.11 Map of the earth showing the orbit of <i>Compton</i> from 17–19 May, 1991	37
2.12 Examples of an energy response vector and a directly inverted photon spectrum	40
2.13 Examples of null-test temporal and energy background distributions.....	44
4.1 Combined COMPTEL/IPN localization of GRB 910601	53
4.2 COMPTEL/IPN distance constraints for GRB 910601.....	57
4.3 The all-sky distribution of 18 COMPTEL gamma-ray bursts in Galactic and Celestial coordinate systems	60
4.4 Expected and observed distributions of Galactic dipole and quadrupole moments for 18 COMPTEL gamma-ray bursts	61

FIGURE	PAGE
4.5 The angular correlation function of 18 COMPTEL gamma-ray bursts.....	64
4.6 COMPTEL maximum-likelihood localizations (1-, 2- and 3 σ confidence) and IPN “triangulation” annuli of GRB 930704 and GRB 940301.....	65
4.7 Comparison of observed gamma-ray burst Galactic dipole and quadrupole moments	71
5.1 Best-fit spectral models (0.75–30 MeV) and two-parameter confidence regions for the time-averaged emission from GRB 910503	85
5.2 Histograms of best-fit spectral shape parameters for each of the spectral models tested	87
5.3 Histograms of “goodness-of-fit” estimates for each spectral model and the shape expected from random statistical fluctuations.....	89
5.4 (a) Multi-instrument energy spectrum of GRB 910503.....	94
(b) Multi-instrument energy spectrum of GRB 910814.....	94
(c) Multi-instrument energy spectrum of GRB 911118.....	95
(d) Multi-instrument energy spectrum of GRB 920622	95
(e) Multi-instrument energy spectrum of GRB 940217.....	96
5.5 Extended emission spectra of GRB 930131 and GRB 940217 comparing COMPTEL upper limits to the allowed range of fitted EGRET–SC power laws and TASC data points.....	100
5.6 Lightcurves of the most intense COMPTEL bursts.....	107
6.1 Schematic outline of Rapid Burst Response operations and typical response times during Phases I and II of the program.....	122
A.1 GRB 910425.....	141
A.2 GRB 910503.....	141
A.3 GRB 910601.....	142
A.4 GRB 910627.....	142
A.5 GRB 910709.....	143
A.6 GRB 910814.....	143
A.7 GRB 911118.....	144
A.8 GRB 920622.....	144

FIGURE	PAGE
A.9 GRB 920830.....	145
A.10 GRB 930118.....	145
A.11 GRB 930131.....	146
A.12 GRB 930309.....	146
A.13 GRB 930612.....	147
A.14 GRB 930704.....	147
A.15 GRB 931229.....	148
A.16 GRB 940217.....	148
A.17 GRB 940301.....	149
A.18 GRB 940314.....	149
B.1 The systematic effect of PSF statistics on source localization.....	151
B.2 Systematic effect of background modeling on burst source localization.....	153
B.3 The systematic effect of assumed response spectrum on deconvolution.....	154
B.4 The systematic effects of assumed source location (left) and response vector statistical coverage (right) on spectral deconvolution.....	155
B.5 The systematic effect of background on spectral analysis.....	156
C.1 Effective telescope detection area as a function of zenith angle for typical power law burst spectra as determined from simulation.....	159
C.2 COMPTEL burst exposure maps in Galactic and Celestial coordinate systems for the first three years of the Compton Observatory mission.....	160

ABSTRACT

LOCATIONS AND SPECTRA OF COSMIC GAMMA-RAY BURSTS

by

R. Marc Kippen
University of New Hampshire, May, 1995

The COMPTEL instrument aboard the Compton Gamma Ray Observatory is used to study the phenomena of cosmic gamma-ray bursts. Three years of observations from April 1991 through April 1994 reveal 18 significant gamma-ray burst detections. The locations (mean accuracy $\sim 1^\circ$) and spectra (0.75–30 MeV) of these bursts are measured and are used to investigate the spatial distribution of burst sources and the characteristics of their emission at MeV energies. Rapidly determined COMPTEL burst localizations obtained through direct imaging are used to search for fading burst counterpart emission in a coordinated effort with ground-based optical and radio telescopes.

The COMPTEL burst localizations are consistent with an isotropic angular distribution of sources, yet the spatial coincidence of two bursts indicates the possibility of repetition from at least one source. The combination of COMPTEL burst images with Interplanetary Network triangulation data significantly reduces the uncertainty in burst directions. The lack of an observable parallax between COMPTEL and Interplanetary Network localizations indicates that two of the strongest bursts must have originated more than ~ 100 AU from the earth.

Nearly all of the time-averaged COMPTEL burst spectra are consistent with a single power law model with spectral index in the range 1.5–3.5. Exponential, thermal bremsstrahlung and thermal synchrotron models are statistically inconsistent with the full COMPTEL burst sample, although they can adequately describe some of the individual burst

spectra. Comparisons of simultaneous and near-simultaneous burst spectra measured by COMPTEL, BATSE and EGRET show wide-band emission that is characterized by a variable turnover around a few hundred keV, followed by a single power law out to ~ 100 MeV. The relation between burst emission measured by COMPTEL at MeV energies and that measured by EGRET at GeV energies is still unclear, but there is no evidence to indicate a spectral change or temporal delay between the two. Measurement of rapid variability at MeV energies in the stronger bursts provides evidence that either the sources are nearby isotropic emitters within the Galactic disk or the gamma-ray emission is relativistically beamed to avoid the opacity of two-photon pair production.

No obvious fading burst counterpart emission has been identified in the deepest optical and radio searches ever performed with time delays of hours. The upper limits on such emission suggest that fading optical counterparts after delays of \sim hours are fainter than 16th visual magnitude and radio emission is weaker than ~ 0.2 Jy. These results indicate that low-energy burst emission (if it exists) is very weak and/or very short-lived. Future low-energy burst counterpart search efforts will have to concentrate on obtaining deep measurements with time-delays significantly shorter than a few hours.

I. INTRODUCTION

A. Cosmic Gamma-Ray Bursts

In the middle part of this century, theorists such as Hayakawa (1952), Hutchinson (1952) and Morrison (1958) suggested the possibility that observable fluxes of gamma radiation could be produced in astrophysical environments. The advent of the space age and advanced detector technology has turned this possibility into reality. Modern gamma-ray astronomy has revealed the hidden aspects of the most violent and energetic processes in the universe—including unique observations of such intriguing phenomena as supernovae, pulsars, accreting neutron stars, black holes, active galactic nuclei and solar flares. Of all the sources observed in gamma rays, however, none are as enigmatic as the cosmic gamma-ray bursts (GRBs). These numerous and powerful brief transient phenomena are the most obvious and plentiful astronomical sources of gamma rays known, yet their origin is an enigma that has tantalized observers and theorists alike since their discovery in the late 1960s. It is not surprising that historically, GRBs were among the first gamma-ray sources to be detected, for their intensities are such that they can momentarily dominate the gamma-ray emission from the entire sky. However, their discovery was nonetheless surprising, for few could have predicted such intense outbursts of high-energy radiation (but see Colgate 1968). One of the most puzzling aspects of GRBs is that most of their radiation lies in the gamma-ray region of the electromagnetic spectrum with very little (if any) emission at lower energies. It is ironic that although GRBs are intense and commonplace, making them more easily detectable than most other steady and transient gamma-ray sources, their origin remains a mystery. A profusion of theoretical work has resulted in source models that have the bursts originating from a wide variety of different objects located as near as the solar system to as far as the outer reaches of the observable universe. Unfortunately, many of these diverse scenarios cannot be excluded by the observational data, making the situation appear insoluble. It is the great mystery of gamma-ray bursts which we will address in this work. The following is a brief

introduction to the study of gamma-ray bursts concentrating on recent observational and theoretical results. More detailed explanation of some of these results are found in the remainder of the text and several excellent reviews of this field have been given by: Cline (1983, 1986), Liang (1987, 1989), Hurley (1989, 1992), Higdon & Lingenfelter (1990), Hartmann (1991), Vedrenne (1991), Harding (1991, 1994), Mészáros (1992), Ramana Murthy & Wolfendale (1993) and Blaes (1994).

B. Observational Constraints

The first measurements of a gamma-ray burst were recorded accidentally in 1967 by instruments on the *Vela* satellites designed to detect the signature of exploding nuclear weapons in the atmosphere and outer space (as violations of the Nuclear Test Ban Treaty of 1963). It was not until several years later that Klebesadel, Strong & Olson (1973) accumulated enough evidence that this event and other similar detections were of cosmic origin that they announced their discovery (an account of the discovery was given by Strong & Klebesadel 1976). The *Vela* burst measurements indicated rapid (<0.1 s) gamma-ray flux increases in the energy range ~ 0.3 – 1 MeV that lasted typically several seconds and resulted in energy fluences of $\sim 10^{-5}$ – 10^{-4} erg cm^{-2} . Furthermore, each burst appeared to be markedly different, with some lasting only a fraction of a second while others persisted for nearly a minute. Near-simultaneous detections on different *Vela* satellites ruled out an instrumental origin and were used to determine a crude localization that excluded the earth, moon, sun and planets as potential sources.

In the years since the discovery, a large amount of observational data on gamma-ray bursts has been collected from various spacecraft and balloon-borne instruments. Some of the more important experiments in this effort have been the KONUS detectors aboard the *Venera* spacecraft, the GRB detectors aboard *Pioneer Venus Orbiter (PVO)* and *Ginga* and the Gamma-Ray Spectrometer (GRS) aboard the *Solar Maximum Mission (SMM)*. However, the greatest amount of information on many aspects of bursts has come from recent observations made by the Burst and Transient Source Experiment (BATSE) aboard the Compton Gamma Ray Observatory

(*Compton*). With its high sensitivity and 4π field-of-view, BATSE has in a few years of operation more than doubled the number of burst observations of all other experiments combined. It is important to point out that all burst observations are based on only a few basic measurable quantities: the intensity (i.e., the amount of radiation being detected), time, energy and direction of gamma-ray emission. The value of a GRB instrument lies in how well it can determine these basic observables. Thus, although BATSE has given us the most complete sample of bursts obtained so far, the observations of other instruments with different (often better) measurement capabilities are also valuable.

i. Temporal Characteristics

There are three basic time scales on which burst emission can be characterized (1) the *variability* time-scale of the emission during a burst, (2) the total *duration* of a burst and (3) the time-scale for burst *recurrence* from individual sources. Measurement of the characteristics of each of these time scales involves different observational biases. For example, the temporal structure and duration of individual bursts is highly dependent on the energy range and the intensity threshold of the measurement (Lingenfelter, Wang & Higdon 1994) and the ability to measure burst recurrence is strongly dependent on spatial coverage and angular resolution (Hartmann *et al.* 1994).

The variability of emission within bursts is in many cases rapid, as was noted in the very first *Vela* observations. Temporal features (i.e., pulses, rise-times, trailing edges, etc.) have been observed that are as short as instruments have been able to measure (typically a few ms). In general, the increasing time resolution of more sophisticated instruments has resulted in the observations of faster variability. The shortest non-instrumental variations in burst flux are unknown (Mitrofanov 1989), but bursts probably do not consist of a significant fraction of very short ($\sim\mu\text{s}$) pulses (Schaefer *et al.* 1993). Through causality, the characteristic size of the gamma-ray burst emitting region ℓ is constrained by $\ell \leq c\delta t$, where δt is the variability time-scale. The $\sim\text{ms}$ flux variations observed in most bursts thus imply emission regions that are smaller than

~1000 km. This does not necessarily imply that the sources themselves are compact objects, only that the site where the intense emission originates is small. The combination of high flux *and* rapid variability during intense bursts means that the density of photons at the emission site must be large and increases with source distance. As we will discuss in Chapter V, this implies that photon-photon interactions could be an important source of high-energy gamma-ray opacity if burst sources are more distant than a few kpc (Schmidt 1978).

The only known temporal feature that *all* gamma-ray bursts share in common is that they all begin (i.e., rise in intensity above the background level) and they all eventually end (i.e., fade back into the background level). The structure of the intensity of emission within this interval for each burst is different, although some general morphological similarities have been observed by examining the intensity–time profiles (or lightcurves) of large burst samples. For instance, many bursts show complex and varied structure consisting of multiple pulses of emission, often superimposed on a broad envelope, while others show relatively featureless lightcurves that exhibit a fast rise followed by a slow decay. However, a diverse range of intermediate cases have also been observed such that bursts defy quantitative classification based on temporal variability (Fishman 1993; Kouveliotou 1994). That there is no characteristic GRB lightcurve suggests that a wide variety of physical conditions may be present at the burst emission sites. It is even suggestive that different mechanisms or sources may be at work. Studies of the emission pulses within BATSE bursts have suggested that there may be a correlation between pulse width and peak burst intensity, with the most intense bursts having shorter pulses (on average) than the dim bursts (Norris *et al.* 1994). Such a correlation *could* indicate the signature of cosmological time dilation from a source population with average redshift $z \sim 1$ (Wickramasinghe *et al.* 1993; Wijers & Paczynski 1994). However, it has also been suggested that the pulse duration–burst intensity correlation is an intrinsic feature of the burst source population that is not necessarily related to source distance (Band 1994).

The overall durations of GRB emission are in some sense as diverse as the temporal variations within the bursts. Burst durations span a broad range of times from as short as a few

ms (Fishman 1993) to as long as an hour (Hurley *et al.* 1994e), but most bursts last ~ 1 –100 s. As noted earlier, the definition of burst duration is highly dependent on the energy range and intensity threshold of the measurement. The distribution of burst durations measured by individual instruments has been studied extensively to search for possible divisions between different classes of objects (Norris *et al.* 1984; Klebesadel 1992; Hurley 1992). One such division has been suggested in the data from several instruments for a number of years, but it is most evident in the large sample of BATSE bursts, which spans the greatest range of durations. Kouveliotou *et al.* (1993a) found a clear bimodality in the distribution of burst durations between short and long events, with the division occurring around 2 s. The two classes of bursts are further distinguished in that the spectra of the short events are harder (on average) than the longer bursts. These findings have been used to suggest that two (or more) different populations of bursting objects are being measured (e.g., Lamb, Graziani & Smith 1993). However, there is no clear evidence that the two classes come from different objects; they could be the result of different mechanisms and/or emission geometries on the same type of source (Kouveliotou *et al.* 1994a).

Of the more than 1000 individual gamma-ray burst sources known to exist, only three have been observed to emit repeated events (e.g., Atteia *et al.* 1987b; Norris *et al.* 1991; Kouveliotou *et al.* 1993b). These three sources are now regarded as a strictly separate class of rare objects—the soft gamma-ray repeaters (SGRs). The bursts from SGR activity are characterized not only by their recurrence, but also by their short and simple temporal profiles and soft thermal spectra. The SGR phenomena is far from solved, but two of the sources have been convincingly identified with supernova remnants, so they are thought to originate from highly magnetized neutron stars (e.g., Kulkarni *et al.* 1994; Duncan & Thompson 1994). We are concerned in this work only with the much larger class of bursting objects—the so-called “classical” gamma-ray bursts. None of the classical GRB sources have been observed to emit repeated bursts, although several attempts to identify such behavior have been made. Combined with the observed rate of burst occurrence, the lack of repetition is a constraint on the nature and total number of burst sources. In Chapter

IV we will discuss the subject of burst recurrence in more detail.

ii. Spectral Characteristics

The distribution (or spectrum) of photon energies as well as the total amount of energy observed from GRBs provide important clues about the gamma-ray emission and absorption mechanisms at burst sources. Bursts have been observed whose total energy flux (or fluence) ranges from $\sim 10^{-8}$ to $\sim 10^{-3}$ erg cm^{-2} . Since the observed flux scales as the source luminosity divided by the square of the source distance (assuming isotropic emission), very distant bursts must be exceedingly energetic phenomena. For example, even with a fairly nearby source distance of ~ 1 kpc the typical burst must emit $\sim 10^{39}$ erg of energy to explain the observed flux. The spectra of bursts have been observed from ~ 2 keV to more than 1 GeV, but this entire range has never been observed simultaneously. There are thus many questions of how the different parts of burst spectra are related to each other. Most dedicated GRB instruments (including BATSE) have only been sensitive in the energy range ~ 20 keV to ~ 1 MeV, where bursts emit most of their power. It is fortunate that other instruments have provided at least some information at lower and higher energies. Most of the observations indicate that bursts emit their energy over a broad, smooth continuum. However, there have been several (some disputed) observations of emission and/or absorption features superimposed on the continuum. The absorption features (deficits below the continuum) are observed around ~ 20 – 70 keV whereas the emission features (excesses above the continuum) are around ~ 400 keV.

Modeling of burst continuum spectra has evolved as instrumentation has improved and spectral range has been extended. The earliest GRB spectra, measured in the energy range ~ 100 keV to ~ 1 MeV by detectors aboard the *IMP-6* spacecraft, were well-described by a soft exponential photon number spectrum (Cline *et al.* 1973). Later observations in this same general energy range performed by several other instruments—including more than 100 burst spectra measured by the KONUS detectors—were all adequately described by a low-energy power law with an exponential cutoff around a few hundred keV (Mazets *et al.* 1981b). These soft spectra

predicted little or no observable flux above 1 MeV, but the detectors also lacked the sensitivity at high energies to measure such emission. There were some early indications in a few bursts measured by detectors on *IMP-7* and *Apollo 16* that an additional high-energy power law component was required (Cline & Desai 1975; Metzger *et al.* 1974). However, it was not until several high-energy observations were obtained with the *SMM*–GRS that the general picture of burst spectra changed significantly. The *SMM* observations showed that *most* bursts emit significant flux above 1 MeV (Matz *et al.* 1985). A few strong events were even observed to have significant emission up to nearly 100 MeV (Share *et al.* 1986). The recent observations of BATSE have confirmed that the basic continuum shape of GRB spectra can be described by two different power laws connected with a smooth transition in the region around a few hundred keV (Band *et al.* 1993a). Recent *Compton*–EGRET measurements have observed significant burst emission up to ~ 1 GeV with no evidence of a cutoff (Dingus *et al.* 1994). There are very few measurements of burst spectra at energies below ~ 10 keV. The observations that have been made indicate spectra that are flatter than at higher energies. The result is that emission below ~ 10 keV is weak—less than 2% of that observed above 100 keV (Laros *et al.* 1984). GRBs are thus a truly gamma-ray phenomena. We will discuss burst spectra and their implications on physical emission processes in more detail in Chapter V. In summary, thermal bremsstrahlung, synchrotron and inverse Compton emission models all adequately describe the data below a few hundred keV, but non-thermal mechanisms are usually required to explain the power law shape above ~ 1 MeV.

The general spectral shapes discussed above are applicable to the individual pulses within bursts as well as the total emission, but it is important to note that the spectral shape is *not* constant throughout a burst. This indicates that the physical conditions or emission mechanisms of burst sources are dynamic. Burst spectra have been observed to vary on all measurable time-scales from hundreds of seconds down to ~ 2 ms (Kouveliotou *et al.* 1994b; Bhat *et al.* 1994). The most common form of burst evolution is a softening of the spectra over time (Norris *et al.* 1986). However, bursts that harden with time as well as bursts with no evidence of evolution at

all have also been observed (Kargatis *et al.* 1994; Ford *et al.* 1995). A further form of evolution has been observed where the spectral hardness is correlated with the intensity of emission, but this is not always the case (Golenetskii *et al.* 1983; Kargatis *et al.* 1994). Outside the typical GRB energy regime, soft X-ray emission has been observed to both precede and last much longer than higher energy emission (Murakami *et al.* 1991, 1992) and there is some evidence that GeV emission in a few bursts may persist long after that at lower energies (Hurley *et al.* 1994e).

Absorption features were originally discovered in about 20% of the bursts observed by the KONUS detectors. They appeared as flux deficits that were typically ~40–50% below the continuum emission, had widths ~10–20 keV and accounted for a ~1–2% loss of the total fluence (Mazets *et al.* 1981a, 1982). They were immediately interpreted as the first harmonic of cyclotron absorption in a strong magnetic field. The energies of the absorption features ranged from ~20–70 keV and implied field strengths in excess of 10^{12} G. However, these results were regarded with some skepticism as it was suggested that the features could also be explained by other processes such as spectral evolution (Lamb 1982), the superposition of different continuum components (Lasota & Belli 1983) or artifacts of the spectral deconvolution process (Fenimore, Klebesadel & Laros 1983). The most significant evidence of absorption features came from observations made by *Ginga*, which found significant absorption features in four of 23 burst detections (Murakami *et al.* 1988; Yoshida *et al.* 1992; Murakami *et al.* 1992). The *Ginga* observations included not only single features around ~40 keV, but also pairs of significant lines spaced apart by a factor of two in energy (~20 keV and ~40 keV). These observations were interpreted as the first and second harmonics of cyclotron absorption in a strong magnetic field and were seen as dramatic confirmation of the KONUS results. The line widths were narrow (~4 keV for the 20 keV features), implying cool temperatures in the absorption region. The *Ginga* observations also showed that the line strength is variable—being detectable only at certain times during the bursts. The great dilemma is that BATSE has yet to observe any statistically significant absorption features in over three years of observations, even though it is capable of doing so (Palmer *et al.* 1994; Band *et al.* 1994).

Emission features between 400–500 keV were also detected first and most frequently by KONUS, which observed them in about 15% of the bursts. These broad lines were characterized by widths ~ 250 keV and accounted for $\sim 10\%$ of the burst energy (Mazets *et al.* 1981a, 1982). They have been interpreted as gravitationally redshifted 511 keV e^+e^- annihilation radiation. If this is indeed the case, the observed redshifts of $\sim 10\text{--}30\%$ imply a surface gravity compatible with that of a one solar-mass neutron star. However, the emission features observed by KONUS and other instruments are only marginally significant detections. In many cases, the arguments used to dispel the early KONUS absorption features are applicable. Furthermore, emission features have yet to be confirmed in any of the most recent burst observations—including those of *SMM*, *BATSE* and *COMPTEL* which all have sensitivity in this energy range (Nolan *et al.* 1984; Messina & Share 1992; Hanlon *et al.* 1994).

Despite numerous thorough searches, no burst emission has been detected at energies below ~ 2 keV or above ~ 20 GeV. The search for low-energy counterparts has been performed on a variety of different time-scales (from coincident with the gamma-ray emission to several years before or after) and at different wavelengths (radio through X rays) without success—suggesting that if such emission exists it is weak and short-lived. This is the subject of discussion in Chapter VI. Air Cherenkov telescopes have yet to observe a burst within any of their small fields-of-view. It is thus unknown whether burst spectra extend to \sim TeV energies (Connaughton *et al.* 1994). Several burst locations have been observed with extended air shower arrays, which have failed to identify any evidence of burst emission above ~ 100 TeV. This suggests that either burst spectra intrinsically soften at TeV energies, or they are absorbed by the photon-photon process operating over cosmological distances (Schnee *et al.* 1994). Searches for excess neutrino flux in the energy range 20–100 MeV at the times of known GRBs have failed to identify any significant correlations (Agleitta *et al.* 1993; Miller *et al.* 1994).

iii. Burst Directions and Frequency

The directions of gamma-ray bursts are used to search for objects at other wavelengths (e.g.,

as mentioned earlier) and to investigate the angular distribution of the sources on the sky. For the former purpose, accurate source positions (\sim arc-minute) are required to allow sensitive counterpart searches to be performed using powerful (but limited field-of-view) telescopes. One of the only ways to measure such accurate positions is through the analysis of burst arrival-times between widely separated spacecraft organized in an Interplanetary Network (IPN; Hurley 1982). The difference in burst arrival times between two spacecraft constrains the source position to a thin annular ring on the sky whose radius depends on the time-delay and the distance between the spacecraft and whose width depends on the accuracy of the timing measurements. Additional spacecraft pairs provide additional annuli, the intersections of which constrain the burst direction. Four spacecraft are needed to determine an unambiguous burst direction, but frequently three spacecraft suffice if some other means of crude localization is available (see e.g., Strong & Klebesadel 1976). Since interplanetary spacecraft have stringent weight limits, the burst detectors they carry must necessarily be small and therefore relatively insensitive. This means that IPN burst locations have typically only been measured for the strongest bursts, of which there are few. Many more burst directions have been determined using the relative intensities observed between different detectors on the same spacecraft (e.g., KONUS and BATSE). These positions are typically only accurate to several degrees, but they suffice to investigate the overall angular distribution of burst directions. The subject of burst localization will be discussed further in Chapter IV.

The earliest angular distribution studies were problematic due to insufficient statistics, but most indicated that bursts are not concentrated in any particular direction, but rather they are evenly distributed throughout the sky. As larger samples of burst positions became available (Golenetskii *et al.* 1988; Atteia *et al.* 1987a), the angular isotropy of burst directions became more apparent. These bursts showed no significant concentration towards the center or plane of the Galaxy, nor were they clustered around any of the nearby galaxies (Hartmann & Epstein 1989; Hartmann & Blumenthal 1989). The isotropy of burst directions suggested three possible source populations: (1) a nearby population contained well within the Galactic disk (≤ 100 pc),

(2) a roughly spherical halo around the Galaxy ($\sim 50\text{--}100$ kpc) or (3) a cosmological population well-beyond any of the known clusters of galaxies (~ 0.5 Gpc). However, these studies were based primarily on the strongest bursts, which are more easily localized.

The frequency of bursts (or simply the number of bursts) as a function of burst size (or intensity, or brightness) yields information about the radial distribution of sources. If the intrinsic luminosities of all burst sources are roughly the same (i.e., bursts are “standard candles”), then source distance is inversely proportional to the square-root of burst size. For a homogeneous spatial distribution of sources, where the number of sources is proportional to the volume (i.e., distance cubed), we thus expect the number (or frequency) of bursts N to be related to the burst size S through $N \sim S^{-3/2}$. Deviations from this $-3/2$ power law indicate that either the assumption of standard candles is incorrect or the sources are distributed non uniformly.

Measures of burst size have typically been the total energy flux (i.e., fluence) or the peak flux observed during a burst and most studies have examined the size–frequency distribution in terms of the number $N(>S)$ of bursts whose fluence is greater than S (i.e., the cumulative burst size distribution often referred to as the “log N –log S ” relation). The first size–frequency studies with good statistics were based on the bursts detected by KONUS, which indicated a deficit of weaker bursts below the $-3/2$ power law (Jennings & White 1980; Mazets *et al.* 1981b). This was interpreted as evidence that the detectors were sampling bursts from beyond the edge of the spatial distribution of sources. However, the size–frequency studies were prone to significant instrumental biases, where the apparent dearth of weak events could be explained fully in terms of selection effects due to variations in burst energy spectra and durations (Higdon & Lingenfelter 1986). A solution to the problem of selection biases was suggested by Higdon & Schmidt (1990), who examined the burst size–frequency distribution in a different way using the V/V_{\max} test. The V/V_{\max} test is less susceptible to selection effects because burst size is compared directly to the instrumental detection limit at the time of each burst independently. Applied to the 123 KONUS bursts, the V/V_{\max} test indicated spatial uniformity. However, a non-uniform distribution (dearth of weak events) was indicated in larger burst samples from other instruments (Atteia *et al.* 1991;

Matz *et al.* 1992). Furthermore, several balloon-borne instruments sensitive to very weak events failed to detect bursts with the frequency expected from a uniform distribution (e.g., Meegan, Fishman & Wilson 1983). The apparent deficit of weak bursts was taken as evidence of a Galactic plane distribution of sources. This conclusion conflicted with the isotropy of burst directions. However, the existing burst directions were mainly from stronger (i.e., closer) events that would not necessarily show a significant concentration towards the Galactic plane.

BATSE, which detects bursts that are an order-of-magnitude weaker than most previous instruments, has revealed a size–frequency distribution (or V/V_{\max}) that is consistent with the earlier indications of a deficit of weak events below the $-3/2$ power law. More importantly, however, BATSE observations have shown that the directions of both strong *and* weak bursts are isotropically distributed throughout the sky (Meegan *et al.* 1992, 1994). In the simplest interpretation, this indicates that BATSE samples bursts beyond the edge of some spherical distribution of sources centered at the earth. As more bursts are detected, the constraints on this spatial distribution become exceedingly stringent. At present, the only viable source distributions are either very nearby (≤ 10 pc) or very distant (≥ 0.5 Gpc). Extended Galactic halo (or corona) distributions are also acceptable, but the ~ 8.5 kpc offset of the sun from the Galactic center combined with the BATSE isotropy measure requires halo distances in excess of 200 kpc (Hartmann *et al.* 1994a, 1994b; Hakkila *et al.* 1994b). There is no known distribution of objects in such a corona. Furthermore, at this size, the halo of our nearest neighbor galaxy M31 (Andromeda) should be evident, but no concentration of bursts from this direction is observed. Galactic disk or nearby Galactic halo source distributions are unlikely even when the standard candle assumption is relaxed by allowing a range of intrinsic burst luminosities (Mao & Paczynski 1992a; Hakkila *et al.* 1994a). However, it has been shown that two (or more) populations of different types of sources (e.g., a Galactic disk population plus a Galactic halo population) could also explain the BATSE data (Lingenfelter & Higdon 1992; Smith & Lamb 1993; Higdon & Lingenfelter 1994). Indications of a dual population are suggested by the bimodal distribution of burst durations, but the directions of both short and long bursts have been

shown to be consistent with isotropy (Kouveliotou *et al.* 1993a). The overall, all-sky rate of bursts observed by BATSE (fluence above $\sim 10^{-7}$ erg cm $^{-2}$) is ~ 800 yr $^{-1}$. Combined with the apparent lack of repetition, this implies that burst sources must be numerous.

C. Theoretical Burst Source Scenarios

Observations have shown us that gamma-ray bursts are a dynamic and variable phenomena that are difficult to characterize in general terms. This makes it fairly easy to describe them with many vastly different types of source models, while at the same time makes it difficult for any one model to explain *all* the details of *all* the different bursts. The diversity of burst properties, combined with the vast uncertainty in burst distance, has created a situation where theory is constrained little by the observations. More than 100 different *viable* theoretical explanations have been suggested and this number continues to grow almost as fast as new observations are published (see Nemiroff 1994). Many of the explanations are little more than possible scenarios, rather than detailed models. A complete burst model would have to explain the energy source, the conditions that trigger the energy release, how the energy is converted into gamma rays and how the radiation reaches the earth. This is a difficult task given that little is known about burst source objects. Traditionally, burst models have therefore concentrated on explaining the most obvious features of the burst phenomena such as the total energy requirements, the short time-scale variability and the overall spectral shapes and durations.

Because the nature of burst source objects is unknown, the theoretical study of gamma-ray bursts deals with many diverse areas of astrophysics from the orbital dynamics of comets and asteroids to cosmology and the origin of the universe. The discussion presented here is thus necessarily abbreviated by grouping the theoretical burst source scenarios by their historical significance. The clear dividing line in this characterization is the advent of the observations provided by BATSE. The following discussion focuses mainly on the sources of energy, leaving the discussion of radiation mechanisms to Chapters V and VI.

i. The Pre-BATSE Paradigm

In the few years prior to the burst observations obtained by BATSE, a body of circumstantial evidence was accumulating in favor of a Galactic neutron star (NS) burst origin. The observations of rapid variability, emission and absorption features in the energy spectra and an indication of a deficit of weak bursts in the size–frequency distribution all pointed to a compact, highly magnetized object distributed in the plane of the Galaxy—i.e., neutron stars within ~ 1 kpc. Further supporting evidence of the neutron star origin of bursts was the lack of quiescent optical counterparts down to very faint magnitudes and the knowledge that neutron stars produce other similar transient phenomena (X-ray bursts). Several burst source scenarios were developed (some in great detail) in order to explain the observed features of GRBs in the context of the known properties of Galactic neutron stars. The most obvious constraint is the required total energy release of $\sim 10^{35}$ – 10^{39} erg (assuming isotropic emission). It is important to note that although the Galactic neutron star paradigm was widely accepted, several other very different theories were proposed in this same time-frame. For instance, Paczynski (1986) suggested that bursts could originate from the merger of a compact binary system at cosmological distances.

The original Galactic neutron star burst scenario involved the impact of a comets onto the surface of neutron stars (Harwit & Salpeter 1973). Several similar models have since been developed (e.g., Newman & Cox 1980; Tremaine & Zytlow 1986; Joss & Rappaport 1984). These involve the impact of comets and asteroids or the sudden collapse of an unstable accretion disk. The burst energy is derived from the kinetic energy of the infalling mass, which for reasonable comet/asteroid/disk masses could provide the required energy for a GRB. The main difficulties in this scenario are that the rate of occurrence of such phenomena is probably too low to explain the observed burst frequency and the time-scale for the impact/collapse is too short ($\sim 10^{-4}$ s) to explain typical burst durations. Later incarnations of these scenarios attempted to solve these problems by having the masses interact with the NS magnetosphere at large radii, thereby increasing the interaction time-scale (Colgate & Petschek 1981; Colgate 1992). The frequency of these events could be increased due to the presence of a companion object

(presumably a sub-luminous star or a white dwarf) or the perturbations of nearby stars (Tremaine & Zytkow 1986).

Another type of burst scenario involves the *slow* accumulation of matter onto the NS surface, where it builds up to the point of initiating nuclear burning—releasing a flash of gamma radiation (Woosley & Taam 1976). The source of the accreted material could either be from the stellar wind of a nearby companion, or the interstellar medium. The most advanced thermonuclear models invoke a strong magnetic field to channel the slowly accreting material along the field lines and contain it at the NS polar caps (Hameury *et al.* 1982; Woosley & Wallace 1982). When the accreted material reaches a critical mass (depending on the assumed conditions of the NS surface), hydrogen burning is initiated, followed by a more explosive runaway helium reaction which results in particle acceleration and eventually a flash of gamma rays. The burst emission depends on the details the helium burning, but could account for the overall energy and temporal requirements of GRBs. Some of the energy in this scenario will be directed towards NS surface, resulting in a long thermal X-ray afterglow (Eichler & Cheng 1989). This agrees with the observations of extended emission below 10 keV in some bursts.

The other widely applied NS scenario derives energy directly from the neutron star itself through small, abrupt changes in the star's rotation rate (observed as pulsar timing “glitches”). Such changes cause large adjustments in the rigid NS surface, resulting in what is referred to as a “starquake” (Pacini & Ruderman 1974). The physics of NS interiors is not well understood, such that the exact consequences of crustal or core adjustments are not known, but the overall energy ($\sim 10^{42}$ – 10^{43} erg) is more than enough to power a GRB (Epstein 1988). One of the best developed explanations has the mechanical energy of the crust motion transferred to a strong magnetic field rooted on the surface. If there is plasma in the NS atmosphere, the oscillating magnetosphere will cause non-thermal particle acceleration which could result in a GRB (Blaes *et al.* 1989; Epstein 1992; Miller & Epstein 1992).

All the scenarios where the gamma rays are produced near the surface of a highly magnetized neutron star have problems in explaining the paucity of X rays and the abundance of gamma rays

above 1 MeV in GRB spectra. If burst emission is isotropic, some of the gamma rays will heat the neutron star surface to temperatures where it will radiate in X rays. Such strong X-ray emission is not seen, indicating that either the gamma-ray source is far from the NS surface, or the emission is outwardly beamed (Imamura & Epstein 1987). Furthermore, if MeV burst emission takes place in regions of high field strength near the NS surface, photon-field pair production interactions will attenuate the spectrum above ~ 1 MeV. No attenuation is observed, again implying that either the emission takes place far from the surface in regions where $B \leq 10^{12}$ G or the emission is beamed such that pair production attenuation is reduced (Matz *et al.* 1985).

ii. The Post-BATSE Dilemma

The observations provided by BATSE have resulted in a drastic change in the prevailing theoretical view of gamma-ray bursts. The Galactic neutron star paradigm is no longer an acceptable explanation given the observed isotropy of even the weakest bursts. Furthermore, the failure of BATSE to observe spectral line features calls into question the entire notion that bursts are associated with neutron stars. The simplest interpretation of the BATSE data leads to the dilemma that we are near the center of an unknown roughly spherical distribution of burst sources that is of limited spatial extent. The only source distributions compatible with this interpretation are (1) an extended Oort cloud around the solar system within ~ 1 pc, (2) an extended Galactic halo larger than ~ 100 kpc and (3) a cosmological distribution at ~ 1 Gpc (redshift $z \sim 1-2$). The other possibility, as mentioned earlier, is that the burst population is composed of two or more distinct distributions, in which case Galactic neutron star scenarios might still be viable.

The major difficulty with heliospheric and Galactic halo source scenarios is that no likely source objects are *known* to populate these distributions. Nonetheless, there is some evidence to support these possibilities. For instance, a roughly spherical cloud of comets surrounding the solar system is thought to extend to $\sim 10^5$ AU. If these comets are somehow associated with GRBs, they could explain the observed distributions. The problem is how to generate a gamma-

ray burst with the required energy of $\sim 10^{28}$ erg from a comet. Some possible explanations are discussed in Chapter IV, but these can probably only explain bursts from comets within a few hundred AU. Extended Galactic halo scenarios also lack a likely source of GRBs. Recently, however, observations of high-velocity neutron stars with the capability of escaping the Galaxy (Frail & Kulkarni 1991) have suggested the possibility that there is a distribution of neutron stars that populate an extended halo. Thus, many of the traditional Galactic plane neutron star scenarios have been re-assessed in the context of an extended halo distribution—the most important new constraint being the required gamma-ray energy release of $\sim 10^{41}$ erg. The most viable neutron star scenarios for halo bursts are those involving starquakes, where the larger energy per burst is a result of larger quake regions on the stellar surface (Blaes *et al.* 1992). Solid body accretion (i.e., asteroids and comets) could also yield the required energy if the mass of the secondary object were sufficiently large (Colgate & Leonard 1994). Other suggestions include the collapse of a white dwarf into a neutron star (Woosley & Baron 1992) and the merger of a white dwarf binary system (Eichler & Silk 1992), which both have difficulty in explaining the observed rate of bursts. All extended halo scenarios are pushed to their limits as more BATSE bursts continue to indicate a higher degree of isotropy—requiring a larger halo (Meegan *et al.* 1994).

One of the most straightforward interpretations of the BATSE results is that burst sources reside at cosmological distances ($z \sim 1$), where the distribution is known to be highly isotropic and an apparent deficit weak bursts is expected due to inflationary redshift effects (Mao & Paczynski 1992b; Fenimore *et al.* 1993). In this regime, bursts must liberate $\sim 10^{50}$ ergs of energy (assuming isotropic emission). This would appear to be difficult given the rapid variability of GRB intensities. However, several viable scenarios have been suggested and the cosmological interpretation of bursts can now be considered the popular favorite. Cosmological burst scenarios involving supernovae, AGN, black holes and more exotic phenomena have been suggested ever since the first burst observations (see Nemiroff 1994), but they have not been given much consideration until the recent BATSE results. The mechanisms most often invoked are the

collapse of a compact object (e.g., neutron star or a black hole) or the merger of a compact binary (Woosley 1993; Paczynski 1986; Goodman 1986). Both scenarios result in the release of $\sim 10^{53}$ erg of energy in the form of neutrinos, which will rapidly annihilate to form e^+e^- pairs that eventually produce a gamma-ray burst of sufficient luminosity (Eichler *et al.* 1989). Four binary pulsars have been observed in our Galaxy. If, through gravitational radiation, these systems eventually decay and merge, the suggested rate is around 10^{-6} yr $^{-1}$ per galaxy (Narayan, Piran & Shemi 1991). When integrated out to redshifts $z \sim 1$, this is consistent with the rate of ~ 800 bursts per year observed by BATSE. If GRBs do originate at cosmological distances, we would occasionally expect them to be gravitationally lensed by foreground galaxies. No lensed events have been detected so far, but this is not inconsistent with the expected rate (Nemiroff *et al.* 1994a; Grossman & Nowak 1994). As mentioned earlier, one interpretation of the BATSE conclusion that weak bursts are longer (on average) than strong bursts is cosmological time dilation—implying sources at $z \sim 1$. In this interpretation, the weaker bursts should also be softer than the strong events due to redshift. There is now some indication of this effect in the BATSE data (Nemiroff *et al.* 1994b). Thus, the body of evidence now appears to be accumulating in support of cosmological burst scenarios. However, the history of gamma-ray bursts indicates we should be wary.

D. Present Work

From the preceding discussion, it is obvious that many questions remain in the gamma-ray burst mystery. The fact that theoretical explanations have failed to yield much insight implies that more observations are probably the only way to make any significant progress. Two of the most important gaps in our observational understanding of the burst phenomena are that we lack a clear picture of the broad-band spectra of bursts (especially at high and low energies) and that we lack an understanding of the small-scale angular distribution of burst directions. In the present work, we study the gamma-ray burst phenomena with a new instrument that allows us to investigate these important questions.

The Imaging Compton Telescope (COMPTEL), one of four instruments aboard *Compton*, is a valuable tool with which to study gamma-ray bursts for several reasons. First, COMPTEL can localize burst sources through direct imaging with a mean accuracy of $\sim 1^\circ$, allowing us to probe the small-scale distribution of source directions and explore the possibility of burst recurrence with good sensitivity. The combination of COMPTEL burst localization with Interplanetary Network timing information constrains burst directions with sufficient accuracy to allow them to be searched for quiescent low-energy counterparts. Second, COMPTEL measures burst spectra above ~ 1 MeV with good sensitivity due to its clean response and low background. This capability is used to investigate the properties of high-energy (MeV) burst emission. The ability to examine such emission on short time scales is a significant feature that is used to constrain burst attenuation mechanisms. Furthermore, since COMPTEL operates in coordination with the other *Compton* instruments (e.g., BATSE) it is possible to examine the relation of MeV burst emission to that at other energies through simultaneous observations. Finally, in coordination with BATSE, COMPTEL has the ability to rapidly determine burst directions. This ability is used to obtain deep, rapid observations of bursts at optical and radio frequencies, where no previous measurements exist. The primary disadvantage of COMPTEL in the study of GRBs is that not many bursts are detected due to the limited field-of-view and poor sensitivity at low energies where bursts emit most of their power. However, even the limited number of burst observations provide important new information in areas where previous instruments have been most limited.

II. INSTRUMENTATION AND ANALYSIS TECHNIQUES

A. COMPTEL: The Imaging Compton Telescope

The successful launch and deployment of the Compton Gamma Ray Observatory (Figure 2.1) in April 1991 began a new era in gamma-ray astronomy. Orbiting the earth at a height of ~450 km, it provides us with the first long-term wide-band survey of the high-energy sky. The Imaging Compton Telescope (COMPTEL), one of four scientific instruments aboard *Compton*, is a wide-field imaging gamma-ray detector observing the sky in the unexplored MeV transition region of the energy spectrum. As such, its primary mission is to provide a global first-look at the cosmic

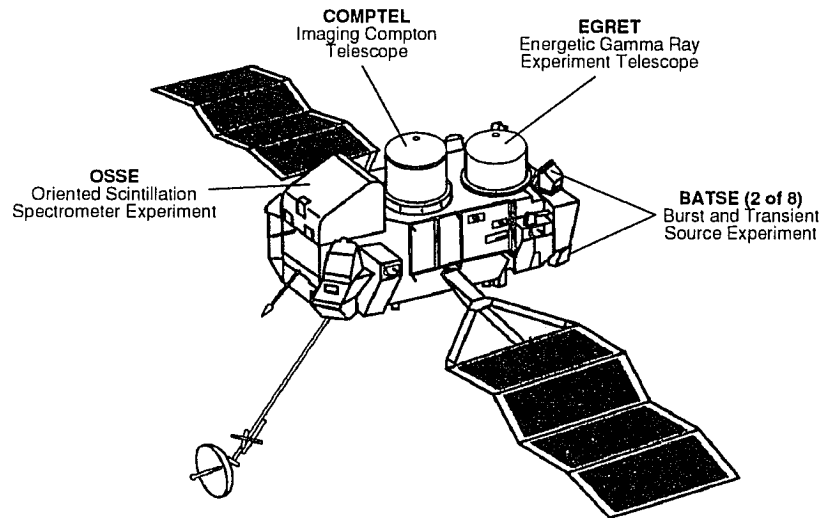


Fig. 2.1. Schematic diagram of the Compton Gamma Ray Observatory spacecraft showing its four scientific instruments.

gamma radiation at these energies—including an all-sky survey of galactic and extragalactic sources (e.g., pulsars, X-ray binaries, active galactic nuclei, etc.), diffuse continuum and line emission. The COMPTEL survey would not be complete, however, without an investigation of the transient sources that can momentarily dominate the gamma-ray sky. Foremost in this investigation is the study of gamma-ray bursts. With its unique imaging and spectral capabilities

COMPTEL provides a valuable tool with which to probe these enigmatic sources. In this chapter, the COMPTEL instrument and burst analysis techniques are discussed.

i. Instrument Characteristics

As a Compton telescope, COMPTEL shares its basic “double-scatter” detection principle with several earlier balloon-borne instruments (see e.g., Schönfelder, Himer & Schneider 1973; Herzo *et al.* 1975). It consists of two layers of scintillation detector modules, D1 and D2, separated by a distance of 1.5 m (Figure 2.2). An incident gamma-ray photon first interacts in one of seven D1 modules which are filled with a low Z scintillating liquid (NE213A), optimizing the chance of a single Compton scatter. Ideally, the scattered photon is then completely absorbed in one of 14 high Z, NaI(Tl) D2 modules. The interaction location (\bar{x}_1, \bar{x}_2) and energy deposit (E_1, E_2) in each module are indirectly measured by a collection of photomultiplier tubes (PMTs) whose gains are monitored using two ^{60}Co calibration units. The D1, D2 interaction sequence is identified by a time-of-flight coincidence measurement (TOF; resolution ~ 1 ns) and the absolute time of each such “telescope event” coincidence is recorded with an accuracy of 125 μs (see Schönfelder *et al.* 1984, 1993).

For an ideal telescope event the incident photon’s energy $E_\gamma = E_{\text{tot}} \equiv E_1 + E_2$ and its direction is constrained to an annular ring on the sky (see Figure 2.2). This “event circle” of possible source locations is centered on the scatter direction ($\bar{x}_2 - \bar{x}_1$) and has an angular radius $\bar{\varphi}$ defined by the kinematics of Compton scattering with

$$\cos(\bar{\varphi}) = 1 - m_0 c^2 \left[\frac{1}{E_1} - \frac{1}{(E_1 + E_2)} \right], \quad (2.1)$$

where $m_0 c^2$ is the rest energy of the electron (0.511 MeV). Azimuthal ambiguity in the photon arrival direction *along* the event circle is removed by combining many events from the same source. Uncertainty in the derived source location depends on the number of source events and the accuracy of the individual D1, D2 measurements. Complicating matters are non-ideal events (e.g., multiple scattering in D1, incomplete absorption in D2, etc.) resulting in event circles which do not intersect the source location. These events are difficult to distinguish from the ever-

present background.

To reduce the background, each COMPTEL detector layer is surrounded by two active plastic anticoincidence shields (Veto domes) that reject charged-particles. Pulse-shape measurement in D1 (PSD) is used to reject neutron-induced events. The time-of-flight coincidence measurement also significantly reduces background by discriminating “forward” moving source events (D1 → D2) from “backward” moving photons (e.g., background from Earth’s atmosphere).

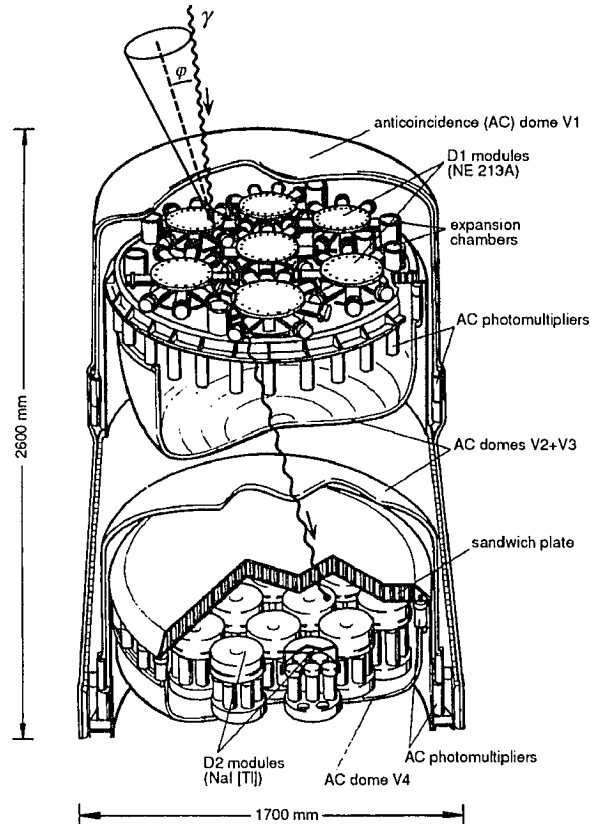


Fig. 2.2. Schematic diagram of the Imaging Compton Telescope (COMPTEL) illustrating its principle of detection.

Hardware energy thresholds in the D1 and D2 detector modules further limit COMPTEL’s background by reducing the overall count rate, thus decreasing the chance of accidental coincidences. The in-flight thresholds of ~ 50 keV in D1 and ~ 600 keV in D2 set the lower limit of the COMPTEL energy range to $E_{\gamma} \geq 650$ keV. An upper limit on the effective energy range (~ 30 MeV) results from the decreasing efficiency of Compton scattering in D1 at higher energies.

The energy thresholds also limit the field-of-view (FOV) by bounding the range of possible $\bar{\varphi}$ scatter angles. The nominal FOV is ~ 1 sr, but *strong* sources from a considerably wider field (up to zenith angles $\theta \approx 50^\circ$) can be measured. Data selections applied during analysis can significantly alter the effective COMPTEL energy range and FOV. These selections are chosen (depending on the application) so as to optimize signal and minimize background.

ii. General Instrument Response

The performance of COMPTEL was measured prior to launch in a series of calibrations with monoenergetic gamma-ray sources (Diehl *et al.* 1992). These calibrations determined the overall performance characteristics of the telescope and all of its sub-systems. However, the calibration measurements are inadequate for full response determination due to their sparse coverage, close source proximity and background contamination. Rather, a Monte Carlo simulation system (based on the CERN-GEANT package) is used incorporating a detailed model of COMPTEL's mass distribution and empirically-determined instrumental characteristics such as thresholds, resolutions, TOF and PSD distributions (Kippen 1991). This simulation system is employed throughout this work to determine the energy and angular response of COMPTEL to a variety of different sources.

The full COMPTEL response \mathfrak{R} to a monoenergetic point-source with energy E_γ can be described in general terms by

$$\mathfrak{R} = \mathfrak{R}(E_{\text{tot}}, \bar{\varphi}, \chi, \psi | E_\gamma, \chi', \psi'), \quad (2.2)$$

where (χ, ψ) and (χ', ψ') represent azimuth and altitude coordinates of the scatter direction and source location in an arbitrary spherical sky coordinate system (e.g., $\{\chi, \psi\}$ could represent $\{\alpha, \delta\}$ or $\{l, b\}$). Because of its complexity, this multi-dimensional response function is not used directly. Rather, assumptions about the source location or spectrum are made (depending on the application) that reduce the number of “data-space” dimensions. The details of these different representations of the COMPTEL response function will be discussed in later sections of this chapter. Here, only the fundamental measures are discussed.

The most basic measure of instrument response is the efficiency with which incident photons are detected (the total integrated response). A related quantity, the effective detection area (product of telescope efficiency and exposed D1 detector area) as determined from simulation, is shown in Figure 2.3. The COMPTEL efficiency peaks at only $\sim 10^{-2}$ in the range 2–4 MeV. It is only through multi-parameter background rejection that good sensitivity is achieved (Schönfelder *et al.* 1993). At low energies (< 1 MeV) the efficiency falls off sharply due to the D1, D2 energy thresholds (reducing the range of allowable $\bar{\varphi}$), while at high energies photon interactions in the veto domes cause a gradual efficiency degradation. At all energies the efficiency falls off sharply with incident zenith angle θ in a roughly linear fashion and is weakly dependent on incident azimuth angle ϕ .

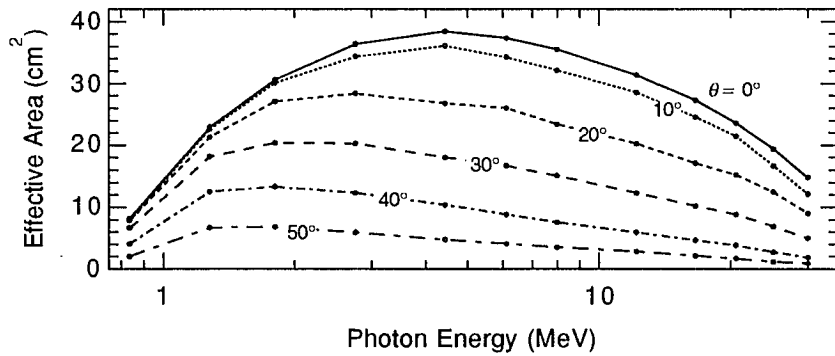


Fig. 2.3. Effective detection area of COMPTEL (as determined from simulation) as a function of energy for several different point-source incident angles (nominal data selections).

The spatial response of COMPTEL to a known point-source is described in simple terms by the quantity $\bar{\varphi} - \varphi_{\text{geo}}$, where φ_{geo} is the true angle between the scatter direction and the known source position. We would expect this quantity, known as the *angular resolution measure* (ARM), to be equal to zero for an ideal telescope event with no measurement errors. In reality, energy and event location measurement errors produce a finite width (angular resolution) in the ARM distribution and non-ideal events produce an asymmetry with $\bar{\varphi} > \varphi_{\text{geo}}$ (see Figure 2.4). Above ~ 2 MeV the intrinsic angular resolution is roughly a constant ($\sim 1^\circ$) determined mainly by

event location uncertainties within the modules, while at lower energies it is degraded ($\sim 2^\circ$) due to the poorer energy resolution in the detectors. At all energies the angular resolution is roughly independent of source location within the FOV.

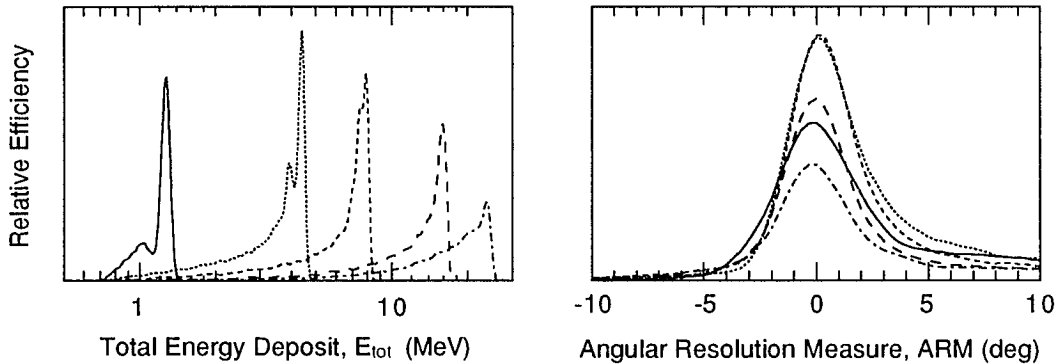


Fig. 2.4. Simulated energy (left) and angular (right) response of COMPTEL to monoenergetic point sources at normal incidence with nominal data selections.

The total energy response of the telescope to a monoenergetic source is much like that of an ordinary NaI detector, with a complete absorption photo-peak, escape peaks and Compton continuum (see Figure 2.4). At energies ≥ 10 MeV the full-energy peak is no longer resolvable and the response becomes a superposition of all the energy loss processes. Since E_{tot} is the sum of the individual energy deposits in D1 and D2, the total energy resolution is dependent both on the intrinsic detector resolutions and the details of individual scatters. The total energy resolution $\Delta E_{\text{tot}}/E_\gamma$ decreases continuously from $\sim 10\%$ (FWHM) at 1 MeV to $\sim 4\%$ at 20 MeV.

iii. In-Flight Performance and Background

COMPTEL began astronomical measurements on 21 April 1991—shortly after the successful launch and deployment of *Compton*. After a brief verification phase, normal observing mode began with fixed-pointing observation periods each lasting about two weeks. During the subsequent three years COMPTEL has maintained a relatively constant level of performance although several of its detector modules have been inoperative for considerable intervals and the D2 energy thresholds have increased somewhat over time. The actual in-flight background is ~ 3 –

4 times higher than predicted prior to launch, but COMPTEL is still more sensitive than previous instruments in its energy range (Schönfelder *et al.* 1993).

An example of the COMPTEL background is shown in Figure 2.5, where the telescope event rate (0.75–30 MeV) with nominal data selections for a typical day early in the mission is displayed. The events in this figure represent a conglomerate of instrumental background, astrophysical sources and Earth albedo photons. Also plotted in this figure is the minimum angle from the COMPTEL zenith to the earth's horizon or *earth horizon angle* (EHA). The highest event-rates are clearly caused by the presence of the earth in the FOV (EHA < 0) every orbital period (~90 min).

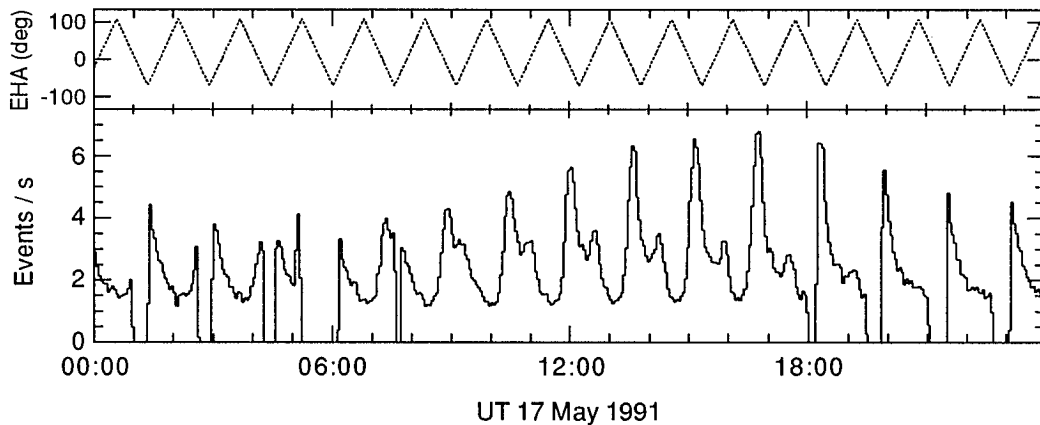


Fig. 2.5. Orbital variations of the telescope event-rate (lower panel) and earth horizon angle (EHA; upper panel) over a typical observing day.

Even when the Earth is not in the FOV (EHA > 0) the background rate is modulated by the geomagnetic environment (e.g., as traced by the magnetic cut-off rigidity; den Herder *et al.* 1992). These effects are affixed roughly to the earth and are weakly time-variable so that as the spacecraft orbits the earth, COMPTEL experiences a changing magnetic field that modulates the background rate. Further complicating matters is the background caused by charged-particle activation in the spacecraft material. The activation-induced background depends not on geomagnetic conditions, but rather on the time since activation. This is most apparent just after

the spacecraft passes through the South Atlantic Anomaly (SAA). While passing through the SAA COMPTEL detectors are disabled to avoid excessive count rates. These periods are evident as data gaps in Figure 2.5.

iv. Burst Detection Capabilities

COMPTEL employs two independent operating modes when observing transient phenomena such as solar flares and cosmic gamma-ray bursts. In parallel to the main telescope mode, two D2 modules accumulate time-resolved energy spectra in the range 0.1–10 MeV. This “burst mode” (or burst system analyzer; BSA) is in principle sensitive to sources in all 4π sr. However, blockage from D1 and the surrounding spacecraft material limit the burst mode sensitivity in many directions. At the onset of events triggered by the BATSE instrument, the BSA detectors accumulate six 1 s spectra and 256 6 s spectra before returning to normal background operation with 100 s integration (Winkler *et al.* 1986). This work is concerned mainly with observations made in the telescope mode. The BSA data are employed only for comparison.

In detecting gamma-ray bursts, COMPTEL (telescope) is in *most* cases a photon-limited instrument whose sensitivity is governed by its low detection efficiency and not by background. The minimum detectable burst fluence $S(>E; \text{erg cm}^{-2})$ is limited to (Winkler *et al.* 1986)

$$S_{\min}(>0.75 \text{ MeV}) = \frac{\bar{E} N(>0.75 \text{ MeV})}{A_{\text{eff}}}, \quad (2.3)$$

where \bar{E} is the spectrum-dependent mean photon energy in the range 0.75–30 MeV, A_{eff} is the effective detection area for completely absorbed events and N is the number of completely absorbed events from the source (say, within a 5° radius). If we require at least 20 events from an on-axis $E^{-2.0}$ power law burst source ($A_{\text{eff}} = 31 \text{ cm}^2$; $\bar{E} = 3.7 \text{ MeV}$) then the minimum detectable fluence S_{\min} is $4.5 \times 10^{-6} \text{ erg cm}^{-2}$ (assuming a fully functional COMPTEL). The burst sensitivity calculated in this manner (Figure 2.6a) is a strong function of zenith angle and energy spectral shape of the flux.

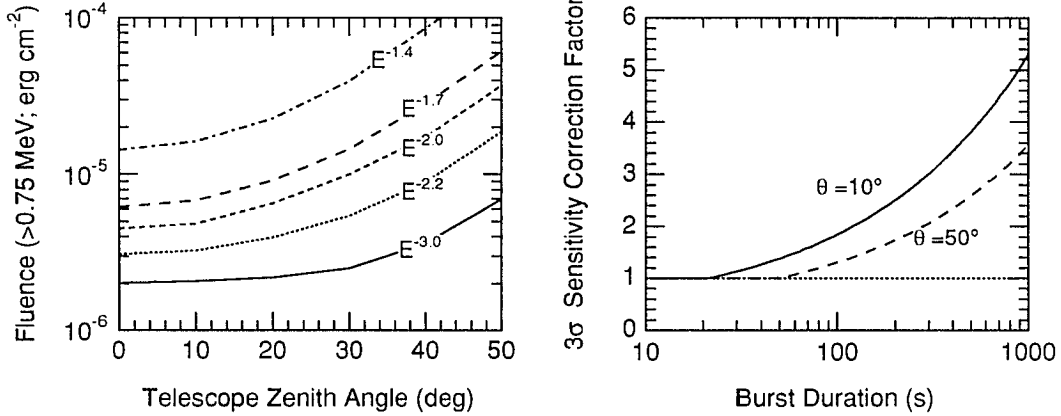


Fig. 2.6. a. (left) COMPTEL telescope burst sensitivity (photon-limited) as a function of burst zenith angle for several different power law spectra. b. (right) Background (3σ) sensitivity correction factors as a function of burst duration for two different zenith angles (correction factors for intermediate zenith angles lie between these two curves).

The average background rate in a 5° -radius element of the FOV over a typical two week observation period ranges from 0.2 Hz at $\theta = 50^\circ$ to 0.6 Hz at $\theta = 10^\circ$ (0.75–30 MeV). Orbital background variations can be as large as a factor of two, and are a problem in longer duration, low fluence bursts. The detection significance for such bursts is given by (Li & Ma 1983)

$$\sigma_{\text{det}} = \frac{N_S}{\sqrt{N_S + 2N_B}}, \quad (2.4)$$

where N_S is the number of source counts (related to the burst fluence through equation 2.3) and N_B is the number of background counts (proportional to the burst duration). If the number of source counts required for a significant detection above background (N_S) exceeds the number of counts required for imaging ($N_S \sim 20$) then the detection is background-limited, rather than photon-limited. In this case, the sensitivity estimates of Figure 2.6a are too low. Correction factors (roughly independent of spectral shape) for $\sigma_{\text{det}} = 3$ are plotted as a function of burst duration in Figure 2.6b. From this figure it is evident that bursts shorter than ~ 25 s are always photon-limited regardless of zenith angle. For bursts longer than 25 s, background becomes increasingly important, especially at smaller zenith angles. Fortunately, the temporal structure of most bursts is quite spiky, so that even long duration events contain short time-scale structures.

For example, a 200 s burst at the COMPTEL sensitivity limit could easily be detected if most of its fluence occurs in a 10 s pulse.

For intense bursts, or burst intervals with $S \geq 10^{-4}$ erg cm⁻², electronics and telemetry deadtime limit COMPTEL's ability to register events. These limitations do not usually effect the overall source detection and localization since bursts are seldom intense over their entire duration. However, deadtime severely limits the ability to perform spectral analysis. In this case, correction factors must be estimated using counting rates accumulated onboard the spacecraft at various points in the telescope event detection and telemetry process. Unfortunately these onboard rates are recorded with low time-resolution (2.048 s or 16.384 s), so deadtime estimates over short intervals are only approximate.

B. Fundamental Analysis Techniques

In this section, the techniques used to reduce raw COMPTEL data into source locations and energy spectra are discussed. Some of these techniques are applied generally to COMPTEL data, but have been significantly modified for use with gamma-ray bursts.

i. Data Processing and Selection

The telescope measures directly the following quantities for each event:

- pulse height in each detector module PMT
- pulse shape in each D1 module PMT
- detector module identifiers in D1 and D2
- time-of-flight between D1 and D2
- absolute time of the event
- event type identifier (as selected onboard)

In addition to these time-tagged measurements, several other parameters are recorded at a lower frequency (engineering data, onboard count rates, orbit and aspect data, etc.). These raw data are reduced through the following processes (see e.g., den Herder *et al.* 1992):

- (1) Bulk telemetered data are divided into several different data sets based on common usage

(e.g., raw event data, orbital data, calibration data, etc.).

- (2) D1 and D2 PMT pulse heights are converted into energies (E_1 , E_2) using ^{60}Co events (so-called in-flight calibration).
- (3) Interaction locations within the D1 and D2 modules (\bar{x}_1 , \bar{x}_2) are determined from the relative PMT pulse heights using the Anger camera principle (Connors *et al.* 1992).
- (4) Background sensitive parameters (i.e., TOF, PSD) are corrected for energy dependence and are used to classify events.

Final processed event quantities include scatter direction (χ , ψ), scatter angle ($\bar{\varphi}$) and total energy deposit (E_{tot}). The processed events (combined with orbital and livetime information) are the basis for all further analysis.

In the analysis, processed event data are selected to optimize signal and minimize background. In general, data selections depend on the application. Nominal data selections include (Schönfelder *et al.* 1993):

- (1) $70 \text{ keV} \leq E_1 \leq 20 \text{ MeV}$: to minimize the effect of the in-flight energy thresholds ($\sim 50\text{--}65$ keV) and reduce the neutron-induced background (difficult to distinguish from gamma rays with high D1 energy deposits).
- (2) $650 \text{ keV} \leq E_2 \leq 30 \text{ MeV}$: to minimize the effect of the in-flight energy thresholds ($\sim 600\text{--}650$ keV) and reduce instrumental effects (e.g., unrealistically high energy deposits).
- (3) $E_{\text{tot}} \geq 750 \text{ keV}$: to further minimize the effect of the D1/D2 energy thresholds.
- (4) $115 \leq \text{TOF} \leq 130$ channels: to preferentially select forward (D1 \rightarrow D2) moving events (centered at channel 120 ± 4) and reject backward moving events (centered at channel 80 ± 4).
- (5) $\text{PSD} \leq 110$ channels: to accept gamma-ray events (centered around channel 80) and reject neutron-induced events (centered around channel 120).
- (6) $\bar{\varphi} \leq 50^\circ$: to improve signal-to-noise ratio (S/N).

For high S/N sources like GRBs, these nominal data selections can be relaxed somewhat to improve statistics and sidestep instrumental effects (e.g., the dependence of TOF and PSD

selections on measured energy deposits).

ii. Burst Source Localization

Although the simple concepts of event circles and ARM distributions presented earlier are illustrative of the operation and performance of COMPTEL, they do not include enough response information for accurate source localization. Rather, localizing gamma-ray sources with COMPTEL involves recognizing the known source signature in an observed multi-parameter distribution. A description of the details (as related to burst localization) follows.

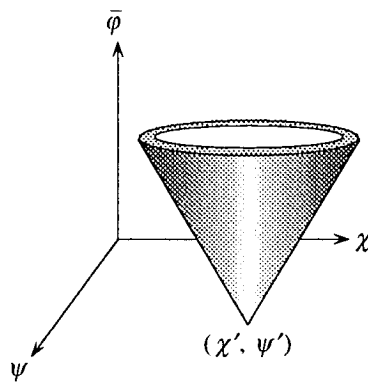


Fig. 2.7. Illustration of the COMPTEL spatial response to a point-source of gamma rays located at sky-coordinates (χ', ψ') .

a. Spatial Response Representation. As discussed earlier, the general COMPTEL response to a point-source given by equation (2.2) is a complicated function of many dimensions and is therefore not directly used for analysis. Rather, for source localization, one assumes an incident photon energy spectrum and integrates E_{tot} over some range of interest. The resulting spatial response $\mathfrak{R} = \mathfrak{R}(\chi, \psi, \bar{\varphi} | \chi', \psi')$ is viewed in the remaining three data-space dimensions as a partially filled cone with 45° opening angle (Figure 2.7) whose vertex is centered on the source position (χ', ψ') . Ideal singly-scattered, completely absorbed events occupy the cone mantle (blurred by measurement errors) while non-ideal events are interior to the cone.

This version of the response is still too complicated to use practically since it depends strongly on the source position within the FOV. Fortunately, much of this dependence is a purely

geometrical effect reflecting the finite dimensions and discrete elements of the instrument. The full response is therefore factored into two parts: one which depends only on geometry (g) and one which contains the inherent physical response of the instrument (f). In this representation the expected number of detected events in a single data-space element $(\chi, \psi, \bar{\varphi})$ is to good approximation given by the convolution (Strong *et al.* 1992)

$$n(\chi, \psi, \bar{\varphi}) = g(\chi, \psi) T \int d\Omega \int d\chi' d\psi' I(\chi', \psi') A(\chi', \psi') f(\chi, \psi, \bar{\varphi}; \chi', \psi'), \quad (2.5)$$

where $d\Omega$ is the solid angle of the data-space element, g is the geometrical probability that a photon scattered in D1 will encounter a D2 module, I is the sky intensity distribution (e.g., $I = \delta(\chi - \chi', \psi - \psi')$ in the case of a point-source), A is the physical area of the D1 detecting surface, T is the integration time and f is the probability that a photon encountering D1 physically interacts in both the D1 and D2 planes (the geometry-independent instrument response or *point spread function*; PSF).

In this simplified spatial response representation, the cone-shaped PSF, which incorporates all of the inaccuracies and non-ideal response of the instrument, is independent of source location. Thus, a single PSF can be used to image sources anywhere in the FOV (or even an extended source). However, it is important to note that the PSF *is* dependent on the assumed energy spectrum of the source. The effect of this dependence on burst source localization is small as discussed in Appendix B. The PSF is determined by simulating a point-source of photons with an assumed energy spectrum. To minimize computation, the resulting simulated telescope events (subject to data selections) are binned into a two dimensional version of the full 3-D data-space (see Figure 2.8), $\tilde{f}(\varphi_{\text{geo}}(\chi, \psi), \bar{\varphi})$, with bin sizes on the order of the instrumental resolution. The geometrical-dependence of this 2-D response is removed through division by the geometry function g that is dependent only on the scatter direction coordinate (φ_{geo}). Assuming azimuthal symmetry, the final 3-D PSF is “unfolded” from the 2-D version using

$$f(\chi, \psi, \bar{\varphi}) = \tilde{f}(\varphi_{\text{geo}}, \bar{\varphi}) \frac{\Delta\Omega}{\Delta\bar{\Omega}}, \quad (2.6)$$

where the solid angle factor ($\Delta\Omega/\Delta\tilde{\Omega}$) accounts for the discrepancy between the spherical and radial grids in the 3-D and 2-D coordinate systems, respectively (Diehl *et al.* 1992).

The PSF used for all burst source localization discussed in this text is depicted in Figure 2.8 (2-D representation). This PSF was generated by simulating an $E^{-2.0}$ power law spectrum at $\theta = 10^\circ$. The simulated events were subject to standard selections with the exception of a relaxed TOF window (channels 110–130) to improve statistics. Standard energy selections were employed to minimize the effects of the changing D1/D2 thresholds over the three years of observation, thus allowing the use of a single PSF for all COMPTEL GRBs. The resulting events ($>10^5$) were binned according to instrumental resolution into the 2-D data-space (1° bins in φ_{geo} and 2° bins in $\bar{\varphi}$) to create the PSF shown in Figure 2.8.

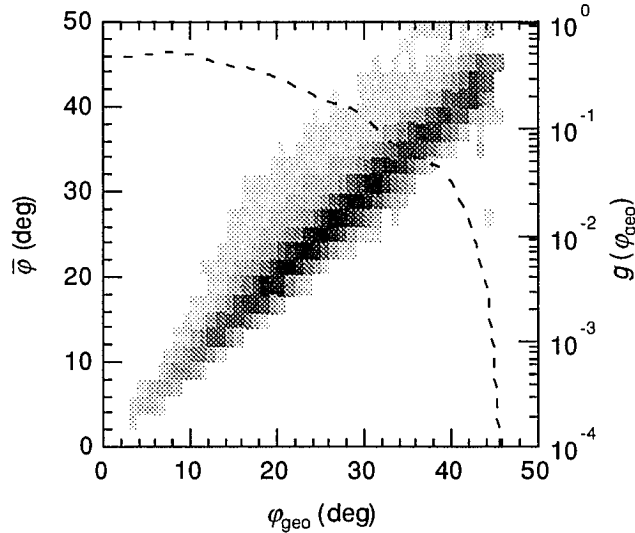


Fig. 2.8. COMPTEL point spread function (determined from simulation) in two dimensions for an assumed $E^{-2.0}$ power law spectrum in the range 0.75–30 MeV. The dashed line shows the contribution of geometry (right axis) as a function of φ_{geo} .

Imaging proceeds by searching for the PSF signature (corrected for in-flight geometry and exposure) in the binned 3-D data-space distribution of observed telescope events (subject to data selections as above). In addition to the normal geometrical factors, the in-flight geometry function must account for the earth in the FOV. Several different imaging techniques have been applied to COMPTEL data, the most common being the maximum-entropy (Strong *et al.* 1992)

and maximum-likelihood (de Boer *et al.* 1992) methods. Whereas the primary aim of the maximum-entropy method is the production of sky intensity images, the aim of the maximum-likelihood technique is to constrain the actual source parameters (statistical significance, flux, source position, etc.). The maximum-likelihood method is therefore employed for all burst source localization in this work.

b. Maximum-Likelihood Imaging. Starting with *a priori* knowledge of source (PSF; f) and background (B) signatures in the COMPTEL data-space, the *expected* number of counts m in a data-space element i given a single point-source located in sky pixel j is (from equation 2.5)

$$m_i = B_i + (g_i I_j X_j f_{i,j}), \quad (2.7)$$

where B is the number of background counts and X is the exposure ($A \times T$). If a distribution of $\{n_i\}$ counts are *observed* in the full data-space (with elements $i = 1 \dots N$), then the likelihood of a source at this location is (assuming Poisson statistics)

$$L(\{n_i\} | H_{S+B}) = \prod_{i=1}^N \frac{m_i^{n_i} e^{-m_i}}{n_i!}, \quad (2.8)$$

where H_{S+B} denotes that this hypothesis includes both source and background contributions. A similar expression, $L(\{n_i\} | H_B)$, is obtained for the background-only hypothesis by substituting $m_i = B_i$ in place of equation (2.7).

Adopting source and background distribution scale-factors (but not shape) as variable model parameters in equation (2.7), the likelihood of the two different hypotheses can be independently maximized (denoted by \hat{L}) for any trial source position on the sky. This is the computationally-intensive task of the maximum-likelihood method. The resulting sky-map of the quantity

$$\lambda = 2 \ln \left(\frac{\hat{L}(\{n_i\} | H_{S+B})}{\hat{L}(\{n_i\} | H_B)} \right) \quad (2.9)$$

(log likelihood ratio) is then used to estimate and constrain the source parameters. The most likely position of an unknown source (e.g., cosmic burst) corresponds to the maximum $\lambda \equiv \hat{\lambda}$ which formally obeys the χ^2 probability distribution with three degrees of freedom (source flux and position; see de Boer *et al.* 1992). Thus, $\hat{\lambda} \geq 14.2$ indicates a statistically significant 3σ

detection (Lampton, Margon & Bowyer 1976). For such significant detections the source location is constrained by the quantity $\Delta\lambda = \bar{\lambda} - \lambda$, which is distributed as χ^2_2 so that formal 1σ , 2σ and 3σ confidence regions are defined where $\Delta\lambda \approx 2.3, 6.2$ and 11.8 , respectively.

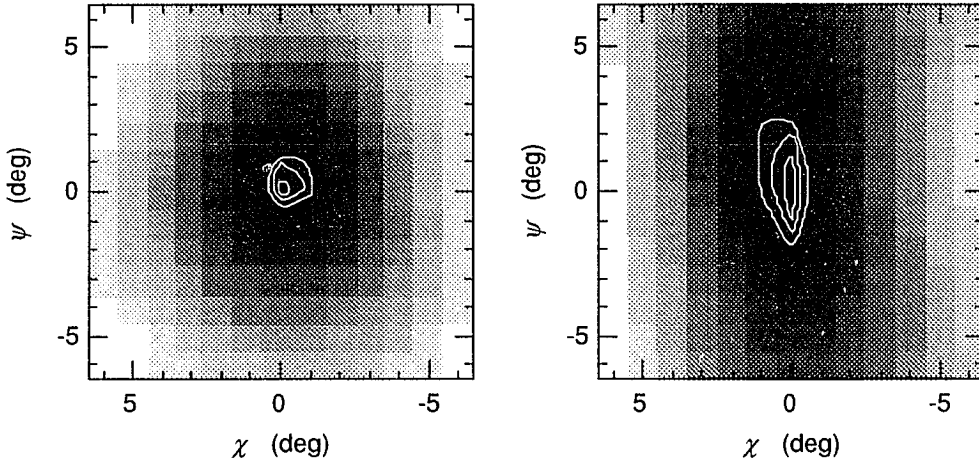


Fig. 2.9. Maximum likelihood ratio sky-maps of two simulated point sources located at different zenith angles: $\theta = 0^\circ$ (left) and $\theta = 40^\circ$ (right). The darkening gray-scale indicates increasing source likelihood (λ), while white contours indicate source location constraints at the 1σ , 2σ and 3σ confidence levels.

Examples of maximum-likelihood imaging are shown in Figure 2.9, where λ sky-maps for two simulated $E^{-2.0}$ power law sources at different zenith angles (θ) are displayed. These sky-maps were generated using the simulated PSF shown in Figure 2.8 and a simple flat background model. The simulated sources each incorporate ~ 200 telescope events in the range 0.75–30 MeV. Since no background events are included in these simulations, the sources are very statistically significant with peak $\lambda > 400$ and the source locations ($\chi = 0^\circ, \psi = 0^\circ$ in both cases) are well constrained within the 1σ error contours. The elongation apparent in the $\theta = 40^\circ$ image is an artifact of COMPTEL's azimuthal ambiguity in determining photon directions. This feature of the COMPTEL spatial response becomes increasingly apparent for sources at large zenith angles.

It is important to note that the source parameter constraints computed with maximum-likelihood technique incorporate only statistical errors (e.g., the location of a source with infinite counts will be perfectly constrained with zero statistical uncertainty). Systematic errors such as

those arising from inaccuracies in the PSF and/or background model must be determined separately (see Appendix B).

c. Background Determination. From the preceding discussion, it is evident that the most important ingredients in the COMPTEL imaging process are the source (PSF) and background models in data-space. For cosmic bursts, with a high signal-to-noise ratio, accurate determination of the background is not as crucial as for weaker sources (e.g., diffuse Galactic emission). However, it is still important since the formal behavior of the λ -statistic implicitly assumes accurate source and background models. The background model for burst sources must reflect the full distribution of non-source events in $(\chi, \psi, \bar{\varphi})$ present during the burst. The transient nature of GRBs makes the determination of this distribution different from other COMPTEL imaging applications since one cannot integrate over long intervals of time to sample the background distribution.

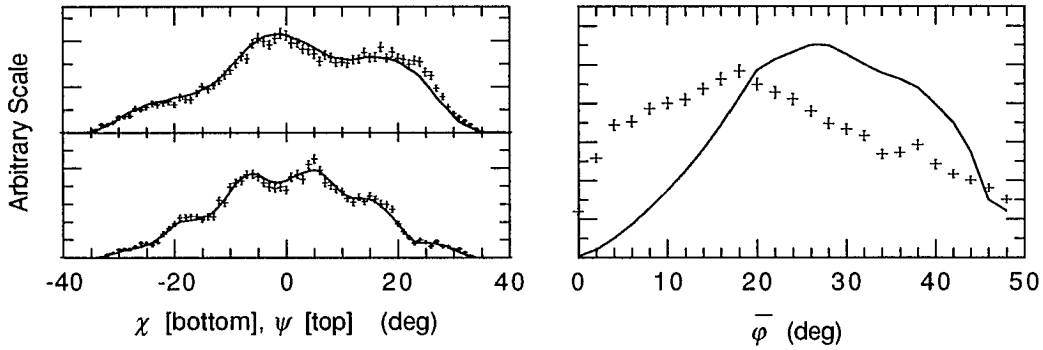


Fig. 2.10. Typical background data-space distributions from isotropic model (solid lines) and direct measurement (data points).

A simple model of the background is obtained by convolving an isotropic, all-sky distribution of photons with the PSF. The resulting data-space in (χ, ψ) closely resembles the geometry function, while the $\bar{\varphi}$ -distribution resembles that of the PSF. In (χ, ψ) this is a fairly good approximation to the actual background since the geometry function incorporates Earth-blockage effects and is roughly independent of energy spectrum. In $\bar{\varphi}$, however, this is a poor approximation, since the complicated mixture of lines and continua that contribute to the energy

spectrum of the background are *much* different than the spectrum used to compute the PSF. An example of isotropic model distributions are compared to measured background from a typical 30 minute interval in Figure 2.10. Note the agreement in (χ, ψ) and the discrepancy in $\bar{\phi}$.

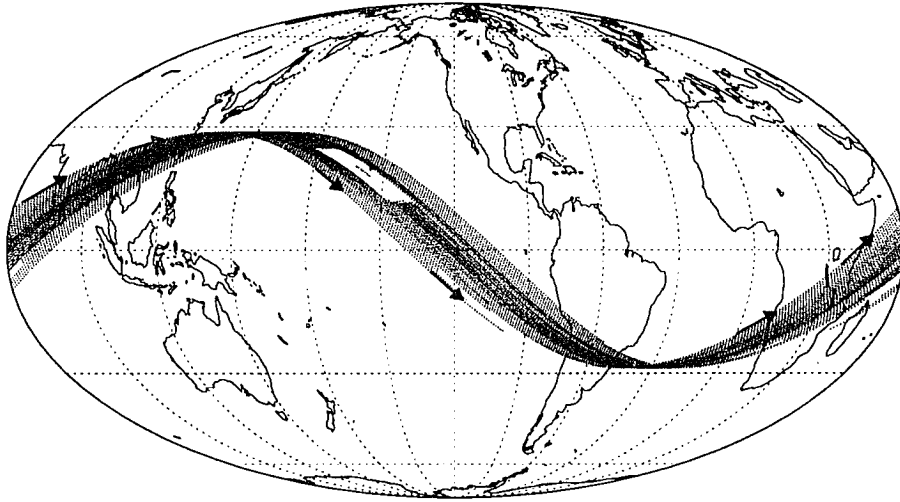


Fig. 2.11. Map of the earth showing the orbit of *Compton* from 17–19 May 1991. Arrows show the direction of motion over a single orbit and the white rectangular region indicates a typical background sampling window.

The only practical way to incorporate all of the background contributions into the imaging background model is to directly sample events which were detected under orbital history conditions similar to the source observation. The rotation rate of the earth and orbital period of the spacecraft are such that *Compton* nearly returns to the same geographic location every 15 orbits (the nearest integral number orbits in a single rotation of the earth). However, the exact geomagnetic conditions (and therefore the background) are never fully duplicated because of orbital precession, the non-integral number of orbits in 24 hours and time-variability of the earth's magnetosphere (see Figure 2.11). A convenient pair of parameters to use in describing the orbital history of the spacecraft are the *ascending node* Ω (geographic longitude of the last intersection of the spacecraft orbit and the equatorial plane when moving in a northerly direction) and the

fraction of orbit F (defined since the time of the last ascending node). These two parameters record both the geographic location (tracing the geomagnetic conditions affecting atmospheric background) and orbit history (tracing activation effects) of the spacecraft. Background sampling for GRBs then amounts to accumulating events from within a small window of orbital parameters (Ω , F) around the values occurring during the burst. The size of the sampling window is important—if it is too wide, the events will no longer accurately reflect the background distribution during the burst, whereas if it is too small, there will be insufficient statistics to accurately determine the background distribution.

Balancing these considerations, a good choice of parameters for GRB background sampling was found to be a 10° window in Ω and a 10% window in F integrated over a three day interval centered on the burst. The path of *Compton's* orbit over such a three day interval is shown in Figure 2.11, where the white rectangular region indicates an $10^\circ \times 10\%$ window in (Ω, F) centered on an arbitrary point in the orbit. Even with this fairly wide selection window, there are too few events ($\sim 10^5$) to sufficiently (i.e., smoothly) sample the background in the entire 3-D data-space. Thus, the direct sampling is used only to determine the background $\bar{\varphi}$ -distribution and the geometry function is used for (χ, ψ) dependence. The two distributions are combined into the full data-space by normalizing the geometry function with the number of the directly sampled events in each independent $\bar{\varphi}$ layer.

The validity of this particular type of imaging background model was confirmed by performing null-tests whereby randomly chosen intervals of data (not containing GRBs or solar flares) were subject to the full imaging and background-determination process. These tests were performed for a variety of different orbital conditions, including periods of high and low background. The largest observed excesses in the resulting sky-maps were at the $\sim 2\sigma$ level (i.e., $\tilde{\lambda} \sim 8$), which is consistent with random statistical fluctuations in the background. The systematic errors in burst localization introduced in using this particular background model are small as discussed in Appendix B.

iii. Burst Spectral Analysis

Although it is possible to derive the energy spectrum of a source using maximum-likelihood imaging in different energy bands (e.g., McConnell *et al.* 1994; Schönfelder *et al.* 1993), it is not practical for GRBs because of the substantial number of events required for imaging (i.e., for most bursts it is not possible to perform imaging in different energy bands due to insufficient statistics). However, as we have seen earlier, for GRBs the number of counts required for a statistically significant signal above background is in most cases much lower than the number of events required for imaging (~ 20). Thus, more information can be extracted by using an alternate method of analysis.

a. Energy Response and Spectral Deconvolution. Starting with the general COMPTEL response given by equation (2.2), one takes the maximum-likelihood source location and integrates over a suitably-chosen interval in $(\chi, \psi, \bar{\phi})$. The resulting instrument response $R = R(E_{\text{tot}} | E_{\gamma})$ is then a function only of the incident and measured energies (and the data selections). Examples of this response (determined from simulation) at several different incident energies are shown in Figure 2.4a. In a convolution analogous to equation (2.5) the number of counts n expected in a measured energy element E_{tot} is given by

$$n(E_{\text{tot}}) = A T \int dE_{\text{tot}} \int dE_{\gamma} I(E_{\gamma}) R(E_{\text{tot}}; E_{\gamma}) , \quad (2.10)$$

where $A T$ is the exposure ($\text{cm}^2 \text{s}$), dE_{tot} is the range of measured energies, I is the intensity (flux) spectrum of the source ($\text{cm}^{-2} \text{s}^{-1} \text{MeV}^{-1}$) and R is the probability that a photon of energy E_{γ} will be measured with energy E_{tot} (the COMPTEL energy response). Although it is possible to simulate R for any given incident energy (thus forming an energy response *matrix*), the computational requirements for a statistically sufficient sample at all energies are enormous due to the low telescope efficiency after data selections. Furthermore, since R is dependent on the source location, a different response matrix for each source is required. A simpler, less computationally-intensive form of the energy response is therefore employed.

To further simplify the energy response, data are selected so as to make the response as

diagonal as possible. For a source with known (or measured) location, this is done by making an ARM selection on the data (around $\text{ARM} = 0^\circ$), that preferentially rejects many of the incompletely absorbed (off-diagonal) events. Although the ARM selection reduces the telescope detection efficiency, it also significantly improves S/N since only those events that originate from a small

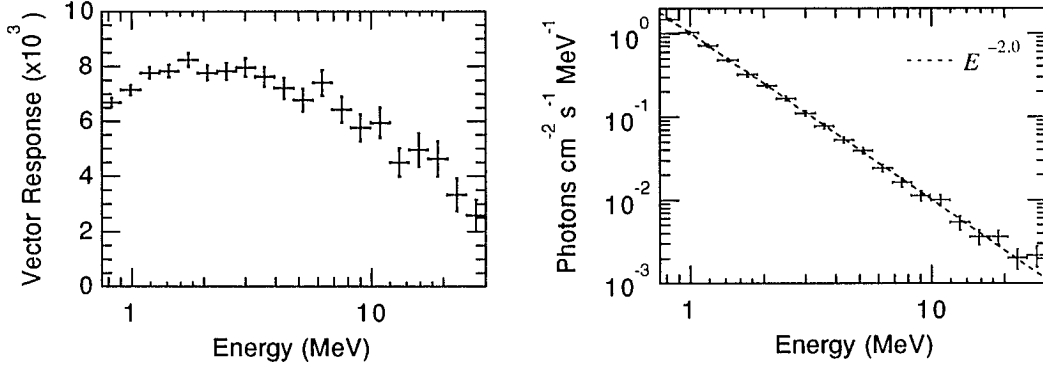


Fig. 2.12. Examples of an energy response vector (left) and a directly inverted photon spectrum (right) for an $E^{-2.0}$ power law source at 10° zenith.

radius around the source are selected. In this semi-diagonal case a simplified form of the energy response is determined by simulating a trial energy spectrum of photons and binning the incident photons n_γ and simulated events n in identical energy intervals $\Delta E_\gamma = \Delta E_{\text{tot}}$. The approximate response (efficiency) in each bin is then simply $r = n / n_\gamma$, which for many bins forms an energy response *vector* (see Figure 2.12). Although still dependent on the source position, the amount of computation required to determine a statistically-sufficient response vector is *significantly* less than for a full matrix.

Employing this simulated vector form of the energy response, deconvolution of equation (2.10) is achieved simply by division. Using an estimate of the measured background, the source flux in an energy bin ΔE_i is given by

$$I_i = \frac{1}{A T_S \Delta E_i} \left(\frac{n_i - b_i (T_S/T_B)}{r_i} \right) , \quad (2.11)$$

where n (b) are the counts observed during source (background) integration times T_S (T_B)

(corrected for instrument deadtime). The statistical uncertainty in the directly inverted spectrum is then computed from the number source and background events (systematic errors are discussed in Appendix B).

The vector response is relatively insensitive to the choice of trial spectrum, if the spectrum is relatively smooth and the energy bins are significantly wider than the COMPTEL energy resolution. By modifying the trial spectrum and deconvolving with the new response vector, the source flux can be accurately determined in very few iterations. An example is shown in Figure 2.12, where the directly inverted spectrum of a simulated power law source with ~ 8000 events is shown. This method of spectral deconvolution has been successfully employed with Compton telescopes in the past to calculate the fluxes of atmospheric gamma rays and neutrons (e.g., Ryan *et al.* 1979; Ait-Ouamer, Zych & White 1988). It is applicable in our case since GRBs have relatively featureless spectra in the MeV range and wide energy bins are already demanded by the low statistics in COMPTEL bursts.

In analyzing the COMPTEL GRBs, initial response vectors (first iteration) are computed by simulating $E^{-2.0}$ power law sources at the most-likely burst positions. Accurate in-flight D1/D2 energy thresholds are incorporated into these simulations by modeling data from the full day of each burst. Hence, the D1/D2 energy selections are fully relaxed ($0 < E_1 \leq 20$ MeV; $0 < E_1 \leq 30$ MeV). The TOF data selection is significantly relaxed ($95 \leq \text{TOF} \leq 145$ channels) to minimize the systematic effects introduced by its dependence on energy and the $\bar{\varphi}$ -selection is fully relaxed ($0^\circ < \bar{\varphi} \leq 180^\circ$) to improve statistics. A relatively wide ARM selection ($-10^\circ \leq \text{ARM} \leq +10^\circ$) is applied balancing the competing requirements for optimum S/N ($\sim \text{ARM} \pm 5^\circ$), reduction of off-diagonal response (small ARM window) and improved statistics (large ARM window). After application of these data selections each resulting response vector (15 logarithmically-spaced energy bins in the range 0.75–30 MeV) is required to contain $> 10^5$ events to insure adequate statistical coverage. If the directly-inverted photon spectra differ significantly from the assumed $E^{-2.0}$ power law, the trial spectra are updated and the process is repeated for *one* additional iteration.

b. Parameter Estimation and Model Testing. The low COMPTEL background and detection efficiency means that for GRBs relatively few telescope events are required for a statistically significant signal. With typically few counts per energy bin the statistical errors on the counts are not well described by a Gaussian distribution and therefore the traditional χ^2 -test used for model fitting (e.g., Bevington 1969) is *not* applicable. Rather, the likelihood-ratio test of Cash (1979) is used, which assumes Poisson-distributed counting statistics and reduces to the χ^2 -test in the limit of many counts. Spectral fitting performed by Nousek & Shue (1989) indicates that the Cash test is applicable even with very few counts per bin, whereas the χ^2 -test introduces significant errors (~50% errors when fitting 100 counts with 25 bins).

In Cash's fitting technique one minimizes the C -statistic

$$C = -2 \ln L = -2 \sum_{i=1}^N (n_i \ln m_i(q) - m_i(q) - \ln n_i!) \quad (2.12)$$

that follows from equation (2.8), where n is the number of observed counts and m is the number of counts expected from a model of the source and background energy spectra (with q adjustable parameters). The best-fit model parameters are where C is a minimum and statistical confidence limits are determined using the fact that $\Delta C = C - C_{\min}^{\infty}$ obeys the χ^2 probability distribution with q degrees of freedom (Lampton, Margon & Bowyer 1976), analogous to maximum-likelihood imaging.

Since the Cash-test is based on discrete Poisson counting statistics, all model testing must be performed in count-space rather than in deconvolved photon-space. This requires that a "forward-folding" technique (e.g., Lored & Epstein 1989) be used to determine the count-space distribution expected from a photon-space model of the source flux. Using the response vector, forward-folding is a simple multiplicative convolution. Inverting equation (2.11) we get

$$m_i = b_i (T_s/T_b) + A T_S \Delta E_i I_i(q) r_i, \quad (2.13)$$

where I is now a source flux model with q free parameters. Note that the measured background b is treated as a fixed model in this scheme. This ignores the effects of possible statistical fluctuation in the background. However, if we can determine a sufficient statistical background

sample this approximation is justified due to the low background for COMPTEL GRBs.

The primary disadvantage of using the C -statistic is that there is no goodness-of-fit estimator corresponding to the familiar reduced χ^2 (χ^2/ν). Unlike χ^2 , the C -statistic behaves differently for each model so it can be used only to determine the best-fit model parameters and estimate confidence regions, but not to reject different model hypotheses (Nousek 1992). For the latter a “bootstrap” test is used wherein random, Poisson-distributed fluctuations are introduced to the best-fit model count-spectrum (the bootstrap). The C -statistic is then evaluated between each random sample and the bootstrap. The goodness-of-fit is estimated by examining where the best-fit C of the real data (C_{obs}) falls in the distribution of C from the random simulations. The parameter of interest in this procedure is Q_b —the fraction of random samples with $C > C_{\text{obs}}$ or the probability of exceeding C_{obs} purely by chance. If Q_b is very small (analogous to $\chi^2/\nu \gg 1$), then random fluctuations of the model cannot explain the data and the model can be rejected with $(1 - Q_b)$ confidence. Acceptable models will therefore have $Q_b \sim 0.5$ (corresponding to $\chi^2/\nu \sim 1$).

As in the case of maximum-likelihood imaging, parameter uncertainties and goodness-of-fit estimated using the Cash test and bootstrapping incorporate only statistical effects. The systematic errors must be estimated separately (see Appendix B).

c. Background Determination. As discussed in the previous sections, for spectral analysis we desire a properly normalized measured background estimate with sufficient statistics. The requirement of proper normalization makes the method used to determine the imaging background impractical in this case. A far simpler method is to estimate the background during a GRB by sampling events from 15 orbits before and after the burst in each energy bin and averaging the before and after estimates. To insure an adequate statistical sample, events are accepted from ± 15 orbits ± 100 s and then normalized to the burst livetime as in equation (2.11). If data from one (or both) of these background intervals are unavailable (e.g., due to loss of telemetry), 14 or 16 orbit intervals are used with some loss of accuracy.

As in the case of the imaging background, the validity of this background technique is estimated by performing null-tests whereby background is subtracted from arbitrary intervals that

do not contain GRBs or solar flares. The resulting distributions must be consistent with zero. Such null-tests are performed for a variety of cases including high and low background intervals. In nearly all cases the resulting background-subtracted energy and temporal distributions are statistically consistent with zero. A typical example is illustrated in Figure 2.13.

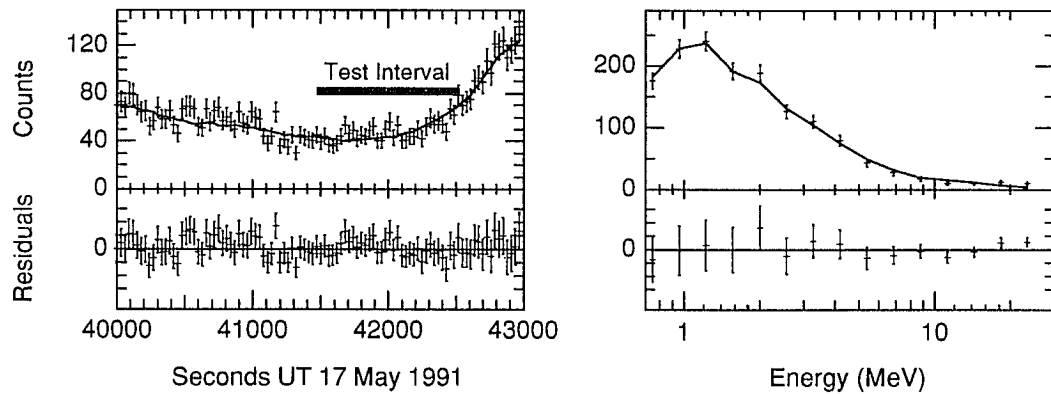


Fig. 2.13. Examples of null-test temporal (left) and energy (right) background distributions. Datapoints represent observed counts and solid lines are the background estimate from a ± 15 orbit interval average. The temporal distribution includes energy deposits from 0.75–30 MeV and the energy distribution was sampled from the time-interval marked “Test Interval”. In each case, the background-subtracted residuals (lower panels) are statistically-consistent with zero.

III. COMPTEL OBSERVATIONS OF GAMMA-RAY BURSTS

As we have seen earlier, COMPTEL is sensitive to GRBs occurring in its ~ 1 sr field-of-view with fluence $S(>0.75 \text{ MeV})$ exceeding $\sim 5 \times 10^{-6} \text{ erg cm}^{-2}$ (depending on background and burst spectrum). It is known, based on *SMM* observations, that emission above 1 MeV is a common feature in GRBs (Matz *et al.* 1985). Given the all-sky rate of bursts ($> 1 \text{ MeV}$) detected by *SMM* ($\sim 50 \text{ yr}^{-1}$) and assuming an isotropic, homogeneous spatial distribution of burst sources, we would expect COMPTEL to detect $\sim 10\text{--}20$ bursts yr^{-1} (Winkler *et al.* 1986). Due to Earth blockage, telemetry losses and SAA passages, however, the actual COMPTEL detection rate can be expected to be lower. In this chapter, bursts observed by COMPTEL during its first three years of operation are discussed.

A. Burst Search Strategy

To identify GRBs, COMPTEL (as well as the other *Compton* instruments) utilizes the onboard transient event triggering system of the *Compton*–BATSE instrument. This system is automatically activated whenever the BATSE large area detectors (LADs) measure statistically significant count rates above background in the energy range 50–300 keV (see e.g., Fishman *et al.* 1989). This can occur for a variety of reasons including gamma-ray bursts, solar flares, magnetospheric activity, Earth occultation of strong celestial sources and terrestrial gamma flashes (Fishman *et al.* 1994b). After a trigger, the BATSE system is insensitive to weaker new events for a period of ~ 90 min. When the system is triggered, normal COMPTEL telescope mode operation continues, while BSA burst mode detectors are signaled to begin accumulating spectra in faster cadence. Searching for COMPTEL GRBs then amounts to examining data from the times of all candidate BATSE burst triggers; where candidate triggers are chosen based on preliminary BATSE source location and classification. The BATSE source classification scheme effectively selects only gamma-ray burst triggers for consideration (Mallozzi *et al.* 1993). Since BATSE is a full-sky monitor, COMPTEL (telescope) burst candidates represent only the small

subset of GRB triggers which are located within the COMPTEL FOV. This search strategy is effective in identifying all COMPTEL GRB candidates since BATSE is more sensitive at low energies where bursts exhibit higher flux. The exception is during the ~ 90 min periods after all triggers, when BATSE is insensitive to new weaker events.

During the period from 21 April 1991 through 21 April 1994 (*Compton's* first three years of observations) there were 2941 BATSE transient event triggers, 967 of which have been classified as GRBs. Of these, 248 have preliminary BATSE locations (accurate to $\sim 5^\circ$ – 10° , 1σ) with zenith angles $< 60^\circ$ and are thus potential candidates for COMPTEL imaging and spectral analysis. Unfortunately, COMPTEL data are unavailable for several of these candidates due to telemetry losses caused by the failure of *Compton's* data recorders at the end of its first year of operation. These losses are particularly severe during the period from January 1992 to January 1993.

COMPTEL data around the time of each of the ~ 190 candidate burst triggers have been searched for significant emission above background by binning the telescope events in time on a variety of different scales ranging from 100 ms to 100 s. Candidates showing significant (i.e., $\geq 3\sigma$) emission above background were further tested by applying the maximum-likelihood imaging process (as explained in Chapter II) to events from the interval of the most significant excess. A final burst detection threshold was applied to the resulting images by requiring that the peak log likelihood ratio $\hat{\lambda}$ be greater than 20 (formally indicating a 3.8σ detection). Since $\hat{\lambda}$ depends on the accuracy of the source (PSF) and background models used in the imaging process, it is only an upper limit to the true detection significance. This is accounted for in the choice of a relatively high threshold in $\hat{\lambda}$, insuring that only significant ($\geq 3\sigma$) detections will be accepted. Note that this imaging-based burst detection threshold is sensitive to fluence rather than flux. Thus, it is biased against low-fluence, short duration bursts (< 1 s) that do not produce enough telescope events for imaging (~ 15 – 20) but whose flux *is* statistically significant due to the low background rate on short time-scales.

B. Observations

Using the search strategy described above, 18 events have been identified which satisfy the $\tilde{\lambda} > 20$ detection requirement. This is consistent with the predicted detection rate of $\sim 10\text{--}20$ bursts yr^{-1} taking into account the *effective* exposure-time ($\sim 30\%$) over the three-year observation interval. Results of the search are given in Table 3.1, where each COMPTEL burst detection is

Table 3.1 COMPTEL Burst Detection Parameters

Burst Name	BATSE Burst Trigger*			$\tilde{\lambda}$	Significance		Other#
	no.	(TJD:s) [†]	UT		σ^{\S}	σ^{\parallel}	
GRB 910425	109	8371: 2265.74	00:37:46	40.3	5.7	5.7	B,U,P
GRB 910503	143	8379: 25452.68	07:04:13	174.1	12.8	12.6	B,E,U,P
GRB 910601	249	8408: 69734.54	19:22:15	218.2	14.4	10.6	B,E,O,U,G
GRB 910627	451	8434: 16157.77	04:29:18	21.5	3.9	5.3	B,U,P,G
GRB 910709	503	8446: 41602.12	11:33:22	36.4	5.4	5.2	B
GRB 910814	678	8482: 69273.03	19:14:33	190.9	13.4	11.5	B,U,P
GRB 911118	1085	8578: 68258.05	18:57:38	42.0	5.9	5.2	B,U,P
GRB 920622	1663	8795: 25504.52	07:05:05	194.0	13.5	10.4	B,U,G,Y
GRB 920830	1883	8864: 6317.59	01:45:18	35.7	5.4	4.3	B,U
GRB 930118 [‡]	2137	9005: 64427.00	17:53:47	20.9	3.9	3.8	B,U
GRB 930131	2151	9018: 68231.68	18:57:12	32.6	5.1	5.2	B,E,U
GRB 930309	2228	9055: 11269.79	03:07:50	42.7	5.9	5.9	B,U
GRB 930612	2387	9150: 2657.67	00:44:18	23.3	4.1	4.8	B,U
GRB 930704	2428	9172: 60545.72	16:49:06	22.1	4.0	3.9	B,U,M
GRB 931229	2715	9350: 26165.91	07:16:06	31.6	5.0	4.0	B
GRB 940217	2831	9400: 82962.07	23:02:42	366.7	18.8	16.2	B,E,U
GRB 940301	2855	9412: 72637.08	20:10:37	148.7	11.8	11.0	B,E,U
GRB 940314	2881	9425: 35989.15	09:59:49	33.7	5.2	6.4	B

*BATSE information from (Meegan *et al.* 1994) and C. Meegan (private communication).

[†]Truncated Julian date (Julian date - 2440000.0) and decimal seconds past midnight.

[‡]This burst was detected by BATSE while accumulating a solar flare.

[§]Detection significance from $\tilde{\lambda}$.

^{||}Detection significance from direct estimation of background.

#B=Compton-BATSE; E=Compton-EGRET; O=Compton-OSSE; U=Ulysses; P=Pioneer Venus Orbiter; G=Granat; M=Mars Observer; Y=Yohkoh

identified by the number, date and time of its corresponding BATSE trigger. Hereafter, these bursts will be referenced by the date of their corresponding BATSE trigger (e.g., *GRB yymmdd*). One event (GRB 930118) occurred while BATSE was accumulating a strong solar flare, thus its

trigger refers to the flare and not the burst (C. Meegan, private communication).

The COMPTEL detection significance for each burst (expressed in units of standard deviations σ above background) was estimated both from $\tilde{\lambda}$ and by direct measurement using the ± 15 orbit background method described in Chapter II. The two estimates are in rough agreement except for very significant detections, where the $\tilde{\lambda}$ -based significance appears to be somewhat overestimated. In one case (GRB 910609; Varendorff *et al.* 1992), a statistically significant detection based on temporal analysis (6 events in a 14 ms interval where the background rate was $\sim 1 \text{ event s}^{-1}$) did not pass the imaging-based threshold (i.e., $\tilde{\lambda} \geq 20$). This burst is not included here because the six events it produced (no data selections) are too few for meaningful imaging, especially since the burst was (according to BATSE measurements) far off-axis ($\theta > 60^\circ$).

Telescope event-rate plots of the bursts listed in Table 3.1 are displayed in Appendix A. Within the COMPTEL catalog, a wide variety of different temporal shapes, structure and duration can be seen. These range from very intense, short duration events (e.g., GRB 930131 and GRB 910709) to relatively smooth, long-duration events (e.g., GRB 930309) to purely chaotic events (e.g., GRB 940217) which contain both smooth and impulsive features. In terms of temporal structure, the COMPTEL bursts appear to represent a random sample of the entire burst population (e.g., as observed by BATSE; Fishman 1993).

Several of the COMPTEL bursts have been measured by different experiments (in addition to BATSE and the COMPTEL BSA detectors). Those experiments with burst localization capability are included in Table 3.1. Of particular interest to this work are the high energy ($> 30 \text{ MeV}$) observations by EGRET and the burst localizations determined by Interplanetary Network (IPN) gamma-ray experiments on the *Ulysses* and *Pioneer Venus Orbiter* spacecraft.

IV. RESULTS OF SPATIAL ANALYSIS

The gamma-ray bursts observed by COMPTEL constitute an independent sample of relatively well-localized events which can be used to investigate the spatial distribution of the burst source population. Although small in overall size, the COMPTEL burst sample is useful due to its superior angular resolution (as compared to BATSE) and good coverage over the full-sky (when integrated over three years). In these respects, the COMPTEL GRB sample is well suited to probe the small-scale angular distribution of sources, where the total number of events is not as important as location accuracy (see e.g., Hartmann *et al.* 1994a; Strohmayer, Fenimore & Miralles 1994). For the large-scale spatial distribution, where sensitivity is dominated by sample size, BATSE has made the most accurate measurements of the isotropy and inhomogeneity of burst sources (e.g., Meegan *et al.* 1992). However, the COMPTEL measurements do provide a useful consistency check. In this chapter the spatial distribution (both large and small-scale) of burst sources is investigated using the COMPTEL burst location sample from the first three years of the *Compton* Observatory mission. The angular resolution of this sample is improved by combining (where possible) the COMPTEL localizations with those from Interplanetary Network timing measurements.

A. Burst Source Localization

i. COMPTEL Localizations

The 18 significant COMPTEL burst detections identified in Table 3.1 have been analyzed using the maximum-likelihood imaging technique in combination with the imaging background model and instrument response function (PSF) described earlier. Log-likelihood-ratio (λ) sky-maps were computed for each burst using telescope events selected from the time-interval of most-significant emission observed by COMPTEL. The sky-maps (and therefore the burst localizations) are only weakly dependent on the exact choice of time-interval.

The most-likely direction of each burst source was estimated by computing the coordinates of the peak log-likelihood-ratio ($\hat{\lambda}$) in each sky-map. To improve the accuracy of this computation beyond the $1^\circ \times 1^\circ$ bin-size, the λ sky-maps were first interpolated onto a finer coordinate grid (0.1° bins) using a bi-cubic approximation. Statistical uncertainty regions around the most likely source positions have been estimated by computing smoothed (cubic spline) contours of the λ sky-maps at levels corresponding to the desired confidence (as described in Chapter II). The resulting burst localization parameters are listed in Table 4.1 and statistical location uncertainty contour sky-maps of each burst are shown in Appendix A.

In general, the COMPTEL burst location contours enclose irregularly shaped regions, thus uncertainties between different bursts are difficult to compare. A convenient approximate measure of location uncertainty is the radius of a circle having the same area as the region enclosed by the observed contours. Such *effective error radii* for 1σ and 2σ confidence levels (denoted by $1\sigma_{\text{eff}}$ and $2\sigma_{\text{eff}}$, respectively) are listed for each burst in Table 4.1. The location uncertainty determined with the maximum-likelihood method only includes statistical effects, so the size of the effective error radius is approximately inversely related to the number of detected counts. Thus, the error radius of a high-fluence burst like GRB 940217 ($\sigma_{\text{eff}} = 0.3$) is much smaller than that of a weaker detection like GRB 930118 ($\sigma_{\text{eff}} = 1.5$). This behavior is complicated, however, by the off-axis telescope response, which introduces additional uncertainty in the azimuthal direction (in spacecraft coordinates) for all bursts at large zenith angle ($\theta \geq 30^\circ$).

The average *statistical* location uncertainty (as approximated by σ_{eff}) for the full COMPTEL burst sample is ~ 1.1 . Systematic effects due to the approximations and inaccuracies of the imaging process have been estimated to be less than 0.5 in magnitude and probably smaller for bursts located at zenith angles below $\sim 30^\circ$ (see Appendix B for a detailed investigation of systematic burst location errors). When the 0.5 systematic offset (independent of burst size) is added in quadrature ($\sqrt{\sigma_{\text{eff}}^2 + \sigma^2}$) to the statistical error radius, the average location uncertainty of the COMPTEL sample increases to ~ 1.3 .

Table 4.1 COMPTEL Burst Localization Parameters

Burst Name	Most-Likely Burst Location Coordinates						Statistical		Other		
	Celestial*		Galactic†		Spacecraft‡		Uncertainty§		Experiments		
	α_{2000}	δ_{2000}	l	b	ϕ_c	θ_c	$1\sigma_{\text{eff}}$	$2\sigma_{\text{eff}}$	Δ_B^{\parallel}	$S_{\text{min}}^{\#}$	
GRB 910425	90.2	-22.2	228.1	-20.6	266.2	44.4	0.92	1.90	4.15	0.28	
GRB 910503	87.0	+38.6	172.0	+5.4	124.9	23.5	0.44	0.86	1.01	0.30	
GRB 910601	309.9	+32.7	74.1	-5.4	69.5	8.0	0.46	0.81	1.60	0.37	
GRB 910627	199.4	-5.0	315.1	+57.3	223.0	10.8	1.63	3.36	1.90	0.71	
GRB 910709	144.1	+75.6	136.3	+36.0	32.5	37.5	1.80	3.69	¶39.65	—	
GRB 910814	343.8	+29.5	94.7	-26.9	85.6	29.5	0.39	0.88	7.65	0.17	
GRB 911118	166.3	-22.5	273.0	+34.1	253.3	36.7	1.11	2.58	7.01	0.23	
GRB 920622	162.5	+49.2	161.3	+57.9	238.7	46.0	0.81	1.40	3.51	2.45	
GRB 920830	259.0	-74.5	318.0	-20.0	352.7	16.6	1.35	2.39	1.11	—	
GRB 930118	221.8	-34.8	328.4	+22.3	21.9	15.7	1.47	2.46	5.46	—	
GRB 930131	186.2	-7.9	291.6	+54.4	231.1	27.9	1.77	2.80	3.54	2.93	
GRB 930309	322.7	+55.2	96.9	+2.8	100.2	29.9	0.74	2.15	6.57	4.67	
GRB 930612	106.5	-71.0	282.0	-24.4	83.4	24.1	1.60	2.65	5.06	0.17	
GRB 930704	100.7	+62.5	153.0	+22.9	77.7	18.8	1.08	2.60	5.51	0.07	
GRB 931229	241.9	+21.0	36.2	+45.1	314.3	49.2	2.35	5.58	10.63	—	
GRB 940217	31.1	+3.1	154.5	-55.5	307.2	10.4	0.32	0.69	2.90	0.94	
GRB 940301	102.4	+63.9	151.7	+24.0	255.2	8.1	0.40	0.95	0.33	0.18	
GRB 940314	356.0	-1.4	88.0	-59.6	48.8	14.5	1.43	2.69	2.41	—	
Average:							1.12	2.15	6.11	1.04	
Including 0.5 Systematic:							1.25	2.32			

Note: All coordinates and angles are expressed in decimal degrees; “—” indicates that an IPN annulus is unavailable for this burst.

*Right ascension and declination (epoch J2000.0).

†Longitude and latitude.

‡COMPTEL coordinates azimuth and zenith.

§Radius of a circle having the same area as the observed (1σ , 2σ) localization region.

¶Angular separation between the most likely COMPTEL and BATSE burst positions.

#Minimum angular separation between BATSE/*Ulysses* IPN annulus and most likely COMPTEL position.

¶Large statistical uncertainty in BATSE burst location.

Angular separations between the most-likely COMPTEL and BATSE burst positions are in most cases consistent with the combined uncertainty of the two instruments ($\sim 4^\circ$ – 5° for BATSE). In one case, however, there is a significant discrepancy. Although the COMPTEL localization of this burst (GRB 910709) is relatively poor, it cannot explain the nearly 40° offset. However, the

reported BATSE statistical location uncertainty for GRB 910709 (Fishman *et al.* 1994a) is unusually large ($\sim 15^\circ$; 1σ), which may indicate a similarly large systematic error. Excluding this burst, the average separation of $\sim 4^\circ$ between the BATSE and COMPTEL locations is entirely consistent with the combined errors of the two instruments.

Most of the COMPTEL bursts (13 out of 18) have been localized with the arrival-time analysis technique using some combination of Interplanetary Network spacecraft (see Appendix A for IPN references). These localizations consist of *at least* a single “triangulation” annulus constructed using the difference in burst arrival times between the widely-separated (several AU) *Compton*–BATSE and *Ulysses* gamma-ray detectors. The BATSE/*Ulysses* annuli (where available) are compared to the independent COMPTEL localizations by computing for each burst the *minimum* separation S_{\min} between the annulus and the most-likely COMPTEL position (cf. Hurley *et al.* 1994a). The values of S_{\min} given in Table 4.1 indicate consistency between the COMPTEL and IPN localizations in that the average minimum separation ($\sim 1^\circ$) agrees with the average COMPTEL location uncertainty (IPN uncertainties are negligible compared to those of COMPTEL). Detailed comparison of the individual bursts (see sky-map figures in Appendix A) shows that each IPN annulus is consistent with the corresponding COMPTEL localization within statistical errors. For example, as expected statistically, the IPN annuli intersect within the COMPTEL 1σ uncertainty contours in $\sim 68\%$ of the bursts observed and within the 2σ contours for all the bursts. These results indicate that the IPN annuli are consistent with the statistical COMPTEL source location constraints as computed here. Further comparison using single annuli is problematic since the true source location of a given burst could lie anywhere along the annulus with equal probability.

Four of the 13 bursts observed by COMPTEL, BATSE and *Ulysses* have been measured by detectors on an additional IPN spacecraft (either *PVO* or *Mars Observer*). In such cases, less ambiguous source localization is possible if the individual (two spacecraft) “triangulation” annuli are precise and intersect at sufficiently large angles. Only for GRB 911118 and GRB 930704 was the inter-spacecraft geometry capable of yielding annuli which intersect at large angles. The

precise annuli intersection “error-box” ($\sim 2' \times 4'$) of GRB 911118 is consistent with the COMPTEL localization within 1σ uncertainties (Cline *et al.* 1993, 1994). The less-precise IPN error-box of GRB 930704 ($\sim 14' \times 13''$) is also consistent with the COMPTEL localization within the larger uncertainties. In these limited cases at least, the COMPTEL localizations are in good agreement with the more precise IPN positions. Interplanetary Network measurements alone can only constrain the remainder of the COMPTEL bursts to lie on long thin annuli covering a sizable region of the sky.

ii. Combined COMPTEL/IPN Localizations

By combining COMPTEL and IPN measurements, the size of individual burst location uncertainty regions is reduced by over an order-of-magnitude and the angular resolution of the full sample is correspondingly improved. Combined burst localizations are estimated by interpolating the COMPTEL likelihood ratio sky-maps at regular intervals along the IPN annuli using a bi-cubic approximation. Neglecting the width of the annuli (negligible compared to the COMPTEL uncertainties), the most-likely *combined* COMPTEL/IPN burst location corresponds

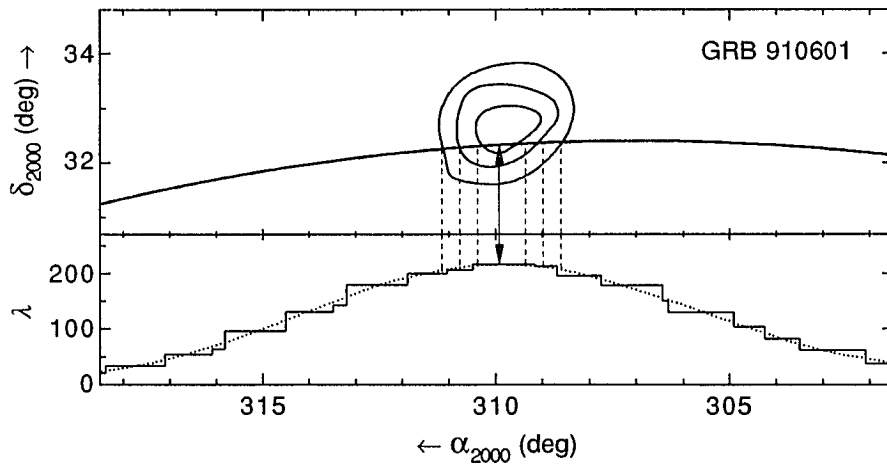


Fig. 4.1. Combined COMPTEL/IPN localization of GRB 910601. COMPTEL likelihood ratios (λ ; bottom panel) are evaluated (solid stepped line) / interpolated (dots) at points along the IPN annulus (Cline *et al.* 1993; K. Hurley, private communication), where they are used to estimate the most-likely combined source position (arrow) and statistical confidence limits (1σ , 2σ and 3σ ; dashed lines).

to the maximum likelihood ratio along the annulus and formal statistical 1σ , 2σ and 3σ confidence limits are determined where λ has decreased from the maximum by 1, 4 and 9, respectively (corresponding to the χ^2 probability distribution with one DOF—distance along the annulus). This process is illustrated for GRB 910601 in Figure 4.1.

Table 4.2 Combined COMPTEL/IPN (BATSE/*Ulysses*)[¶] Burst Localization Parameters

Burst Name	Most-Likely Combined Location				Statistical Uncertainty		
	Celestial*		Galactic [†]		COMPTEL [‡]		IPN [§]
	α_{2000}	δ_{2000}	l	b	$\langle 1\sigma \rangle$	$\langle 2\sigma \rangle$	δR
GRB 910425	89.78	-22.30	227.99	-21.03	0.55	1.14	0.053
GRB 910503	87.43	+38.62	172.13	+5.73	0.28	0.61	0.010
GRB 910601	309.92	+32.33	73.82	-5.67	0.44	0.76	0.011
GRB 910627	198.63	-4.35	313.91	+58.04	1.61	2.85	0.031
GRB 910814	343.78	+29.31	94.54	-27.09	0.36	0.72	0.018
GRB 911118	166.16	-23.21	273.30	+33.46	1.60	3.56	0.017
GRB 920622	161.42	+46.86	165.83	+58.44	0.33	0.69	0.009
GRB 930131	183.65	-9.72	288.10	+52.10	1.10	1.97	0.011
GRB 930309	324.93	+50.72	94.90	-1.43	0.54	1.31	0.035
GRB 930612	106.88	-70.88	281.94	-24.21	0.90	1.98	0.053
GRB 930704	99.46	+62.98	152.32	+22.48	0.60	2.54	0.113
GRB 940217	29.50	+3.83	152.97	-55.11	0.33	0.61	0.050
GRB 940301	102.01	+64.20	151.35	+23.88	0.43	0.82	0.136
Average:					0.70	1.50	0.036

Note: All coordinates and angles are expressed in decimal degrees.

*Right ascension and declination (epoch J2000.0).

[†]Longitude and latitude.

[‡]Mean angular uncertainty (1σ , 2σ confidence) along the IPN annulus.

[§]Mean uncertainty (3σ confidence) in the radius of the IPN annulus.

[¶]See Appendix A for IPN references.

In all cases, the annuli employing BATSE and *Ulysses* measurements are the most precise. In Table 4.2 the results of combined COMPTEL/IPN localization are given for all 13 COMPTEL bursts where BATSE/*Ulysses* annuli are available. In general, the statistical confidence limits are not symmetric about the most probable position. The *mean* angular uncertainty in either direction ($\langle 1\sigma \rangle$, $\langle 2\sigma \rangle$) provides a convenient measure for comparison between different bursts. The average combined localization of all the bursts is a thin arc-segment only $\sim 4'$ wide with

$\langle 2\sigma \rangle \sim 1.5^\circ$ (i.e., 3° in total length). As in the case of the COMPTEL-only burst positions, the combined confidence limits incorporate only statistical uncertainty. Due to the reduced degrees-of-freedom, the largest systematic effects (along the circumference of the annuli) are probably somewhat smaller than the 0.5° systematic error estimated for the COMPTEL-only positions.

With its three unique annuli, GRB 911118 provides a convenient (although limited) consistency check on the validity of combined COMPTEL/IPN burst localization. Each annulus can be used to construct an independent combined localization, which can be compared to the intersection of all three annuli (presumably containing the true burst location). The combined localizations for two of the three annuli include the intersection point within their estimated 1σ confidence limits. As is expected statistically, the intersection point is outside the combined 1σ confidence limit for the third annulus, but well within the 2σ confidence limit. Thus, for this burst at least, combined COMPTEL/IPN localization appears to yield statistically consistent results.

B. COMPTEL/IPN Burst Distance Constraints

The distance scale to gamma-ray burst sources remains almost completely unknown, therefore any observable constraints are useful. For example, bursts could originate from a fairly local population of sources (e.g., within an extended solar system $< 10^5$ AU) and still be consistent with the angular and intensity distributions observed by BATSE (Horack *et al.* 1994 and references therein). As pointed out by Hurley (1982), Interplanetary Network timing differences between 4 or more widely separated spacecraft in a favorable configuration could be used to distinguish between spherical and planar wavefronts (i.e., parallax) if gamma-ray burst sources are nearby—thereby triangulating their distances. However, to date only a few bursts have been observed by this many instruments (see e.g., Atteia *et al.* 1987b and references therein) and no distance limits using this technique have been published.

If a burst is measured by two Interplanetary Network spacecraft separated by a distance b (e.g., one orbiting the Earth and another orbiting Venus), the angle θ between the burst direction

and the inter-spacecraft baseline (e.g., measured from the spacecraft at the Earth) follows the relation

$$\cos \theta = \left(\frac{c\Delta t}{b} \right) + \frac{b}{2D} \left\{ 1 - \left(\frac{c\Delta t}{b} \right)^2 \right\}, \quad (4.1)$$

where D is the distance to the burst (as measured from the Earth-orbiting spacecraft) and Δt is the observed difference in burst arrival times between the two spacecraft (Connors *et al.* 1993). Thus, for a nearby source, $\cos \theta$ is larger than that inferred from the time-delay alone ($c\Delta t/b$) by a parallax factor which is inversely related to the source distance. That is, the opening angle of an IPN “triangulation” annulus, $\cos^{-1}(c\Delta t/b)$, is always greater than or equal to the true burst angle θ . The fact that COMPTEL burst localizations agree with BATSE/*Ulysses* annuli within COMPTEL’s statistical uncertainties places a lower limit on the distance to the burst sources which does not require additional spacecraft observations. For example, if the COMPTEL localization agrees with an IPN annulus (5 AU baseline) within 2° , the source must be farther than ~ 50 AU, depending on the source/baseline geometry. The severity of this limit improves with the accuracy of the COMPTEL localization (more importantly, the accuracy of the localization in the direction perpendicular to the IPN annulus) and the length of the IPN baseline.

COMPTEL/IPN distance constraints for individual bursts are estimated by interpolating (as in the previous section) the COMPTEL likelihood ratios at regular intervals along concentric annuli with opening angles θ smaller than that of the BATSE/*Ulysses* annulus. For each individual annulus, the maximum COMPTEL likelihood ratio is determined, yielding the highest probability that the source position lies on that particular annulus. For many concentric annuli, this procedure determines—with the use of equation (4.1)—the source likelihood λ as a function of burst distance (a single degree of freedom). Distance lower limits with 1σ , 2σ and 3σ confidence are then estimated where λ has decreased from that evaluated along the BATSE/*Ulysses* annulus by 1, 4 and 9, respectively (χ^2 with one DOF as in the previous section). The uncertainty of the IPN annulus width is ignored and as in all analyses using the COMPTEL likelihood ratio maps, this procedure (illustrated in Figure 4.2) does not include systematic localization errors.

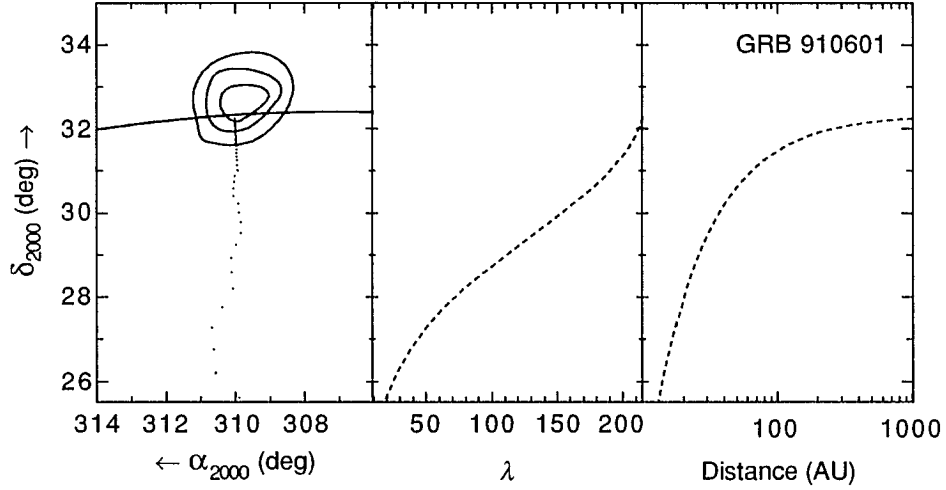


Fig. 4.2. COMPTEL/IPN distance constraints for GRB 910601 (cf. Figure 4.1). COMPTEL likelihood ratios (λ ; center panel) are maximized along concentric annuli corresponding to different source distances (right panel). Each point in the sky map at left represents the position of the maximum for a single annulus (see text for details).

Table 4.3 COMPTEL/IPN (BATSE/*Ulysses*)[§]
Burst Distance Limits

Burst Name	b^*	D_{\min}^{\dagger}	D_{\min}^{\ddagger}
GRB 910425	2.85	33	25
GRB 910503	3.04	45	31
GRB 910601	3.71	223	110
GRB 910627	4.22	45	41
GRB 910814	4.92	126	77
GRB 911118	4.97	33	24
GRB 920622	5.80	94	79
GRB 930131	4.22	33	28
GRB 930309	4.00	18	16
GRB 930612	4.87	90	64
GRB 930704	5.09	75	55
GRB 940217	3.04	250	145
GRB 940301	2.95	130	70

*BATSE/*Ulysses* baseline separation (AU).

[†] 2σ lower limit on the source distance (AU).

[‡]Same as above *including* systematic errors.

[§]See Appendix A for IPN references.

The effects of such errors are conservatively accounted for by shifting the observed COMPTEL likelihood distribution in space by 0.5° —the largest estimated systematic location error (see Appendix B)—and repeating the lower limit estimation procedure.

Results for each of the 13 COMPTEL/BATSE/*Ulysses* bursts are given in Table 4.3. As expected, the most constraining distance limits are for those bursts with the smallest location uncertainties perpendicular to the IPN annuli, i.e., strong bursts such as GRB 910601 and GRB 940217. Note that this behavior alone does not imply that strong bursts are closer, only that they produce more stringent limits on distance due to their smaller statistical location errors. Even when systematic effects are conservatively included, the distance to these bursts must be greater than ~ 100 AU to be consistent with the COMPTEL/IPN measurements.

C. Large-Scale Angular Distribution

The observed distribution of the directions to gamma-ray bursts is one of the most important pieces of information we have about the nature of burst sources. The large-scale or all-sky distribution of locations yields significant clues about where the burst sources reside in the universe, their association with known objects, distance and luminosity.

Traditionally, studies of large-scale angular structure have been most concerned with the question of whether the burst source population resides inside or outside our Galaxy. As pointed out by several authors (e.g., Hartmann & Epstein 1989; Paczynski 1990; Briggs 1993), the most sensitive tools for this purpose are the Galactic dipole and quadrupole moment statistics. The dipole moment (most often expressed as $\langle \cos \Theta \rangle$, where Θ is the angle between the burst and the Galactic center) measures the amount of concentration towards the Galactic center, while the quadrupole moment (often expressed as $\langle \sin^2 b - \frac{1}{3} \rangle$, where b is the Galactic latitude of the burst) indicates the amount of concentration towards the Galactic plane. Measurement of a significant non-zero $\langle \cos \Theta \rangle$ or $\langle \sin^2 b - \frac{1}{3} \rangle$ indicates deviation from an isotropic distribution. Similar tools expressed in Sun or Earth-referenced coordinate systems are used to investigate heliocentric burst origin scenarios (Horack *et al.* 1994), while other more powerful tests have been used to identify

large-scale concentrations in arbitrary (coordinate system independent) directions (Briggs 1993).

The major uncertainties inherent in all studies of large-scale angular distributions are statistical and instrumental in nature. Statistical uncertainty is inversely related to the square-root of the burst sample size. Thus large samples have an outstanding advantage in terms of sensitivity. Instrumental uncertainty arises from imperfect burst localization and non-uniform sky exposure and is independent of the sample size if the ability to localize sources is not related to the number of bursts. In most cases the statistical uncertainty dominates the instrumental effects even for the largest of samples and even with fairly poor angular resolution. For example, the large BATSE burst sample provides the most accurate measure of the large-scale angular distribution of burst sources yet measured, despite BATSE's poor angular resolution.

The distribution on the sky of the 18 COMPTEL bursts is displayed in Figure 4.3. These all-sky maps were computed by interpolating the individual likelihood-ratio maps of each burst onto equal-area grids in Galactic and Celestial coordinates. Celestial coordinates are included because instrumental effects would be most evident in this system. The maps show statistical source location constraints as described earlier. As before, the strongest bursts have the smallest location uncertainties and the weakest detections have the largest. No obvious spatial concentration in either coordinate system is evident. However, the raw maps are biased by COMPTEL's non-uniform sky exposure.

A simple estimate of the COMPTEL sky-exposure is obtained by accumulating the product of the time spent observing each point in the sky and the angular response during each pointed observation period (typically lasting ~1–3 weeks). Exposure maps incorporating observation periods over the first three years of the COMPTEL mission have been computed in this manner (see Appendix C). The greatest exposure is in the direction of the center and plane of the Galaxy and in the direction of Virgo, while the least exposure is towards the south Galactic polar region. Fortunately, all areas of the sky were observed for at least eight days.

COMPTEL GAMMA-RAY BURSTS APRIL 1991 - APRIL 1994

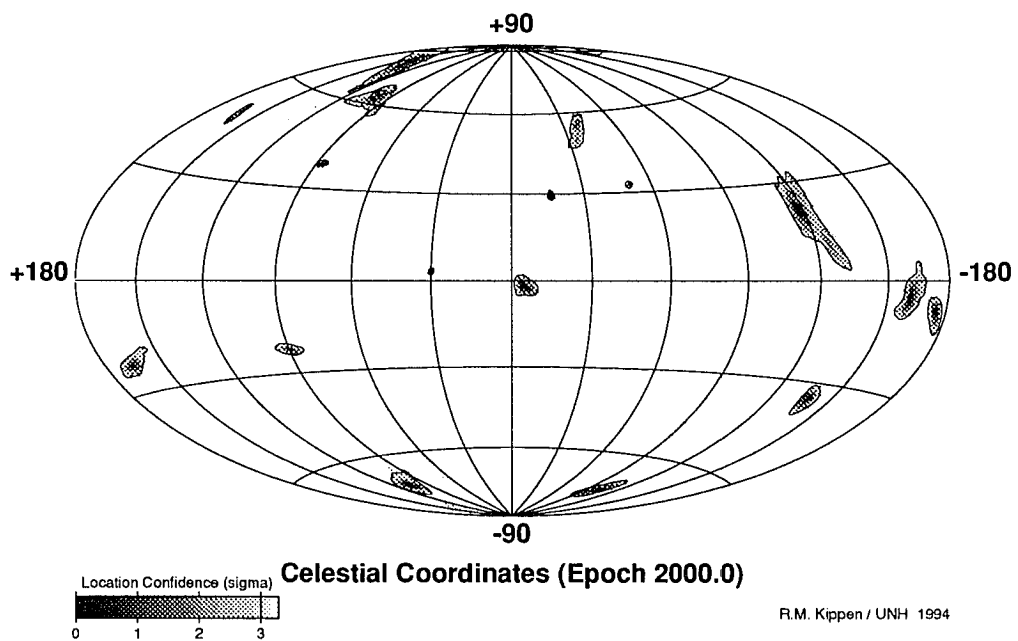
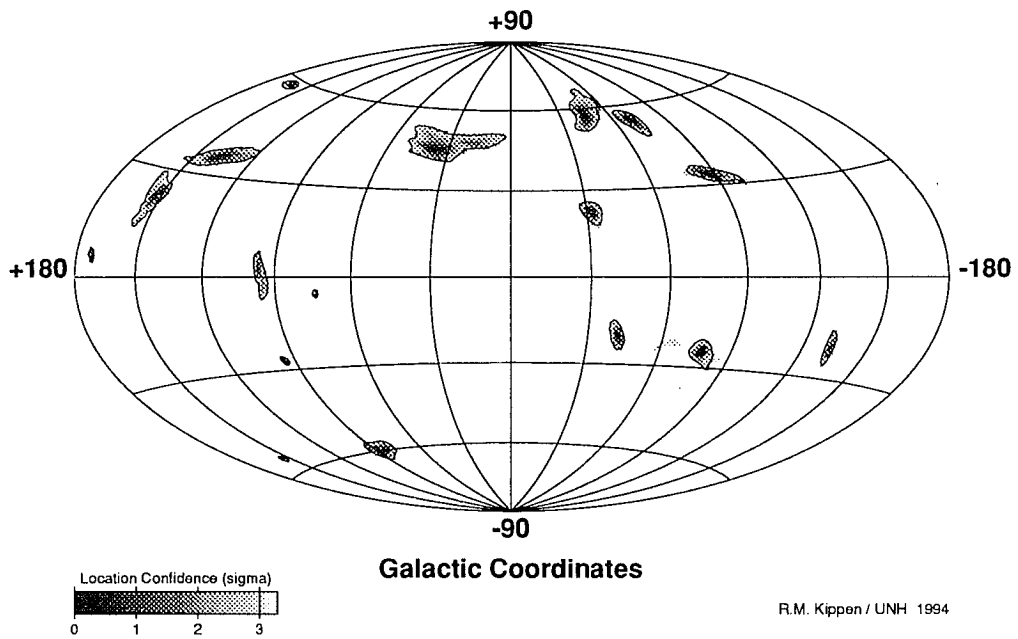


Fig. 4.3a-b. The all-sky distribution of 18 COMPTEL gamma-ray bursts in Galactic (a; top) and Celestial (b; bottom) coordinate systems. Gray-scales indicate burst location confidence in units of standard deviations (σ). Solid contours mark 3σ confidence limits.

Dipole and quadrupole moment statistics of the angular distribution of COMPTEL bursts are given in Table 4.4. The values and statistical uncertainties *expected* for an isotropic distribution of 18 burst sources were estimated by simulating random samples of isotropically distributed

Table 4.4 Angular Distribution Moments for 18 COMPTEL Gamma-Ray Bursts

Statistic	Expected*	Observed†	Deviation (σ)
Galactic Coordinates			
$\langle \cos \Theta \rangle$	$+0.029 \pm 0.139$	-0.102 ± 0.006	-0.94
$\langle \sin^2 b - \frac{1}{3} \rangle$	-0.019 ± 0.070	-0.013 ± 0.004	+0.09
Celestial Coordinates (Epoch J2000)			
$\langle \cos \Theta \rangle$	-0.096 ± 0.134	-0.071 ± 0.005	+0.19
$\langle \sin^2 \delta - \frac{1}{3} \rangle$	$+0.001 \pm 0.069$	$+0.071 \pm 0.004$	+1.01

*Expected value for an isotropic distribution of 18 bursts including non-uniform sky exposure.

†Observed value including localization errors.

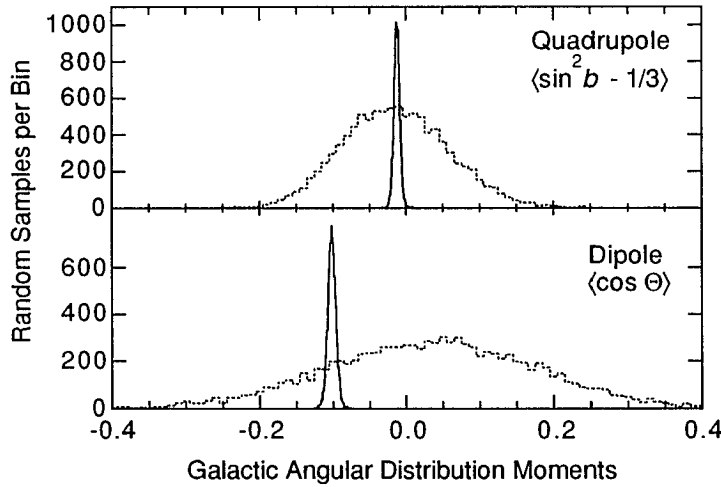


Fig. 4.4. Expected (dotted-lines; isotropic distribution influenced by non-uniform exposure) and observed (solid-lines; including localization uncertainty) distributions of Galactic dipole and quadrupole moments for 18 COMPTEL gamma-ray bursts .

burst locations (18 per sample) weighted by the COMPTEL exposure maps. *Observed* values and uncertainties were estimated by randomly distributing each of the most-likely burst locations according to the measured likelihood-ratio maps, thereby accounting for the particular

instrumental uncertainties of each burst (not including systematic errors). The values in Table 4.4 reflect the mean and standard deviation of the resulting distributions; each containing 10^5 samples. As expected, the statistical uncertainty due to the small sample size is much larger than that caused by instrumental localization errors. This is evident in Figure 4.4, which shows the distributions of expected and observed Galactic dipole and quadrupole moments. Within the large uncertainties, there is no significant deviation from isotropy evident in the COMPTEL sample in either Galactic or Celestial systems.

D. Small-Scale Angular Distribution and Burst Recurrence

The dipole and quadrupole moment statistics are good for revealing structure on large angular scales, but they are insufficient to probe the distribution of sources on small scales ($\leq 10^\circ$) since information is lost by averaging over the entire sample. Testing for the existence of small scale structure is important since it may identify, for example, clusters of bursts associated with known objects (e.g., nearby galaxies or globular clusters), repeated events from the same source (whose locations are blurred by instrumental uncertainty) or gravitationally lensed multiple images of individual bursts (see e.g., Paczynski 1986).

Small-scale structure in the angular distribution of burst sources would be obvious if gamma-ray instruments had perfect (or even moderate; arc-minute) angular resolution. Unfortunately, most burst locations are not known to better than a few degrees, thus statistical tools must be employed—making conclusive study problematic. This point is exemplified in recent analyses of BATSE data which indicate evidence of spatial clustering (Quashnock & Lamb 1993) and clustering in both space and time (Wang & Lingenfelter 1993). Both of these findings have been interpreted as the signature of repetitive bursts from individual sources on time-scales of months. These early findings have been disputed by several subsequent studies of larger samples of BATSE bursts, where no significant evidence for small-scale structure has been reported (e.g., Hartmann *et al.* 1994a; Strohmayer, Fenimore & Miralles 1994; Brainerd *et al.* 1994; Narayan & Piran 1993, 1994). With its relatively good angular resolution, COMPTEL is well-suited to

investigate small-scale angular structure where BATSE is less sensitive.

The statistical tools most commonly used to analyze small-scale angular structure are the two-point angular autocorrelation function and the nearest neighbor statistic. These two techniques are similar and both are suitable for detecting small-scale structure due to either spatial clustering or repetition.

For a given angular distribution of astrophysical sources, the autocorrelation function $w(\theta)$ measures the probability of finding a *pair* of sources separated by an angle θ (Peebles 1973). In practice, it is calculated by comparing the number of measured source pairs N_{obs} with angular separations in the interval $(\theta, \theta + d\theta)$ to the number expected (N_{ran}) from a purely random (Poisson) distribution with

$$w(\theta) = (N_{\text{obs}} / N_{\text{ran}}) - 1. \quad (4.1)$$

In the case of gamma-ray bursts, the underlying distribution of N_{ran} is isotropic. Small-scale angular clustering is then clearly evident as a positive deviation from zero in $w(\theta)$ at small angles. Angular correlation analysis was first applied to gamma-ray bursts by Hartmann & Blumenthal (1989) and Hartmann, Linder & Blumenthal (1991) and has recently been used on BATSE data to search for evidence of burst recurrence (Narayan & Piran 1993; Blumenthal *et al.* 1994; Hartmann *et al.* 1994a). All of these studies conclude that there is no statistically significant evidence of small-scale structure in the angular correlation functions of the gamma-ray bursts measured thus far. This constrains the fraction of repeating bursts to be less than $\sim 10\%$ – 20% (Hartmann *et al.* 1994a; Strohmayer, Fenimore & Miralles 1994). However, they also recognize that the inability to detect small-scale structure may be a result of poor angular resolution.

The angular autocorrelation function of the 18 COMPTEL bursts is shown in Figure 4.5. The effect of non-uniform sky exposure on the correlation function is small compared to statistical fluctuations ($w(\theta) \leq 0.1$), but has nonetheless been included using Monte Carlo simulation to compute the values of N_{ran} expected from an isotropic distribution weighted with the COMPTEL exposure map. The distribution of correlation function values in each bin is not Gaussian,

therefore statistical deviations from the values expected from isotropy have been estimated using the Monte Carlo simulations. The *only* obvious deviation from isotropy in the COMPTEL correlation function is a sharp excess at angular separations less than 2° .

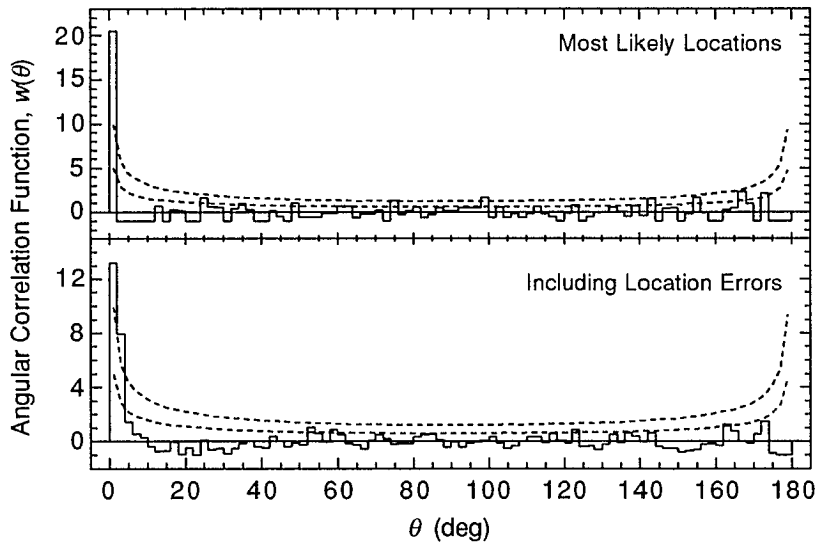


Fig. 4.5. The angular correlation function of 18 COMPTEL gamma-ray bursts in 2° bins. The upper panel shows the distribution computed using the most-likely burst positions, while the lower panel includes the effect of location errors. Dashed curves represent the one and two standard deviation statistical excesses expected from an isotropic distribution (determined by Monte Carlo simulation).

The correlation function computed using simply the most-likely COMPTEL locations (upper plot in Figure 4.5) does not accurately reflect the intrinsic source distribution since the location of each source is not precisely measured. To account for this effect, the most-likely burst locations were randomized according to the measured likelihood-ratio maps, thereby accounting for the particular location errors of each burst. The lower panel in Figure 4.5 shows the *mean* value of the correlation function in each angular bin obtained using 10^5 randomized COMPTEL samples. The overall effect of this process is that the small-angle enhancement observed using only the most-likely burst positions is spread out into several bins. The observed excess ($\theta < 4^\circ$) including the effect of location errors is still, however, 2.9 standard deviations above the value expected for an isotropic distribution and the probability of observing such an excess purely by

chance is only $\sim 1.8\%$.

The observed excess in the autocorrelation function results from the fact that two bursts, occurring eight months apart (GRB 930704 and GRB 940301), are localized within a small region of the sky (Ryan *et al.* 1994a; Kippen *et al.* 1995a). The locations of these two spatially-coincident events are entirely consistent with the same position within instrumental errors given that the 2σ uncertainty region of GRB 940301 is completely enclosed inside that of GRB 930704 (see Figure 4.6). At the time of the latter event, COMPTEL had observed a total of 17 bursts. As in the previous section, this sample of bursts is also found to be consistent with an isotropic distribution of sources. Given COMPTEL's good angular resolution, the chance of observing a spatial coincidence of two bursts in a randomly chosen, isotropic sample of 17 is small, but not negligible.

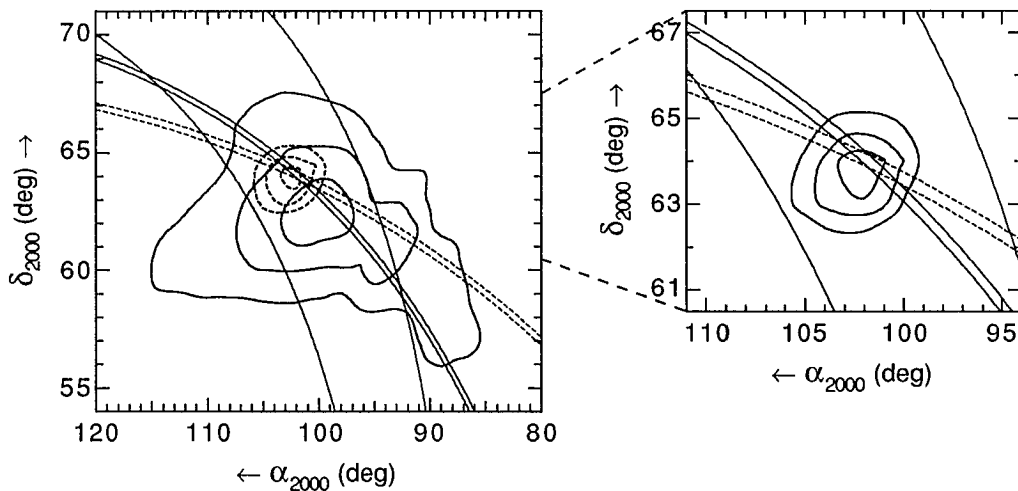


Fig. 4.6. COMPTEL maximum-likelihood localizations (1-, 2- and 3σ confidence) and IPN “triangulation” annuli of GRB 930704 (solid lines and contours) and GRB 940301 (dashed lines and contours). The enlarged region at right shows the *combined* COMPTEL localization of both bursts (with the assumption that they originated from a single source).

In an isotropic distribution of N non-repeating burst sources, one expects to find, on average, n sources which have at least one neighboring source within an angle θ given by

$$n(\theta) = N \left[1 - \left\{ \frac{1}{2} (1 + \cos \theta) \right\}^{N-1} \right] . \quad (4.2)$$

This is the so-called nearest neighbor probability distribution function (Scott & Tout 1989) which was employed by Quashnock & Lamb (1993, 1994) to suggest that there is evidence of burst repetition in the first BATSE catalog. Small angle ($\theta \sim$ instrumental resolution) deviations from the values predicted by equation (4.2) are indicative of small-scale clustering or repeating sources. The most-likely locations of GRB 930704 and GRB 940301 are separated in space by $\sim 1^\circ 7$. Thus, for the 17 COMPTEL bursts observed through GRB 940301, we expect only $n(\theta = 1^\circ 7) = 0.06$ random occurrences—yet $n = 2$ have been observed (i.e., GRB 930704 and GRB 940301 *both* have a nearest neighbor within $1^\circ 7$). The statistical significance of this observation was estimated by generating random samples containing $N = 17$ burst sources drawn from an isotropic distribution (weighted with the COMPTEL exposure map valid through GRB 940301). Only $\sim 3.0\%$ of the samples had two or more sources with nearest neighbors within $1^\circ 7$. As in the case of the angular correlation function, the effect of COMPTEL's non-uniform sky exposure is small (contributes less than 0.1 of the 3%). It was shown by Quashnock & Lamb (1994) that for isotropic sources, the nearest neighbor distribution is unaffected by localization errors when the errors are independent of position on the sky. This is demonstrated by the fact that when random, COMPTEL-like, location errors are included in the simulations the results remain essentially the same. Thus, using only COMPTEL data, the hypothesis that GRB 930704 and GRB 940301 are a chance spatial coincidence of two unrelated sources (drawn from an isotropic distribution) can be rejected with $\sim 97\%$ confidence. This result suggests the *possibility* that these two bursts somehow originated from a single source or an unresolved cluster of sources.

With the assumption of a single source, addition of the individual likelihood ratio skymaps determines the most probable *combined* source location and uncertainty region (see Figure 4.6).

This combined localization is heavily weighted by the stronger burst (GRB 940301; see Table 3.1), but overlaps the 1σ regions of both individual events. This is another indication that the individual COMPTEL localizations are consistent with a single, unresolved, source.

Independent localizations of GRB 940301 were obtained by the BATSE (C. Meegan, private communication) and EGRET (B. Dingus, private communication) instruments—both of which agree with the combined COMPTEL localization within their 1σ uncertainties (BATSE $\sim 4^\circ$; EGRET $\sim 3^\circ$). The combined COMPTEL localization is outside the BATSE 1σ error-radius of GRB 930704, but well within BATSE’s estimated 2σ uncertainties ($\sim 6^\circ\text{--}8^\circ$; C. Meegan, private communication). Interplanetary Network spacecraft observations (K. Hurley, private communication) provide two “triangulation” annuli for GRB 930704 (using BATSE/*Ulysses*/*Mars Observer* arrival-time analysis) and a single annulus for GRB 940301 (BATSE/*Ulysses*). These individual IPN annuli are fully consistent with the separate COMPTEL localizations—each passing well within the corresponding COMPTEL 1σ uncertainty contours. If the two bursts originated from a single source, the intersection of all the IPN annuli would contain its position. The fact that the intersection region of all the annuli lies inside the *combined* COMPTEL 1σ localization is consistent with (but does not require) a single source origin. In principle, the third IPN annulus (using *Mars Observer* measurements) could conclusively rule out a single source. However, its large uncertainty makes it consistent with both double and single source hypotheses.

Combination of the COMPTEL and IPN measurements of these two bursts further constrains their locations (see Table 4.2). Even with these further constraints, the two events are still consistent with a single source in that the IPN intersection lies within the 1σ COMPTEL/IPN uncertainty region of GRB 940301 and within the 2σ uncertainties of GRB 930704. The chance of observing of two coincident (i.e., overlapping) COMPTEL/IPN localizations was estimated using further Monte Carlo simulations wherein randomly oriented, isotropically distributed arc segments were generated. The length of these segments was conservatively set to the average 2σ length of all the COMPTEL/IPN bursts ($\sim 3^\circ$; see Table 4.2) and their negligible widths and

curvatures were ignored. In random samples each containing 17 arc segments, intersections were found to occur with a frequency of only $\sim 1.5\%$. As in the other simulations, the effect of non-uniform sky exposure is small. Thus, while combination of COMPTEL and IPN measurements decreases the probability of random spatial coincidence from $\sim 3\%$ to $\sim 1.5\%$, the chance is still not negligible.

E. Discussion

In essence, this chapter has been most concerned with the ability of COMPTEL to accurately and precisely localize the sources of gamma-ray bursts. This ability has been demonstrated on several different levels and the resulting COMPTEL burst positions are seen to be consistent with all other available measurements within the confidence limits computed here. Although the COMPTEL burst location sample is limited in number, it is clearly an important new piece of information with which to probe the nature of burst sources. The ability to compute combined COMPTEL/IPN confidence regions for the majority of the bursts further enhances the value of this independent catalog of locations. Analysis of these locations has shown that the sources are not of local origin, that they are consistent with an isotropic angular distribution and that two of the bursts could possibly originate from a single source. The implications of these findings are discussed in the remainder of this section.

i. Distance Constraints

Ever since the BATSE discovery/confirmation (e.g., Meegan *et al.* 1992) that burst sources are isotropically distributed, yet radially-inhomogeneous, it has generally been recognized that a fairly local origin near the sun is a possibility. The major theoretical difficulty in this distance regime has been the lack of likely energy sources which are numerous and powerful enough to explain the observations. Nonetheless, at least a few scenarios have been suggested. Some of these involve the interactions of relativistic particles within the heliosphere, while the others invoke fast-moving, long-period comets from the Oort cloud—a roughly spherical distribution surrounding the solar system at a typical distance of $\sim 10^4$ AU (Oort 1950).

It was proposed very early-on that gamma-ray bursts could be the result of highly relativistic dust grains from interstellar space (perhaps originating from nearby pulsars or outside the Galaxy) encountering the heliosphere (Grindlay & Fazio 1974; Dasgupta 1979). In this model a dust grain with Lorentz factor $\Gamma = (1 - v^2/c^2)^{-1/2} \sim 1000$ would break up at a distance of ~ 100 AU due to heating by ultraviolet solar radiation. The resulting ionized fragments would efficiently upscatter solar photons to energies in the range ~ 10 keV to 1 MeV—producing a beamed “burst” of gamma rays. For example, a dust grain composed of 10^{-2} g of iron could produce enough gamma rays to explain the typical observed burst fluences ($\sim 10^{-5}$ erg cm^{-2} ; Grindlay & Fazio 1974). The burst would last ~ 0.01 – 10 s (depending on the number, size and Γ of the fragments) until the grains are completely dissipated. Of course, the incident grains would have to isotropically distributed around the sun to explain the observed isotropy of bursts.

Comets residing in the Oort cloud are frequently perturbed by the gravitational forces of the planets into trajectories which bring them much closer to the sun (less than a few hundred AU). It has been suggested that through electrostatic processes, the collision of two comets might release a small fraction of their combined kinetic energy in the form of a burst of gamma rays (Katz 1993; White 1993). With typical velocities ~ 3 km s^{-1} , the collision of two comets at a distance of ~ 100 AU would provide $\sim 10^{28}$ erg of energy—more than 100 times that required to explain the energy of a typical gamma-ray burst (White 1994, 1993). Although collisions could also occur at much greater distances, the gamma-ray production mechanism would have to be extremely efficient in order to meet the energy requirements. White (1993, 1994) therefore suggested that a cloud of comets (as yet unobserved) from 40–400 AU would be quite stable in the evolution of the solar system and could explain many of the observed features of GRBs—including the spatial distribution, energetics, time-scales, lack of counterparts and lack of recurrence.

A more exotic possibility has been discussed by Bickert & Greiner (1993) wherein GRBs are produced by collisions between comets and small-mass primordial black holes (assumed to be distributed throughout the comet cloud). In this scenario cometary matter is compressed in the intense gravitational field of the black hole and heated to several MeV. The energy liberated in

the form of gamma rays could be sufficient to place the sources anywhere from $\lesssim 100$ AU to $\sim 10^4$ AU, depending on the mass of the black hole. Like the comet-comet model, this explanation could also explain many of the observed features of GRBs.

The distance constraints required by the COMPTEL/IPN burst location measurements clearly dispute any models which place the *nearest* GRB sources (and therefore the strongest; assuming bursts are “standard candles”) closer than ~ 100 AU (approximately the distance to the solar wind termination shock). Thus, the relativistic dust grain model is excluded and the 40–400 AU source distribution proposed by White (1993, 1994) appears unlikely. The observed BASTE spatial and intensity distributions are marginally consistent with Oort cloud sources at larger distances (~ 500 – 10^4 AU; Horack et al. 1994; Maoz 1993), but it is difficult to explain (1) the source of energy at such distances and (2) why bursts would *only* originate in the outer portions of the cloud. Using statistical arguments based on the observed distribution of comets in the solar system, Clarke, Blaes & Tremaine (1993) have convincingly argued that if bursts are produced (by whatever means) in the Oort cloud at all, they should originate from the inner region ($\lesssim 500$ AU). While the COMPTEL/IPN constraints cannot completely rule out an inner Oort cloud distribution, they do severely constrain the range of distances. Other instruments with better angular resolution (e.g., EGRET or 4 IPN spacecraft) will increase the minimum burst distance even further. It thus appears improbable that bursts can originate from the Oort cloud. Lacking further energy sources, it is difficult to explain bursts originating from anywhere within the heliosphere.

ii. Large-Scale Distribution

As pointed out earlier in this chapter, the ability to measure large-scale angular structure in the distribution of burst locations is dominated by statistical errors related to sample size, with large samples having an outstanding advantage. The COMPTEL measurements are thus clearly limited due the small number of bursts. They do, however, provide a useful consistency check on the more constraining BATSE measurements. The COMPTEL results are compared to those of

BATSE and *Granat*-WATCH in Figure 4.7. Following Meegan *et al.* (1994), the BATSE bursts through April 1994 have been divided into three inclusive samples (1B-262 bursts, 2B-585 bursts and all three years-964 bursts). The WATCH results include 32 bursts observed between December 1989 and September 1992. All of the results are consistent with an isotropic distribution of sources. However, the BATSE results are clearly the most constraining measure due to the large sample size. As pointed out by several authors, location errors do not severely effect the ability to measure large-scale structure (e.g., Hartmann & Epstein 1989). In fact, more than 5000 COMPTEL bursts would be required before the statistical errors would be of the same order as those caused by location uncertainty.

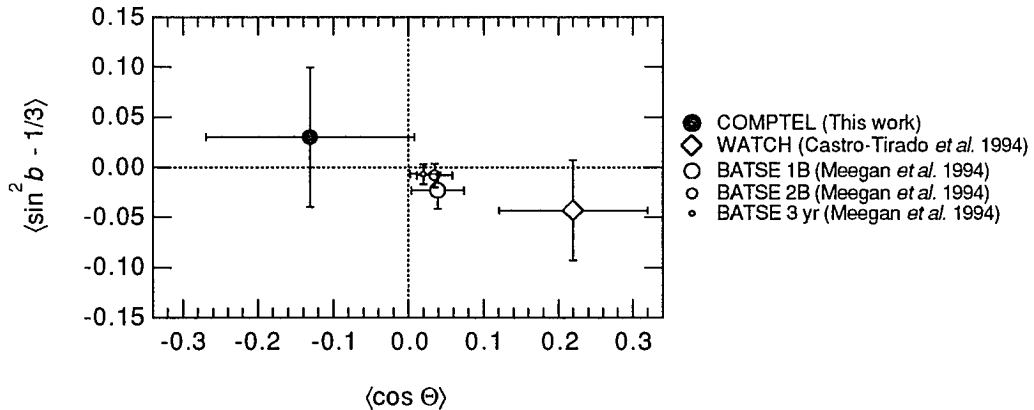


Fig. 4.7. Comparison of observed gamma-ray burst Galactic dipole and quadrupole moments (corrected for non-uniform sky exposure).

The COMPTEL observations independently confirm that a subset of some of the brightest bursts measured by BATSE are consistent with an isotropic distribution. This is an important consistency check on the BATSE results especially since if burst sources reside in the Galactic halo the strongest events (i.e., closest) will eventually be expected to exhibit some anisotropy due to the ~ 8.5 kpc offset of the sun from the Galactic center. Furthermore, this finding disputes the claim that the brightest BATSE bursts are not isotropically distributed. Whitmire, Whitman & Matese (1994) found that the mean vector of the ~ 20 brightest BATSE bursts is slightly anisotropic (at the $\sim 2\sigma$ level) and that it points in the direction of known indicators of large-scale

($z \sim 0.5$) structure in the universe (e.g., clusters of low-redshift quasars and galaxies). They point out that if GRB sources are a cosmological distribution at redshifts $z \sim 1$, one would expect the strongest (and therefore closest) bursts to be associated with known large-scale structures at $z \sim 0.5$. While it is still possible that such an association might exist at a low level, the COMPTEL results do not support this conclusion since the COMPTEL bursts are consistent with isotropy and do not indicate any preference towards the suggested direction. Another important consequence of the COMPTEL measurement is that it justifies the use of an isotropic parent distribution in the investigation of small-scale angular structure.

iii. Small-Scale Distribution

Many spatially-coincident “classical” gamma-ray bursts have been observed in the past, but the coincidence has generally been attributed to chance, given the large (several degrees) location uncertainties involved. Using separate samples of relatively well-localized bursts, Schaefer & Cline (1985) and Atteia *et al.* (1987b) independently estimated that in order to fit the observed rate and spatial distributions, the burst recurrence time-scale $\tau_\gamma \geq 10$ yr—assuming that repeated bursts are monoluminous. However, if the distribution of recurrent burst luminosities is broad, τ_γ could be as short as a few months. Recently, coincident bursts have been observed even by instruments with fairly good location accuracy. In a sample of 32 bursts, the WATCH detectors on *Granat* found two pairs of overlapping $\sim 1^\circ$ localizations (Castro-Tirado *et al.* 1994a). However, both coincidences have been dismissed as chance occurrences by Interplanetary Network observations (K. Hurley, private communication). This shows the inherent statistical dangers present when observing small-scale correlations using small samples of bursts.

It was shown that the spatial coincidence of GRB 930704 and GRB 940301 observed by COMPTEL is consistent with a single, unresolved, source or cluster of sources and consistent with independent localizations provided by BATSE, EGRET and IPN. There are three possible explanations for this coincidence: (1) that it is the result of a chance overlap of unrelated sources, (2) that a single source (or cluster of sources) produced two separate bursts and (3) that the two

events are time-delayed images of a single burst which has been gravitationally lensed by an intervening massive object.

If burst sources lie at cosmological distances, they should be lensed by foreground galaxies about as frequently as are quasars, with time delays between the images ranging from a few months to years—depending on the geometry and mass of the lens (Paczynski 1986; McBreen & Metcalfe 1988; Mao 1991). If the two bursts are an artifact of gravitational lensing, we would expect the lensed images to be unresolved spatially and to have identical time-profiles and spectra to within a scale factor. The statistics of the COMPTEL measurements alone are insufficient to conclusively test this hypothesis. However, using *Compton*–OSSE and BATSE data, Hanlon *et al.* (1995) have measured significant differences in the time-profiles and spectra of the two bursts—ruling out the possibility of gravitational lensing.

If the spatial coincidence is due to recurrent outbursts from a single source, any model which invokes a singular, cataclysmic (i.e., the destructive merger of two objects) event would be unlikely. Such “merger” models have been the most often used theory to explain bursts at cosmological distances through collisions between compact stellar objects such as neutron stars and black holes (Mészáros & Rees 1992a; Narayan, Paczynski & Piran 1992). The predicted rate of such collisions ($\sim 10^{-6}$ yr⁻¹ per host galaxy) is insufficient to explain repeated bursts from individual galaxies (or even clusters of galaxies) on time-scales of months (Hartmann *et al.* 1994a). Similar considerations hold for “failed type 1B supernova” models, where bursts derive their energy from accretion discs around massive extragalactic black holes (Woosley 1993). The observation of a repeating burst source would thus be difficult to explain with currently favored cosmological models. Conversely, most galactic models (e.g., nearly all galactic neutron star models) and some non-merger cosmological models (e.g., extragalactic jets; Brainerd 1992) actually predict recurrence on a variety of time-scales, ranging from seconds to years.

Although it was shown that the probability of observing a spatial coincidence like this one by chance is a non-negligible $\sim 1.5\%$ (including COMPTEL/IPN measurements), the possibility that the coincidence was non-random cannot be overlooked as it is the most constraining measurement

possible with current instrumentation (i.e., the *Compton* Observatory). A conclusive (say, $\geq 4\sigma$ significance) measurement with only two coincident bursts would require location accuracies better than 0.1° . This kind of accuracy is beyond the limitations of current wide-field imaging gamma-ray instruments and is only achievable by IPN triangulation with three or more spacecraft. Without arc-minute positioning, the only definitive measurement of the existence of a repeating burst source would be the observation of more coincident events or simply a third outburst from the combined COMPTEL localization region of GRB 930704/GRB 940301. Thus, it may be that bursts do repeat and that this behavior has been masked by the poor resolution of previous studies. Unfortunately, without more examples like the one discussed here, this cannot be conclusively shown.

V. RESULTS OF SPECTRAL ANALYSIS

In this chapter, COMPTEL spectral measurements are used to investigate the characteristics of MeV burst emission. It is important to discuss how these measurements relate to the physical mechanisms that could be operating in burst sources. Since the COMPTEL data cover a fairly small energy range, it is important to relate them to lower and higher energy measurements. This is possible for several bursts where simultaneous observations have been obtained from the other *Compton* instruments from keV (i.e., via BATSE) to GeV (i.e., via EGRET) energies.

A. COMPTEL Measurements of MeV Burst Emission

The time-averaged energy spectrum of each COMPTEL gamma-ray burst was determined by accumulating telescope events over intervals chosen so as to include at least all significant burst emission. In some cases the accumulation time-intervals were expanded slightly to match those of other experiments (in particular, the COMPTEL–BSA detectors). This practice does not significantly alter the resulting spectra, since the additional accumulations are small and are accounted for in the background estimation process. The background contribution (both instrumental and cosmic diffuse) during each burst was estimated by averaging the number of counts accumulated during intervals 15 orbits before and after the burst. In several cases, due to telemetry gaps and changes in spacecraft attitude, 14 or 16 orbit intervals were substituted with little loss of accuracy.

Instrument livetime during burst and background intervals was estimated using scalar count rates measured at various points in the COMPTEL telescope event detection and data telemetry process. Due to the poor temporal resolution of these scalars (2.048 s or 16.384 s), livetime estimates determined in this manner are typically only reliable over the full duration of a burst or over the full duration of well-separated pulses within a burst. The COMPTEL measurements are thus insufficient to study spectral variations *within* individual pulses. Errors in livetime estimation could be significant (perhaps as large as 20%–50%; see Appendix B), but they effect

mainly the overall normalization of a spectrum and not the shape. However, an important consequence of instrument deadtime is that the presence of spectral evolution in impulsive bursts (where deadtime causes the impulsive intervals to be under-sampled) could influence the shape of time-averaged spectra. Livetime fractions and spectral accumulation intervals used in the analysis of each burst are listed in Table 5.1. For reference, the typical livetime fraction during background intervals is $\sim 95\%$ – 98% .

Table 5.1 Spectral and Temporal Burst Parameters

Burst Name	t_o^*	Δt^\dagger	f_{live}^\ddagger	δt_{min}^\S	E_{max}^\parallel	$E_{3\sigma}^\#$
GRB 910425	2267.79	39.26	0.95	0.50	17.1	7.4
GRB 910503	25454.74	57.34	0.40	0.05	12.9	8.1
GRB 910601	69750.00	19.83	0.50	0.10	3.75	2.3
GRB 910627	16159.82	9.13	0.96	0.50	33.0	2.9
GRB 910709	41604.00	0.60	0.87	0.05	3.2	2.6
GRB 910814	69275.08	33.24	0.44	0.10	20.0	7.2
GRB 911118	68260.10	9.12	0.95	0.50	17.4	2.7
GRB 920622	25506.57	24.17	0.92	0.25	7.0	3.4
GRB 920830	6317.61	4.05	0.96	0.50	6.2	3.6
GRB 930118	64427.00	4.00	0.94	0.50	10.4	1.7
GRB 930131	68231.58	1.02	0.12	0.05	28.3	12.1
GRB 930309	11280.02	39.98	0.95	1.00	27.8	1.6
GRB 930612	2657.00	12.83	0.96	5.00	8.8	3.3
GRB 930704	60545.73	18.15	0.96	1.00	14.4	1.9
GRB 931229	26165.80	0.60	0.96	0.10	1.6	1.5
GRB 940217	82962.12	162.79	0.53	0.10	18.2	8.8
GRB 940301	72643.22	42.20	0.74	0.10	14.7	8.3
GRB 940314	35989.00	51.00	0.96	10.00	34.1	4.1

*Start time of spectral accumulation (seconds UT).

†Integration time (s) for spectral analysis.

‡Instrument livetime fraction.

§Shortest estimated intensity variability time-scale (s).

∥Maximum measured energy deposit (MeV) during burst interval.

#Maximum significant ($\geq 3\sigma$) energy deposit (MeV).

The accumulated burst and background count rates (corrected for livetime) were combined into 15 logarithmically-spaced energy intervals over the full COMPTEL energy range from 0.75 to 30 MeV. These measured count rate spectra were directly inverted (see Chapter II) using the simulated vector response of COMPTEL to an assumed trial spectral shape (power law). To

minimize systematic effects, the procedure was refined by updating the trial spectrum to more closely match the data and again inverting the measured count-rate spectra. Due to the nearly diagonal COMPTEL response, the resulting deconvolved photon fluxes are only weakly dependent on the shape of the trial spectrum, thus a single iteration is sufficient. The errors introduced by this deconvolution technique are small ($\leq 10\%$) compared to the statistical uncertainties inherent in the measured spectra—even when the spectral shapes of the burst and response differ significantly. This was shown through simulations wherein different burst spectra were inverted with the same instrument response vector (see Appendix B).

The time-averaged differential photon number energy spectrum ($N_E \equiv dN/dE$ photons $\text{cm}^{-2} \text{s}^{-1} \text{MeV}^{-1}$) of each burst is displayed in Appendix A. Within statistical uncertainties, the deconvolved spectra are all roughly consistent with the power law shape assumed in the direct inversion process, but the spectral slopes differ considerably from burst to burst. This will be discussed in more detail in the next section. The burst statistics also differ considerably—depending on burst fluence, viewing efficiency and spectral shape. These effects influence the maximum energy at which significant emission is observed (see Table 5.1).

Higher energies are generally detected from the bursts with harder spectra, but only if the burst fluence and detection efficiency are great enough. The maximum significant energy for each burst (Table 5.1) was estimated by computing, in the interval (E_1, ∞) , the cumulative Poisson “tail” probability of measuring *at least* the observed number of counts, given the number expected from background (see e.g., Press *et al.* 1986). The energy E_1 was increased until the tail probability dropped below the 3σ significance level, thus indicating the maximum energy at which significant flux is measured. This method accounts properly for the non-Gaussian statistics inherent with the low COMPTEL count rates at high energies. As can be seen in the table, most of the bursts show significant emission beyond ~ 2 MeV. This is not surprising, since COMPTEL’s sensitivity to typical burst-like spectra peaks in this range. However, several of the strong bursts are significant past 8 MeV. The highest *absolute* total energy deposit (source *or* background) observed during each burst interval is also listed in Table 5.1. This is nearly always

larger than the maximum significant energy from the burst, indicating that the high-energy measurements are constrained by low statistics and not by instrumental limits.

B. Spectral Modeling

The greatest breakthrough in modeling gamma-ray burst spectra would be the identification of a characteristic feature such as a line, dip or cutoff due to some emission, absorption or attenuation process. Although significant keV emission and absorption features have been reported in past observations (e.g., Mazets *et al.* 1981a; Hueter 1984; Murakami *et al.* 1988) they have not yet been observed in any of the bursts detected by BATSE (Palmer *et al.* 1994), nor in any observed by the COMPTEL burst mode (Hanlon *et al.* 1994). Without confirmation of spectral features, we are left only with the continuum shape as a diagnostic of the burst emission processes.

An inherent problem in all studies of continuum burst spectra is the fact that the spectral shape changes throughout the duration of a burst (see e.g., Golenetskii *et al.* 1983; Norris *et al.* 1986; Ford *et al.* 1995). It is thus difficult to separate intrinsic spectral properties from evolutionary effects when studying time-averaged emission. Spectral variations have been observed on 2 ms time-scales (Kouveliotou *et al.* 1994b; Bhat *et al.* 1994), so they appear to be a common phenomena that effect all measurements—no matter how short the accumulation.

Modeling of burst continuum spectra has undergone several changes as instrumentation has improved and high-energy coverage has been extended. While some spectral models are used simply to explain the observed data with a convenient mathematical form, others attempt to do so based on an assumed gamma-ray production mechanism. Important considerations in spectral modeling are the energy range being fitted and the statistical quality of the data. Most models can explain spectra measured over a small energy range or data with limited statistics, but few are capable of describing high-significance, wide-band measurements.

BATSE measurements have shown that the time-averaged continuum energy spectra of most gamma-ray bursts on nearly all measurable time-scales can be well-described from ~ 30 keV up to

~ 1 MeV by a power law with an exponential cutoff, $N_E(E) \propto E^{-\alpha_L} \exp(-E/E_b)$, and by a steeper power law, $N_E(E) \propto E^{-\alpha_H}$ ($\alpha_H > \alpha_L$), at higher energies (Band *et al.* 1993a; Band *et al.* 1993b; Ford *et al.* 1995). This general form (the so-called ‘‘GRB model’’) agrees with the spectra observed by other instruments that are most commonly fit below ~ 1 MeV with α_L fixed at 1.0 (Mazets *et al.* 1982) and a variable power law at higher energies (Matz *et al.* 1985) or alternatively by a combination of two variable ‘‘broken’’ power laws (Schaefer *et al.* 1992, 1994b; Barat 1993; Pelaez *et al.* 1994). Although a wide range of parameters are required to fit *all* the observed bursts (or even a single burst at different times), several physical models of the gamma-ray emission process have been developed which attempt to explain the observed spectral shapes.

i. Continuum Emission and Attenuation Mechanisms

The bremsstrahlung, synchrotron and inverse Compton processes operating in the environment of a hot, optically thin plasma have all been invoked to explain the observed GRB spectra. Depending on the nature of burst sources, there are arguments for and against each of these thermal emission models (Liang 1987; Lamb 1984), but all three can generally describe most of the observed spectra below about 1 MeV (see e.g., Schaefer *et al.* 1994b). It is at higher energies where the deficiencies of thermal emission models become most apparent. Therefore, non-thermal mechanisms are often used to explain the observed hard emission spectra at energies above ~ 1 MeV. Any burst emission mechanism (thermal or non-thermal) must compete with several attenuation processes that could be at work in burst sources. The most important of these is pair production.

The optically thin thermal bremsstrahlung mechanism (OTTB) produces gamma rays through radiative collisions between particles contained in a hot ionized gas. The resulting spectrum of photon energies takes the *approximate* form

$$N_E(E) \propto g(E,T) E^{-1} \exp(-E/kT), \quad (5.1)$$

where T is the plasma temperature, k is the Boltzmann constant and g is the energy and temperature dependent Gaunt factor (Blumenthal & Tucker 1974). Typically, the Gaunt factor is

assumed to have a weak dependence on energy and temperature and is usually taken to be a constant of order unity (Karzas & Latter 1961). However, the exact form of the OTTB spectrum depends on the range of photon energies and plasma temperatures involved. At high temperatures and high energies ($E \sim kT \gtrsim m_0c^2$) the spectral form of equation (5.1) must be modified for relativistic effects and the contribution of electron-electron bremsstrahlung (Gould 1980, 1982). Neglecting these effects, the approximate OTTB spectral shape was the model used to explain the bulk of pre-BATSE spectra (<1 MeV) with plasma temperatures kT of order ~ 250 keV (Mazets *et al.* 1982).

The OTTB model has been criticized in the past in part because at the temperatures inferred by the best-fits to GRB spectra, bremsstrahlung is not always an efficient means of cooling a hot plasma. Fenimore *et al.* (1982) suggested that inverse Compton scattering of nearby low-energy photons would be a more likely energy release mechanism. Inverse Compton (IC) up-scattering of thermal energy photons from a cool source by an overlying hot e^+e^- pair plasma produces a spectral shape approximated by

$$N_E(E) \propto E^\alpha \exp(-E/E_e). \quad (5.2)$$

The temperature of the plasma is *related* to E_e and the spectral index α depends on the combination of the hot and cold plasma temperatures and the Compton scattering optical depth of the overlying region (Shapiro, Lightman & Eardley 1976; Sunyaev & Titarchuk 1980). Low Compton opacity results in a spectrum which resembles that of the thermal photon distribution, whereas high opacity results in a Wein spectrum with $\alpha = 2$ (Sunyaev & Titarchuk 1980). Fenimore *et al.* (1982) found acceptable fits to burst spectra suggesting that the low-energy photons come from a thermal X-ray source ($kT \sim 2$ keV) while the overlying plasma has $kT \sim 150$ keV and a column density of $\sim 10^{24}$ electrons cm^{-2} . Different combinations of hot and cool source temperatures, densities and geometries in this process allow for great flexibility in modeling burst spectra (Harding 1991).

If gamma-ray burst source regions are accompanied by a strong magnetic field ($B \gtrsim 10^{12}$ G;

e.g., as might be expected near a neutron star), synchrotron emission will dominate both bremsstrahlung and inverse Compton as the most efficient means of cooling a hot plasma (Liang 1982). The gamma-ray spectra produced through the thermal synchrotron process (TS) are harder, on average, than either OTTB or IC emission with the spectrum of photon energies approximately (Petrosian 1981) given by

$$N_E(E) \propto \exp\left\{-\left(4.5 E/E_c\right)^{1/3}\right\}, \quad (5.3)$$

The critical energy E_c in the TS model is related both to the temperature and magnetic field of the plasma through the relation $E = E_B \langle \sin \theta \rangle [kT_e / m c^2]^2$, where E_B is the Larmor energy, T_e is the plasma temperature and θ is the angle between the magnetic field and the observer line of sight. It is assumed that $kT_e \leq m_0 c^2$ and that $E \gg E_B / kT_e$. Liang, Jernigan & Rodrigues (1983) found that the approximate TS model could describe many GRB spectra (<1 MeV) as well as either OTTB or IC, with the best-fit E_c in the range 2–10 keV. The approximate form of equation (5.3) breaks down when the radiated photon energy becomes comparable to (or greater than) the average thermal energy of the electrons. In this case, the TS spectrum is significantly *softer* at higher energies, but can still explain some of the observed GRB spectra (Imamura, Epstein & Petrosian 1985). In regions where the magnetic field is reduced, OTTB and IC will become more efficient than TS. In regions of intermediate magnetic field strength, the spectrum of gamma rays could be a complicated mixture of all three processes.

Due to the hardness of burst spectra that have been measured above 1 MeV, emission models in this regime have generally invoked non-thermal processes. The simpler of these mechanisms involve synchrotron or inverse Compton emission from a non-thermal plasma (Lamb 1984). Depending on the initial energy distribution of the plasma, these emission models generally predict a hard power law (PL) spectrum above 1 MeV in agreement with the burst observations. In addition, Zdziarski & Lamb (1986) have shown that the change in burst spectra below and above a few hundred keV can be explained by repeated Compton scattering of low-energy photons by a power law distribution of relativistic electrons. A collisionless shock could produce

the required non-thermal particle distribution as could acceleration along intense magnetic field lines before Comptonization takes place (Ho & Epstein 1989). Another process which would produce a sufficiently hard spectrum at high energies is the Comptonization of a TS photon source by a hot plasma (McBreen, Plunkett & Metcalf 1993). In order to be efficient, the magnetic field in this scenario would have to be reduced in the region where the Comptonization takes place.

In distant burst source environments, the required large energy release on short time scales necessitates a high density of photons. In such environments, the two-photon pair production process ($\gamma\gamma \rightarrow e^+e^-$) is an important source of gamma-ray opacity at high energies. For the γ - γ interaction to take place between two photons of energy E_1 and E_2 , momentum conservation requires that

$$E_1 E_2 \geq 2m_0^2 c^4 / (1 - \cos \theta), \quad (5.4)$$

where θ is the angle between the two photon momentum vectors (Stecker 1971). Thus, the absolute threshold for pair production is for the case of a head-on collision ($\theta = \pi$), where the product of the two photon energies must exceed $(0.511 \text{ MeV})^2$. In the center-of-mass frame of reference, the electron and positron are created in this mechanism with velocity βc , where $\beta^2 = 1 - 2m_0^2 c^4 / [E_1 E_2 (1 - \cos \theta)]$. The cross section for unpolarized two-photon pair production peaks at twice the threshold energy with a value of $1.7 \times 10^{-25} \text{ cm}^2$ and is given by

$$\sigma_{\gamma\gamma}(E_1, E_2) = \frac{3}{16} \sigma_T (1 - \beta^2) \left\{ (3 - \beta^4) \ln \frac{1 + \beta}{1 - \beta} - 2\beta(2 - \beta^2) \right\}, \quad (5.5)$$

where σ_T is the Thompson cross section (Jauch & Rohrlich 1955). When integrated over a dense cloud of high-energy photons, this cross section yields a significant opacity that will severely attenuate a gamma-ray spectrum above the threshold. The details of γ - γ attenuation depend on the initial spectrum of photon energies and the source geometry (see e.g., Epstein 1985a). The fact that hard power law burst spectra have been observed to extend at least to several MeV without evidence of a turnover implies that γ - γ opacity is unimportant at these energies (Schmidt 1978). The resulting implications for burst sources will be discussed later.

In the presence of a magnetic field, gamma rays can be further attenuated by the single-photon pair production ($\gamma B \rightarrow e^+e^-$) and photon splitting ($\gamma B \rightarrow \gamma\gamma$) mechanisms that are different manifestations of pair production and Compton scattering. These processes are important only in strong fields ($B \geq 10^{12}$ G), where the field can be viewed as a cloud of virtual photons (Erber 1966). In this case, the single-photon interaction is much like the field-free γ - γ process, with a threshold energy of $E_\gamma \geq 2m_0c^2/\sin \theta$, where θ is the angle between the photon direction and the magnetic field. The probability of a single-photon interaction depends on the photon energy E_γ and the field strength transverse to the photon direction $B\sin\theta$. Near the threshold, pair production becomes important for $B \sim 2 \times 10^{12}$ G, while above the threshold, the γ - B optical depth increases exponentially with energy and transverse field strength (Daugherty & Harding 1983; Baring 1988). The sharp rise in the opacity means that virtually all photons above the threshold are attenuated. The lack of an observed cutoff out to several MeV in some GRB spectra has been used to place an upper limit on the magnetic field of $B \leq 10^{12}$ G (Matz *et al.* 1985, 1986). However, Baring (1990) showed that several observed “broken” power law burst spectra could be explained through γ - B pair production attenuation of a thermal synchrotron spectrum in the presence of a 10^{12} G field. The photon splitting process is a lower order effect which is unimportant above the γ - B pair production threshold but could be significant at slightly lower energies. In this process, a single photon is converted into two photons of roughly equal energy in the presence of a strong magnetic field. Because it does not involve particle creation, photon splitting does not have a threshold and can occur at energies below $2m_0c^2$. The details of photon splitting are not well-known, but it is efficient mainly at energies of about half the pair production threshold and does not produce as sharp an attenuation (Baring 1992). Photon splitting could thus be used to explain spectral breaks below ~ 1 MeV.

The short time-scale intensity variations observed in bursts imply a small emission region where an enormous energy density is required for very distant burst sources (cosmological or Galactic halo). In this situation an alternative emission mechanism is possible. Cavallo & Rees (1978) were first to point out that the release of a large amount of energy in the form of gamma

rays (>1 MeV) into a compact region on short time-scales will produce a dense photon field (or “fireball”) that is optically thick due to $\gamma\gamma \rightarrow e^+e^-$ reactions. For a cosmological (Galactic halo) source, the initial temperature of this dense photon field is $kT_0 \sim 10$ (0.1) MeV (Piran & Shemi 1992). The resulting high density of pairs would also make the fireball optically thick to Compton scattering, inevitably producing a thermalized pair plasma with a temperature $kT \sim m_0c^2$. Except for a thin photosphere that would immediately dissipate its energy through radiation, the optically thick fireball cools by bulk relativistic expansion (Paczynski 1986; Goodman 1986). The expansion continues until the temperature decreases to a point where the plasma becomes optically thin to pair production and Compton scattering and the remaining energy can freely escape as radiation. The temperature in the plasma frame at this point is only ~ 20 keV, but the relativistic bulk motion of the expanding flow blueshifts the spectrum so that it is roughly the same temperature as it was before the expansion began (Paczynski 1986; Goodman 1986). The spectrum of the resultant photons can thus extend to high energies, but it is roughly thermal in shape. This presents a problem since some observed burst spectra at high energies are distinctly non-thermal. However, as pointed out by Goodman (1986), the overall spectrum could be significantly hardened if there is a distribution of initial temperatures kT_0 resulting in several fireballs (e.g., as might be expected given the chaotic temporal behavior of GRB intensities). A further problem with the fireball model is that if even a small amount baryonic matter is present at the onset, most of the gamma-ray energy will be dissipated into kinetic energy of the expanding baryon flow (Shemi & Piran 1990). A possible solution to both the thermal spectrum and baryon contamination problems is that the kinetic energy of the baryonic fireball could be converted back into gamma rays through interactions with an external cloud of matter (Rees & Mészáros 1992; Mészáros & Rees 1992b; Katz 1994a) or instabilities within the fireball outflow (Mészáros & Rees 1994a). The resulting shock waves and/or compressed magnetic fields could accelerate ionized matter and produce an additional non-thermal (power law) component in the final photon spectrum. This idea has been developed in more detail by Mészáros & Rees (1993a, 1993b) and Mészáros, Laguna & Rees (1993), where the synchrotron and inverse Compton processes have

been identified as potential emission mechanisms.

ii. Modeling of COMPTEL Spectra

The COMPTEL burst spectra are observed mainly at energies above 1 MeV, so they are not sufficient to support all the components (4 free parameters) of the generalized “GRB” model used to describe BATSE data at lower energies. The goal in spectral modeling is to adequately describe the data with the simplest model possible. The great flexibility of the GRB model (or the comparable broken power law) would certainly allow it to fit the COMPTEL data, but it would not reveal the fundamental characteristics of the sample. The simpler, more conventional models (power law, simple photon exponential and the approximate OTTB and TS forms) were therefore tested against the data. The two variable parameters in each model consist of a normalization factor (in units of photons $\text{cm}^{-2} \text{s}^{-1} \text{MeV}^{-1}$) and a spectral shape factor (α , kT , E_c or E_0).

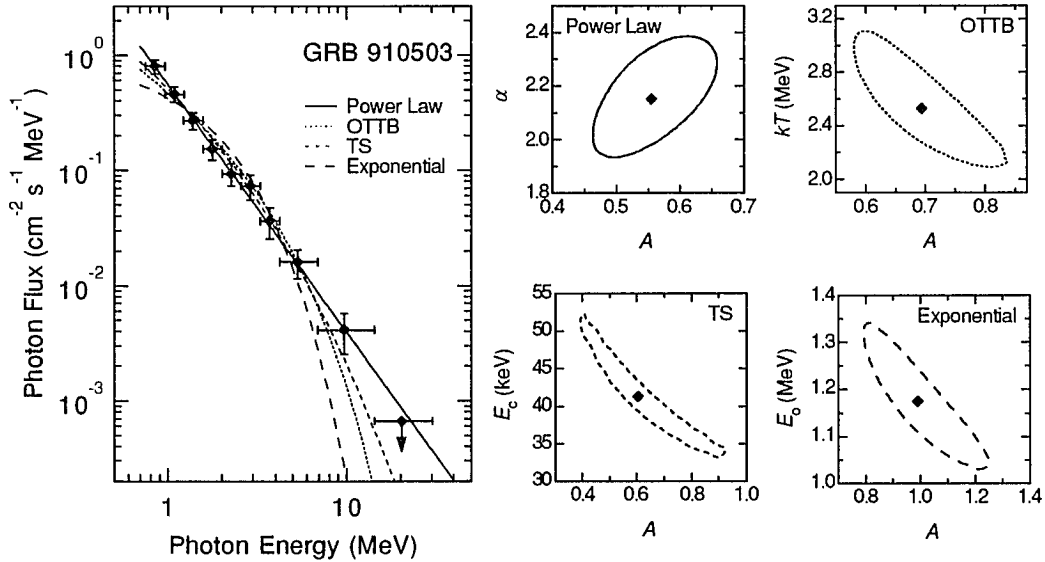


Fig. 5.1. Best-fit spectral models (0.75–30 MeV) and two-parameter confidence regions (1σ) for the time-averaged emission from GRB 910503.

Table 5.2 Time-Averaged Spectral Fit Parameters

Burst Name	Photon Power Law [*]				Thermal Bremsstrahlung [†]		Thermal Synchrotron [‡]		Photon Exponential [§]	
	A	α	Q_b	S	kT	Q_b	E_c	Q_b	E_o	Q_b
GRB 910425	0.26 ± 0.04	1.80 ± 0.18	0.6441	8.78	6.42 ± 2.43	0.0540	87.17 ± 33.35	0.0607	2.25 ± 0.45	<1.E-4
GRB 910503	0.56 ± 0.05	2.15 ± 0.11	0.9847	15.14	2.53 ± 0.34	0.0839	41.31 ± 07.18	0.5842	1.18 ± 0.10	<1.E-4
GRB 910601	1.12 ± 0.10	3.44 ± 0.19	0.1753	3.72	0.67 ± 0.07	0.8054	6.64 ± 01.23	0.5555	0.47 ± 0.04	0.6903
GRB 910627	0.16 ± 0.04	2.31 ± 0.26	0.4063	0.56	1.80 ± 0.53	0.5120	32.15 ± 13.60	0.5418	1.00 ± 0.18	0.5627
GRB 910709	4.35 ± 1.02	2.95 ± 0.48	0.7482	0.57	0.98 ± 0.32	0.5774	11.49 ± 05.50	0.6482	0.62 ± 0.14	0.3957
GRB 910814	0.81 ± 0.06	2.45 ± 0.13	0.0326	8.85	1.26 ± 0.18	0.0002	20.94 ± 04.31	0.0089	0.68 ± 0.06	0.0003
GRB 911118	0.51 ± 0.09	3.55 ± 0.58	0.3715	0.74	0.56 ± 0.32	0.0212	5.53 ± 03.52	0.1180	0.27 ± 0.07	0.0099
GRB 920622	1.03 ± 0.10	2.75 ± 0.18	0.2604	6.19	1.00 ± 0.16	0.0267	14.30 ± 03.37	0.1702	0.61 ± 0.06	0.0062
GRB 920830	0.33 ± 0.08	2.49 ± 0.35	0.5636	0.42	1.85 ± 0.66	0.3156	25.93 ± 08.54	0.4096	1.01 ± 0.26	0.0893
GRB 930118	0.20 ± 0.07	2.40 ± 0.53	0.2557	0.28	1.12 ± 1.03	0.0204	21.20 ± 18.52	0.0786	0.62 ± 0.25	0.0074
GRB 930131	9.57 ± 2.29	1.84 ± 0.26	0.4199	7.54	8.71 ± 5.38	0.1458	95.36 ± 49.23	0.1252	2.84 ± 0.65	0.0006
GRB 930309	0.09 ± 0.02	2.69 ± 0.35	0.2392	0.96	0.90 ± 0.22	0.1302	20.89 ± 08.61	0.1080	0.59 ± 0.11	0.1148
GRB 930612	0.11 ± 0.03	2.03 ± 0.26	0.7987	0.82	2.80 ± 0.96	0.9194	52.83 ± 24.90	0.8964	1.39 ± 0.30	0.8185
GRB 930704	0.08 ± 0.02	2.42 ± 0.38	0.8060	0.54	1.90 ± 0.68	0.1714	27.37 ± 16.17	0.3340	1.09 ± 0.26	0.0244
GRB 931229	3.68 ± 1.25	3.34 ± 0.74	0.7389	0.39	0.63 ± 0.26	0.8316	8.40 ± 05.03	0.7991	0.45 ± 0.14	0.8828
GRB 940217	0.38 ± 0.02	2.61 ± 0.07	0.5226	17.40	1.26 ± 0.10	<1.E-4	19.41 ± 02.13	0.1556	0.72 ± 0.04	<1.E-4
GRB 940301	0.30 ± 0.03	2.71 ± 0.11	0.8965	3.28	1.77 ± 0.19	0.0003	22.39 ± 03.43	0.1918	0.98 ± 0.09	<1.E-4
GRB 940314	0.11 ± 0.02	2.71 ± 0.25	0.4450	1.47	1.39 ± 0.43	0.0012	16.06 ± 01.76	<1.E-4	0.33 ± 0.07	0.0005
Average:	1.31 ± 0.55	2.59 ± 0.12		4.31	2.09 ± 0.49		29.40 ± 5.83		0.95 ± 0.15	

^{*}Power law: $N_E(E) = A$ (photons $\text{cm}^{-2} \text{s}^{-1} \text{MeV}^{-1}$) $(E/1 \text{ MeV})^{-\alpha}$; fluence $S(0.75\text{--}30 \text{ MeV})$ in units of $10^{-5} \text{ erg cm}^{-2}$.

[†]Thermal Bremsstrahlung (OTTB): $N_E(E) \propto (E/1 \text{ MeV})^{-1} \exp(-E/kT)$; kT in MeV

[‡]Thermal Synchrotron (TS): $N_E(E) \propto \exp(-(4.5 E/E_c)^{1/3})$; E_c in keV

[§]Exponential: $N_E(E) \propto \exp(-E/E_o)$; E_o in MeV

— Parameter uncertainties reflect the *mean* (\pm) statistical errors at the 1σ confidence level.

— Q_b is the probability of getting a better fit purely by chance fluctuations of the model.

Model testing was performed with the forward-folding method in count space using the C -statistic and bootstrap goodness-of-fit estimation procedure (see Chapter II). Models were fit over the full energy range from 0.75–30 MeV in all 15 energy intervals to determine the most-likely values of the variable parameters. Statistical confidence limits on the individual model parameters were determined by searching the full parameter space for changes in the Cash statistic according to the desired confidence level (systematic errors are discussed in Appendix

B). For single parameters, the change ($C-C_{\min}$) required for a 1σ confidence limit is 1.0, whereas $C-C_{\min} = 2.3$ when the confidence region of two parameters simultaneously is desired (as shown in Figure 5.1). As in the case of the source localization constraints discussed in Chapter IV, the confidence limits for individual spectral parameters are generally not symmetric about the best-fit values. For comparative purposes, we use the mean of the uncertainties in either direction (\pm) about the best-fit. As an example, Figure 5.1 shows the four best-fit spectral models and parameter confidence regions for GRB 910503. Spectral shape fit-parameters and uncertainties for all of the bursts are given in Table 5.2 along with the bootstrap goodness-of-fit estimator (Q_b) for each model ($Q_b \ll 0.5$ indicates a poor fit to the data). For the power law model, the normalization parameter A (photons $\text{cm}^{-2} \text{s}^{-1} \text{MeV}^{-1}$) and integrated fluence $S(0.75\text{--}30 \text{ MeV})$ are also given in Table 5.2.

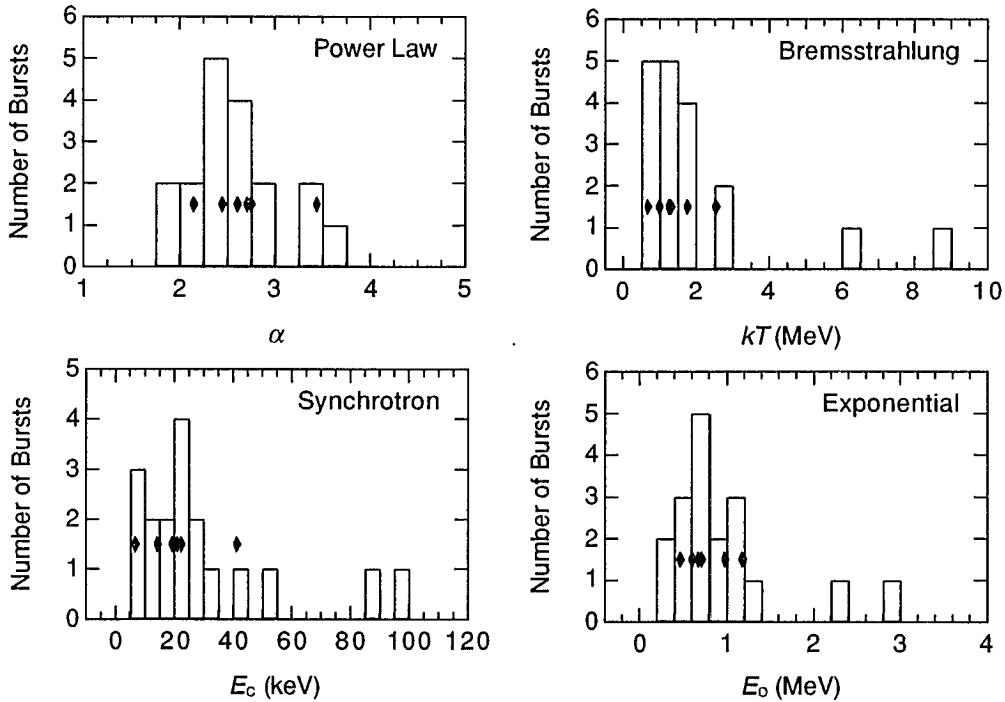


Fig. 5.2. Histograms of best-fit spectral shape parameters for each of the spectral models tested. Diamonds represent values from the six bursts with the highest detection significance.

Histograms of the best-fit spectral shape parameters for all the bursts are shown in Figure 5.2. For comparison, parameters for the six bursts with the highest detection significance (and therefore the smallest parameter uncertainties) are highlighted. The extremely high values of kT , E_c and E_o for a few of the bursts (e.g., GRB 930131) indicate that the OTTB, TS and exponential models are probably inadequate to explain the hardness of these spectra. In order to fit the data, these models must have extremely high characteristic energies such that their inherent curvature is small. This forces the spectral shape parameters of these bursts to fall well outside the range of the majority. In contrast, the fairly well-contained distribution of power law indices suggests that the entire group of spectra can be well-described by the power law model. There is, however, a clear distribution of spectral indices ($\alpha \sim 3.5-1.8$) that has a mean value of $\alpha = 2.6 \pm 0.1$.

Several of the individual model fits listed in Table 5.2 can be rejected with a high degree of confidence on the basis of a small value of Q_b . For instance, the observed spectrum of GRB 910503 (see Figure 5.1) is clearly inconsistent with the exponential model—it can be rejected with >99.99% confidence (i.e., $1-Q_b$). However, most of the weaker bursts are well fit by all the models due to their low statistics. It is of interest to examine the acceptability of the different models for the *entire* sample of bursts. The *distribution* of goodness-of-fit estimators for all the bursts provides a measure of the acceptability. If a model is consistent with all the COMPTEL burst spectra, the distribution of Q_b should reflect only statistical fluctuations. Such distributions for each of the four simple spectral models are shown as histograms in Figure 5.3. For convenience, the values of Q_b have been converted into the corresponding number of standard deviations n_σ expected for a Gaussian distribution of random fluctuations, with

$$Q_b = \frac{2}{\sqrt{\pi}} \int_{n_\sigma}^{\infty} \exp(-x^2/2) . \quad (5.6)$$

For a particular model/burst fit, n_σ represents the confidence (in units of Gaussian standard deviations) with which the model can be rejected on statistical grounds. If all the bursts were drawn from the same model, the differential distribution of n_σ should follow a Gaussian with zero mean and unit variance. Significant deviations from this expected shape for a given model

indicate that the model cannot adequately describe all the bursts. In Figure 5.3, the expected distributions are plotted normalized so that the integral is equal to the total number of bursts (18).

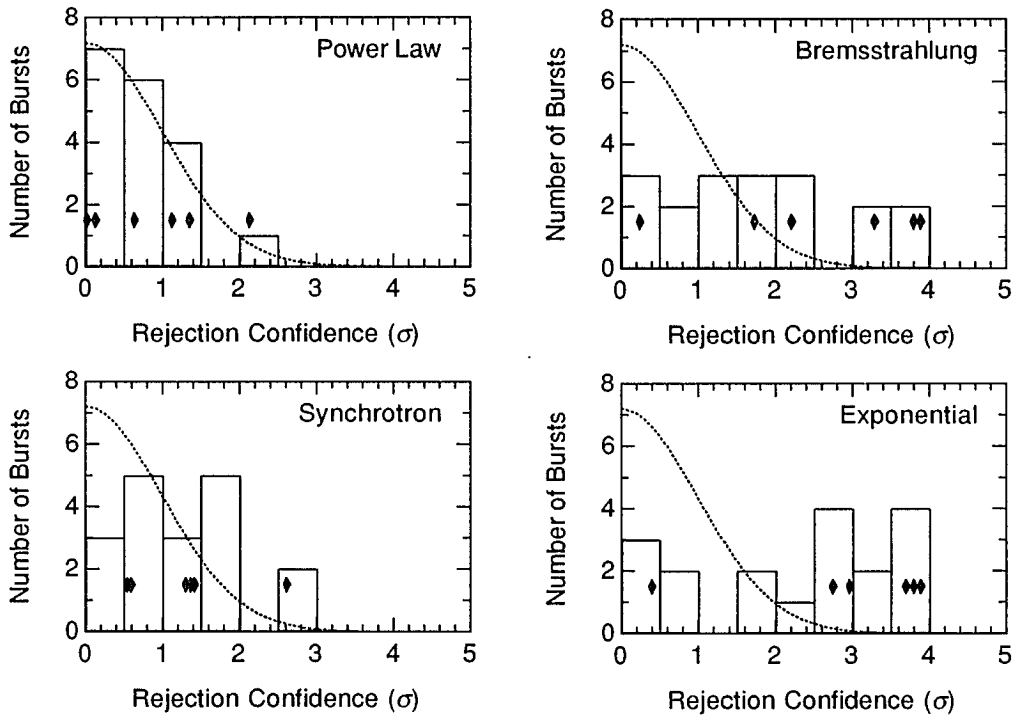


Fig. 5.3. Histograms of “goodness-of-fit” estimates for each spectral model and the shape expected from random statistical fluctuations (dotted-line). Diamonds represent the values from the six bursts with the highest detection significance.

The histograms in Figure 5.3 indicate that the power law is the only model which yields a distribution of spectral fits that is consistent with random fluctuations only. The poor fits of the OTTB and exponential models are clearly inconsistent with a distribution of random deviations. Further evidence of this inconsistency is seen when looking at the bursts with the best statistics, which are almost always poorly fit by these models. In contrast, the PL model sufficiently describes nearly all the high-statistics bursts in addition to those with low-statistics (which can be fit with any model). To quantify the “rejectability” of the OTTB, TS and exponential models, Monte Carlo simulations of the statistical fluctuations expected in a random sample of 18 bursts were performed. The C -statistic (equation 2.12) was evaluated between the simulations and the

expected Gaussian—producing the distribution of C -statistics that arises purely from random variations. This distribution was then compared to the individual C -statistic values obtained between the Gaussian and each of the four spectral model histograms in Figure 5.3. The fraction of simulations with C -statistics lower than that of the spectral model indicates the confidence with which the model can be rejected. The result is that only the power law model is consistent with purely statistical fluctuations (9.4% confidence of rejection). The OTTB and exponential models can be rejected with greater than 99.9999% confidence. The TB model, although somewhat more acceptable, can be rejected with 98.9% confidence.

It is not surprising that the OTTB, TS and exponential models cannot adequately explain the data, for they are all too soft, in general, to produce the observed high-energy emission. Although the power law model is the most acceptable, it is not necessarily the true burst spectrum. The power law model does, however, adequately describe the spectra of most bursts in this energy range. More complicated models can also provide acceptable fits, but Occam's razor instructs us to accept the simplest possible description of the data. Inverse Compton (IC) and broken power law (BPL) model fit parameters for the six bursts with the *best* statistics (highest detection significance) are given in Table 5.3.

Table 5.3 Advanced Model Spectral Fit Parameters

Burst Name	Inverse Compton*			Broken Power Law†			
	α	E_e	Q_b	α_1	α_2	E_b	Q_b
GRB 910503	1.89 ± 0.13	11.00 ± 5.40	0.9680	2.04 ± 0.20	2.86 ± 0.55	4.73 ± 1.61	0.9764
GRB 910601	0.53 ± 0.40	0.55 ± 0.24	0.7703	2.70 ± 0.32	7.48 ± 2.17	2.14 ± 0.31	0.9315
GRB 910814	1.12 ± 0.25	1.34 ± 0.14	0.0004	0.49 ± 0.30	2.81 ± 0.25	1.11 ± 0.08	0.1908
GRB 920622	2.12 ± 0.69	3.15 ± 1.87	0.1530	0.01 ± 1.01	3.12 ± 0.24	1.08 ± 0.10	0.8138
GRB 940217	2.30 ± 0.10	8.26 ± 7.40	0.5520	1.98 ± 0.40	2.87 ± 0.10	1.41 ± 0.26	0.9952
GRB 940301	2.40 ± 0.13	10.28 ± 8.75	0.8962	2.59 ± 0.10	5.27 ± 2.10	7.72 ± 1.16	0.9338

*Inverse Compton (IC): $N_E(E) \propto (E/1 \text{ MeV})^{-\alpha} \exp(-E/E_e)$; E_e in MeV

†Broken Power Law (BPL): $N_E(E) \propto (E/1 \text{ MeV})^{-\alpha_1}$, $E \leq E_b$
 $\propto (E/1 \text{ MeV})^{-\alpha_2}$, $E > E_b$; E_b in MeV

Although, as expected, these advanced models yield good fits to most of the burst spectra (as good or better than the single power law model), the fitted parameters indicate that they are simply mimicking the power law shape over much of the energy range. For example, the characteristic energy E_c of the IC model and the break energy E_b of the BPL model are forced to be very high in order to fit the observed spectra of GRB 910503 and GRB 940301. This indicates that both models are explaining most of the energy range with a simple power law and then turning over at higher energies (≥ 10 MeV) where there are poorer statistics. In other cases, the added flexibility of the BPL model appears to turn over at low energies by fitting only one data point below 1 MeV (e.g., GRB 920622, GRB 910814). This behavior *could* be indicative of a real breaks or turnovers in the spectra *or* the models could be “over-fitting” the statistical fluctuations of a few datapoints. It is interesting to note that the spectrum of GRB 910814 rejects ($>2\sigma$ confidence) all models *except* the broken power law. This is an indication that perhaps there is a real turnover in the spectrum of this burst below ~ 1 MeV. However, the significance of this feature is only marginal. If turnovers or “breaks” do exist in these spectra, they are most likely outside (or just at the edge) of the COMPTEL energy range. The COMPTEL data alone are insufficient to significantly detect such features. Low- and high-energy data help to resolve this question.

C. Wide-Band Gamma-Ray Burst Spectra

The COMPTEL burst measurements provide spectral information in a fairly small energy window. It is thus important to investigate how burst emission in this limited energy range relates to that at lower and higher energies. Wide-band measurements yield a more complete picture of the spectral properties of bursts that can only be suggested by the COMPTEL data alone. For instance, at low energies, the COMPTEL spectra of some bursts appear to indicate a turnover near 1 MeV, while at high energies, there is the possibility of another turnover above ~ 10 MeV. The existence of such features is investigated in several of the COMPTEL bursts that have been observed *simultaneously* over a wide range of energies by the other *Compton* instruments. In

particular, all of the bursts examined in this work were also observed at lower energies by the COMPTEL burst mode (or burst system analyzer; BSA) and by the BATSE large area (LAD) and spectroscopy (SD) detectors (Fishman *et al.* 1989) and most were observed at higher energies (1–200 MeV) by the EGRET total absorption shower counter (TASC; Schneid *et al.* 1992a). In addition, a few of the bursts were observed at very high energies (30 MeV to 20 GeV) by the EGRET spark chamber (SC; Thompson *et al.* 1983).

There are several difficulties in comparing the burst spectra obtained by different instruments. Foremost among these is the problem of matching the time-intervals over which spectra are accumulated. This is an important consideration because both the intensity and shape of burst spectra are variable. It is a problem since the accumulation intervals of some instruments (e.g., BATSE, COMPTEL–BSA and EGRET–TASC) are fixed. In principle, COMPTEL telescope spectra can be accumulated over arbitrary intervals, but in practice instrument deadtime limits the ability to sample *within* impulsive phases. Thus, multi-instrument spectral comparisons must be made using intervals which contain *at least* the full extent of impulsive emission. Fitted BATSE spectra during suitable accumulation intervals are available for several of the bursts (Table 5.4). In most cases, the BATSE intervals include slightly more accumulation than the intervals used in Table 5.1. Only for GRB 910503 was the accumulation much different in that it included only one of the two well-separated pulses (see lightcurve in Appendix A). The COMPTEL spectra of these bursts have been re-computed to match the BATSE accumulation intervals and the resulting power law fit parameters are listed in Table 5.4.

The range of fitted models allowed by the BATSE measurements (statistical uncertainties *only*) have been overlaid with the COMPTEL spectra in Figures 5.4a–d. In these figures, the photon number fluxes $N_E(E)$ have been multiplied by E^2 to provide a clearer picture of the changes in spectral shape. The quantity $E^2 N_E$ (erg cm⁻² s⁻¹) is the energy flux emitted per logarithmic energy band and is proportional to the energy flux per decade of frequency νF_ν . Thus, an E^{-2} photon power law is characterized by a constant indicating that an equal amount of energy (or power) is radiated in all energy intervals. Note that in the $E^2 N_E$ representation, the

COMPTEL data points are strongly dependent on the assumed spectrum and should not be taken literally (unlike the photon flux spectra $N_E(E)$ shown in Appendix A that are only *weakly* dependent on the assumed spectral shape). Here, they serve only to indicate changes in the broad-band spectral shape between the different instruments.

Table 5.4 Multi-Instrument Spectral Comparisons

Burst Name	BATSE/ COMPTEL	BATSE Spectral Model	COMPTEL Power Law Fit Parameters		EGRET Interval*	
	Interval*		A	α	TASC	SC
GRB 910503	9.47	GRB ⁽¹⁾	2.44 ± 0.30	2.19 ± 0.16	$7.0^{(7)}$	$84.0^{(2,4)}$
GRB 910814	33.47	BPL ⁽⁶⁾	0.80 ± 0.64	2.45 ± 0.13	$22.9^{(5)}$	—
GRB 911118	16.58	GRB ⁽¹⁾	0.27 ± 0.05	3.60 ± 0.84	—	—
GRB 920622 [†]	25.90	GRB ⁽³⁾	0.97 ± 0.10	2.77 ± 0.18	$32.0^{(3)}$	—
GRB 940217	180.00	IC ⁽⁴⁾	0.35 ± 0.02	2.58 ± 0.07	$180.0^{(4)}$	$180.0^{(4)}$

Notes from Tables 5.1–5.3 apply.

*Spectral accumulation time in seconds since BATSE trigger.

[†]BATSE LAD used rather than SD.

References (indicated by superscripts in parentheses):

⁽¹⁾Band *et al.* (1993a)

⁽²⁾Dingus *et al.* (1994)

⁽³⁾Greiner *et al.* (1995)

⁽⁴⁾Hurley *et al.* (1994e)

⁽⁵⁾Kwok *et al.* (1993)

⁽⁶⁾Schaefer *et al.* (1994b)

⁽⁷⁾Schneid *et al.* (1992b)

Different models were used to fit the BATSE data from the different bursts (see Table 5.4), but they are all roughly comparable (at least at low energies) and each is sufficient to indicate changes in the spectra. For instance, the BPL, IC and GRB models are each capable of indicating a break or turnover in the spectrum. EGRET measurements have also been included in the figures. However, note that only for GRB 940217 were the EGRET spectra (TASC and SC) accumulated over the same intervals as the COMPTEL and BATSE data. In this case, the allowed range of EGRET power laws are included in Figure 5.4d. For the remaining bursts, the available best-fit EGRET power laws (accumulation times given in Table 5.4) have been included in the plots, but the normalization factors are those of the COMPTEL spectra. This suffices to give a rough indication of any significant changes in spectral *shape* at high energies above the COMPTEL range.

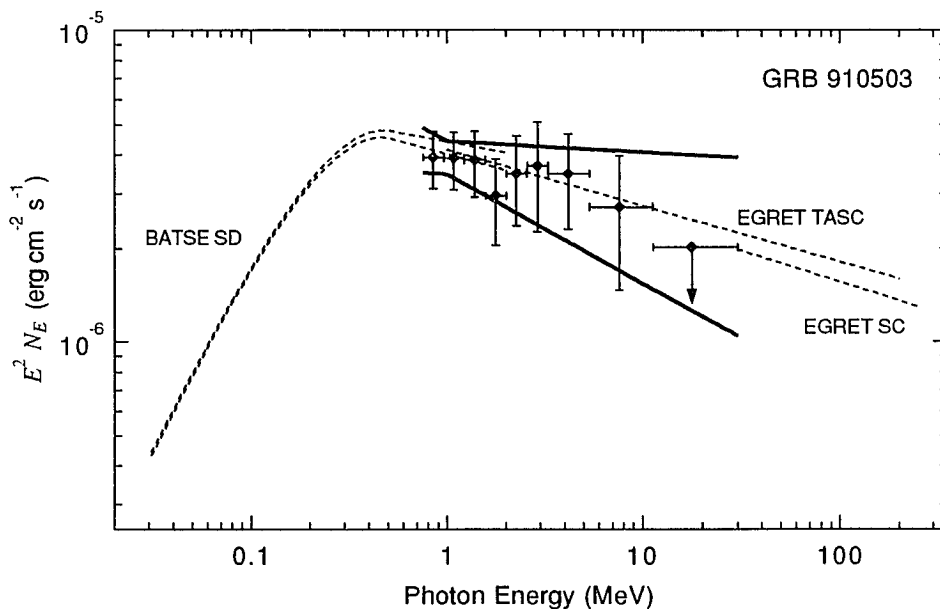


Fig. 5.4. (a) Multi-instrument energy spectrum of GRB 910503. The COMPTEL energy fluxes (diamonds) are plotted with 1σ error bars along with the acceptable range ($\pm 1\sigma$ statistical uncertainties) of fitted power laws (heavy solid lines). The acceptable range of BATSE spectral models and best-fit EGRET power laws are plotted with dashed lines as indicated. See text and Table 5.4 for details.

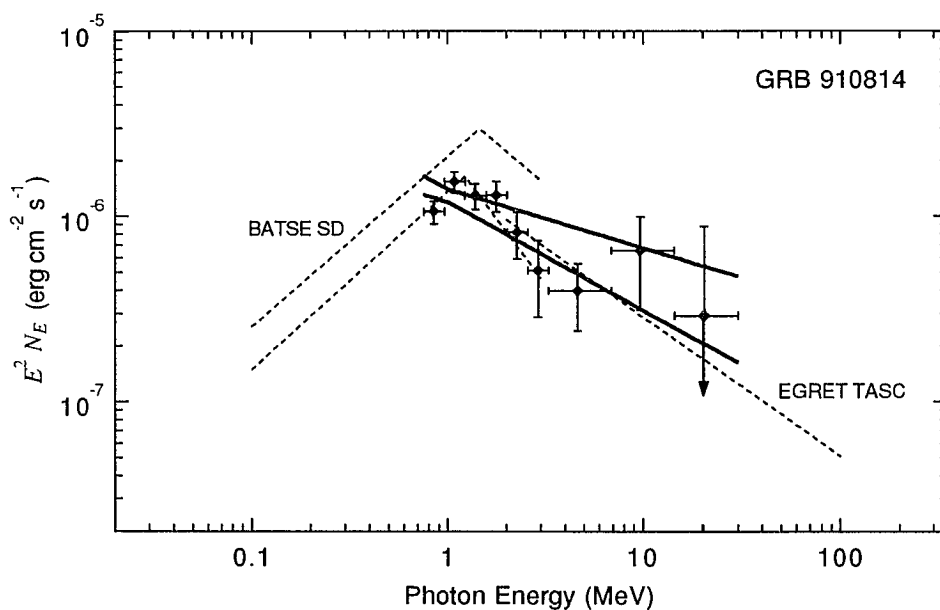


Fig. 5.4. Continued (b) Multi-Instrument energy spectrum of GRB 910814.

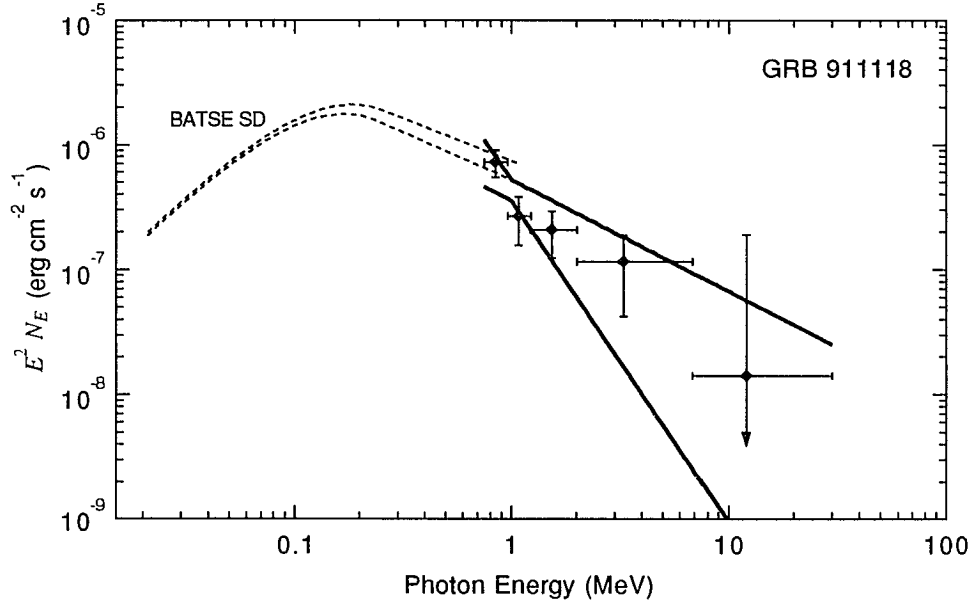


Fig. 5.4. Continued (c) Multi-Instrument energy spectrum of GRB 911118.

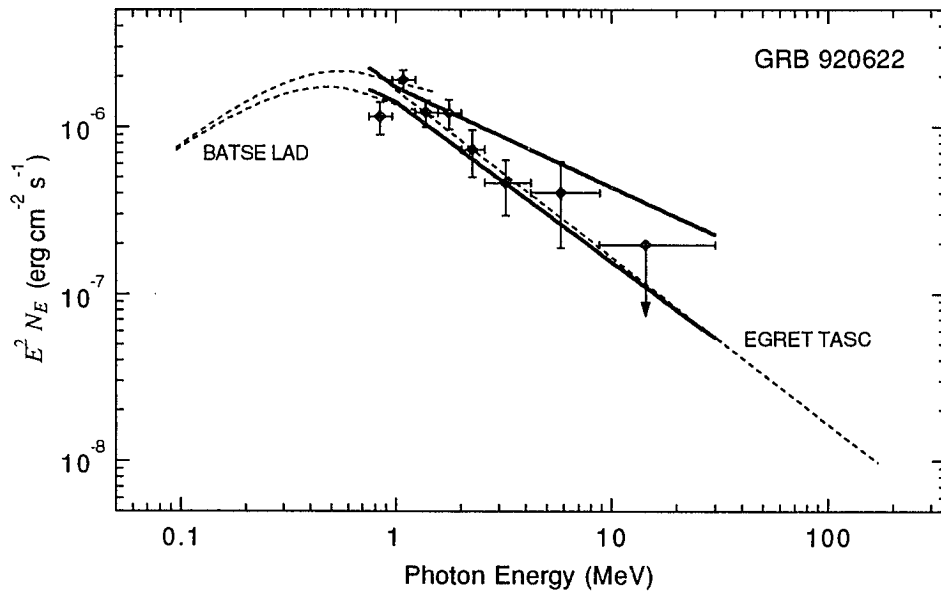


Fig. 5.4. Continued (d) Multi-Instrument energy spectrum of GRB 920622.

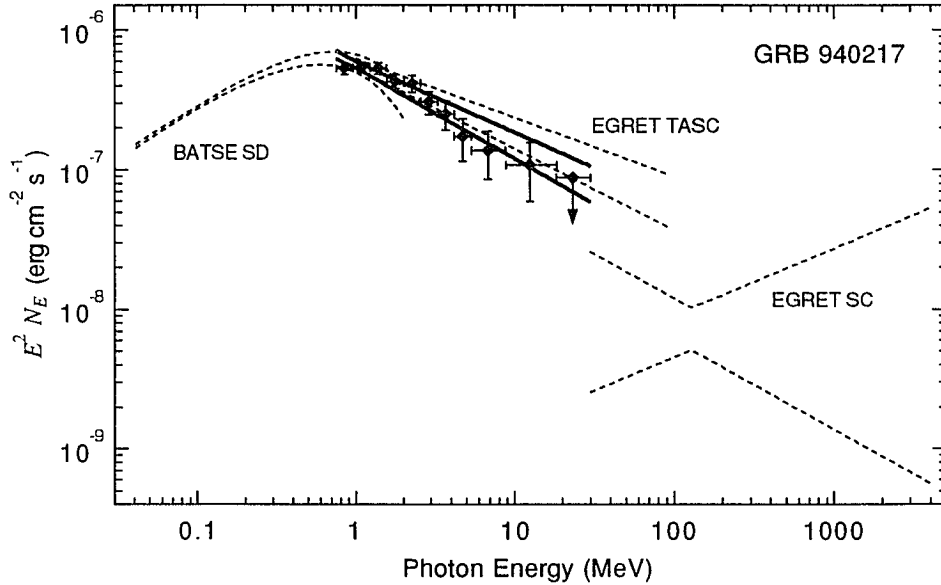


Fig. 5.4. *Continued (e)* Multi-Instrument energy spectrum of GRB 940217. Note that for this burst the EGRET spectra were accumulated over the same interval as were the BATSE and COMPTEL spectra.

In all cases the normalization of the COMPTEL and BATSE spectra are in reasonable agreement in the overlap region around ~ 1 MeV. Where BATSE-SD spectra are used, there is also reasonable agreement in the high-energy spectral slopes. The fits to BATSE-LAD spectra (GRB 920622 and GRB 940217), however, do not compare as favorably to the hardness of the COMPTEL spectra. This is to be expected since the BATSE-LAD statistics above ~ 1 MeV are limited. Nonetheless, the BATSE measurements are a reasonable approximation in that they appear to correctly describe the general change in hardness from low to high energies. The COMPTEL BSA spectra are not shown in the plots, but they are consistent with both the BATSE and COMPTEL (telescope) measurements (see e.g., Hanlon et al. 1994; Kippen *et al.* 1995b; Winkler *et al.* 1995). The EGRET-TASC and SC spectral slopes are in good agreement with the COMPTEL measurements. It is more difficult to assess the agreement in normalization because the accumulation intervals differ considerably. Detailed comparisons using all the available EGRET-TASC data over wider intervals indicate good agreement with the other *Compton* instruments (Schaefer *et al.* 1994a; Share *et al.* 1994). Furthermore, in the case of GRB 940217

(identical accumulation intervals) the COMPTEL, BATSE and EGRET–TASC normalizations all agree within the uncertainties. There is, however, a clear discrepancy in the normalization of the EGRET–SC spectrum of this burst. Since GRB 940217 contained very intense pulses of emission, the EGRET–SC flux in this case is probably significantly underestimated due to instrument deadtime (~110 ms deadtime per gamma-ray detection; Sommer *et al.* 1994a).

i. Spectral Breaks

We have seen that the shape of COMPTEL burst spectra can be well-described by a single power law model, but this model is obviously too simple to explain the wide-band spectra observed by multiple instruments. The most striking feature in these spectra is a significant change (or “break”) in the spectral slope from the hard X-ray to gamma-ray energy regimes resulting in a peak in the $E^2 N_E$ distribution. This indicates that for each burst there is a limited range of energy where the most power is radiated. However, as can be seen in the figures, this peak energy—as well as the hardness below and above the peak—is different for each burst. For example, the peak occurs below 200 keV for GRB 911118 and above 1 MeV for GRB 910814. It is thus not surprising that GRB 910814 showed the strongest evidence for a turnover in the COMPTEL data, because its peak energy falls within the COMPTEL range.

As discussed earlier, BATSE measurements alone have indicated that most bursts are well-described only by models which allow for a transition in the spectrum such as the “GRB” model or the broken power law. However, there is no universal set of parameters that can describe all bursts. In a sample of 54 time-averaged BATSE burst spectra, Band *et al.* (1993a) found a continuous distribution of turnover energies for different bursts that extends from below 100 keV to more than 1 MeV and has a maximum below 200 keV. They point out that bursts such as GRB 910814 that have a high-energy turnover above 1 MeV represent the exception. One problem noted in the BATSE study was the inability to determine conclusively the high energy power law part of the spectrum due to poor statistics.

The general agreement in normalization and spectral slope between the COMPTEL and

BATSE spectra shown here indicates that the high-energy power law tails determined by BATSE (SD) alone are roughly correct and that they continue out to at least ~ 10 MeV. This picture is consistent with *GRANAT*–*SIGMA* burst measurements that indicate a broken power law is a good description of the spectra from ~ 200 keV to several MeV (Pelaez *et al.* 1994). *SIGMA* observed spectral breaks in both GRB 910814 and GRB 920622 that are consistent with the wide-band spectra shown here (although the accumulation intervals were somewhat different). At higher energies, agreement between the *COMPTEL* and *EGRET* spectra indicate that the power law shape continues *without further change* out to ~ 200 MeV. The *EGRET*–*SC* detection of very high energy photons in GRB 940217 suggests that the hard power law continuum may extend to GeV energies—at least in this particular burst.

ii. Extended High-Energy Emission

Before gamma-ray bursts were observed by the *EGRET* instrument, the highest measured energies were around 100 MeV during only one burst (Share *et al.* 1986). It was thus uncertain whether very high energy photons are a common feature of burst emission. *EGRET* has now measured emission above 100 MeV in several bursts—four of which were discussed earlier (see Table 5.4). The most interesting cases have been those bursts during which GeV photons were detected in the *EGRET* spark chamber. Over the three-year period covered by this work, *EGRET* has detected spark chamber events in five bursts—three of which had photons with energies above 1 GeV (Hurley *et al.* 1994e and references therein). Even though only few GeV photons were observed in each of these three events, the measurements are significant because the *EGRET* background at these energies is extremely low. *EGRET*'s ability to localize individual photons lends further credibility to the measurements.

The most puzzling aspect of the *EGRET* observations is the apparent tendency of the high energy emission to continue well after the main pulses of emission measured at lower energies have subsided. For instance, a single photon with energy 9.6 ± 1.2 GeV was detected (probability of chance detection $\sim 10^{-6}$) from the direction of GRB 910503 more than 80 s after the start of the

burst, whereas the intense low-energy emission subsided 10–15 s earlier (Dingus *et al.* 1994). More striking examples were observed in GRB 930131 (Sommer *et al.* 1994a) and GRB 940217 (Hurley *et al.* 1994e), where several GeV photons were detected at times when little or no significant emission was measured at lower energies. For these bursts, enough photons were detected in the SC to construct a spectrum of the extended, high-energy emission. The important question about the EGRET results is how the GeV emission relates to that at lower energies. Hurley *et al.* (1994e) suggested that the GeV photons are actually delayed with respect to the low-energy emission—implying a fundamental change in the spectrum at the later stages of burst evolution. Delayed high-energy emission contradicts the findings at lower energies which indicate that the spectra of most bursts soften with time (e.g., Norris *et al.* 1986; Ford *et al.* 1995). However, it has not been demonstrated that the observed GeV emission is really delayed. It could be that the EGRET–SC, with its extremely low background, is detecting a low-intensity, extended emission tail that cannot be measured at lower energies due to insufficient sensitivity. In this case, the spectrum of the weak emission tail may be essentially unchanged from that of the impulsive part of the burst—only its intensity is reduced to a point where it is undetectable at low energies where there is high background. To check for spectral change, the COMPTEL data have been examined in the extended intervals of GRB 930131 and GRB 940217 where EGRET detected GeV photons.

Significant emission from the intense burst GRB 930131 was observed by COMPTEL to follow a hard $\sim E^{-1.8 \pm 0.3}$ power law spectrum that lasted for only ~ 1 s. However, BATSE observed an additional extended emission tail that lasted for about 50 s and was over an order-of-magnitude lower in intensity than the first impulsive second of the burst (Kouveliotou *et al.* 1994b). During the intense interval, EGRET detected six photons with energies from 30–500 MeV following an $\sim E^{-2.0}$ power law spectrum. In the subsequent period from 1–25 s, ten more photons were observed with a power law shape fitted by $(5.9 \pm 0.2) \times 10^{-6} (E/129 \text{ MeV})^{-2.1 \pm 0.5}$ photons $\text{cm}^{-2} \text{ s}^{-1} \text{ MeV}^{-1}$. Two of these photons had energies of about 1 GeV (Sommer *et al.* 1994a). COMPTEL upper limits on the MeV emission from this extended part of the burst were

computed by directly inverting the background-subtracted count rate with the vector response method described earlier. This was done in three logarithmic energy bands covering the full COMPTEL range. The results are compared to the allowable range of fitted EGRET spectra acquired over the same interval in Figure 5.5. The upper limits in each of the three COMPTEL energy bands are consistent with the fluxes predicted by the extrapolation of the EGRET spectrum within its uncertainties. The largest deviation is for the third energy band (8.77–30 MeV), where the lower bound (-1σ) of the extrapolated EGRET spectrum is at the 1.2σ COMPTEL sensitivity limit. The COMPTEL data from this time-interval were also searched for MeV emission by computing a maximum-likelihood image of the source region. No significant excesses were observed and the upper limits are compatible with those obtained from the direct inversion method. There is thus no evidence that the spectrum of extended emission from this burst below 30 MeV is different from that observed above ~ 100 MeV.

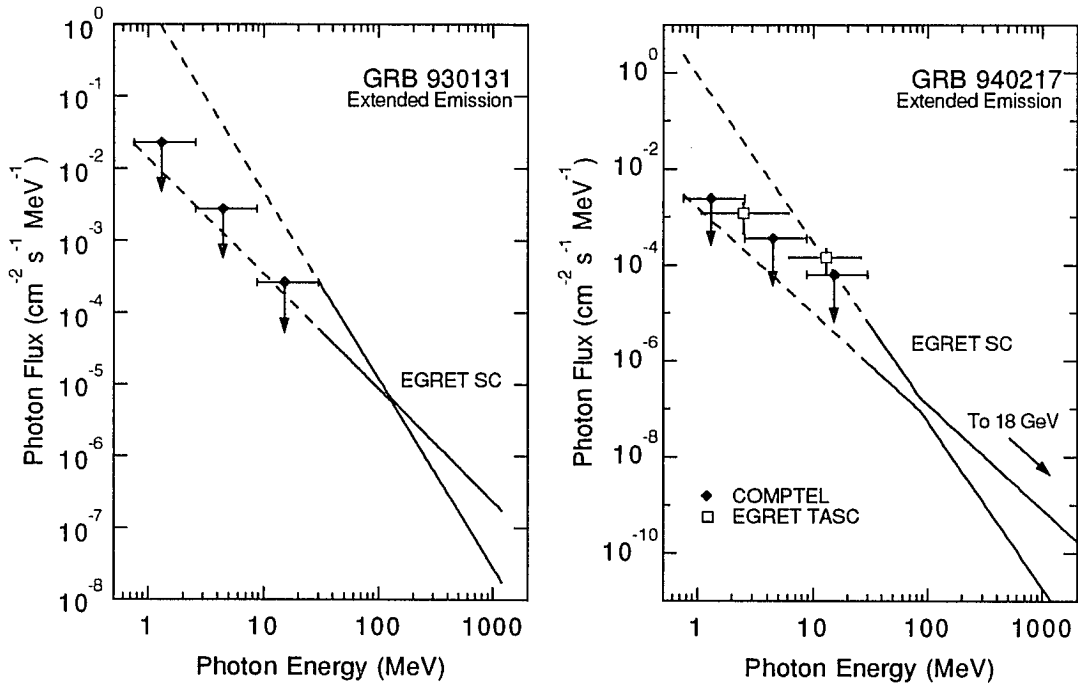


Fig. 5.5. Extended emission spectra of GRB 930131 and GRB 940217 comparing COMPTEL 2σ upper limits to the allowed range (1σ uncertainties) of fitted EGRET-SC power laws and TASC data points. EGRET data from: GRB 930131—Sommer *et al.* (1994a) and GRB 940217—Hurley *et al.* (1994e).

The EGRET measurements of GRB 940217 are even more surprising. As observed by COMPTEL and BATSE, the intense part of this burst lasted for ~ 180 s, yet EGRET continued to measure photons in the SC for another 90 minutes—including one with an energy of 18 ± 4 GeV (Hurley *et al.* 1994e). These measurements represent both the highest energy and longest duration burst yet observed. In the 87 minutes following the intense episode, EGRET measured 18 photons fit by a power law spectrum with $(1.3 \pm 0.4) \times 10^{-7} (E/86 \text{ MeV})^{-2.83 \pm 0.64}$ photons $\text{cm}^{-2} \text{s}^{-1} \text{MeV}^{-1}$. The spectral index of the extended emission is consistent with that measured by EGRET and COMPTEL during the intense portion of the burst (cf. Figure 5.4e), but the intensity is reduced by over an order-of-magnitude. The COMPTEL upper limits on the flux during the extended emission interval are consistent with the EGRET-SC power law extrapolation within its uncertainties (Figure 5.5). COMPTEL imaging analysis yields comparable results. There is thus no conclusive evidence that the spectrum measured by EGRET does not continue into the MeV range. On the contrary, in this same time-interval, the EGRET-TASC detected a weak flux below 30 MeV that is consistent with the extrapolation of the SC power law (see Figure 5.5). From the flux observed by the EGRET-TASC, we would have expected to measure 190 ± 119 and 65 ± 33 counts with COMPTEL in the energy ranges 1.1–6.1 MeV and 6.1–26.2 MeV, respectively. Although no significant emission above background (1740 and 163 counts, respectively) was detected, we can conclude that the COMPTEL upper limits are not inconsistent with the TASC detections given the large statistical uncertainties.

D. Pair Production and Relativistic Motion

Photon-photon pair production severely attenuates gamma rays with energies above $\sim m_0 c^2$ if there is a sufficiently high density of photons. The short time-scale intensity variations ($\delta t \sim 1$ ms) observed in most bursts imply a small emission region with characteristic size $\ell \sim c \delta t \approx 10^6$ – 10^7 cm. The surface photon density n_γ (photons cm^{-3}) at distant burst sources must therefore be stupendous in order to explain the photon flux f_γ (photons $\text{cm}^{-2} \text{s}^{-1}$) observed at the earth since

$$f_\gamma = n_\gamma c \frac{\ell^2}{d^2}, \quad (5.7)$$

where d is the source distance (assuming isotropic emission). Even for a fairly “nearby” source in the Galactic halo at a distance $d \sim 100$ kpc, the typical density of photons at the emission site is $n_\gamma \sim 10^{23} \text{ cm}^{-3}$, making the pair production opacity significant.

Schmidt (1978) was first to point out that the lack of an observed cutoff in GRB spectra above $m_0 c^2$ implies that the pair production opacity $\tau_{\gamma\gamma}$ must be less than one at the source to allow the photons to escape. This, in turn, places an upper limit on the source distance *if* we assume that the radiation is emitted isotropically. Following Schmidt (1978), the optical depth of a test photon with energy E propagating through a radiation field with photon number density spectrum $n(\varepsilon)$ is

$$\tau_{\gamma\gamma}(E) = \ell \int_{\varepsilon_t}^{\infty} n(\varepsilon) \sigma_{\gamma\gamma}(E, \varepsilon) d\varepsilon, \quad (5.8)$$

where ε_t and $\sigma_{\gamma\gamma}$ are the pair production threshold energy (eq. 5.5) and cross section (eq. 5.6), respectively. Combining this result with equation (5.7) and assuming an optical depth of order unity for photons with energy below E , the source distance is constrained by

$$d(E) \leq \left(\frac{1}{\ell c} \int_{\varepsilon_t}^{\infty} N_E(\varepsilon) \sigma_{\gamma\gamma}(E, \varepsilon) d\varepsilon \right)^{-1/2}, \quad (5.9)$$

where N_E (photons $\text{cm}^{-2} \text{ s}^{-1} \text{ MeV}^{-1}$) is the observed differential photon spectrum above the threshold energy ε_t . If the distance were greater, the γ - γ optical depth would exceed unity and the flux of photons at energies above E would be attenuated. Note that this distance constraint depends on the intensity *and* shape of the observed photon spectrum and also that there is a hidden dependence on the source geometry as well as the overall source size ℓ (i.e., the γ - γ threshold depends on the angle θ between photon directions).

Schmidt (1978) used the absence of a cutoff in the power law spectra of bursts up to $E = 1$ MeV (the highest observed energies at that time) to argue that typical isotropically emitting burst sources must be within a few kpc. He assumed for simplicity that $\theta = 90^\circ$ as might be expected on average from a truly isotropic emitter, but pointed out that the result would be changed only

slightly if all the photons were to originate from a surface around the source, where the average θ would be smaller. Epstein (1985a) applied these same arguments to limit the source distance to a few hundred pc assuming specific neutron star geometries (and size) and maximum observed energies ~ 10 MeV. Both of these studies assumed that burst spectra above $\sim m_0 c^2$ are a simple power law.

Earlier it was shown that bursts *do* exhibit spectral turnovers, which in some cases could be viewed as evidence of pair production attenuation (e.g., Schaefer *et al.* 1992; 1994b). If the observed spectral breaks are the result of pair production, the distance constraint of equation (5.9) would be valid only up to the energy of the start of the observed turnovers. However, the observed turnover energies (peak in $E^2 N_E$) are not always above the pair production threshold (see Figure 5.4). In fact, the full BATSE sample studied by Band *et al.* (1993a, 1993b) showed a continuous distribution of spectral turnover energies, most of which are in the range 100–300 keV. Neglecting cosmological effects, it is impossible for these low-energy turnovers to be a result of pair production attenuation. If bursts are at cosmological distances, the low-energy turnovers could be redshifted γ - γ cutoffs, but a wide range of redshifts would be required to explain all the different observed turnover energies (Band *et al.* 1993a). It is thus reasonable to assume that the observed spectral turnovers are not caused by pair production opacity, in which case the distance constraint of equation (5.9) is still valid.

One way to avoid the high γ - γ opacity altogether is to beam the radiation anisotropically so that the average angle between photon directions is small ($\theta < 1^\circ$). This raises the pair production threshold energy by a factor $(1 - \cos \theta)^{-1}$ and the optical depth at a particular energy E drops considerably, depending on the shape of the initial photon spectrum. Anisotropic beaming could result from the collimation geometry of the source (e.g., Zdziarski 1984), but it is most easily explained as a natural consequence of bulk relativistic motion of the emitting plasma. In this case, radiation is beamed in the direction of motion into a cone with opening half-angle $\theta_B \sim 1/\Gamma_B$, where Γ_B is the Lorentz factor of the bulk motion. The general result of equation (5.8) can be integrated over the range of beaming angles to determine the γ - γ optical depth of a

relativistically moving source. This has been done for the case of a power law photon spectrum by Krolik & Pier (1991) and Baring (1993, 1994). The resulting opacity depends on the source size ℓ , the photon spectral index α and the beaming angle θ_B with $\tau_{\gamma}(E) \propto \ell \theta_B^{2\alpha} E^{\alpha-1}$, where it is assumed that $\theta_B \ll 1$. Baring (1993, 1994) noted that the observed intensity variations can be much more rapid for relativistically beamed photons than for isotropic emission since the narrow beam can quickly sweep by the observer. This means that the actual source size ℓ is larger than that inferred from the short time-scale variability ℓ_v such that $\ell_v \sim \ell \theta_B \sim \ell/\Gamma_B$. This relation can be combined with equation (5.7) and the full expression for τ_{γ} to yield a lower limit on the bulk Lorentz factor for any assumed source distance. Baring (1994) showed that if a power law photon spectrum is unattenuated ($\tau_{\gamma} = 1$) out to an energy E_B , the lower limit on the bulk Lorentz factor of the emitting plasma is given by

$$\Gamma_B^{1+2\alpha} \geq 10.2 \frac{(3.83)^\alpha (1+z)^{\alpha-1}}{\alpha^{5/3} (4/3 + \alpha)^{27/11}} \left(\frac{d}{1 \text{ kpc}}\right)^2 \left(\frac{\ell_v}{10^6 \text{ cm}}\right)^{-1} \left(\frac{E_B}{1 \text{ MeV}}\right)^{\alpha-1} F_{\text{obs}}(1 \text{ MeV}) \quad , (5.10)$$

where F_{obs} is the observed photon flux (photons $\text{cm}^{-2} \text{s}^{-1} \text{MeV}^{-1}$) at 1 MeV, d is the source distance and z is the source redshift. The redshift factor $(1+z)$ slightly enhances the beaming in cosmological sources when the distance d exceeds about 1 Gpc.

The constraints on bulk relativistic motion are somewhat relaxed when one considers a relativistically expanding thin spherical shell (Fenimore, Epstein & Ho 1992; 1993). In this case, the angle between photons is slightly less (on average) than for ordinary (non-spherical) relativistic motion—requiring somewhat lower bulk Lorentz factors. Harding & Baring (1994) have since considered relativistic shells of finite thickness and found constraints on the Lorentz factor that are consistent with those given by equation (5.10). Thus, the relativistic motion implied by the application of equation (5.10), which assumes beaming within an angle $\theta_B \sim 1/\Gamma_B$, can be extended to more general emission geometries.

Assuming a characteristic variability source size $\ell_v \approx 10^6 \text{ cm}$, the spectral breaks observed by BATSE at energies $E_B \sim 1 \text{ MeV}$ imply significant bulk Lorentz factors ($\Gamma_B > 10$) even if the burst sources are as close as 1 Mpc. For cosmological sources ($d \sim 1 \text{ Gpc}$), the amount of beaming

required is at least an order-of-magnitude larger, depending on the spectral slope. The relativistic bulk motion required for extragalactic sources will naturally blueshift the spectrum to higher energies by a factor of Γ_B . In the emitting plasma frame, the cutoff caused by pair production opacity must occur at photon energies above $\sim m_0 c^2$. If γ - γ attenuation occurs at lower energies, the copious amounts e^+e^- pairs will Comptonize the low-energy photons, producing a Wein peak which is not observed in burst spectra. In the observers reference frame, the γ - γ cutoff must therefore occur at energies $E_B \geq \Gamma_B m_0 c^2$. Thus, if burst sources are extragalactic, it reasonable to assume that the observed spectral “breaks” below 1 MeV are not caused by photon-photon opacity (Baring, 1993, 1994; Winkler 1995). This allows us to further constrain the Lorentz factor by considering the absolute maximum observed photon energies.

As discussed earlier, during GRB 930131 and GRB 940217, EGRET has observed hard power law spectra that extend to GeV energies without any indication of γ - γ attenuation. This would *appear* to indicate that the amount of beaming required for extragalactic burst sources is enormous and conversely that an isotropically emitting source would have to be very nearby (e.g., Sommer *et al.* 1994a; Baring & Harding 1993; Dingus *et al.* 1994). However, the distance and beaming constraints provided by equations (5.9) and (5.10), respectively, are only severe *if* one can limit the size of the emitting region. For instance, it could be that the GeV photons observed by EGRET are produced at much larger radii than the emission at lower energies. If this were the case, the photon density (and therefore the γ - γ optical depth) would be lowered considerably. The characteristic source size inferred from rapid intensity variations at low energies does not *necessarily* correspond to the high energy emission. Unfortunately, EGRET is incapable of measuring rapid intensity variations at high energies due to instrument deadtime and poor statistics. The COMPTEL data allow us to correlate fairly high energies with rapid intensity variations.

The maximum energies, rapid intensity fluctuations and spectral fits computed for the full COMTPEL burst intervals (Tables 5.1 and 5.2) provide constraints on the source distance and bulk Lorentz factor. For example, rapid intensity variations (~ 100 ms) and high energies (> 10

MeV) were observed during many of the strongest bursts. However, to properly apply the constraints of equations (5.9) and (5.10) the rapid intensity variations and high energies *must be correlated*. Furthermore, the average flux over the full-burst intervals greatly underestimates the peak flux during intense emission pulses. More realistic constraints are obtained by estimating the peak flux in the high-intensity pulses where rapid high-energy variations are observed. COMPTEL dead-time limits the ability to estimate fluxes during intense intervals. However, for several bursts, scalar accumulation intervals of individual COMPTEL detectors are favorably positioned to allow us to compute reasonable lower limits on the flux during intense pulses.

Lightcurves of the most intense bursts observed by COMPTEL are shown in Figure 5.6, where intervals of impulsive emission have been expanded with higher time resolution. During these impulsive episodes, the COMPTEL deadtime is large ($\geq 90\%$). The most obvious manifestations of this are the gaps during which telemetry buffers have been filled by the high count rates and no data are available. There are, however, regions before the telemetry gaps where high flux is contained in short spikes or rapidly rising edges of intense emission. Fortunately, individual D2-detector scalar count rates (no coincidence requirements and therefore little deadtime) are accumulated on-board the spacecraft every 2.048 s. The D2 count rates measured during the impulsive episodes of each burst (see arrows in Figure 5.6) were used to estimate the peak flux during the high-intensity spikes (or rapidly rising edges). These estimates are conservative lower limits since the deadtime during the impulsive spikes is probably much larger than over the full 2.048 s intervals. There are insufficient statistics to estimate the spectral *shape* during these impulsive spikes. Rather, the power law spectral index is estimated using the telescope events accumulated over the full 2.048 s scalar accumulation intervals. This is a good approximation, since much of the emission in these intervals is contained in the impulsive spikes. Finally, the maximum energy at which the high-intensity spikes are observed was estimated by examining the high time-resolution lightcurves in different energy bands. This provides a lower limit on the maximum energy that is constrained only by the poor statistics at high energies. Individual telescope events with higher energies were observed during some of the intense spikes.

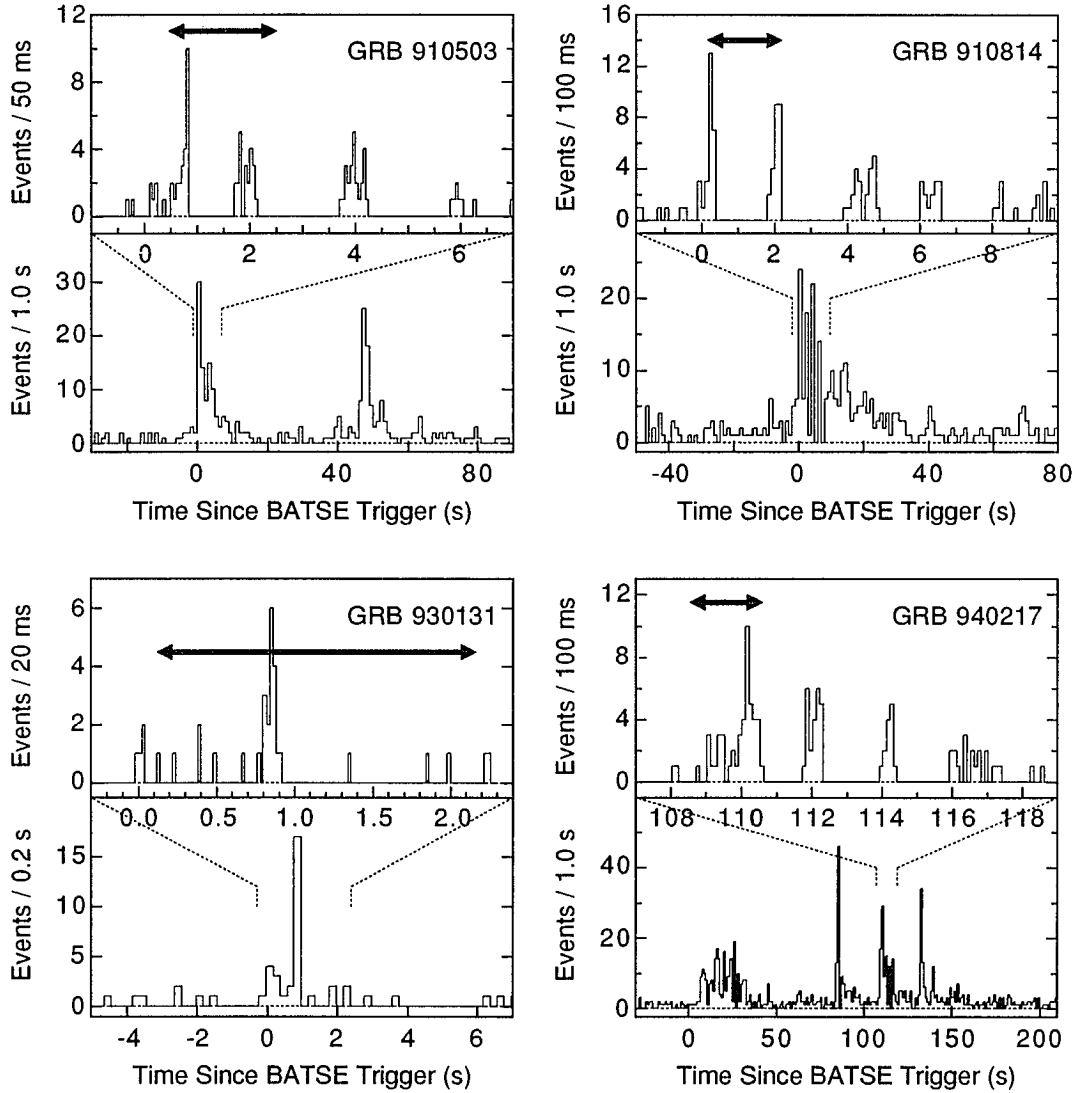


Fig. 5.6. Lightcurves of the most intense COMPTEL bursts (data selections as in Appendix A). The upper panels in each plot show enlarged regions where the most intense emission is observed. Note the large gaps here during which telemetry buffers have been filled and no data is available. The arrows indicate intervals for which single D2-detector scalar rates have been used to estimate peak fluxes.

Results of the analysis of rapid, high-energy variability in each of the four bursts examined here are summarized in Table 5.5. The estimated variability time-scale, maximum energy, peak flux and spectral shape are all conservative limits based on the sparse information available and poor statistics. The actual flux variations could be much more rapid, intense and at higher energies than estimated here. These data have been combined to estimate conservative limits on

the source distance and bulk Lorentz factors through the use of equations (5.9) and (5.10). These limits indicate that if the sources are nearby isotropic emitters, they must be well within 1 kpc and that bulk Lorentz factors in excess of 100 are required for cosmological sources. Note that moderate beaming is required for these bursts even if they are in the Galactic halo at a distance of 100 kpc (the lowest halo distance allowed by BATSE isotropy measurements).

Table 5.5 Limits on Burst Source Distance and Relativistic Bulk Motion

Burst Name	t_o^*	δt_{\min}^\dagger	F_{\min}^\ddagger	α^\S	E_{\max}^\parallel	$d_{\max}^\#$	Γ_{\min}^\parallel	Γ_{\min}^ϵ
GRB 910503	25455.18	0.05	21.2	2.0	4.5	460	4.4	179
GRB 910814	29275.24	0.10	8.1	2.4	3.1	1034	2.7	67
GRB 930131	68231.80	0.05	18.2	1.8	2.0	781	3.9	223
GRB 940217	83070.62	0.10	16.5	2.6	2.5	770	2.8	57

*Start time of 2.048 s spectral accumulation interval (UT).

†Shortest estimated intensity variability time-scale (s).

‡Estimated lower limit on the peak flux during δt_{\min} (photons $\text{cm}^{-2} \text{s}^{-1} \text{MeV}^{-1}$).

§Photon power law spectral index (accumulated over 2.048 s interval).

∥Maximum energy deposit (MeV) for which flux variations $\sim \delta t_{\min}$ are observed.

#Source distance upper limit (pc) from eq. (5.9).

∥Lower limit on the bulk Lorentz factor from eq. (5.10) for a source at 100 kpc.

εLower limit on the bulk Lorentz factor from eq. (5.10) for a source at 1 Gpc.

E. Discussion

The COMPTEL measurements presented in this chapter represent a good sample of burst spectra which characterize the gamma-ray emission at MeV energies. This emission was shown to be inconsistent with models that predict a substantial amount of spectral curvature in this energy range, although the spectral shape of the MeV emission is definitely different from that at lower energies as seen in the multi-instrument comparisons. Through wide-band measurements like the ones shown here, an enhanced view of burst spectra is emerging—one that almost always involves a significant (and variable) change in hardness from the hard X-ray to gamma-ray energy regimes. At higher energies, the featureless power law shape observed by COMPTEL appears to continue without further change, although the temporal aspects of higher energy emission are still unclear. Implications of the hard, rapidly varying MeV emission shown here

are significant considering the effects of known attenuation mechanisms—most notably photon-photon pair production. The remainder of this chapter is devoted to a discussion of the implications of these findings for burst emission models and source scenarios.

i. Overall Spectral Shape

BATSE measurements have shown that the most characteristic feature of gamma-ray burst continuum spectra is a well-contained (but smooth) hard-to-soft transition in the spectral slope that occurs at varying energies up to a few MeV, but mainly below 300 keV. The fact that this spectral turnover is seen in nearly all bursts and on nearly all time-scales means that it could be a valuable indicator of physical emission mechanisms that are common to all bursts. The results presented here confirm—through *simultaneous* observations—the nature of burst emission above the spectral transition observed by BATSE. That is, that above the transition energy, burst continuum spectra are featureless out to at least 10 MeV and they are inconsistent with emission models that predict continuous spectral softening above about 1 MeV. This is evident in the fact that the power law model adequately describes all the burst spectra observed by COMPTEL (at least above 1 MeV). These findings are consistent with earlier *SMM* results which were the first to indicate that most (if not all) bursts extend to MeV energies where their spectra are well-described by the power law model (Matz *et al.* 1985, 1986). The distribution of spectral indices observed by COMPTEL also agrees with that found by *SMM* as well as with the high-energy spectral slopes observed by BATSE (Schaefer *et al.* 1994b). This distribution, that has a maximum at $\alpha \sim 2.5$ for all three independent instrument samples, is another valuable indicator of the burst emission process.

The characteristic turnover in burst spectra will undoubtedly be among the most important criteria by which future emission and source models are judged. The turnover could be related to some fundamental gamma-ray absorption process such as $\gamma\text{-}\gamma$, or $\gamma\text{-}B$ pair production or $\gamma\text{-}B$ photon splitting (Schaefer *et al.* 1992). As was discussed earlier, the distribution of turnover energies is typically much lower than the characteristic threshold energies for pair production. It

is thus difficult to explain most of the observed spectral breaks with such fundamental mechanisms unless the sources are distributed over a wide range of cosmological redshifts (Band *et al.* 1993a). As we have seen, the relativistic motion required for extragalactic sources allows us to rule out γ - γ opacity as the cause of the breaks. Photon-magnetic field interactions are still a viable possibility, but the evidence for strong magnetic fields at burst sites has become tenuous since the keV “cyclotron” absorption features observed in the past have yet to be confirmed.

Band *et al.* (1993a) have pointed out that the wide range of observed turnover energies (below 100 keV to above 1 MeV) and slopes could indicate that the spectral turnovers are related to a correspondingly wide range of physical conditions (temperatures, magnetic fields, densities, etc.) at the burst emission sites and not necessarily to a fundamental absorption process. This view is supported by observations of changing turnover energies and slopes *within* bursts as well as between different bursts (Band *et al.* 1992; Ford *et al.* 1995). In the more traditional neutron star source scenarios, these observations tend to support the more flexible models such as the Compton scattering of thermal photons by ultrarelativistic electrons either with (Dermer 1989; 1990) or without (Zdziarski & Lamb 1986) a strong magnetic field. Such models can explain a variety of different turnovers (break energies and spectral slopes) by adjusting the physical parameters at the emission site. For cosmological (or Galactic halo) source scenarios such as the collapse of a compact object (Woosley 1993) or the merger of a compact binary (Paczynski 1986), it is recognized generally that some sort of fireball mechanism is required in the development of a burst. The spectral predictions of fireball models are considerably less developed those of neutron star models. However, it may be possible to produce spectral turnovers in the context of a fireball, depending on the mechanisms invoked to produce the final gamma-ray spectrum. The most advanced work in this area has focused on internal interactions within fireball ejecta (including especially baryons) and the interactions of the ejecta with an external medium. Inverse Compton and/or synchrotron emission from non-thermal particles accelerated in the resulting shock waves (internal, external or both) allow for flexibility that could possibly explain both the observed spectral turnovers and the continuation of a hard power law at

higher energies. The details of spectral development in fireball models depend on the amount of baryonic matter in the ejecta, the physical conditions of the external media and whether or not either contain strong magnetic fields (Mészáros & Rees 1993b; Mészáros, Rees & Papathanassiou 1994; Katz 1994a).

ii. High-Energy Emission and Relativistic Motion

The EGRET observations of very high-energy burst emission have provided much needed new insight into the problem of GRB production. The agreement between COMPTEL and EGRET spectra below 10 MeV indicates that beyond the low-energy turnover observed at BATSE energies, burst spectra are hard power laws out to at least 100 MeV with no indication of any further turnover. However, since the spectra considered here were time-averaged over much of the burst, there is little to indicate a correlation on short time-scales between the emission below and above 10 MeV. There is even less evidence that the photons observed by EGRET above 100 MeV (extending to at least 1 GeV) have anything to do with the emission observed by COMPTEL and BATSE at lower energies. Thus, while the existence of high-energy burst emission is an important clue into the physics of burst production, conclusions must be made with caution.

As discussed earlier, one of the most constraining implications of high-energy burst emission is that it is difficult to explain rapid variability, high energies and large source distances in the context of isotropic emission given the known effects of photon-photon interactions. The two most natural solutions to this problem—nearby sources or relativistically beamed emission—are constrained considerably by the data. For example, there have been several statements in the literature that the EGRET observations of GeV photons limit isotropically emitting sources to lie within a few pc and require bulk Lorentz factors in excess of 10^3 for cosmological sources (e.g., Sommer *et al.* 1994a; Baring & Harding 1993; Dingus *et al.* 1994). However, as pointed out by Ryan *et al.* (1994b), the mere existence of high-energy gamma rays measured by EGRET does not constrain severely the source distance or the amount of beaming. Rapid flux variations of

high-energy emission are required for meaningful constraints. This has been observed in the COMPTEL data and the resulting bounds on source distance (assuming isotropic emission) and bulk Lorentz factor (assuming extragalactic sources) presented here are among the most constraining limits possible without making more assumptions about the temporal correlation between low- and high-energy emission.

The COMPTEL results indicate that either burst sources are within ~ 1 kpc or the emission is highly collimated by a relativistically moving source with a significant bulk Lorentz factor ($\Gamma_B \geq 100$ for a source at 1 Gpc). A nearby source distribution within 1 kpc is difficult (although not impossible) to reconcile with the BATSE conclusions of spatial isotropy and inhomogeneity. Conversely, beamed emission resulting from bulk relativistic motion is predicted by many source models. Several emission models involving the traditionally favored neutron star sources have been proposed which produced beamed radiation through relativistic particle acceleration along intense electromagnetic fields (e.g., Smith & Epstein 1993; Ho *et al.* 1990; Miller & Epstein 1992). With modification, some of these models can be used to explain gamma-ray bursts from neutron stars in the Galactic halo. Beamed emission models have also been proposed for extragalactic sources. The most common of these involve relativistic jets similar to those observed in AGN, where relativistic particle ejections occur preferentially along the rotation or magnetic axis of the system (Brainerd 1992; McBreen, Plunkett & Metcalf 1993; Roland, Frossati & Teysier 1994). Beamed emission has also been suggested in the context of cosmological neutron star (or neutron star, black hole) merger models, where two oppositely directed relativistic particle beams are formed along the system axis (Mochkovitch *et al.* 1995; Mészáros & Rees 1994a). An advantage of beamed emission is that a smaller luminosity is required at the source since the observed fluence is enhanced by a solid angle factor $\sim 1/\Gamma_B^2$. This somewhat relaxes the gargantuan energy requirements of extragalactic burst sources and at the same time allows us to sample to larger distances. The disadvantage to beaming is that the total number of required sources is increased by a factor $\sim \Gamma_B^2$ because the emission beam is only sometimes in our direction (Krolik & Pier 1991).

The large bulk Lorentz factors required for extragalactic sources by the COMPTEL results do not necessarily imply beaming within an angle $1/\Gamma_B$, but could instead involve relativistically expanding spherical shells of varying thickness (Fenimore *et al.* 1993; Harding & Baring 1994). With expanding shell emission, the COMPTEL constraints on Γ_B can be applied to burst models that invoke the fireball mechanism or one of its derivatives. Traditional fireball models, wherein an optically-thick pair cascade expands radially until it cools sufficiently to allow the escape of high-energy photons, typically invoke bulk Lorentz factors Γ_B ranging from 10^1 to 10^3 , depending on the source distance (Piran & Shemi 1992). More advanced fireball models that contain significant mass in the form of baryons allow less extreme Lorentz factors ($\Gamma_B \sim 10^2$ for cosmological sources) by converting some of the kinetic energy of the baryons back into gamma rays through internal shock mechanisms (Mészáros & Rees 1994a). The major factors that determine the minimum required Lorentz factor in fireball models are the source distance, energy release time-scale and amount of baryonic matter. Woods & Loeb (1994) have estimated limits on these parameters (including the minimum Lorentz factor) by considering the peak fluxes observed by BATSE on short time-scales and assuming a pair production optical depth of unity for photon energies up to ~ 10 MeV. However, they assume implicitly that the 10 MeV emission is temporally correlated with that in the range 50–300 keV (the energy band where BATSE peak fluxes are measured). As pointed out earlier, this assumption is only justified in the COMPTEL data presented here. Constraints on the minimum bulk Lorentz factor obtained using the COMPTEL data are consistent with all the current models involving the fireball mechanism.

The photons with GeV energies that have been observed by EGRET in several bursts long after low-energy emission has subsided have prompted further interest in cosmological fireball models (Hurley *et al.* 1994e). Delayed high-energy emission is a somewhat natural consequence of the more advanced “baryon loaded” fireball models when the relativistically-expanding outflow encounters external matter (Mészáros & Rees 1994b; Katz 1994b). In such models, the familiar low-energy (< 1 GeV) bursts are a result of particle acceleration within the fireball as it expands and eventually cools to the point where it becomes optically thin to γ - γ interactions.

This “primary burst” is thus relatively short (~ 0.1 – 1000 s) and its emission peaks at keV energies. The delayed burst is generated when the relativistic baryon flow is eventually decelerated (time delays of minutes to hours) as it encounters an external medium (either the interstellar medium or a cloud of material from the progenitor object), forming a shock which further accelerates the baryons (Mészáros & Rees 1994b). Nucleon-nucleon interactions resulting in high-energy pions and eventually high-energy gamma rays are a possible photon emission mechanism (Katz 1994b). The resulting spectrum of delayed photons would peak at much higher energies than the primary burst and the emission could last as long as the delay. However, there is no conclusive evidence in the observational data that the “delayed” emission observed by EGRET is either harder or delayed with respect to that of the impulsive phase of the burst. In fact, the upper limits and detections in the MeV range provided by COMPTEL and the EGRET–TASC indicate that the spectrum observed at GeV energies is unchanged from that ~ 1 MeV. Thus, a more likely explanation of the observations is that there is an extended low-intensity tail which is only observable by EGRET due to its extremely low background. Furthermore, this tail *appears* to contain a significant fraction of the burst energy only because EGRET cannot measure all the photons during the intense episodes due to severe instrument downtime. The implications of extended (rather than delayed) emission are that either particle acceleration persists over long periods or that the accelerated particles have a long lifetime (Sommer *et al.* 1994a).

VI. FADING COUNTERPART SEARCH RESULTS

The inability of gamma-ray measurements to solve the burst problem has, from the beginning, led many researchers to concentrate on searching for counterparts at other wavelengths. The positive identification of even one burst counterpart at another energy would be a major breakthrough in our understanding of these enigmatic sources—providing simultaneously the much-needed increase in angular resolution and spectral range. For instance, the identification of a quiescent optical counterpart would not only identify the type of source object, but probably also lead to an unambiguous determination of the source distance. Unfortunately, numerous thorough searches have failed to identify any convincing counterparts at energies below ~ 2 keV. The failure to identify burst counterparts is due in part to the limitations of gamma-ray instruments that have been unable to provide accurate burst locations in a timely manner. Most studies have been forced to concentrate on well-localized bursts (i.e. Interplanetary Network localizations), that have allowed fairly deep searches, but typically only long (days to months) after the gamma-ray emission has faded. The elusive nature of burst counterparts indicates that low-energy emission is probably not very strong and may not exist at all in quiescence. Given the transient nature of the gamma-ray emission, it is natural to search for low-energy counterparts that are transient as well. The ability of COMPTEL to localize burst sources with reasonable accuracy has been exploited in a unique counterpart search program wherein rapidly determined COMPTEL burst localizations are distributed to a world-wide network of multiwavelength observers. The advantage of this program over previous efforts lies in the *combination* of accurate COMPTEL locations (allowing fairly deep searches) and the speed with which they are computed and disseminated (allowing timely searches). The goal of this program is to identify fading low-energy counterparts that would not be detectable long after the burst onset. In this chapter, the rapid COMPTEL burst location distribution program is described and results of the search for fading counterparts are discussed in the context of past efforts and model

predictions.

A. Past Counterpart Search Strategies and Results

The most accurate burst localizations have always been, and continue to be, measured through arrival-time analysis using widely separated spacecraft forming an Interplanetary Network (IPN). The IPN burst locations using three or more spacecraft are typically accurate to arc-minute precision, which allows the fields to be searched using powerful (but limited field-of-view) telescopes. The very nature of this localization technique—requiring significant time-delays and coordination between multiple instruments—means that burst positions have not been available until *at least* days (more often weeks, months or years) after the gamma-ray events (e.g., Hurley *et al.* 1993a). Burst locations determined by other means have sometimes been available sooner, but these locations are typically too inaccurate to allow *deep* counterpart searches. Furthermore, the unknown burst recurrence rate makes pointed “stare” searches unpromising for high-sensitivity, narrow FOV telescopes. The limitations of burst localization with gamma-ray instruments requires several different low-energy counterpart search strategies. Reviews of past and current attempts to identify burst counterparts at different wavelengths have been given by Schaefer (1986, 1992, 1994).

The most often used strategy is to perform searches at different wavelengths (radio through X-ray) using only the most accurate IPN burst locations. This strategy has the advantage of allowing the deepest searches for *quiescent* emission from the object(s) which caused the burst in gamma rays. However, if low-energy emission is transient, this strategy fails by looking too long after the bursts (typically months or years). The fundamental problem is that the nature of quiescent burst source emission is completely unknown. Even the smallest burst fields can (depending on the source position and search wavelength) contain many faint objects and it is impossible to say which, if any, are the burst source. This forces observers to search for “unusual” objects in the burst fields. At optical wavelengths, many of the smallest burst localizations have been searched for objects with peculiar colors, time variability and proper

motions down to faint magnitudes $m_V \approx 24$ (e.g., Verba, Hartmann & Jennings 1992; Verba *et al.* 1994; Harrison, McNamara & Klemola 1994a,b; Schaefer 1992; Ricker, Vanderspek & Ajhar 1986). The fields usually contain faint stars, galaxies and occasionally more exotic objects such as white dwarfs and AGN, but their numbers are always consistent with those expected in a randomly chosen region. Nothing truly out of the ordinary has been identified in any of the burst fields. In some individual burst fields interesting objects have been identified, but there is nothing to indicate similar objects in the remaining burst error-boxes. The lack of optical galaxies in many of the error-boxes down to faint magnitudes is particularly constraining to cosmological models like the compact object merger scenarios that have the bursts originate in host galaxies (Schaefer 1992, 1994). Radio and infrared observations of well-determined burst fields have met with similar difficulties and have failed to identify any peculiar objects associated with the bursts (e.g., Hjellming & Ewald 1981; Schaefer *et al.* 1987, 1989). The deepest radio observations range in sensitivity from 0.1–0.8 mJy in the UHF band, which constrains nearby neutron star and distant cosmological models that both predict radio emission at some level (Schaefer *et al.* 1989; Palmer 1993). The deepest infrared observations reached magnitudes $m_J \sim 17.5$ (Apparao & Allen 1982) and $m_K \sim 13.6$ –19 (Schaefer *et al.* 1987) and are constraining mainly for models that involve cool companion stars or accretion disks. In soft X rays and the extreme ultraviolet (EUV), the *ROSAT* all-sky survey provides the most constraining measurements, but has failed to reveal any unusual quiescent sources from any of the best-localized burst fields with a sensitivity limit of $\sim 10^{-11}$ – 10^{-13} erg cm⁻² s⁻¹ (e.g., Owens *et al.* 1993; Boer *et al.* 1994a, 1994b). This is constraining for any burst models that predict hot plasmas before or after the bursts. Hot plasmas can also produce emission at gamma-ray energies <1 MeV, but no *quiescent* gamma-ray emission has been observed in the range ~ 15 keV to 1.8 MeV from any of the best-localized burst fields (Horack *et al.* 1993; Horack & Emslie 1994).

A related strategy that has produced at least some results is to search for objects within well-localized GRB fields in archival optical photographic plates. The first *optical transient* (OT) was identified by Schaefer (1981) in a blue-band plate from the Harvard College Observatory

collection taken in 1928. The bright ($m_B \sim 3$ assuming a 1 s flash) source was coincident with the IPN error-box of GRB 781119 and did not appear on plates taken 45 min earlier or later. Assuming this OT coincided with a gamma-ray burst similar in magnitude to GRB 781119, the gamma-ray to optical luminosity ratio is $L_\gamma(> 30 \text{ keV})/L_{\text{opt}}(B \text{ band}) \approx 800$. About 12 optical transients have since been identified with this technique using archival optical plates from around the world (e.g., Schaefer 1990; Hudec 1993). Most of the OTs are coincident with known GRB fields and are not visible in earlier or later plates. There are, however, problems with many of these identifications. It has been argued that several of the OTs are photographic plate defects (Zytkow 1990; Greiner 1992), but others show clear evidence that they are real astrophysical sources (Hudec & Soldán 1994; Schaefer 1994). The nature of OT sources is not known primarily because the background for optical flashes is not well understood. Since the most believable OTs appear on plates taken before the advent of airplanes and satellites, these can be ruled out as potential sources. Nonetheless, asteroids, meteors, variable stars, active galaxies and stellar flares all contribute to the unknown OT background (Hudec 1993). The fundamental problem with the identification of OTs is not whether they are real astrophysical sources, but rather whether they are related to gamma-ray bursts. The lack of similar OT identifications in large control regions that do *not* contain known GRB source positions gives some indication that OTs may be related to GRBs (Schaefer 1990). If they are related, the observed OTs constrain the burst recurrence time-scale to be within 0.2–6.5 yr, which roughly agrees with the limits determined from gamma-ray measurements (Schaefer & Cline 1985). However, the only way to confirm that OTs are related to gamma-ray burst activity is through the simultaneous observation of a burst in the optical and gamma-ray regimes.

Simultaneous optical observations of gamma-ray burst source positions have, in fact, been performed. This has been accomplished through serendipitous observations made by wide-field, low-sensitivity cameras that routinely scan large portions of the sky to track comets, meteors and satellites. The earliest simultaneous observations were reported by Grindlay, Wright & McCrosky (1974) using the Prairie Network of optical cameras designed to search for and track

meteor trails. They discovered simultaneous exposures of two fairly well-determined (accurate to $\sim 1^\circ$) burst locations and saw no optical flash with a limiting magnitude $m_V \sim 3$. An optical transient like those found in archival searches *should* have been detected. More recently, serendipitous simultaneous exposures have been obtained for 29 of the bursts observed by BATSE up to March 1993, with a typical limiting sensitivity of $m_{pg} \sim 1-3$ for a 1 s flash (Greiner *et al.* 1992; 1993, 1994; Hudec & Soldán 1994). The optical devices employed in this work have very large fields-of-view (usually $150^\circ \times 150^\circ$), so the relatively imprecise BATSE positions can be used with confidence. No optical flashes have been found in any of the exposures which could be attributed to a gamma-ray burst—placing a limit on the simultaneous gamma-ray to optical flux ratio of $F_\gamma/F_{opt} > 0.5-40$ for a 1 s flash (Greiner *et al.* 1994). Using the same strategy, several near-simultaneous (within ± 24 hours) BATSE burst exposures have been obtained with better sensitivity. No obvious flaring optical sources have been identified, placing a limit on the optical brightness 1–3 hours before or after the burst of around 5–7 mag for a 1 s flash (Greiner *et al.* 1994). Serendipitous simultaneous measurements have also been obtained at radio frequencies using wide-field radio monitors. No coincident bright radio pulses have been observed down to a limiting sensitivity of $\sim 10^4-10^5$ Jy in the UHF and VHF bands (e.g., Baird *et al.* 1975; Cortiglioni *et al.* 1981; Inzani *et al.* 1982).

From these results we can draw a few general conclusions. First, it is clear that *obvious* quiescent burst counterparts do not exist down to very faint magnitudes at a variety of wavelengths. The word “obvious” is the key in that we really don’t know what to expect in a quiescent counterpart. Further, deeper studies at different wavelengths will undoubtedly yield more candidates, but they will probably not lead to the unambiguous identification of a burst counterpart. Second, some of the optical transients found on archival plates are probably real astrophysical phenomena, but their relation to gamma-ray bursts is unknown. Without the simultaneous detection of an OT and a gamma-ray burst, it cannot be proved that these objects are related to GRBs. Third, *bright* simultaneous and near-simultaneous optical and radio emission from bursts can be ruled out. If bursts do flare appreciably at these wavelengths, the emission is

faint (at least below the current sensitivity limits) and could be short-lived. Clearly, what is needed to solve the burst counterpart dilemma are deep, simultaneous observations over a broad range in wavelength. Unfortunately, the only way to get deep exposures is to use powerful telescopes that have limited FOVs. This makes serendipitous exposures highly unlikely. Another strategy is to improve the speed with which accurate gamma-ray burst localizations are determined and distributed to observers. This allows deep, near-simultaneous observations which could detect fading transient emission—if it exists.

Until recently, few attempts had been made to perform deep, time-correlated searches for fading counterpart emission mainly because rapid and accurate burst locations have not been available. With the advent of the *Compton* Observatory and BATSE, preliminary IPN locations started being computed routinely in about 1–3 days (Hurley *et al.* 1993a). The error-boxes of these bursts were searched within a few days to a few weeks for signs of fading emission in radio, optical and X rays. Nothing obvious has been detected in the optical ($m_V \geq 15-20$; $m_R \geq 16-22$; Boër *et al.* 1994c; Barthelmy *et al.* 1994a) or radio ($F_{\nu}[151 \text{ MHz}] \leq 40 \text{ mJy}$; Koranyi *et al.* 1994). A possible X-ray counterpart to one of these events (GRB 920501) was identified by *ROSAT* in a target-of-opportunity observation obtained two weeks after the burst, but its nature is still uncertain (Hurley *et al.* 1993b; Sommer *et al.* 1994b). It thus appears that fading burst counterparts, if they exist, are too weak to be detected after a delay of ~ 1 day. The burst locations provided by COMPTEL (and instruments with similar angular resolution such as *GRANAT-WATCH*; Castro-Tirado *et al.* 1994b) are not as accurate as the IPN error-boxes, but they are sufficiently small to allow deep searches using medium FOV instruments ($\sim 2^\circ \times 2^\circ$) such as Schmidt telescopes. Furthermore, they can be computed much more quickly.

B. Rapid Burst Response

A unique counterpart search program has been implemented to allow the fairly accurate COMPTEL burst positions to be computed and distributed quickly to a large network of multiwavelength observers. The goal of this “Rapid Burst Response” program is to measure

fading GRB counterpart emission—or the lack thereof—as quickly and as sensitively as possible using existing instrumentation. This goal is realized only through the clever and coordinated use of BATSE, COMPTEL and a world-wide network of wide-field observatories. By using BATSE to identify bursts quickly that COMPTEL can image, we are able to perform *deep* optical and radio scans of the degree-sized COMPTEL localizations within hours. BATSE is required to identify the bursts since COMPTEL lacks an on-board transient event triggering system. Due to COMPTEL's limited FOV, only a small fraction of all BATSE burst triggers are candidates for COMPTEL imaging. Furthermore, only a fraction of the BATSE bursts occurring inside the COMPTEL FOV are of sufficient fluence with a sufficiently hard spectrum to be localized. Thus, the key to the success of this program is in the rapid filtering (both in source position and intensity) and communication of promising candidate BATSE burst triggers.

As originally implemented, the Rapid Burst Response program performed the task of filtering unwanted BATSE triggers using special BATSE count rate thresholds that are checked automatically on-board the *Compton* satellite at the onset of all triggers. These thresholds were set to register only those bursts that were of sufficient intensity to be imaged by COMPTEL. BATSE data are monitored continuously in real-time by the Compton Observatory Flight Operations Team (FOT) located at Goddard Space Flight Center (GSFC) and threshold violations (i.e., triggers) were communicated promptly to the BATSE instrument team at Marshall Space Flight Center. The BATSE team used the count rate threshold data to compute rough burst directions ($\pm 20^\circ$) to determine if the bursts were within the COMPTEL field-of-view and of cosmic origin. The occurrence times and rough positions of bursts satisfying these criteria were communicated to the COMPTEL team at the University of New Hampshire (UNH), where readily available COMPTEL data were processed and analyzed in an accelerated manner. The occurrence times were used to identify the bursts in the COMPTEL data and the rough burst positions computed by the BATSE team were used in the maximum-likelihood imaging process to limit the area of the search. The resulting COMPTEL burst localizations were communicated to an observer network distribution site located at New Mexico State University (NMSU), where

they were distributed to appropriate network observers (i.e., those capable of observing the burst locations). The Rapid Burst Response program began operating in this “Phase I” manner in July 1992, but it was not until several months later that it became fully operational. Under optimum circumstances, this entire procedure could be executed in as little as ~4 hours from the time of the burst onset (see Figure 6.1). Unfortunately, major delays in this operation were typically encountered due to faulty communications pathways between team members, occasional problems in obtaining COMPTEL data, limitations of UNH computers and an ill-defined observer network. Furthermore, the Phase I operations suffered from the fact that each step in the procedure required human intervention.

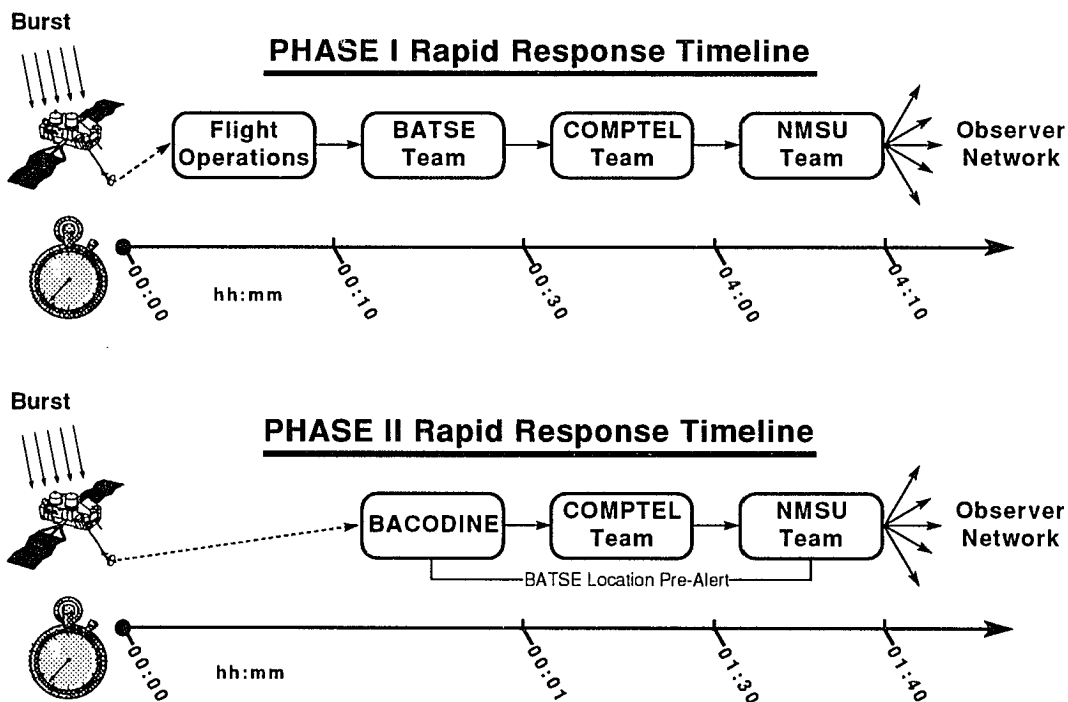


Fig. 6.1. Schematic outline of Rapid Burst Response operations and typical response times during Phases I and II of the program.

In Phase II, which began in 1994, many of the problems encountered with the earlier system were corrected. This included better communications pathways between the different sites, more reliable data transfer, a faster computer at UNH and a well-established observer network. These

changes alone decreased the typical burst response time by nearly a factor of two. The most important change in Phase II, however, was in bypassing the FOT/BATSE team part of the system through the use of the automatic BATSE Coordinates Distribution Network (BACODINE) for burst notification and trigger filtering. The BACODINE hardware and software located at GSFC intercepts real-time BATSE telemetry. In the event of a BATSE burst trigger, BACODINE computes automatically a burst position accurate to about $\pm 10^\circ$ within 5 s of the trigger time and distributes it to the COMPTEL/UNH team (Barthelmy *et al.* 1994b). The use of BACODINE significantly improves the rapid response system by eliminating all of the human intervention at the early stages. When BACODINE burst alerts are received at UNH, the remainder of the plan proceeds as in Phase I, but with improved performance (see Figure 6.1). Observer response is improved considerably by distributing “pre-alerts” as soon as the BACODINE positions have been computed. This allows the observers time to prepare for the forthcoming COMPTEL burst positions. Observers with very large FOVs can even begin observing using the BACODINE burst position as a guide.

In the three-year period covered by this work, the Rapid Burst Response system has been successfully applied to seven of the ten bursts observed by COMPTEL in this interval (Table 6.1). The remaining three bursts were not strong enough to trigger the BATSE thresholds used during Phase I, so they were not “discovered” until several days after the bursts. The first two bursts occurred before everything was operational, so their response times listed in Table 6.1 just serve to indicate how much the response has progressed. The last two bursts were observed during Phase II with BACODINE notification, thus their response times were considerably better than the rest.

Depending on the fluence of the individual bursts and the amount of background, the rapidly determined COMPTEL localizations are typically somewhat different (usually $\leq 1^\circ$ change) from the “final” positions presented in Chapter IV. The final positions benefit from better knowledge of the background using data from ± 15 orbits that are not available until later. In rapid imaging, the simple isotropic background model discussed in Chapter II is used for a quick estimate.

Rapid burst locations also can suffer because the time-interval of the burst chosen for imaging is subjective rather than optimized. Some quality of rapidly determined burst locations must be sacrificed in favor of speed. In attempt to correct for this effect, refined localizations are distributed to the observer network as soon as they become available. Clearly, observers with the largest FOVs have the advantage since they are least affected by such changes in the burst localization.

Table 6.1 Rapid Burst Response Performance

	Burst Name	Response Time*	BACODINE Alert	Searched by Network	Comments
Phase I	GRB 920830	4d 00h 00m			Weak burst, poor location
	GRB 930118	3d 00h 00m			Weak burst, poor location
	GRB 930131	6h 30m		YES	Optical and Radio
	GRB 930309	4h 30m		YES	Radio only, poor viewing
Phase II	GRB 940217	4h 13m	PARTIAL [†]	YES	Optical and Radio
	GRB 940301	1h 40m	YES	YES	Optical and Radio
	GRB 940314	2h 50m	YES		Too close to the Sun

*Time after BATSE trigger when COMPTEL localization was distributed to NMSU

[†]COMPTEL team was not notified of the BACODNE alert

C. Multiwavelength Burst Observations

The rapid response observer network (RRN) was established to aid in the distribution of COMPTEL burst locations and to coordinate counterpart search efforts at a single location (NMSU). The RRN membership consists currently of ~25 (fewer in phase I) wide FOV ground-based observing sites that are distributed throughout the globe to insure quick response and redundant coverage of nearly all possible burst positions. The network contains a variety of instrumentation to allow comprehensive and deep rapid response capability. Hence, most of the instruments are large Schmidt telescopes (or similar devices) that provide deep ($m_v \sim 16-22$) optical coverage of large fields ($0.5^\circ \times 0.5^\circ$ to $6^\circ \times 6^\circ$). Among the most important of these are the large Schmidt-like telescopes of the US Air Force's Ground-Based Electro-Optical Deep Space Surveillance (GEODSS) system. Designed to track near-Earth debris, the GEODSS telescopes

offer rapid slew capability and can image a field of up to $6^\circ \times 6^\circ$ down to $m_V \sim 16$ in a fraction of a second (see Beatty 1982). Other, non-Schmidt optical sites offer both larger FOVs with poorer sensitivity and smaller FOVs with greater sensitivity. These observatories provide redundant longitudinal coverage in the event of poor viewing at the Schmidt sites. In addition to the optical sites, there are several radio observatories that participate in the RRN effort. These consist of wide-field ($0.5^\circ \times 0.5^\circ$ to $10^\circ \times 10^\circ$) dish telescopes, arrays and interferometers. Several sensitive ($m_V \sim 23$) small FOV telescopes are used in follow-up observations to obtain CCD photometry and spectroscopy of interesting objects that are identified in the rapid response surveys.

The typical RRN observing strategy is to obtain exposures with the widest FOV telescopes (radio and/or optical) using the BATSE position first and then refining the pointing of these instruments when the COMPTEL localization becomes available. At this time, the smaller FOV instruments can begin observing. When IPN annuli from BATSE/*Ulysses* timing data become available (usually within 1–3 days), the entire combined COMPTEL/IPN localization can be searched for faint “interesting” quiescent objects with the smaller CCD devices. The follow-up process of identifying the interesting objects through comparisons with source catalogs and detailed photometric/proper motion studies can then proceed.

i. Results from Individual Bursts

As shown in Table 6.1, the RRN responded to four of the BATSE/COMPTEL bursts examined in this work. The response to the first of these events was far from optimum due to inexperience, poor viewing conditions and a rudimentary network. The localizations of these bursts were searched with response times and sensitivities comparable to recent previous studies (a few days delay). Fortunately, the response to the latter two bursts was significantly better—allowing the localizations to be searched for faint optical and radio emission in record time (significantly less than one day). Results of the individual observations are described below.

a. GRB 930131. This burst was the first successful exercise of the Rapid Burst Response system. Optical observations of the COMPTEL localization began 5.5 hours after it was

distributed to the limited observer network and 12 hours after the burst onset. Unfortunately, these early observations were made with a small FOV telescope and did not include the final combined COMPTEL/BATSE/EGRET/IPN error-box (McNamara & Harrison 1994). A serendipitous exposure ($m_{\text{pg}} \sim 6.5$ for a 1 s flash) was obtained with a delay of 6.8 hours, but deep images ($m_{\text{v}} \sim 20$) containing the final position were not taken until ~ 1.5 days after the burst. The localization was subsequently searched in the optical by several different observers during the following days and weeks. The results of these observations were described by Schaefer *et al.* (1994c). In none of the observations was an obvious fading burst counterpart observed. However, several interesting objects were identified. Five variable optical sources were discovered in the deep exposures obtained with 1–2 days delay, but with one exception they were all well outside the final combined error-box. The exception was a weak ($m_{\text{v}} \approx 23$) non-stellar variable object located $23''3$ from the IPN annulus that was identified on a Schmidt plate taken 1.85 days after the burst. McNamara & Harrison (1994) have, in follow-up observations, determined that this object is visible on comparison plates and is probably not variable—suggesting it is not a good burst counterpart candidate. Thus, rapid observations of this burst put a limit of $m_{\text{v}} \leq 20$ on the optical magnitude of fading counterpart emission after a delay of ~ 1 day. This limit is consistent with the results of recent observations performed by Boër *et al.* (1994c) and Barthelmy *et al.* (1994a).

b. GRB 930309. The COMPTEL localization of this burst was poorer than average due to high background and its position far off-axis (see localization in Appendix A). In addition, its proximity to the sun made this field unreachable to optical instruments. However, radio observations were obtained over the next few days at several observatories. An interesting candidate object located within the COMPTEL 1σ localization was identified in observations at $\lambda = 49$ cm obtained three days after the burst. This source exhibited a declining radio flux over time (76 \rightarrow 66 mJy in three days) as might be expected from a fading GRB counterpart (Hanlon, Bennett & Spoelstra 1993; Harrison & McNamara 1993). Unfortunately, due to the poor COMPTEL localization, the position of this radio source was found to be inconsistent with the

BATSE/Ulysses IPN triangulation annulus that was revealed several days later (Hurley *et al.* 1993c). In follow-up observations, the object was later determined to be an extragalactic background object—probably a double-lobed radio galaxy (Beasley, Dwarakanath & Rupen 1993; Hanlon *et al.* 1993).

c. GRB 940217. The COMPTEL position and response time for this burst were both very good, but optical viewing was poor due to the proximity of the burst position to the sun. The region was not observed in the optical until 1.4 days after the burst. No transient sources were identified down to a limiting sensitivity of $m_R \approx 20$ —in agreement with the results of Boër *et al.* (1994c) and Barthelmy *et al.* (1994a). Radio observations at several frequencies were obtained with time delays well-within one day after the burst (McNamara *et al.* 1995). These rapid response observations failed to reveal any new or transient radio sources within the final COMPTEL/BATSE/EGRET/IPN error-box (Hurley *et al.* 1994f). The most constraining rapid response upper limits and time delays were: 0.2 Jy at 151 MHz (0.71 days), 0.8 Jy at 1.4 GHz (0.77 days), 0.5 Jy at 1.6 GHz (0.77 days) and 0.1 Jy at 8.4 GHz (1.0 days). These measurements are more constraining than the earlier results of Koranyi *et al.* (1994), who failed to detect transient radio emission from GRB 920711 two days after the burst with a sensitivity of ~ 0.1 Jy at 151 MHz. The fact that EGRET observed GeV photons from GRB 940217 for a period of 1.5 hours (Hurley *et al.* 1994e) highlights the value of these rapid radio observations.

d. GRB 940301. The position of this burst in the northern hemisphere and well away from the sun made for excellent viewing (apart from poor weather) at many of the RRN sites. The COMPTEL localization was sufficiently small and rapidly distributed to allow deep optical and radio observations to be performed in record time. The complete network response to this burst has been described by Harrison *et al.* (1994). A subset of these observations from the first five days after the burst are listed in Table 6.2. The earliest observations began only one hour after the start of the burst using the BATSE–BACODINE pre-alert position. These data were obtained using a wide-field, non-imaging radio interferometer mode designed to search for transient pulses of emission at 151 MHz—none were detected. The first imaging observations of the COMPTEL

localization were obtained ~ 7 hours after the burst (5.6 hours after the COMPTEL localization was distributed) with wide-field optical and radio telescopes. No new or unusual objects were identified in these early exposures. The resulting upper limits on fading optical ($m_V \approx 16$) and radio (0.2 Jy at 151 MHz) emission are the most constraining to date. Deeper observations were made over subsequent days and weeks after the BATSE/*Ulysses* IPN annulus became available (Hurley *et al.* 1994g).

Table 6.2 Rapid Observations of GRB 940301 (First Five Days)

Time Delay (Days)	Instrument	Area Covered (deg ²)	Wavelength/ Frequency	Depth Limit
0.04	Radio Interferometer	12	151 MHz	*
0.28	34 m Radio Antenna	12	8.42 GHz	80 mJy
0.29	1 m GEODSS Schmidt	10	Optical-V	$m_V = 16^\dagger$
0.38	1 m GEODSS Schmidt	10	Optical-V	$m_V = 16^\dagger$
0.75	Radio Interferometer	16	151 MHz	0.2 Jy
1.74	Radio Interferometer	16	151 MHz	0.2 Jy
1.90	0.5 m Maksutov	9	Optical-pg	$m_{pg} = 18$
2.08	0.9 m Schmidt	25	Optical-R	$m_R = 19.5$
2.96	0.4 m Astrograph	64	Optical-pg	$m_{pg} = 17$
3.10	0.35 m Astrograph	56	Optical-pg	$m_{pg} = 15$
3.15	Radio Synthesis Telescope	4 64	21 cm 74 cm	5 mJy 50 mJy
4.04	0.9 m Schmidt	25	Optical-B	$m_B = 22$
4.95	0.9 m Schmidt	25	Optical-B	$m_B \leq 22$

*This observation was made using a non-imaging radio pulse-detection mode and the limiting flux is presently unknown.

\dagger Unlike photographic plates, the GEODSS observations reach a limiting visual magnitude of 16 in a single 1/33 s exposure.

Three possible optical variable objects were identified in deep R-band exposures taken 9 days after the burst (Pedersen 1994), but none is an obvious GRB counterpart since one expects to find a few faint variable objects in a region of this size (see Schaefer *et al.* 1994c and references therein). Using the COMPTEL/IPN localization of this burst, Frail *et al.* (1994) have performed a deep, long-term radio monitoring campaign to search for the emergence of delayed transient sources. Radio observations at 0.4 and 1.4 GHz were obtained on 15 separate days extending

from 3–99 days after the burst. None of the sources identified within the COMPTEL/IPN error-box showed flux variations above the $\pm 4\sigma$ level. This places a conservative upper limit on the flux density of delayed flaring/fading radio counterpart emission of 3.5 mJy at 1.4 GHz and 55 mJy at 0.4 GHz.

D. Discussion

The unique counterpart search program described here has resulted in the deepest rapid observations of burst locations at low energies ever performed. We have found no evidence of obvious fading optical or radio emission from the direction of any of the four bursts examined. The resulting upper limits on fading burst source emission are the most constraining measurements made thus far. The most restrictive limits have been obtained for GRB 940217 and GRB 940301. These two bursts are among the brightest $\sim 2\%$ of all the GRBs observed by BATSE. If bursts are standard luminosity candles, we would expect these two strong events be the closest in distance independent of the absolute scale and therefore they should have the highest flux of low-energy emission. The limits on transient low-energy emission obtained for these two strong bursts therefore represent definitive limits on the entire GRB population (again, assuming standard candles). The lack of faint optical and radio emission from the direction of GRB 940301 with a time-delay of only 7 hours is the most constraining observation. The best previous optical measurements with similar time delays (i.e., serendipitous exposures) have only been able to reach magnitudes corresponding to $m_V = 6-7$ (Greiner *et al.* 1994) and the quickest prior deep observation ($m_V \approx 16$) was obtained with a delay of ~ 12 hours (Castro-Tirado *et al.* 1994b). In gamma rays, GRB 940301 had a *time-averaged* energy flux (0.75–30 MeV) of $\sim 8 \times 10^{-7}$ erg cm $^{-2}$ s $^{-1}$ (see Chapter V), whereas the optical flux limit corresponding to $m_V = 16$ is $\sim 1.4 \times 10^{-12}$ erg cm $^{-2}$ s $^{-1}$. Thus, the fading optical energy flux after a delay of 7 hours was a factor of at most 1.7×10^{-6} that observed in gamma rays during the ~ 42 s burst. In radio, the energy flux of fading emission 7 hours after this burst must be less than $\sim 3 \times 10^{-16}$ erg cm $^{-2}$ s $^{-1}$ (corresponding to the sensitivity limit of 0.2 Jy at 151 MHz) or less than a factor of 3.8×10^{-10} of

the MeV emission observed during the burst. These results should be compared to the most rapid sensitive radio observations performed in the past, that resulted in similar sensitivity limits (~ 0.1 Jy at 151 MHz), but were obtained with a delay of 2 days (Koranyi *et al.* 1994).

Many GRB models make some prediction of the amount and timing of optical and radio emission that is expected either from the quiescent burst source, or as a result of the burst, itself. In some models, the optical and/or radio emission is expected to be delayed and/or fade on a time-scale longer than that of the gamma-ray emission, while in others the low-energy flux is only briefly transient or non-existent. The wealth of different burst models and unknown source distance makes it difficult to test these predictions with the data. Below, some predictions of broadly categorized burst models are discussed.

For burst source scenarios within the Galaxy, the long-favored source object is a neutron star. Although the basis for Galactic neutron star models is now somewhat tenuous (e.g., Hartmann *et al.* 1994b), these models do provide insight into the physical processes that can produce transient low-energy emission associated with gamma-ray bursts. If bursts do originate from Galactic neutron stars, then there is a good chance that the neutron star will be in a close binary system with a stellar companion. In this scenario, the prodigious flux of gamma radiation during a burst would interact in the atmosphere of the nearby companion object and could be converted into low-energy emission via repeated Compton scattering. London & Cominsky (1983) and London (1984) showed that the reprocessing of a gamma-ray burst in the surface layers of a nearby companion star could produce a transient low-energy (UV through IR) burst with time delays of ~ 10 s to 10 min, depending on the details of the binary system and the burst fluence. If the source were close enough (say, within 1 kpc), the reprocessed low-energy emission from a typical burst would be observable with $m_V \approx 12$. One problem in this scenario is the fact that we should observe the companion object in quiescence. Rappaport & Joss (1985) suggested this problem could be overcome if the companion object were a dark star whose mass ($M \leq 0.06 M_\odot$) has been slowly lost through transfer to the neutron star. Melia, Rappaport & Joss (1986) performed numerical simulations of such systems and found that reprocessed optical bursts from a small-

mass companion star could produce an observable signal (most emission in the optical blue-band) with time-delays of several minutes if the sources are within ~ 100 pc. Furthermore, they point out that lower energy V , R and IR emission could have a significantly longer delay, perhaps longer than 10 min for very strong bursts. A different optical burst mechanism involving binary systems was suggested by Tremaine & Zytlow (1986) wherein comet impacts on white dwarf companion stars causes observable optical/UV bursts that are *uncorrelated* with gamma-ray bursts. With, or without a companion object, low-energy bursts could also result from reprocessing in an accretion disk around the neutron star (Epstein 1985b; Melia 1988, 1989). The lack of expected quiescent IR emission from viscous heating in the disk is a problem in this model unless one starts with a “cold” disk made primarily of degenerate electrons. Epstein (1985b) noted that most of the emission from disk reprocessing should be in the X-ray/EUV regime, but it is possible that significant amounts of radiation could be degraded to the optical range if the disk is large enough ($>10^{12}$ cm). In this case, the time-scale for reprocessed emission would also be longer, perhaps ~ 1 hour. Unfortunately, none these models make any detailed predictions of the optical flux that is expected after time delays of several hours. Thus, although such emission is possible in these scenarios, the null observations do not constrain the models.

If, as is expected in many models, GRBs originate on highly magnetized ($B \sim 10^{12}$ G) neutron stars, other low-energy transient emission mechanisms are plausible. Hartmann, Woosley & Arons (1988) and Woosley (1984) have suggested that IR, optical and UV emission could result from thermal cyclotron reprocessing in the atmosphere of a strongly magnetized lone neutron star. In this model, plasma electrons are energized by the GRB via Compton scattering, then the electrons radiate in the optical via cyclotron emission in the strong field. The resulting luminous flash in the IR to UV spectral range coincides essentially with the GRB, decays on a similar time-scale and could be observable above $\sim 9^{\text{th}}$ magnitude if the sources are within ~ 1 kpc. No significant X-ray or radio emission is expected (partly due to the choice of model parameters) and little or no observable quiescent emission is predicted. Schaefer *et al.* (1989) make the analogy that if GRBs are associated with highly magnetized neutron stars, it might be reasonable to

assume that, like other neutron star sources (e.g., pulsars), they may emit significant radio synchrotron radiation. They noted that the lack of quiescent radio emission from several well-localized bursts means that either the radio emission (if it exists) is transient or for some reason it is obscured from our view (e.g., due to beaming or absorption by ionized matter around the source). The lack of fading radio sources within hours in the localizations of GRB 940217 and GRB 940301 indicates that transient radio emission must be very short-lived (if it exists at all and is observable). Eichler & Cheng (1989) have suggested that *slow* transient emission could be produced if the energy released during a GRB is deposited onto the surface of the neutron star (e.g., due to a “crustquake” or thermonuclear explosion). Thermal afterglow mainly in soft X rays and UV following the large energy release on the NS surface could last for several hours due to the low thermal conductivity of the outer neutron star crust. However, if the energy release is too deep within the crust, the thermal afterglow will last for years. It is unclear in this model how much optical emission is expected, but the lack of an optical afterglow within hours is certainly constraining.

If a significant optical/UV flash accompanies GRBs, as suggested by the reprocessing and thermal afterglow models discussed above, neutral material surrounding the source will be ionized. If the density of the ambient material and UV flux are both sufficiently high, the ionized region may emit an observable flux of atomic line recombination radiation. Jennings (1983) and Band & Hartmann (1992a, 1992b) considered the photoionizing effect of bright optical/UV flashes that might be associated with GRBs on ambient clouds of (primarily) neutral hydrogen (atomic or molecular). They concluded that for reasonable Galactic disk (or even halo) burst source scenarios, $H\alpha$ emission (as well as other atomic lines) fading on time scales of several hours to years could be detectable if the density of ambient material around the source is more than about 10^4 cm^{-3} . However, the presence of dust in the ambient clouds could absorb much of the recombination radiation. While the observations presented in this chapter were not optimized to detect line emission, they were sensitive to variations of the broad-band optical flux containing the lines. If the line emission is intense enough, the broad-band flux would also be enhanced.

The lack of transient optical emission constrains the amount of UV flux associated with GRBs, the density of ambient material surrounding GRB sources and the dust content in the ambient material.

In many GRB scenarios that place the sources at distances outside the Galaxy, some sort of optically-thick fireball mechanism is necessary due to the required large energy release on short time-scales. This is true of both cosmological and Galactic halo models that involve either the collapse of a compact object or the merger of a compact binary (e.g., Paczynski 1986; Woosley 1993). Recent work on the fireball energy release mechanism has shown that broad-band emission extending from optical to TeV energies is expected from the shock wave(s) that form when the expanding fireball outflow reaches an external medium such as a cloud of neutral gas (Mészáros & Rees 1993b; Mészáros, Rees & Papathanassiou 1994; Katz 1994a). Depending on the specific nature of the shock and the external medium (e.g., density, magnetic field, baryonic content, Lorentz factor of the expanding flow, etc.), these models generally predict transient emission that decays on time-scales similar to the gamma radiation (i.e., $\sim 1\text{--}100$ s). However, as the shock propagates through the external medium its constituent particles could dissipate their energy through synchrotron and/or inverse Compton emission. This would result in a significant amount of delayed, slowly fading low-energy emission with the peak energy evolving from gamma rays at the initial contact down to radio frequencies at the final stages. The delay expected for emission in the optical range is short: typically a few minutes. However, emission at radio and microwave frequencies can have a considerable delay and a similarly large time-scale for decay. Paczynski & Rhoads (1993) and Katz (1994a, 1994c) have considered the final stages of fireball evolution, where significant delayed radio emission is expected. Assuming reasonable parameters describing the fireball and the external medium, Paczynski & Rhoads (1993) have shown that the strongest bursts at cosmological distances could produce observable long-duration radio pulses that, for frequencies $\nu \sim 1$ GHz, peak at ~ 0.1 Jy after a delay of about 10 days. The duration of the pulse (FWHM) is expected to be about twice as long as the delay—offering a good chance for observation. The time-delay and peak energy density scale as $\nu^{-3/2}$ and $\nu^{5/8}$,

respectively, so that the expected pulse gets longer and weaker at lower frequencies. This model can also be applied to sources in the Galactic halo, where the smaller source distance results in shorter time delays and higher fluxes. The lack of a time-variable radio signal in the repeated 1.4 GHz observations of GRB 940301 performed by Frail *et al.* (1994) are particularly constraining, since according to this model, we would have expected (assuming a cosmological source distance of ~ 0.5 Gpc) a 3.6 mJy radio pulse delayed by ~ 28 days that should have been observable. For Galactic halo sources, the observations of GRB 940217 obtained at 151 MHz within 17 hours of the burst are constraining since we would expect an observable pulse to be reaching its maximum intensity near the detectable level at that time. If the fireball model is correct, the failure to identify transient radio pulses in these cases suggests that the underlying assumptions need to be adjusted. For instance, both the time-delay and peak flux depend on the assumed particle density of the ambient material (taken to be 10^{-24} cm $^{-3}$). Frail *et al.* (1994) suggested that a lower density might be reasonable to assume, in which case the null-observations would be more consistent with the model predictions. Another possibility noted by Paczynski & Rhoads (1993) is that the fireball could be strongly beamed, in which case the peak radio power is lowered by several orders-of-magnitude—making the delayed pulses undetectable. Given the flexibility of the fireball model, the remaining radio observations of GRB 940217 and GRB 940301 obtained at different frequencies and at different time delays further constrain the physics. However, there are still considerable gaps in both temporal sampling and sensitivity. Future observations could further constrain this model, or perhaps even detect a delayed radio pulse.

VII. SUMMARY AND CONCLUSIONS

In recent years, the most important observational constraints governing our understanding of gamma-ray bursts have been the limits on their spatial distribution interpreted from BATSE observations. While these large-scale measures have provided much insight into the global properties of the burst source distribution, they have not led to a solution of the burst problem. In particular we have not made any significant progress in identifying a likely source object. Rather, the large-scale observations of BATSE have created a new dilemma by apparently requiring the bursts to originate from a distribution of unknown objects that are either very nearby or very far away. The raging debate over whether bursts are Galactic or extragalactic in origin is unlikely to be solved by continued refinement of the measures of large-scale structure, in part because the conclusions drawn from these observations are biased by our interpretation of bursts as a single population of sources. In the post-BATSE study of gamma-ray bursts, several fundamental observational questions remain. In particular, there is little information on the properties of burst emission at high and low energies and we lack an understanding of the small-scale distribution of sources. Such information could be critical in determining the origin of bursts. The work presented here has attempted to address some of these fundamental questions using the unique burst observations provided by COMPTEL.

The burst localizations obtained through direct COMPTEL imaging independently confirm the well known result that the directions of strong gamma-ray bursts are consistent with an isotropic distribution of sources. The constraints on distance obtained from the combination of COMPTEL and IPN localizations indicate that these strong bursts cannot originate from the inner heliosphere within a distance of ~ 100 AU. Combined with the BATSE constraints on the spatial distribution of sources, this finding makes it difficult to explain bursts with *any* of the suggested nearby (< 1 pc) source scenarios. Adopting the simplest interpretation of large-scale spatial distribution measures, this leaves either a source distribution in the Galactic halo or at

cosmological distances. The difference between these two possibilities in terms of theoretical source scenarios is ambiguous, but one way to decide may be through the study of burst recurrence. Repeating bursts are difficult to explain in the most-favored cosmological compact object collapse and binary merger models. The COMPTEL observation of a spatially-coincident burst pair is suggestive that perhaps at least some bursts repeat. While, the single observation presented here is not a conclusive measurement, future COMPTEL burst observations may solve this particular problem. For instance, a future sample composed of ~ 40 – 50 COMPTEL or COMPTEL/IPN burst localizations will conclusively show whether or not most bursts repeat on time-scales of months and constrain the fraction of repeating sources.

The COMPTEL measurements of burst spectra have confirmed the earlier *SMM* findings that above ~ 1 MeV, the spectra are well-described by a simple power law model with no indication of a significant turnover. Although simple thermal models with curvature can also adequately describe the spectra of some individual bursts, they are not consistent with the full COMPTEL burst sample. When the COMPTEL spectra are compared to BATSE and EGRET results, a new wide-band view of burst energetics emerges: bursts exhibit a variable spectral turnover or break in the BATSE energy range around a few hundred keV, but are then well-described by a simple power law out to at least hundreds of MeV. The rapid variability of this high-energy power law emission tail measured by COMPTEL provides the most significant constraint on cosmological burst models due to pair production effects. The COMPTEL data indicate that if the sources are farther than ~ 1 kpc, significant beaming and/or bulk relativistic motion is required. These results are consistent with the predictions of current mainstream cosmological burst scenarios, but provide important constraint. A major new question addressed in this work is the unknown temporal relation between MeV and GeV burst emission. Many earlier studies have assumed that GeV emission is as rapidly varying as that at MeV and keV energies, but as we have seen this is not necessarily the case. Future observations need to address this important point. If burst emission at GeV energies is highly variable and/or delayed with respect to that at lower energies, important new constraints would be imposed on theoretical models. Collaboration between

BATSE, COMPTEL and EGRET for future bursts should help to resolve this question.

One of the few relatively unambiguous ways to solve the burst problem would be the identification of a low-energy counterpart. This undeniable fact has long been recognized, but unfortunately, counterparts remain elusive—suggesting that they are weak and/or short-lived. The Rapid Burst Response system, exploiting COMPTEL's unique burst localization capability, has attempted to address this point by searching for fading optical and radio counterpart emission sooner and deeper than all previous attempts. The failure of this program to detect fading optical and radio counterpart emission on time-scales of hours with high sensitivity indicates that if bursts emit any radiation at all at low energies, it is very faint and/or very short-lived. The upper limits on fading emission obtained with this program are an order-of-magnitude lower than previous efforts. The lack of fading counterparts could be used to argue in favor of cosmological models (by virtue of the large distance). However, we have far from exhausted the possible sensitivity and time-scale domains for low-energy burst emission. Clearly, future observational efforts must concentrate on performing faster, deeper searches than those presented here. Such capability is the goal of a refined COMPTEL Rapid Response program, which will allow deep observations to be performed with a delay of only ~10–15 min.

While the COMPTEL results have not solved the burst mystery, they have provided insight into some of the most fundamental questions and point the way for future observations. For example, to study the question of burst recurrence in detail requires a good sample of arc-minute localizations; the study of burst spectra requires more simultaneous wide-band observations (especially at low and high energies and preferably with higher sensitivity and better energy resolution) and counterpart searchers should concentrate most heavily on obtaining rapid, deep observations. Some of these capabilities are within the scope of future COMPTEL observations, but others await new instrumentation such as the upcoming High Energy Transient Explorer (HETE) mission, which will provide rapid, accurate burst localizations and will perform simultaneous observations in the EUV and gamma rays (Ricker *et al.* 1992).

APPENDICES

APPENDIX A

COMPTEL GAMMA-RAY BURST CATALOG

The following figures show the fundamental properties of each of the COMPTEL gamma-ray bursts analyzed in this work. Each figure shows three plots for a single burst: (a) the intensity-time profile of telescope events, (b) the maximum-likelihood source localization and (c) the deconvolved photon number flux–energy spectrum. The bursts are arranged chronologically and are identified by the burst date (*GRB yymmdd*, where *yymmdd* are the year, month and day of the burst, respectively). More detailed information (Chapters III–V) and a description of the analysis techniques and procedures (Chapter II) can be found in the text. Only summary descriptive information is given here.

Intensity-Time Profiles. The COMPTEL “lightcurve” of each burst was determined by binning the observed telescope events in time (not corrected for instrument deadtime), before and after the BATSE burst trigger. Bin-sizes (indicated by the vertical axis labels) have been determined arbitrarily and do not reflect the accuracy of COMPTEL timing measurements (events are time-tagged with 125 μ s accuracy). Relaxed data selections were applied to accumulate as many events as possible while preserving good signal-to-noise. These selections include [$110 \leq \text{TOF} \leq 130$], [$0 \leq \text{PSD} \leq 110$] and [$-10^\circ \leq \text{ARM} \leq +10^\circ$] (around the most-likely burst position; Table 4.1). No energy or $\bar{\varphi}$ selections were applied, thus the lightcurves include events whose total energy deposits range from the low-energy in-flight threshold of ~ 650 keV to above 30 MeV.

Localizations. Each of the COMPTEL bursts was localized using the maximum-likelihood imaging technique described in the text. Statistical source location constraints were determined by computing smoothed contours of the log-likelihood-ratio skymaps at levels corresponding formally to 1σ , 2σ and 3σ confidence. The burst location constraints are plotted in Celestial coordinates (epoch J2000.0) and are identified by three concentric contours (1σ being the

innermost contour, then 2σ , etc.). For reference, a circle (thick-line) corresponding to the average 1σ area of all the COMPTEL bursts (radius $1^{\circ}12'$) is plotted in each sky-map. Where available, Interplanetary Network triangulation annuli (references are given in the figure captions) have been overlaid on the COMPTEL localizations. Two concentric arcs are plotted for each IPN localization, the separation between the arcs being representative of the $\sim 3\sigma$ uncertainty in the width of the annuli.

Energy Spectra. Photon number flux–energy spectra were determined through direct inversion of the observed counts integrated over the full duration of each burst using the vector response method described in the text. Integration time-intervals were chosen so as to include at least all significant emission observed by COMPTEL. In some cases the intervals were expanded slightly to match those of other experiments (see Chapter V). Each integrated count-spectrum was originally combined into 15 logarithmically-spaced energy bins in the range 0.75–30 MeV. Low-significance bins have been combined, starting at the highest observed energy bin, until a $\geq 2\sigma$ excess above background was achieved. In some cases in order to avoid very large bins the second-highest energy bin was used as a starting point. The deconvolved fluxes are plotted with diamond symbols and error-bars representing 1σ statistical uncertainties in the flux and the bin-size in energy. Spectral fitting was performed using the Cash-statistic as described in the text. The best-fit single power law model to each spectrum is shown in the plots as a dotted line. Model-dependent upper limits in bins containing zero counts are denoted by points with no upper flux error bar and a downward arrow. These upper limits were computed by evaluating the standard deviation (1σ) of the counts predicted by the best-fit model spectrum in each bin and dividing by the energy response in that bin. Low-significance data points ($< 2\sigma$) are plotted with an upper flux error-bar and a downward arrow.

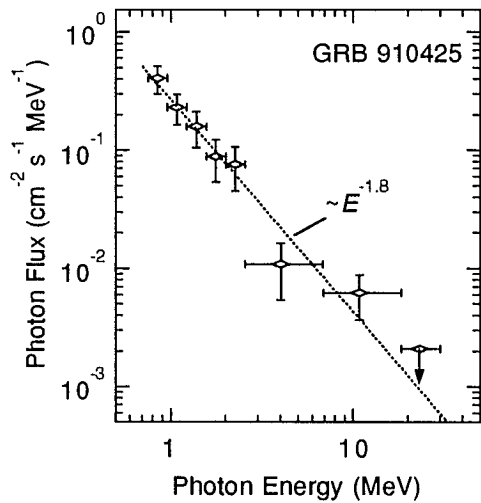
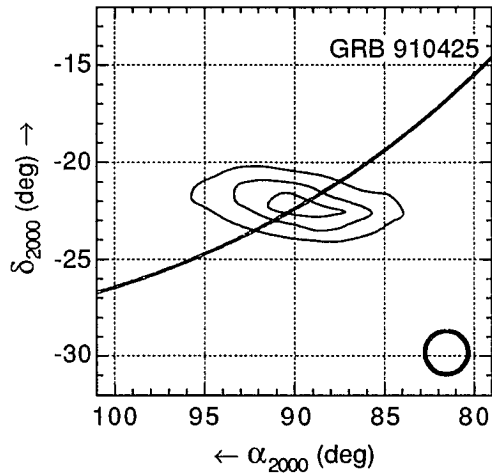
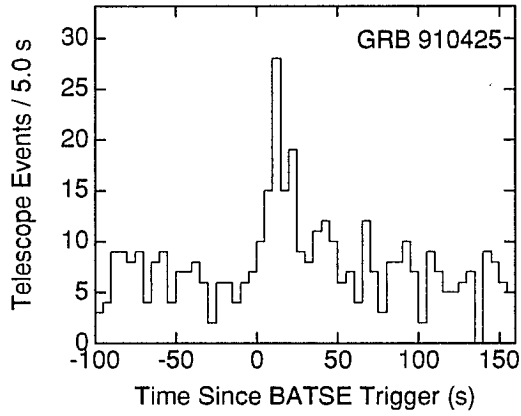


Fig. A.1. GRB 910425 (IPN localization from Hurley *et al.* 1994a).

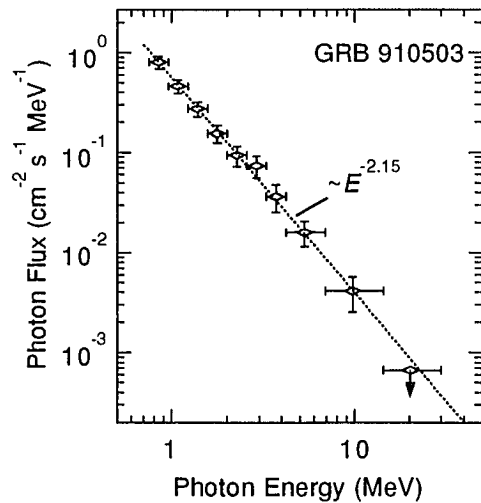
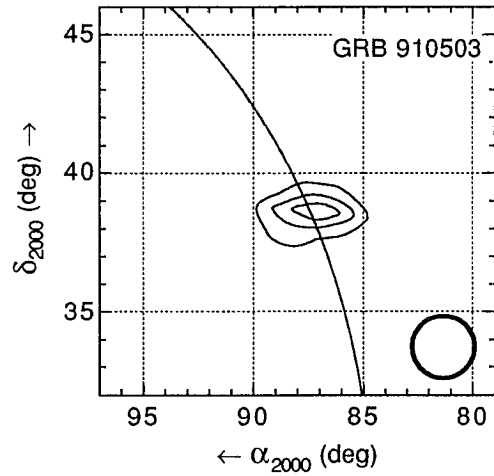
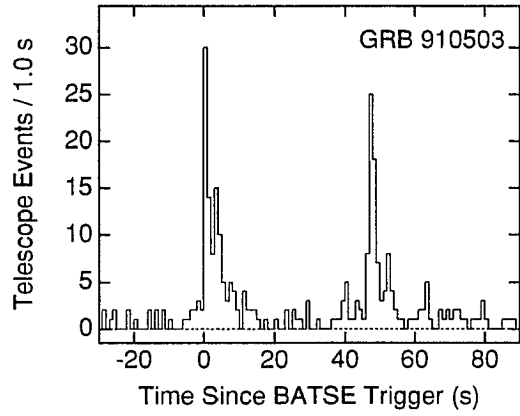


Fig. A.2. GRB 910503 (IPN localization from Hurley *et al.* 1994a).

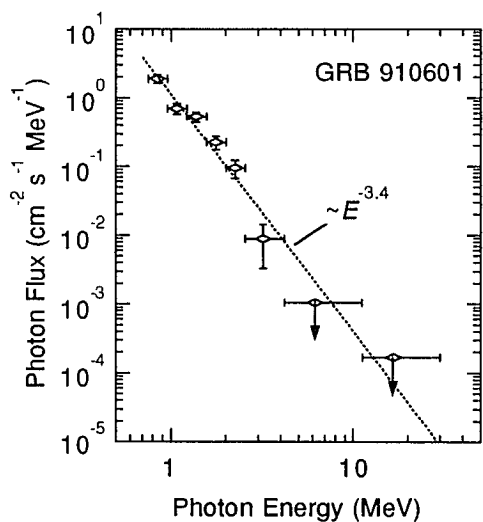
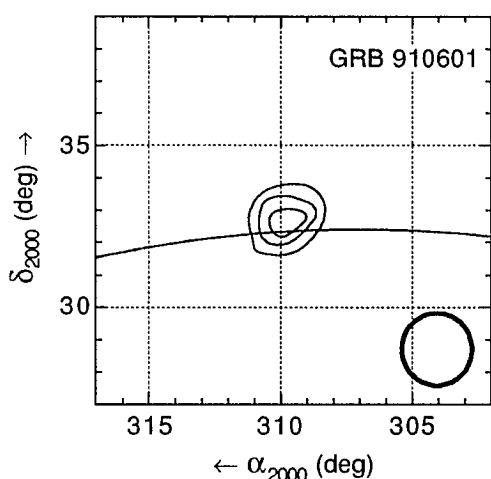
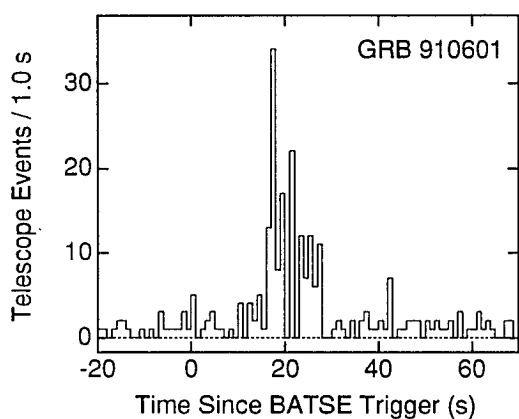


Fig. A.3. GRB 910601 (IPN localization from Hurley *et al.* 1994a).

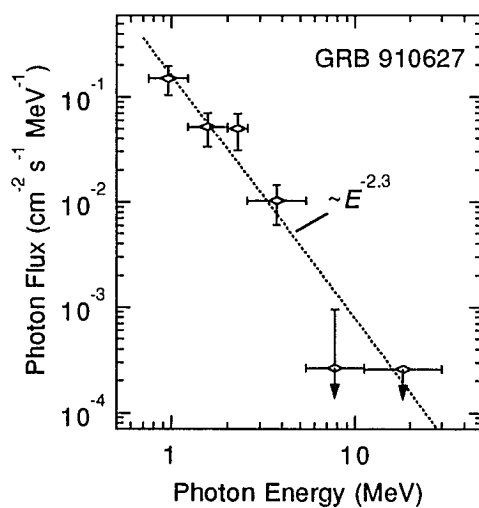
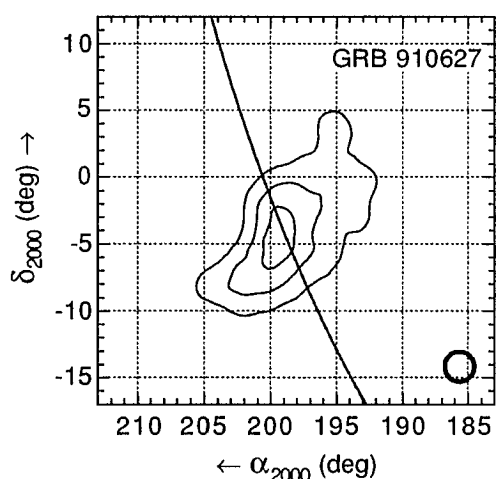
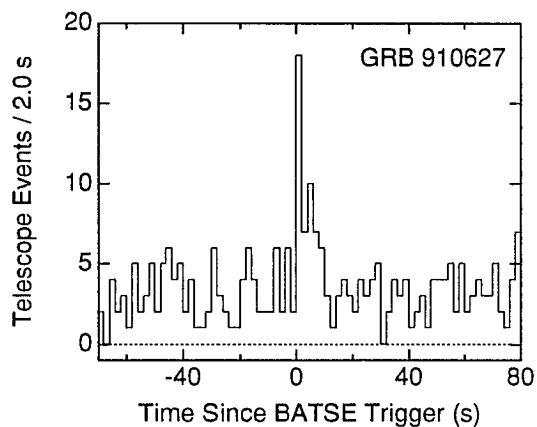


Fig. A.4. GRB 910627 (IPN localization from Cline *et al.* 1993).

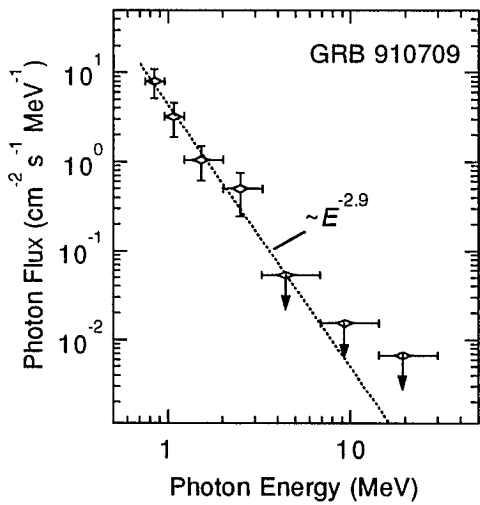
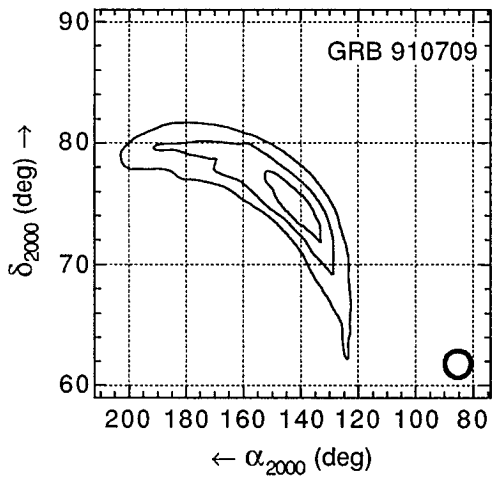
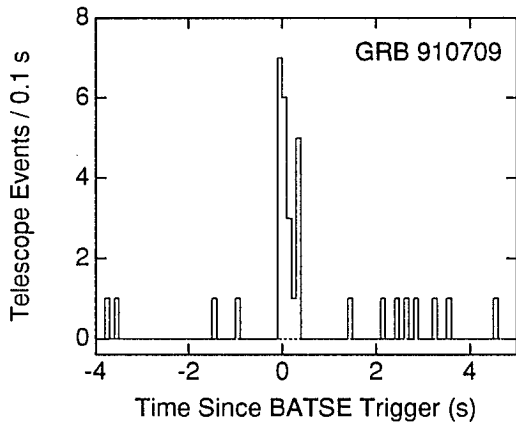


Fig. A.5. GRB 910709 (IPN localization is unavailable for this burst).

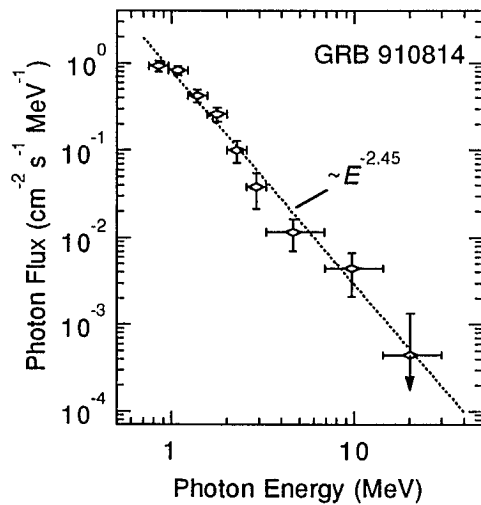
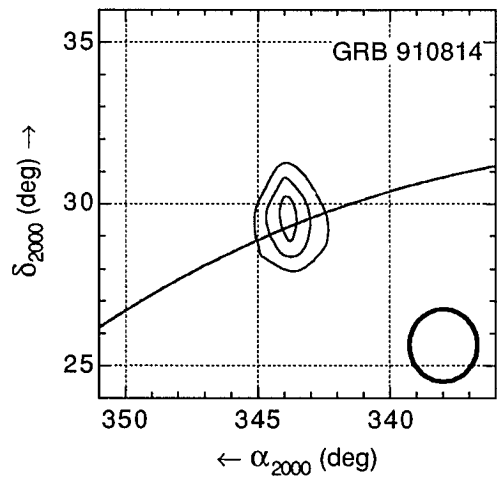
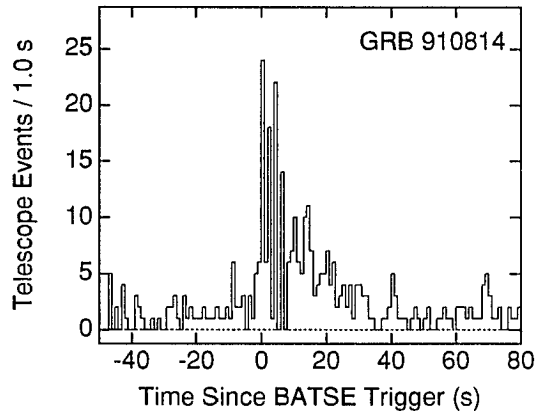


Fig. A.6. GRB 910814 (IPN localization from Cline *et al.* 1993).

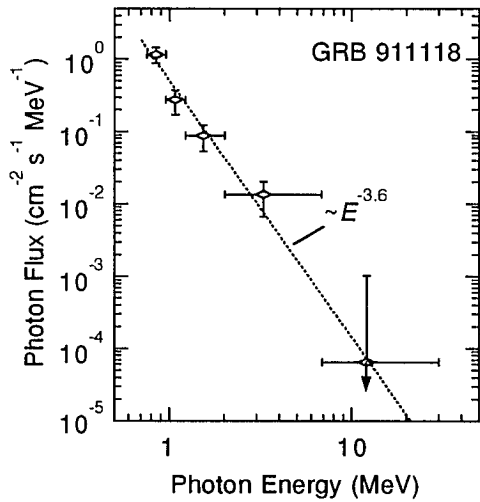
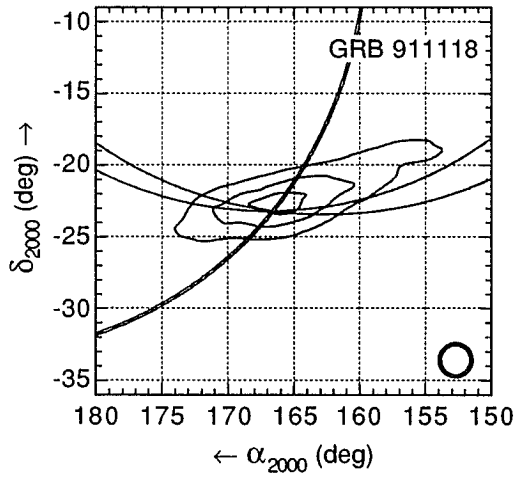
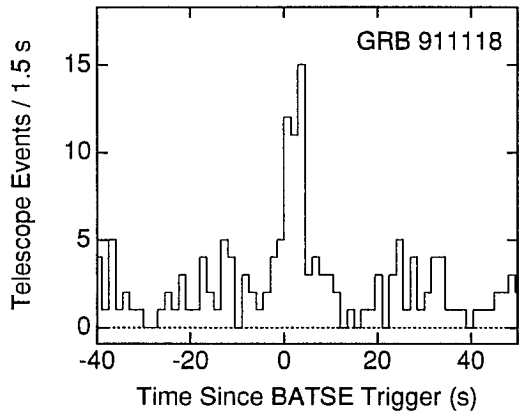


Fig. A.7. GRB 911118 (IPN localization from Cline *et al.* 1993).

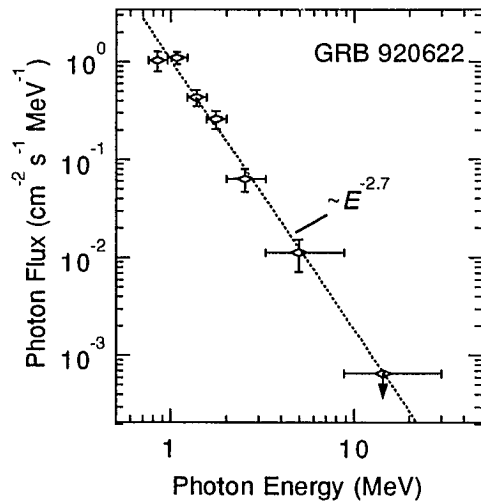
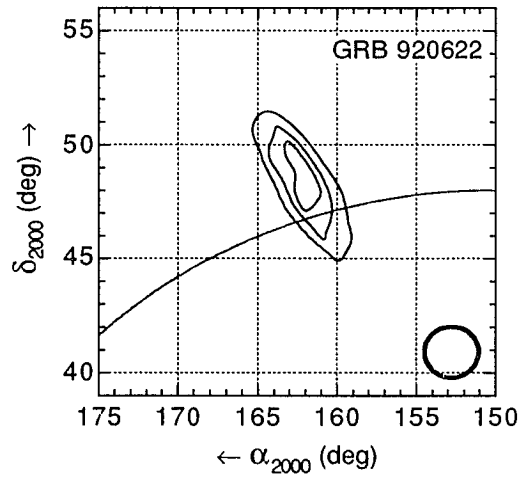
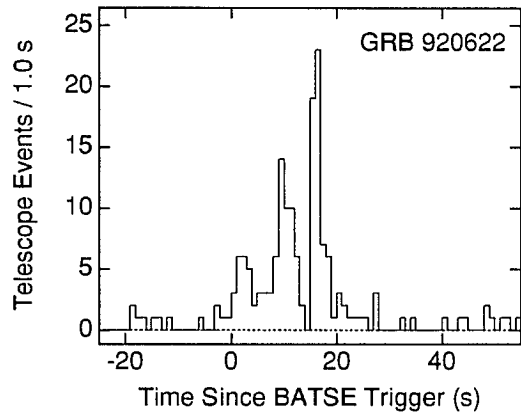


Fig. A.8. GRB 920622 (IPN localization from K. Hurley, private communication).

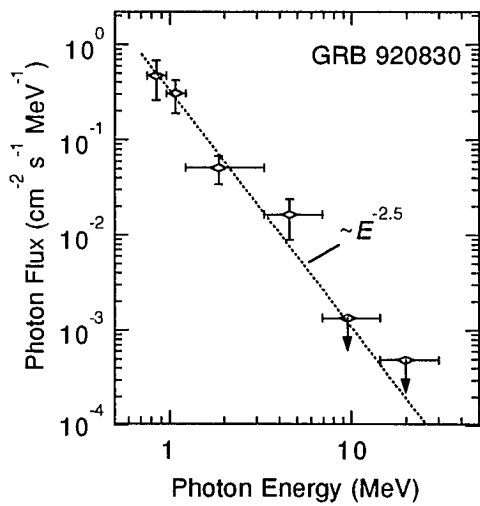
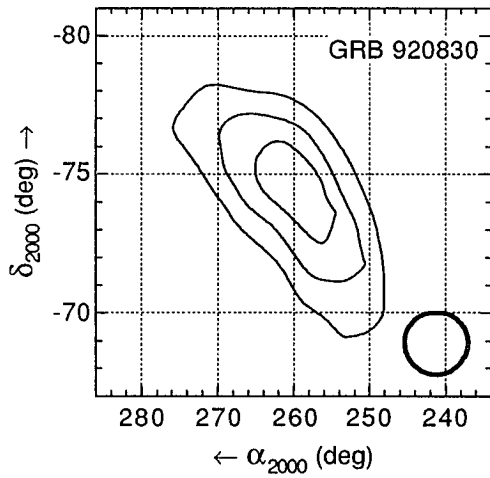
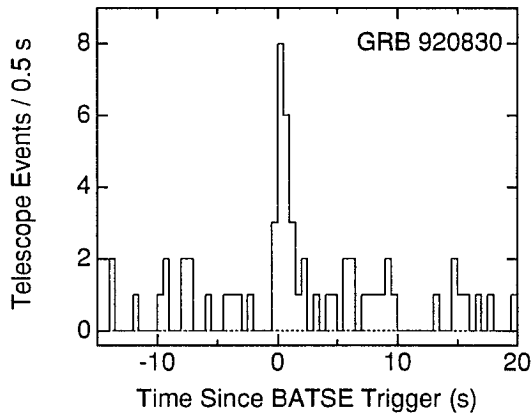


Fig. A.9. GRB 920830 (IPN localization is unavailable for this burst).

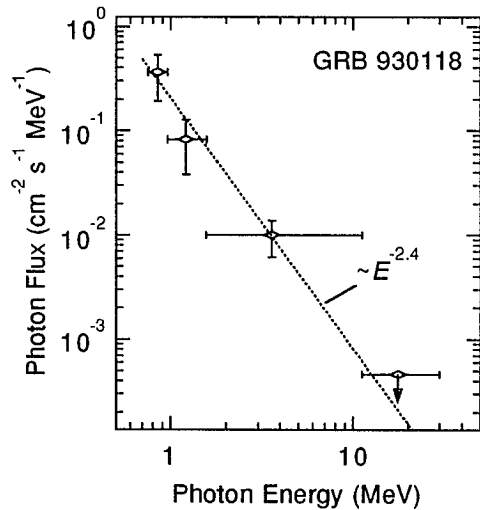
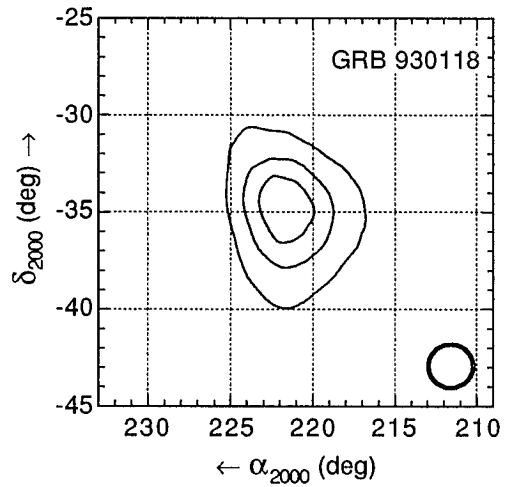
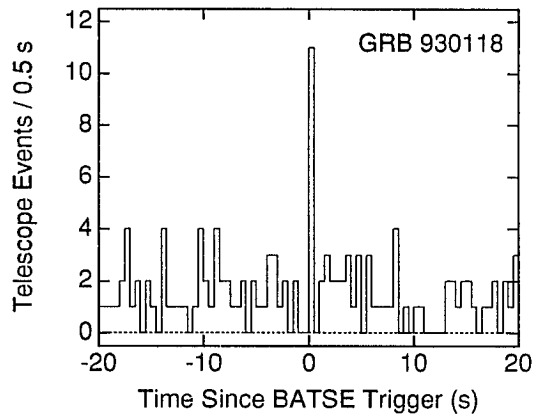


Fig. A.10. GRB 930118 (IPN localization is unavailable for this burst).

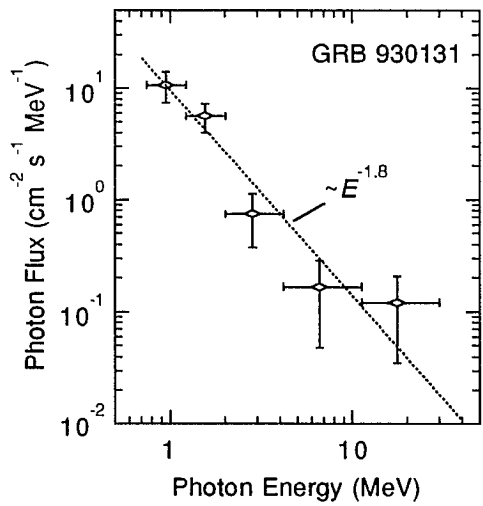
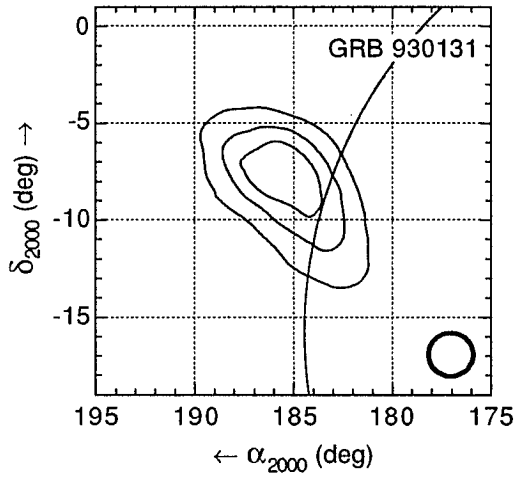
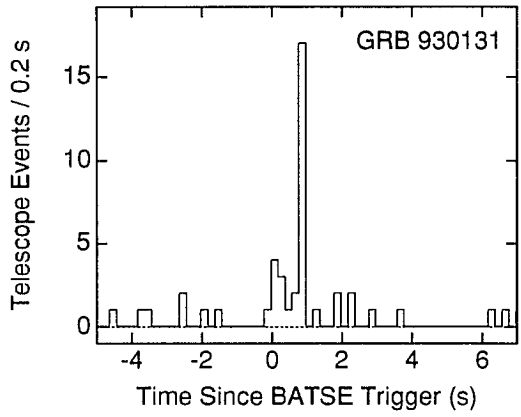


Fig. A.11. GRB 930131 (IPN localization from Hurley *et al.* 1994b).

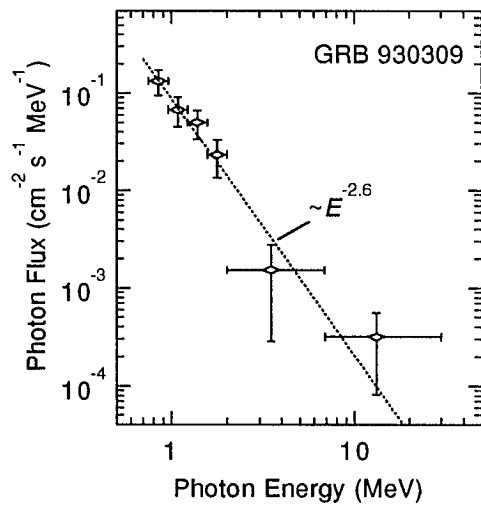
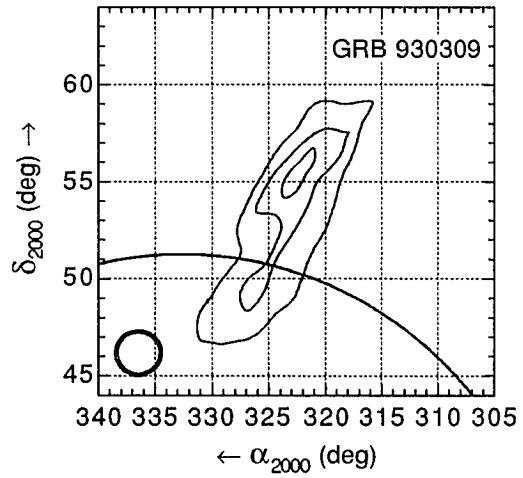
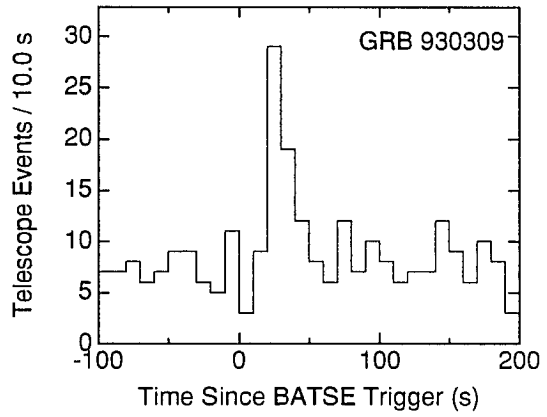


Fig. A.12. GRB 930309 (IPN localization from K. Hurley, private communication).

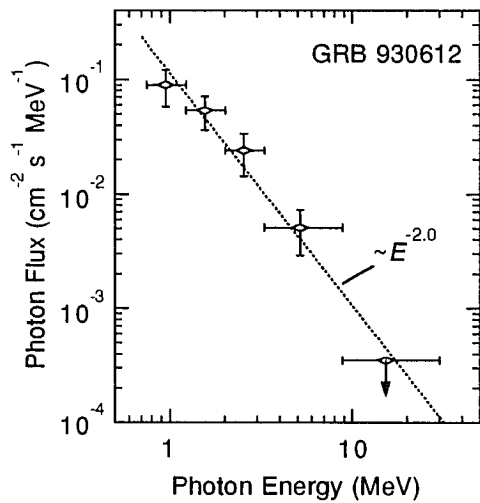
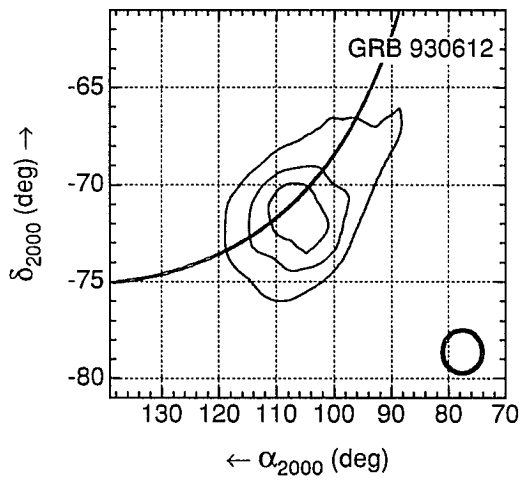
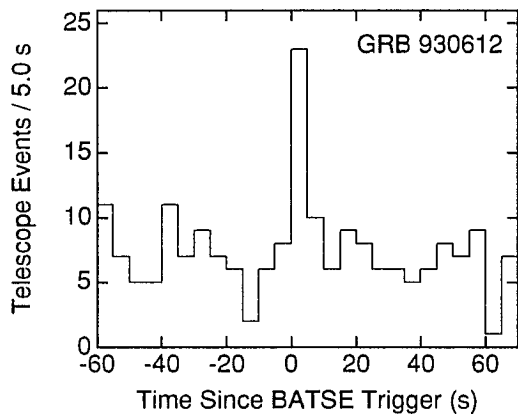


Fig. A.13. GRB 930612 (IPN localization from K. Hurley, private communication).

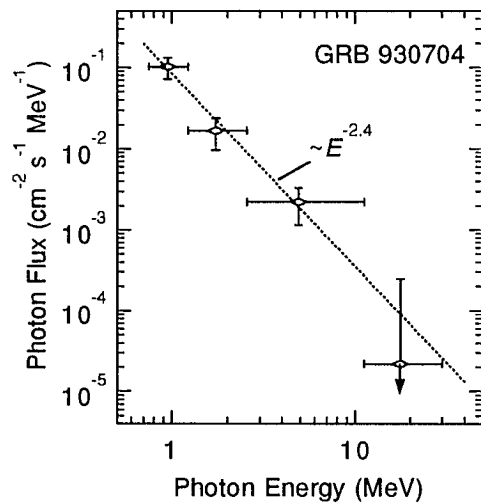
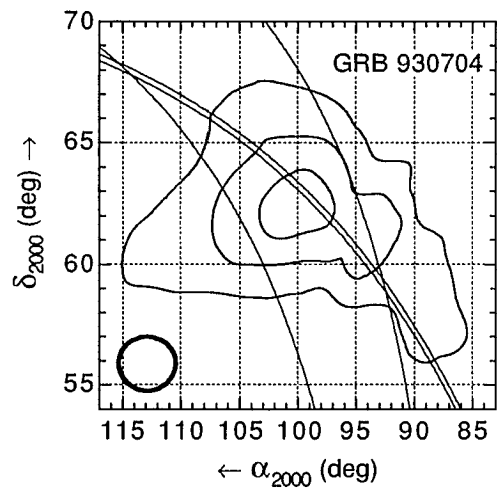
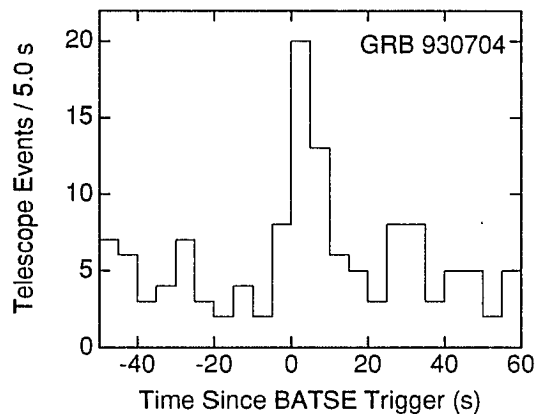


Fig. A.14. GRB 930704 (IPN localization from K. Hurley, private communication).

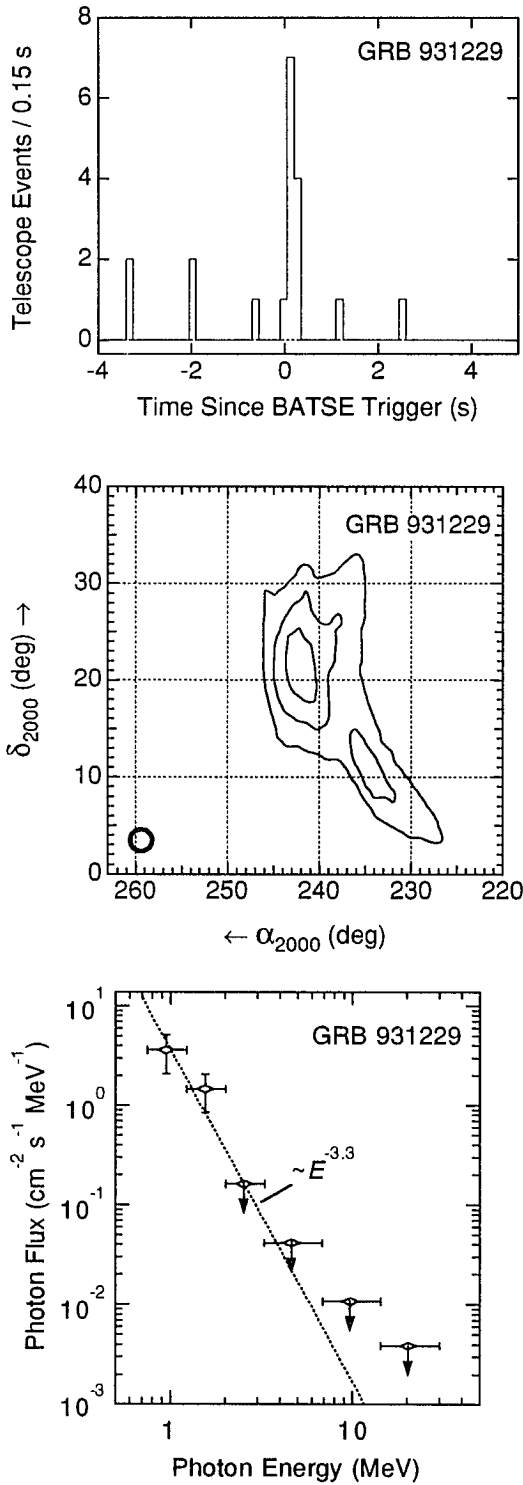


Fig. A.15. GRB 931229 (IPN localization is unavailable for this burst).

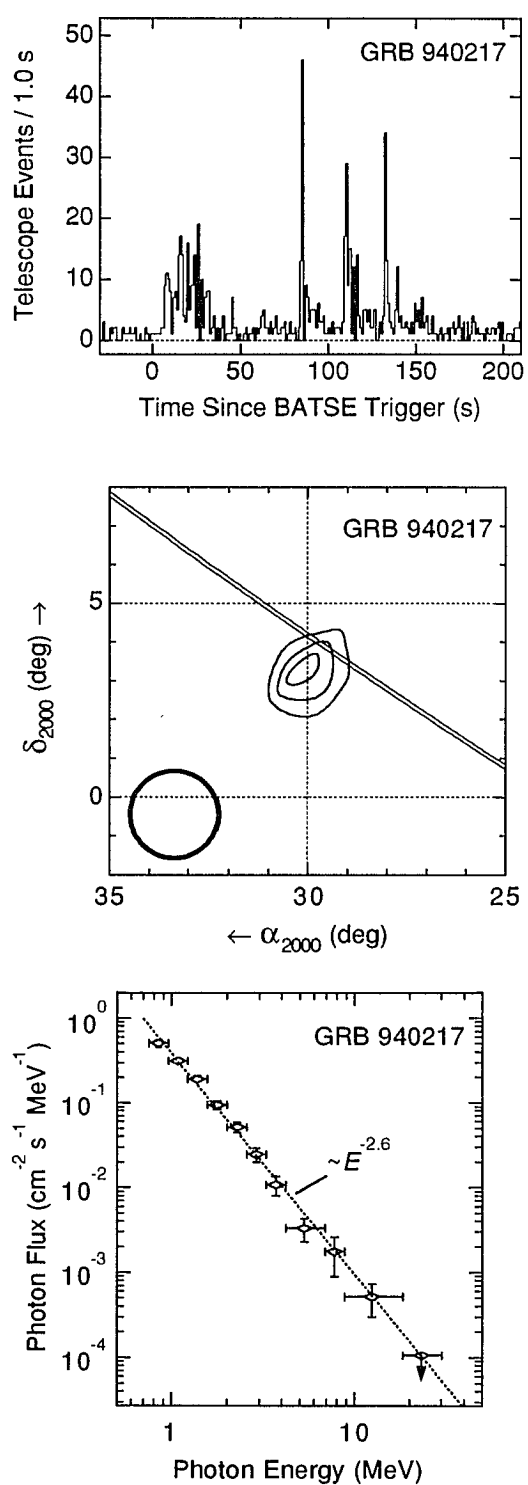


Fig. A.16. GRB 940217 (IPN localization from Hurley *et al.* 1994c).

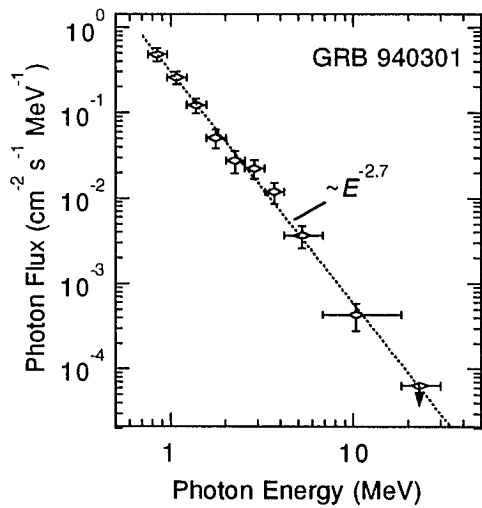
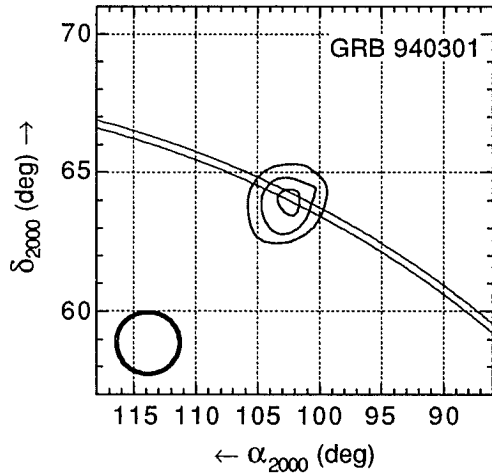
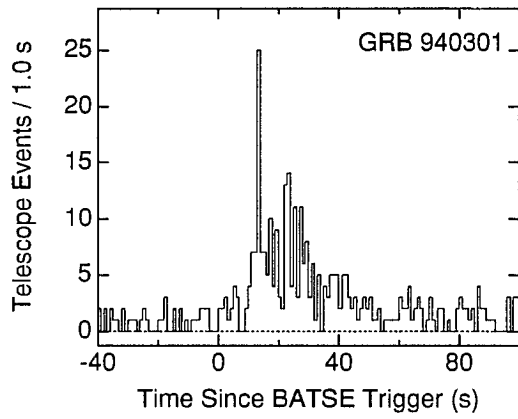


Fig. A.17. GRB 940301 (IPN localization from Hurley *et al.* 1994d).

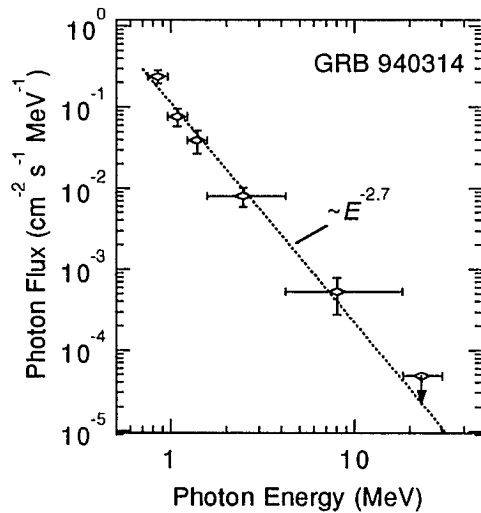
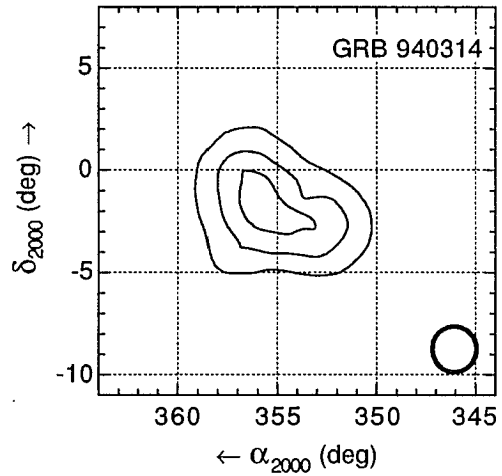
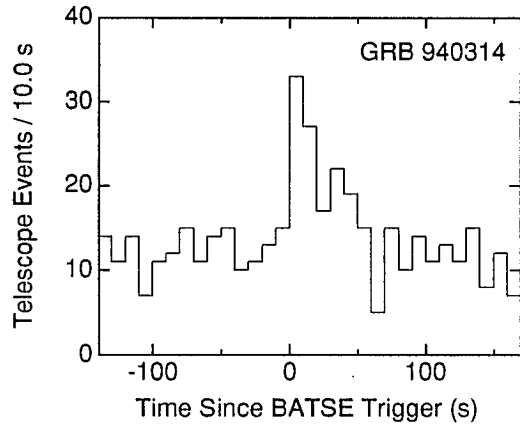


Fig. A.18. GRB 940314 (IPN localization is unavailable for this burst).

APPENDIX B

SYSTEMATIC ERRORS

Following is a discussion of the systematic errors involved in COMPTEL burst localization and spectral analysis. The analysis techniques used to derive the burst locations and energy spectra presented in the text account only for uncertainties due to random statistical fluctuation inherent in the counting-based COMPTEL measurements. Uncertainties arising from all other sources are called systematic and are present even in the limit of zero statistical error. These effects must be estimated separately. Here, the known causes of significant systematic errors are identified and an attempt is made to quantify the magnitude of their effects.

A. Systematic Burst Location Errors

As described in the text, the COMPTEL imaging process is based on several assumptions and approximations, all of which are potential sources of systematic error in the burst locations. The most significant effects are related to the definition and determination of the spatial instrument response function (PSF) and background model.

In localizing GRBs, recall that the same PSF (determined by simulating an $E^{-2.0}$ power law source at $\theta = 10^\circ$, $\phi = 0^\circ$) is used to image all bursts. This practice assumes that localization is relatively independent of source location and energy spectrum. To test the validity of these assumptions, several simulated sources with different burst-like energy spectra and positions were imaged with the maximum-likelihood technique using this same PSF. The background-free simulated sources each contained several thousand events (>10 times more than any GRB), thus minimizing statistical errors. When using the standard data-space binning (1° bins in χ , ψ and 2° bins in $\bar{\varphi}$), the simulated sources were all localized within the correct sky-bin, indicating that the systematic location error is less than 1° . To further quantify the errors, this procedure was repeated with finer binning (0.5° bins in $\varphi_{\text{geo}}(\chi, \psi)$ and 1° bins in $\bar{\varphi}$). In this case, the simulated sources with $\theta < 30^\circ$ were all located in the correct bin, irrespective of energy spectrum.

However, many of the sources more than 30° off-axis were located incorrectly by as much as 1 bin, in most cases towards smaller zenith angle. Thus, systematic location errors due to the inadequacies of the PSF appear to be less than about 0.5 in magnitude. Further quantification is impractical due to the enormous statistical requirements of a PSF with bin-size smaller than 0.5 .

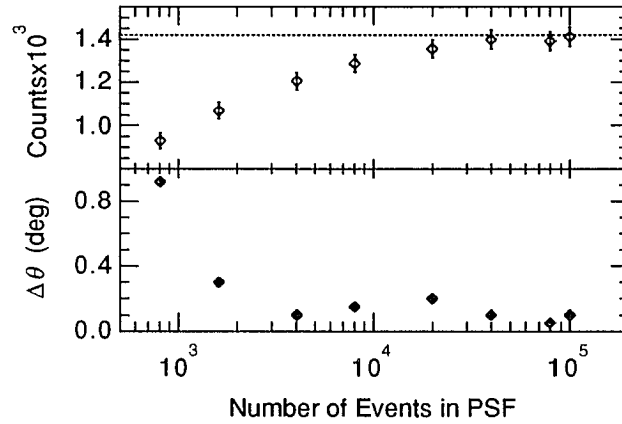


Fig. B.1. The systematic effect of PSF statistics on source localization. The measured location offset ($\Delta\theta$) and computed source counts of a simulated source are plotted as a function of the number of events contained in the PSF. The true number of source counts is indicated by a dotted line in the upper panel.

A further consideration in burst localization is the statistical coverage of the PSF. A simulated PSF with too few events is dominated by statistical fluctuations and does not accurately describe the true data-space distribution of the instrument response. The effect of PSF statistics on burst localization was estimated by imaging a simulated burst source using PSFs containing different numbers of events. In this process, the location ($\theta = 10^\circ$, $\phi = 0^\circ$) and energy spectrum ($E^{-2.0}$) of the source and PSF simulations were identical to insure that only the statistical dependence of the PSF was being measured. The locations and computed source counts (determined by the maximum-likelihood method) were significantly offset from their true values when using PSFs containing $\leq 5 \times 10^4$ events (see Figure B.1). The PSF used for burst localization contains $\sim 10^5$ events, so systematic errors of this type are minimal ($\ll 0.5$).

Since the PSF is determined through simulation, the accuracy of the simulation itself is a

potential source of systematic error. The COMPTEL simulation mass model and response characterization (e.g., Kippen 1991) have been verified through comparison with calibration data and calibration sources have been imaged using simulated PSFs. Although in general the results are favorable (location errors ≤ 0.5), the nearby source proximity and background inherent in the calibration data add additional sources of error which are difficult to separate. Similarly, imaging of 2.2 MeV line emission (i.e., known energy spectrum therefore known PSF) in strong solar flares (low background) yields location errors ≤ 0.5 .

Apart from the PSF, the other potentially significant source of systematic error in burst localization results from the definition and determination of the imaging background model. Recall that the background model used for burst localization is assumed to be only dependent on geometry in the spatial coordinates (χ, ψ) and is directly sampled in $\bar{\phi}$. The effect of these assumptions on burst localization was investigated by imaging several independent simulated burst sources (same spectrum and location as the PSF), combined with a sample of real in-flight background, employing the same type of background model as for real bursts. For each simulated source, the statistical location error was computed by measuring the effective radius of the 1σ likelihood contour (as in Chapter IV) and the location offset from the true source position was determined. Location errors (both the statistical and measured) smaller than the bin size (0.5) were estimated by interpolating the log-likelihood-ratio skymaps onto a finer grid. The results of this investigation are shown in Figure B.2, where the measured location offsets and statistical errors are plotted as a function of signal-to-noise ratio. The dashed-line in these plots is a rough estimate of the statistical location error, which is inversely proportional to the signal-to-noise. The measured errors (a combination of statistical fluctuation and inadequacies of the background model) are consistent with statistical variation *only* since there are no measurable residual systematic errors at high signal-to-noise. This investigation was repeated with different samples of in-flight background and different source positions with similar results. Thus, the imaging background model used for burst localization does *not* appear to be a significant source of systematic location error in these cases. However, each burst has unique background, so

background-induced location errors are not ruled out by this investigation.

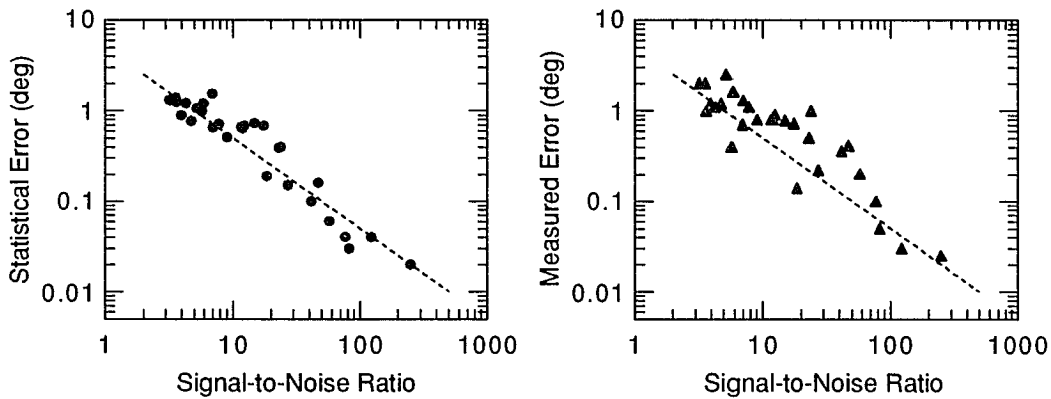


Fig. B.2. Systematic effect of background modeling on burst source localization. Statistical (left) and measured (right) source location errors are estimated by imaging simulated sources added to real background. The dashed line in each figure is a rough fit to the statistical errors.

Combining the contributions of PSF and background model inadequacies, a conservative estimate of the total systematic burst location error is 0.5° (possibly somewhat larger for bursts with $\theta \geq 30^\circ$). The only sure way to measure burst localization errors is by examining bursts which have been independently localized by other experiments. Comparison of COMPTEL locations to those of BATSE, EGRET and the IPN indicate errors which are consistent with those estimated here (statistical plus $\sim 0.5^\circ$ systematic). Unfortunately, the independent locations are all too inaccurate to allow precise quantification of the COMPTEL errors. Only one COMPTEL burst (GRB 911118) has been localized with high precision by the IPN ($\sim 1' \times 1'$; Cline *et al.* 1993) and its location is consistent within the COMPTEL statistical (1σ) uncertainty.

B. Systematic Errors in Spectral Analysis

The causes of systematic errors in spectral analysis are similar to those involved in localization. However, energy spectra are more sensitive to systematic effects because accurate normalization is important (whereas it is only used to estimate significance in imaging). The assumptions that go into the definition and determination of the energy response and background model are potential sources of significant error. Again, simulation is used to measure the

magnitude of these systematic effects. Additional problems are encountered with strong bursts due to uncertainties in determining the instrument lifetime.

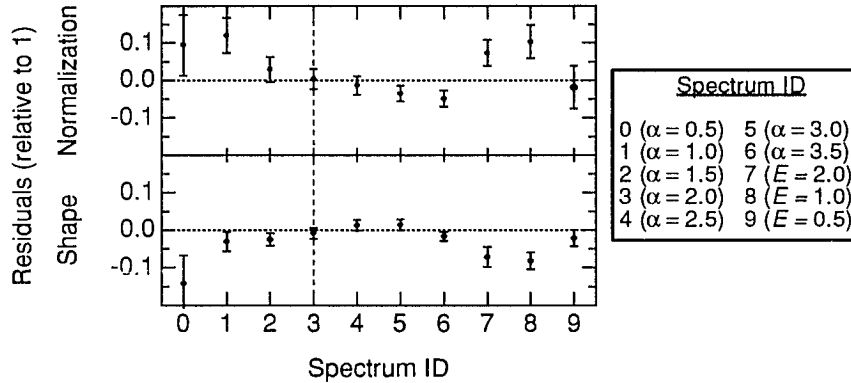


Fig. B.3. The systematic effect of assumed response spectrum on deconvolution. Different simulated spectra (denoted by Spectrum ID) were deconvolved using the same response vector with assumed $E^{-2.0}$ power law spectrum (vertical dashed-line). Error-bars represent 1σ statistical uncertainties in the spectral shape and normalization fit-parameters.

The energy response vector technique used for spectral deconvolution and parameter estimation as described in the text is a potential source of significant error since response vectors are known to depend on (a) assumed spectral shape, (b) statistical coverage, (c) source location and (d) validity of the COMPTEL simulation.

The dependence of spectral deconvolution on assumed spectral shape was estimated by deconvolving simulated sources (no background) with different burst-like energy spectra using a single response vector (assumed $E^{-2.0}$ power law spectrum). The simulated sources were at the same location ($\theta = 10^\circ$, $\phi = 0^\circ$) as the response vector and each source contained several thousand events (>10 times more than any GRB). Each spectrum was fit to the appropriate model using the Cash statistic as explained in the text. Residual normalization and spectral shape fit parameters are plotted in Figure B.3, where the true spectral shapes of the simulated sources are indicated by the Spectrum ID (α = single power law index; E = thermal bremsstrahlung temperature in MeV). There is only a weak dependence ($<10\%$) on the assumed spectral shape, even in cases where the

assumed response vector spectrum is *much* different from the source spectrum. Thus, for a typical COMPTEL burst with significantly fewer events, systematic errors of this type are much smaller than the statistical errors.

In generating energy response vectors through simulation, the choice of source location and the number of simulated events are also potential sources of systematic error. To measure these effects, simulated sources have been deconvolved using response vectors with different statistical coverage and assuming incorrect source positions. Source (several thousand events) and response simulations in this case were both for the same energy spectrum ($E^{-2.0}$). Best-fit normalization and spectral shape parameters are shown in Figure B.4. The effect of statistical coverage is minimal (<1%) for response vectors containing more than 5000 events. Since the response vectors used to deconvolve real GRB spectra are required to contain $>10^4$ events, errors of this type are negligible. The effect of incorrect source location is also small, as long as the location error is less than $\sim 5^\circ$. Since typical COMPTEL burst location errors are $\sim 1^\circ$ – 2° , this systematic effect is also minimal.

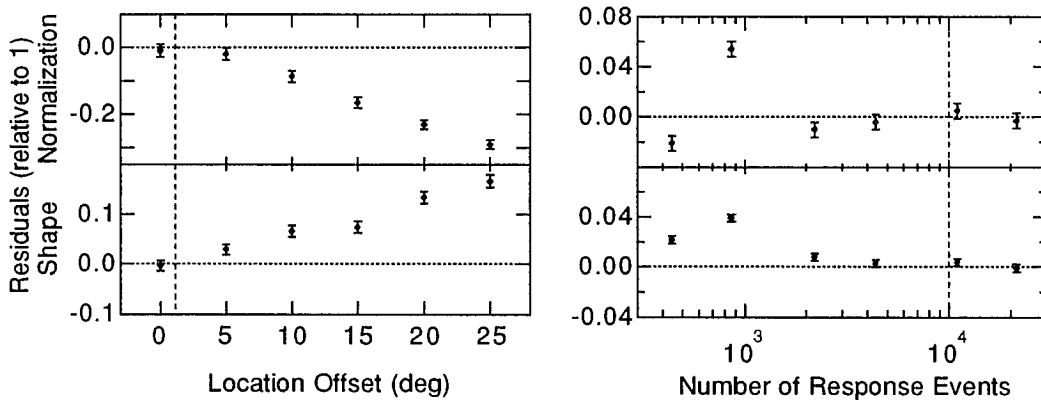


Fig. B.4. The systematic effects of assumed source location (left) and response vector statistical coverage (right) on spectral deconvolution. Vertical dashed-lines indicate typical GRB location errors (left) and the number of response events used for the standard analysis of GRBs (right).

As in source localization, the background model is also a potential source of significant error. It is also similarly difficult to quantify the error since each burst has unique background. The

background-induced errors were investigated by deconvolving simulated source spectra added to real background using the ± 15 orbit sampled background model described in the text. Residual fit-parameters for one case ($E^{-2.0}$ sources at $\theta = 10^\circ$) are shown in Figure B.5, where there appears to be good agreement between the statistical error-bars and the actual errors. Similarly favorable results were obtained for different combinations of simulated sources and real background. Thus, within the limits of this investigation, the ± 15 orbit background model does not appear to induce any significant systematic error in spectral analysis.

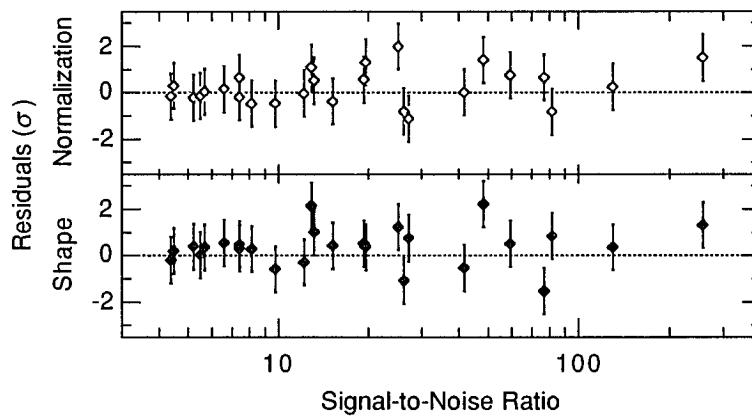


Fig. B.5. The systematic effect of background on spectral analysis. Residual spectral fit parameters (in units of statistical 1σ error) are plotted as a function of signal-to-noise ratio for several simulated sources added to real background.

Perhaps the largest uncertainty in fitting COMPTEL burst spectra is the error in determining the burst livetime. COMPTEL's complex design requiring several coincidence measurements for each telescope event makes instrument deadtime significant for impulsive bursts. As discussed in the text, livetime must be estimated using onboard rates which are available only every 16.4 s. Livetime for bursts (with durations ~ 1 –100 s) is therefore typically difficult to estimate and is highly uncertain. Livetime is only weakly dependent on energy, therefore livetime errors effect mainly the overall normalization of energy spectra and not the shape. However, the time-averaged spectral shape can be biased due to deadtime if the spectrum evolves in time. Livetime errors are difficult to compute directly, however they can be estimated through comparison with

independent measurements. Such comparisons made over the full-burst intervals of GRB 910503 (Schaefer *et al.* 1994a), GRB 910601 (Share *et al.* 1994) and GRB 920622 (Greiner *et al.* 1995) indicate good agreement (within statistical errors; $\sim 7\%$) between BATSE, COMPTEL, EGRET-TASC and OSSE spectra in the 1 MeV overlap region. In general, these instruments are less affected by instrument deadtime than COMPTEL. In addition to measuring livetime errors, these comparisons also serve to validate the simulation model used to generate COMPTEL energy response vectors. Further comparison with the COMPTEL BSA detectors for several sub-burst intervals indicates livetime normalization errors can be as large as 20–50%, but some of this discrepancy could be a result of improper BSA detector response. Thus, depending on the burst and the time-interval used, livetime normalization errors can be significant.

The preceding investigations indicate that combined response and background model inaccuracies do not produce significant systematic errors, while instrument deadtime can. Thus, systematic errors in spectral shape fit-parameters are small ($\leq 10\%$), whereas errors in normalization can be large (possibly as much as 50%).

APPENDIX C

COMPTEL SKY EXPOSURE MAP

COMPTEL is a pointed instrument with a limited field-of-view (FOV), thus its exposure to gamma-ray bursts across the sky is highly non-uniform (i.e., many bursts are not observed because they occur outside the FOV). It is important to account for this effect when analyzing the spatial distribution of burst sources (including the search for burst recurrence), since the distribution will be biased towards those areas which have the highest exposure (cf. Brock *et al.* 1992). A discussion follows of how to construct a simple all-sky map of the COMPTEL exposure.

As the *Compton* Observatory orbits the earth, its attitude and pointing direction are maintained ($\pm 0.5^\circ$) over the duration of an observation period. During such a period, COMPTEL is only sensitive to bursts that originate from within the telescope field-of-view—a roughly circular region of the sky (angular radius of $\sim 50^\circ$) centered on the pointing direction. At a height of 350–450 km, parts (or all) of this portion of the sky are frequently blocked by the earth. The details of Earth blockage depend on the particular pointing direction—the two extremes being when the pointing direction is parallel (maximum Earth blockage) and perpendicular (minimum Earth blockage) to the orbital plane of the satellite. When integrated over several orbits, the general effect is that some parts of the FOV are more highly exposed than others. A crude approximation is obtained by simply scaling the entire exposed region of the sky by the time that the majority of FOV was free from Earth blockage. The *effective* observing time must also include the losses due to lack of telemetry and SAA transit periods during which the COMPTEL detectors are turned off. Effective observing times for individual observation periods typically range from 20% to 50% of the total observation time, depending on the pointing direction.

The sensitivity to a given burst depends on the burst fluence as well as its position within the FOV. For an arbitrary burst the sensitivity within the FOV is approximately distributed like the

effective telescope detection area (product of the detection efficiency and projected D1 area), which falls off roughly linearly with zenith angle θ and is only weakly dependent on azimuth angle. Since the effective detection area is a function of energy, the fact that the energy spectra of bursts cover a wide range also complicates matters. In Figure C.1 the effective area (standard data selections and all modules activated) as a function of zenith angle is shown for two typical power law burst spectra. In computing the burst exposure, the effect of decreasing sensitivity with increasing zenith angle is approximated by assuming a purely linear dependence, which falls to zero at $\theta = 55^\circ$. This simple approximation attempts to describe the detection sensitivity averaged over all bursts. The true dependence on zenith angle is probably much smoother due to the broad distribution of burst fluences and spectra.

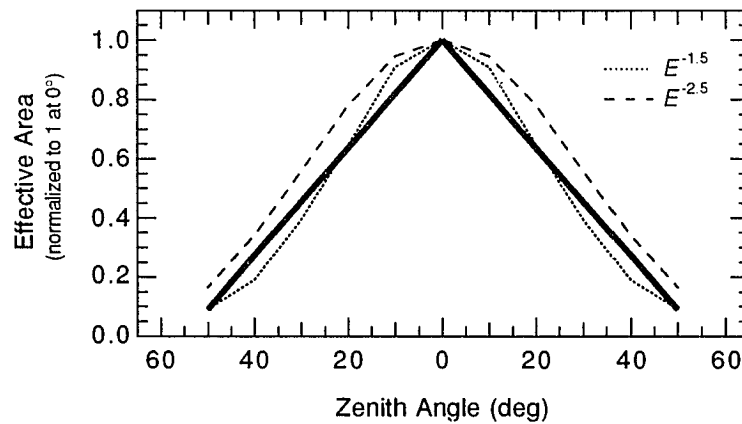


Fig. C.1. Effective telescope detection area as a function of zenith angle for typical power law burst spectra (0.75–30 MeV) as determined from simulation. The dark line indicates the linear approximation used for the exposure to bursts within the FOV.

Over the course of the *Compton* mission there have been many changes in the pointing direction, with each observation period typically lasting about 2–3 weeks. The full sky has been observed, but some areas (e.g., the Galactic plane) were given considerably more attention than others. The *relative* exposure (X_{rel} ; expressed in units of time) at each position on the sky (α , δ) is estimated through the following summation over observation periods:

COMPTEL EXPOSURE MAP APRIL 1991 - APRIL 1994

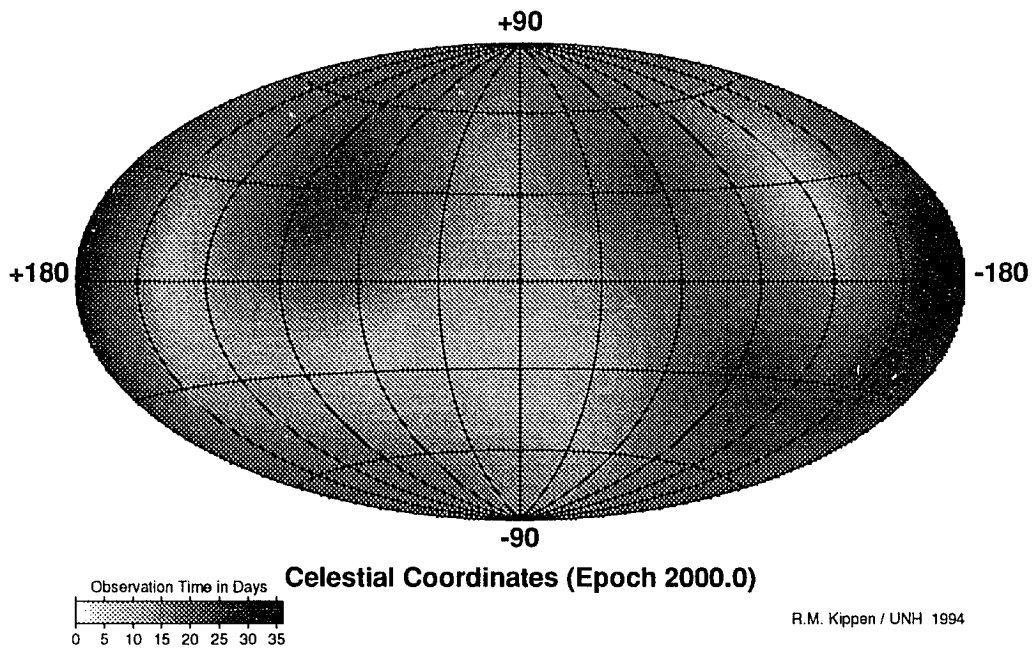
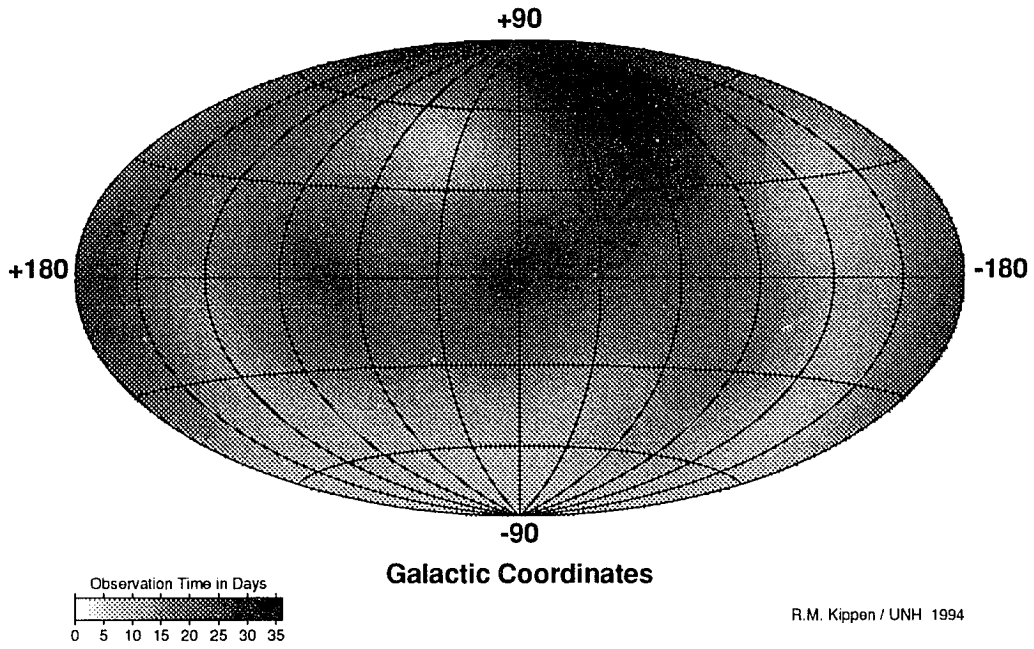


Fig. C.2a-b. COMPTEL GRB exposure maps in Galactic (a; top) and Celestial (b) coordinate systems for the first three years of the *Compton Observatory* mission.

$$X_{\text{rel}}(\alpha, \delta) = \sum_{i=1}^{N_{\text{obs}}} T_i \times A(\theta[\alpha, \delta]) , \quad (\text{C.1})$$

where T_i is the effective observing time (including Earth blockage, etc.) of each observation period (in units of days) and A is the position-dependent effective detection area relative to that at $\theta = 0^\circ$ as shown in Figure C.1. Note that this simple method suffices only to indicate relative differences in exposure between different directions. The absolute exposure (expressed in units of time \times area) is probably more sensitive to changes in data selections, energy spectra and burst fluence. Assuming standard data selections and a typical E^{-2} power law spectrum, one can obtain an approximate measure of the absolute exposure by multiplying the relative exposure by $\sim 36 \text{ cm}^2$ (the effective detection area for this spectrum at $\theta = 0^\circ$).

Relative exposure maps combining the 114 observing periods from the first three years of the *Compton* mission are shown in Figure C.2. The most obvious features in these maps are the exposed regions along the Galactic plane and in the direction of Virgo ($l = 270^\circ$, $b = 60^\circ$). The maximum exposure is 36 days in the direction of Virgo, while the minimum is 8 days towards the south Galactic pole. The average exposure over the full sky for this period is ~ 17 days. Fortunately, the mixture of different pointing directions over the three years of observations has produced good exposure over most areas of the sky, so that the spatial distribution of bursts can be determined without significant correction.

REFERENCES

- Ait-Ouamer, F., Zych, A. D. & White, R. S. 1988, *J. Geophys. Res.* **93**, 2499
- Aglietta, M., *et al.* 1993, in *Proc. 23rd Intl. Cos. Ray Conf.* (Calgary, Canada), **1**, 69
- Apparao, K. M. V. & Allen, D. 1982, *Astron. Astrophys.* **107**, L5
- Atteia, J.-L., *et al.* 1987a, *Astrophys. J.* **320**, L105
- . 1987b, *Astrophys. J. Suppl. Ser.* **64**, 305
- . 1991, *Nature* **351**, 296
- Baird, G. A., *et al.* 1975, *Astrophys. J.* **196**, L11
- Band, D. 1994, *Astrophys. J.* **432**, L23
- Band, D. L. & Hartmann, D. H. 1992a, *Astrophys. J.* **386**, 299
- . 1992b, in *AIP Conf. Proc. No. 265, Gamma-Ray Bursts*, ed. W. S. Paciesas & G. J. Fishman (New York: AIP Press) p. 342
- Band, D., *et al.* 1992, in *AIP Conf. Proc. No. 265, Gamma-Ray Bursts*, ed. W. S. Paciesas & G. J. Fishman (New York: AIP Press) p. 169
- . 1993a, *Astrophys. J.* **413**, 281
- . 1993b, in *AIP Conf. Proc. No. 280, Compton Gamma-Ray Observatory*, ed. M. Friedlander, N. Gehrels & D. J. Macomb (New York: AIP Press), p. 872
- . 1994, *Astrophys. J.* **434**, 560
- Barat, C. 1993, *Astron. Astrophys. Suppl. Ser.* **97**, 43
- Baring, M. G. 1988, *Mon. Not. Roy. Astron. Soc.* **235**, 51
- . 1990, *Mon. Not. Roy. Astron. Soc.* **244**, 49
- . 1992, in *Gamma-Ray Bursts Observations, Analyses and Theories*, ed. C. Ho, R. I. Epstein & E. E. Fenimore (Cambridge: Cambridge University Press), p. 467
- . 1993, *Astrophys. J.* **418**, 391
- . 1994, *Astrophys. J. Suppl. Ser.* **90**, 899
- Baring, M. G. & Harding, A. K. 1993, in *Proc. 23rd Intl. Cos. Ray Conf.* (Calgary, Canada), **1**, 53

- Barthelmy, S. D., *et al.* 1994a, in *AIP Conf. Proc. No. 307, Gamma-Ray Bursts*, ed. G. J. Fishman, J. J. Brainerd & K. Hurley (New York: AIP Press), p. 392
- . 1994b, in *AIP Conf. Proc. No. 307, Gamma-Ray Bursts*, ed. G. J. Fishman, J. J. Brainerd & K. Hurley (New York: AIP Press), p. 643
- Beasley, A. J., Dwarakanath, K. S. & Rupen, M. P. 1993, *IAU Circ.* 5764
- Beatty, J. K. 1982, *Sky Tel.* **63**, 469
- Bevington, P. R. 1969, *Data Reduction and Error Analysis for the Physical Sciences* (New York: McGraw-Hill)
- Bhat, P. N., *et al.* 1994, *Astrophys. J.* **426**, 604
- Bickert, K. F. & Greiner, J. 1993, in *AIP Conf. Proc. No. 280, Compton Gamma-Ray Observatory*, ed. M. Friedlander, N. Gehrels & D. J. Macomb (New York: AIP Press), p. 1059
- Blaes, O. M. 1994, *Astrophys. J. Suppl. Ser.* **92**, 643
- Blaes, O. M., *et al.* 1989, *Astrophys. J.* **343**, 839
- . 1992, *Astrophys. J.* **399**, 634
- Blumenthal, G. H. & Tucker, W. H. 1974, in *X-Ray Astronomy*, ed. R. Giacconi & H. Gursky (Dordrecht Holland: D. Reidel Publishing), p. 99
- Blumenthal, G. R., *et al.* 1994, in *AIP Conf. Proc. No. 307, Gamma-Ray Bursts*, ed. G. J. Fishman, J. J. Brainerd & K. Hurley (New York: AIP Press), p. 117
- Boër, M. *et al.* 1994a, in *AIP Conf. Proc. No. 307, Gamma-Ray Bursts*, ed. G. J. Fishman, J. J. Brainerd & K. Hurley (New York: AIP Press), p. 453
- . 1994b, in *AIP Conf. Proc. No. 307, Gamma-Ray Bursts*, ed. G. J. Fishman, J. J. Brainerd & K. Hurley (New York: AIP Press), p. 458
- . 1994c, in *AIP Conf. Proc. No. 307, Gamma-Ray Bursts*, ed. G. J. Fishman, J. J. Brainerd & K. Hurley (New York: AIP Press), p. 396
- de Boer, H., 1992, in *Data Analysis in Astronomy IV*, ed. V. diGesù, *et al.* (New York: Plenum Press), p. 241
- Brainerd, J. J. 1992, *Astrophys. J.* **394**, L33
- Brainerd, J. J., *et al.* 1994, in *AIP Conf. Proc. No. 307, Gamma-Ray Bursts*, ed. G. J. Fishman, J. J. Brainerd & K. Hurley (New York: AIP Press), p. 122
- Briggs, M. S. 1993, *Astrophys. J.* **407**, 126
- Brock, M. N., *et al.* 1992, in *AIP Conf. Proc. No. 265, Gamma-Ray Bursts*, ed. W. S. Paciesas &

- G. J. Fishman (New York: AIP Press) p. 399
- Cash, W. 1979, *Astrophys. J.* **228**, 939
- Castro-Tirado, A. J., *et al.* 1994a, in *AIP Conf. Proc. No. 307, Gamma-Ray Bursts*, ed. G. J. Fishman, J. J. Brainerd & K. Hurley (New York: AIP Press), p. 17
- . 1994b, in *AIP Conf. Proc. No. 307, Gamma-Ray Bursts*, ed. G. J. Fishman, J. J. Brainerd & K. Hurley (New York: AIP Press), p. 404
- Cavallo, G. & Rees, M. J. 1978, *Mon. Not. Roy. Astron. Soc.* **183**, 359
- Colgate, S. A. 1968, *Can. J. Phys.* **46**, S476
- . 1992, in *Gamma-Ray Bursts Observations, Analyses and Theories*, ed. C. Ho, R. I. Epstein & E. E. Fenimore (Cambridge: Cambridge University Press), p. 75
- Colgate, S. A. & Leonard, P. J. T. 1994, in *AIP Conf. Proc. No. 307, Gamma-Ray Bursts*, ed. G. J. Fishman, J. J. Brainerd & K. Hurley (New York: AIP Press), p. 581
- Colgate, S. A. & Petschek, A. G. 1981, *Astrophys. J.* **248**, 771
- Connors, A., *et al.* 1992, in *Data Analysis in Astronomy IV*, ed. V. diGesù, *et al.* (New York: Plenum Press), p. 271
- . 1993, *Astron. Astrophys. Suppl. Ser.* **97**, 75
- Cortiglioni, S., *et al.* 1981, *Astrophys. Space Sci.* **75**, 153
- Clarke, T. E., Blaes, O. & Tremaine, S. 1994, *Astron. J.* in press
- Cline, T. 1986, *Adv. Space Res.* **6**(4), 5
- . 1983, in *AIP Conf. Proc. No. 115, High Energy Transients in Astrophysics*, ed. S. E. Woosley (New York: AIP Press), p. 333
- Cline, T. L. & Desai, U. D. 1975, *Astrophys. J.* **196**, L43
- Cline, T. L., *et al.* 1973, *Astrophys. J.* **185**, L1
- . 1992, in *AIP Conf. Proc. No. 265, Gamma-Ray Bursts*, ed. W. S. Paciesas & G. J. Fishman (New York: AIP Press), p. 72
- . 1993, in *AIP Conf. Proc. No. 280, Compton Gamma-Ray Observatory*, ed. M. Friedlander, N. Gehrels & D. J. Macomb (New York: AIP Press), p. 774
- Connaughton, V., *et al.* 1994, in *AIP Conf. Proc. No. 307, Gamma-Ray Bursts*, ed. G. J. Fishman, J. J. Brainerd & K. Hurley (New York: AIP Press), p. 470
- Dasgupta, A. K. 1979, *Astrophys. Space Sci.* **63**, 517

- Daugherty, J. K. & Harding, A. K. 1983, in *AIP Conf. Proc. No. 101, Positron-Electron Pairs in Astrophysics*, ed. M. L. Burns, A. K. Harding & R. Ramaty (New York: AIP Press), p. 387
- Dermer, C. 1989, *Astrophys. J.* **347**, L13
- . 1990, *Astrophys. J.* **360**, 197
- Diehl, R., *et al.* 1992, in *Data Analysis in Astronomy IV*, ed. V. diGesù, *et al.* (New York: Plenum Press), p. 201
- Dingus, B. L., *et al.* 1994, in *AIP Conf. Proc. No. 307, Gamma-Ray Bursts*, ed. G. J. Fishman, J. J. Brainerd & K. Hurley (New York: AIP Press), p. 22
- Duncan, R. C. & Thompson, C. 1994, in *AIP Conf. Proc. No. 307, Gamma-Ray Bursts*, ed. G. J. Fishman, J. J. Brainerd & K. Hurley (New York: AIP Press), p. 625
- Eichler, D. & Cheng, A. F. 1989, *Astrophys. J.* **336**, 360
- Eichler, D. & Silk, J. 1992, *Science* **257**, 937
- Eichler, D., *et al.* 1989, *Nature* **340**, 126
- Epstein, R. I. 1985a, *Astrophys. J.* **297**, 555
- . 1985b, *Astrophys. J.* **291**, 822
- . 1988, *Phys. Rep.* **163**, 155
- . 1992, in *Gamma-Ray Bursts Observations, Analyses and Theories*, ed. C. Ho, R. I. Epstein & E. E. Fenimore (Cambridge: Cambridge University Press), p. 1
- Erber, T. 1966, *Rev. Mod. Phys.* **38**, 626
- Fenimore, E. E., Klebesadel, R. W. & Laros, J. G. 1983, *Adv. Space Res.* **3**(4), 207
- Fenimore, E. E., Epstein, R. I. & Ho, C. 1992, in *AIP Conf. Proc. No. 265, Gamma-Ray Bursts*, ed. W. S. Paciesas & G. J. Fishman (New York: AIP Press) p. 158
- . 1993, *Astron. Astrophys. Suppl. Ser.* **97**, 59
- Fenimore, E. E., *et al.* 1982, *Nature* **297**, 665
- . 1993, *Nature* **366**, 40
- Fishman, G. J. 1993, in *AIP Conf. Proc. No. 280, Compton Gamma-Ray Observatory*, ed. M. Friedlander, N. Gehrels & D. J. Macomb (New York: AIP Press), p. 669
- Fishman, G. J., *et al.* 1989, in *Proc. of the Gamma Ray Observatory Science Workshop*, ed. W. N. Johnson (Washington: NASA), p. 39
- . 1994a, *Astrophys. J. Suppl. Ser.* **92**, 229

- . 1994b, *Science* **264**, 1313
- Ford, L. A., *et al.* 1995, *Astrophys. J.* **439**, 307
- Frail, D. A., *et al.* 1994, *Astrophys. J.* **437**, L43
- Frail, D. A. & Kulkarni, S. R. 1991, *Nature* **352**, 785
- Golenetskii, S. V., *et al.* 1983, *Nature* **306**, 451
- Goodman, J. 1986, *Astrophys. J.* **308**, L47
- Gould, R. J. 1980, *Astrophys. J.* **238**, 1026
- . 1982, *Astrophys. J.* **258**, 131
- Greiner, J. 1992, *Astron. Astrophys.* **264**, 121
- Greiner, J., *et al.* 1993, in *AIP Conf. Proc. No. 280, Compton Gamma-Ray Observatory*, ed. M. Friedlander, N. Gehrels & D. J. Macomb (New York: AIP Press), p. 828
- . 1994, in *AIP Conf. Proc. No. 307, Gamma-Ray Bursts*, ed. G. J. Fishman, J. J. Brainerd & K. Hurley (New York: AIP Press), p. 408
- . 1995, *Astron. Astrophys.* in press
- Grindlay, J. E. & Fazio, G. G. 1974, *Astrophys. J.* **187**, L93
- Grindlay, J. E., Wright, E. L. & McCrosky, R. E. 1974, *Astrophys. J.* **192**, L113
- Grossman, S. A. & Nowak, M. A. 1994, *Astrophys. J.* **435**, 548
- Hakkila, J., *et al.* 1994a, *Astrophys. J.* **422**, 659
- . 1994b, *Bull. Am. Astron. Soc.* **26**, No. 2, 881
- Hameury, J. M., *et al.* 1982, *Astron. Astrophys.* **111**, 242
- Hanlon, L., Bennett, K. & Spoelstra, T. 1993, *IAU Circ.* 5749
- Hanlon, L. O., *et al.* 1993, in *Proc. 27th ESLAB Symp.* (Dordrecht: Kluwer Academic Publishers)
- . 1994, *Astron. Astrophys.* **285**, 161
- . 1995, *Astron. Astrophys.* in press
- Harding, A. K. 1991, *Phys. Rep.* **206**, 327
- . 1994, *Astrophys. J. Suppl. Ser.* **90**, 863
- Harding, A. K. & Baring, M. G. 1994, in *AIP Conf. Proc. No. 307, Gamma-Ray Bursts*, ed. G. J.

- Fishman, J. J. Brainerd & K. Hurley (New York: AIP Press), p. 520
- Harrison, T. E., McNamara, B. 1993, *IAU Circ.* 5755
- Harrison, T. E., McNamara, B. J. & Klemola, A. R. 1994a, *Astron. J.* **107**, 254
- . 1994b, *Astron. J.* **108**, 600
- Harrison, T. E., *et al.* 1994, *Astron. Astrophys.* in press
- Hartmann, D. 1991, *Ann. N.Y. Acad. Sci.* **647**, 575
- . 1994, in *AIP Conf. Proc. No. 307, Gamma-Ray Bursts*, ed. G. J. Fishman, J. J. Brainerd & K. Hurley (New York: AIP Press), p. 562
- Hartmann, D., Woosley, S. E. & Arons, J. 1988, *Astrophys. J.* **332**, 777
- Hartmann, D. & Epstein, R. I. 1989, *Astrophys. J.* **346**, 960
- Hartmann, D. & Blumenthal, G. R. 1989, *Astrophys. J.* **342**, 521
- Hartmann, D. H., Linder, E. V. & Blumenthal, G. R. 1991, *Astrophys. J.* **367**, 186
- Hartmann, D. H., *et al.* 1994a, in *AIP Conf. Proc. No. 307, Gamma-Ray Bursts*, ed. G. J. Fishman, J. J. Brainerd & K. Hurley (New York: AIP Press), p. 127
- . 1994b, *Astrophys. J. Suppl. Ser.* **90**, 893
- Harwit, M. & Salpeter, E. E. 1973, *Astrophys. J.* **186**, L37
- Hayakawa, S. 1952, *Prog. Theor. Phys.* **8**, 571
- den Herder, J. W., *et al.* 1992, in *NASA Conf. Proc. 3137, Compton Observatory Science Workshop*, ed. C.R. Shrader, N. Gehrels, B. Dennis (Washington: NASA), p. 85
- Herzo, D., *et al.* 1975, *Nucl. Instr. Meth.* **123**, 583
- Higdon, J. C. & Lingenfelter, R. E. 1986, *Astrophys. J.* **307**, 197
- . 1990, *Annu. Rev. Astron. Astrophys.* **28**, 401
- . 1994, *Astrophys. J.* **434**, 552
- Higdon, J. C. & Schmidt, M. 1990, *Astrophys. J.* **355**, 13
- Hjellming, R. M. & Ewald, S. P. 1981, *Astrophys. J.* **246**, L137
- Ho, C. & Epstein, R. I. 1989, *Astrophys. J.* **343**, 277
- Ho, C., *et al.* 1990, *Astrophys. J.* **348**, L25

- Horack, J. M. & Emslie, A. G. 1994, *Astrophys. J.* **425**, 766
- Horack, J. M., *et al.* 1993, in *AIP Conf. Proc. No. 280, Compton Gamma-Ray Observatory*, ed. M. Friedlander, N. Gehrels & D. J. Macomb (New York: AIP Press), p. 778
- . 1994, *Astrophys. J.* **429**, 319
- Hudec, R. 1993, *Astro. Lett. Comm.* **28**, 359
- Hudec, R. & Soldán, J. 1994, in *AIP Conf. Proc. No. 307, Gamma-Ray Bursts*, ed. G. J. Fishman, J. J. Brainerd & K. Hurley (New York: AIP Press), p. 413
- Hueter, G. J. 1984, in *AIP Conf. Proc. No. 115, High Energy Transients in Astrophysics*, ed. S. E. Woosley (New York: AIP Press), p. 373
- Hurley, K. 1982, in *AIP Conf. Proc. No. 77, Gamma-Ray Transients and Related Astrophysical Phenomena*, ed. R. E. Lingenfelter, H. S. Hudson & D. M. Worrall (New York: AIP Press), p. 85
- . 1989, *Ann. N.Y. Acad. Sci.* **571**, 442
- . 1992, in *AIP Conf. Proc. No. 265, Gamma-Ray Bursts*, ed. W. S. Paciesas & G. J. Fishman (New York: AIP Press), p. 3
- Hurley, K., *et al.* 1993a, in *AIP Conf. Proc. No. 280, Compton Gamma-Ray Observatory*, ed. M. Friedlander, N. Gehrels & D. J. Macomb (New York: AIP Press), p. 769
- . 1993b, in *Proc. 23rd Intl. Cos. Ray Conf.* (Calgary, Canada), **1**, 116
- . 1993c, *IAU Circ.* 5763
- . 1994a, in *AIP Conf. Proc. No. 307, Gamma-Ray Bursts*, ed. G. J. Fishman, J. J. Brainerd & K. Hurley (New York: AIP Press), p. 27
- . 1994b, in *AIP Conf. Proc. No. 307, Gamma-Ray Bursts*, ed. G. J. Fishman, J. J. Brainerd & K. Hurley (New York: AIP Press), p. 369
- . 1994c, *IAU Circ.* 5940
- . 1994d, *IAU Circ.* 5944
- . 1994e, *Nature* **372**, 652
- . 1994f, *IAU Circ.* 5940
- . 1994g, *IAU Circ.* 5944
- Hutchinson, G. W. 1952, *Phil. Mag.* **43**, 847
- Imamura, J. N. & Epstein, R. I. & Petrosian, V. 1985, *Astrophys. J.* **296**, 65

- Imamura, J. N. & Epstein, R. I. 1987, *Astrophys. J.* **313**, 711
- Inzani, P., *et al.* 1982, in *AIP Conf. Proc. No. 77, Gamma Ray Transients and Related Astrophysical Phenomena*, ed. R. E. Lingenfelter, H. S. Hudson & D. M. Worrall (New York: AIP Press), p. 79
- Jauch, J. M. & Rohrlich, F. 1955, *Theory of Photons and Electrons* (Addison Wesley: Reading, MA), p. 301
- Jennings, M. C. 1983, *Astrophys. J.* **273**, 309
- Jennings, M. C. & White, R. S. 1980, *Astrophys. J.* **238**, 110
- Joss, P. C. & Rappaport, S. 1984, in *AIP Conf. Proc. No. 115, High Energy Transients in Astrophysics*, ed. S. E. Woosley (New York: AIP Press), p. 555
- Kargatis, V. E., *et al.* 1994, *Astrophys. J.* **422**, 260
- Karzas, W. & Latter, R. 1961, *Astrophys. J. Suppl. Ser.* **6**, 167
- Katz, J. I. 1993, in *AIP Conf. Proc. No. 280, Compton Gamma-Ray Observatory*, ed. M. Friedlander, N. Gehrels & D. J. Macomb (New York: AIP Press), p. 1090
- . 1994a, *Astrophys. J.* **422**, 248
- . 1994b, *Astrophys. J.* **432**, L27
- . 1994c, *Astrophys. J.* **432**, L107
- Kippen, R. M. 1991, *Monte Carlo Simulation of the COMPTEL Gamma-Ray Telescope*, (Master's thesis, University of New Hampshire, Durham, N.H).
- Kippen, R. M., *et al.* 1995a, *Astron. Astrophys.* **293**, L5
- . 1995b, *Adv. Space Res.* **15**(5), 139
- Klebesadel, R. W. 1992, in *Gamma-Ray Bursts Observations, Analyses and Theories*, ed. C. Ho, R. I. Epstein & E. E. Fenimore (Cambridge: Cambridge University Press), p. 161
- Klebesadel, R. W., Strong, I. B. & Olson, R. A. 1973, *Astrophys. J.* **182**, L85
- Koranyi, D. M., *et al.* 1994, *Mon. Not. Roy. Astron. Soc.* **271**, 51
- Kouveliotou, C. 1994, *Astrophys. J. Suppl. Ser.* **92**, 637
- Kouveliotou, C., *et al.* 1993a, *Astrophys. J.* **413**, L101
- . 1993b, *Nature* **362**, 728
- . 1994a, in *AIP Conf. Proc. No. 307, Gamma-Ray Bursts*, ed. G. J. Fishman, J. J. Brainerd & K. Hurley (New York: AIP Press), p. 167

- . 1994b, *Astrophys. J.* **422**, L59
- Krolik, J. H. & Pier, E. A. 1991, *Astrophys. J.* **373**, 277
- Kulkarni, S. R., *et al.* 1994, *Nature* **368**, 129
- Kwok, P. W., *et al.* 1993, in *AIP Conf. Proc. No. 280, Compton Gamma-Ray Observatory*, ed. M. Friedlander, N. Gehrels & D. J. Macomb (New York: AIP Press), p. 855
- Lamb, D. Q. 1982, in *AIP Conf. Proc. No. 77, Gamma Ray Transients and Related Astrophysical Phenomena*, ed. R. E. Lingenfelter, H. S. Hudson & D. M. Worrall (New York: AIP Press), p. 249
- . 1984, in *AIP Conf. Proc. No. 115, High Energy Transients in Astrophysics*, ed. S. E. Woosley (New York: AIP Press), p. 512
- Lamb, D. Q. Graziani, C. & Smith, I. A. 1993, *Astrophys. J.* **413**, L11
- Lampton, M., Margon, B. & Bowyer, S. 1976, *Astrophys. J.* **208**, 177
- Laros, J. G., *et al.* 1984, *Astrophys. J.* **286**, 681
- Lasota, J. P. & Belli, B. M. 1983, *Nature* **304**, 139
- Liang, E. 1982, *Nature* **299**, 321
- . 1987, *Comments Astrophys.* **12**, 35
- . 1989, in *Proc. of the Gamma Ray Observatory Science Workshop*, ed. W. N. Johnson (Washington: NASA), p. 4-397
- Liang, E. P., Jernigan, T. E. & Rodrigues, R. 1983, *Astrophys. J.* **271**, 766
- Li, T. & Ma, Y. 1983, *Astrophys. J.* **272**, 317
- Lingenfelter, R. E. & Higdon, J. C. 1992, *Nature* **356**, 132
- Lingenfelter, R. E., Wang, V. C. & Higdon, J. C. 1994, in *AIP Conf. Proc. No. 307, Gamma-Ray Bursts*, ed. G. J. Fishman, J. J. Brainerd & K. Hurley (New York: AIP Press), p. 222
- London, R. A., 1984, in *AIP Conf. Proc. No. 115, High Energy Transients in Astrophysics*, ed. S. E. Woosley (New York: AIP Press), p. 581
- London, R. A. & Cominsky, L. R. 1983, *Astrophys. J.* **275**, L59
- Loredo, T. J. & Epstein, R. I. 1989, *Astrophys. J.* **336**, 896
- Mallozzi, R. S., *et al.* 1993, in *AIP Conf. Proc. No. 280, Compton Gamma-Ray Observatory*, ed. M. Friedlander, N. Gehrels & D. J. Macomb (New York: AIP Press), p. 1122
- Mao, S. 1991, *Astrophys. J.* **389**, L41

- Mao, S. & Paczynski, B. 1992a, *Astrophys. J.* **389**, L13
- . 1992b, *Astrophys. J.* **388**, L45
- Maoz, E. 1993, *Astrophys. J.* **414**, 877
- Matz, S. M. 1986, *On the Spectra of Gamma-Ray Bursts at High Energies*, (Ph.D. diss., University of New Hampshire, Durham, NH).
- Matz, S. M., *et al.* 1985, *Astrophys. J.* **288**, L37
- . 1992, in *Gamma-Ray Bursts Observations, Analyses and Theories*, ed. C. Ho, R. I. Epstein & E. E. Fenimore (Cambridge: Cambridge University Press), p. 175
- Mazets, E. P., *et al.* 1981a, *Nature* **290**, 378
- . 1981b, *Astrophys. Space Sci.* **80**, 3
- . 1982, *Astrophys. Space Sci.* **82**, 261
- McBreen, B. & Metcalfe, L. 1988, *Nature* **322**, 234
- McBreen, B., Plunkett, S. & Metcalfe, L. 1993, *Astron. Astrophys. Suppl. Ser.* **97**, 81
- McConnell, M., *et al.* 1994, *Astrophys. J.* **424**, 933
- McNamara, B. J. & Harrison, T. E. 1994, *Astron. J.* **107**, 1825
- McNamara, B. J., *et al.* 1995, in preparation
- Meegan, C. A., Fishman, G. J. & Wilson, R. B. 1983, in *AIP Conf. Proc. No. 115, High Energy Transients in Astrophysics*, ed. S. E. Woosley (New York: AIP Press), p. 422
- Meegan, C. A., *et al.* 1992, *Nature* **355**, 143
- . 1994, *The Second BATSE Gamma-Ray Burst Catalog*, Compton Observatory Science Support Center Online Service
- Melia, F. 1988, *Astrophys. J.* **324**, L21
- . 1989, *Nature* **338**, 322
- Melia, F., Rappaport, S. & Joss, P. C. 1986, *Astrophys. J.* **305**, L51
- Messina, D. C. & Share, G. H. 1992, in *AIP Conf. Proc. No. 265, Gamma-Ray Bursts*, ed. W. S. Paciesas & G. J. Fishman (New York: AIP Press), p. 206
- Metzger, A. E., *et al.* 1974, *Astrophys. J.* **194**, L19
- Mészáros, P. 1992, *High-Energy Radiation from Magnetized Neutron Stars* (Chicago: University of Chicago Press), p. 370

- Mészáros, P. & Rees, M. J. 1992a, *Astrophys. J.* **397**, 570
- . 1992b, *Mon. Not. Roy. Astron. Soc.* **257**, 29P
- . 1993a, *Astrophys. J.* **405**, 278
- . 1993b, *Astrophys. J.* **418**, L59
- . 1994a, *Astrophys. J.* **430**, L93
- . 1994b, *Mon. Not. Roy. Astron. Soc.* **269**, 41p
- Mészáros, P., Rees, M. J. & Papathanassiou, H. 1994, *Astrophys. J.* **432**, 181
- Mészáros, P., Laguna, P. & Rees, M. J. 1993, *Astrophys. J.* **415**, 181
- Miller, G. S. & Epstein, R. I. 1992, in *Gamma-Ray Bursts Observations, Analyses and Theories*, ed. C. Ho, R. I. Epstein & E. E. Fenimore (Cambridge: Cambridge University Press), p. 24
- Miller, R. S., *et al.* 1994, *Astrophys. J.* **428**, 629
- Mitrofanov, I. G. 1989, *Astrophys. Space Sci.* **155**, 141
- Mochkovitch, R., *et al.* 1995, *Astron. Astrophys.* **293**, 803
- Morrison, P. 1958, *Nuovo Cimento* **7**, 858
- Murakami, T., *et al.* 1988, *Nature* **355**, 234
- . 1991, *Nature* **350**, 592
- . 1992, in *Gamma-Ray Bursts Observations, Analyses and Theories*, ed. C. Ho, R. I. Epstein & E. E. Fenimore (Cambridge: Cambridge University Press), p. 239
- Narayan, R. & Piran, T. 1993, *Mon. Not. Roy. Astron. Soc.* **265**, L65
- . 1994, in *AIP Conf. Proc. No. 307, Gamma-Ray Bursts*, ed. G. J. Fishman, J. J. Brainerd & K. Hurley (New York: AIP Press), p. 132
- Narayan, R., Piran, T. & Shemi, A. 1991, *Astrophys. J.* **379**, L17
- Narayan, R., Paczynski, B. & Piran, T. 1992, *Astrophys. J.* **395**, L83
- Nemiroff, R. J. 1994, *Comm. Astrophys.* **17**, 189
- Nemiroff, R. J., *et al.* 1994a, *Astrophys. J.* **432**, 478
- . 1994b, *Astrophys. J.* **435**, L133
- Newman, M. J. & Cox, A. N. 1980, *Astrophys. J.* **242**, 319

- Nolan, P. L., *et al.* 1984, *Nature* **311**, 360
- Norris, J. P., *et al.* 1984, *Nature* **308**, 434
- . 1986, *Astrophys. J.* **301**, 213
- . 1991, *Astrophys. J.* **366**, 240
- . 1994, *Astrophys. J.* **424**, 540
- Nousek, J. A. 1992, in *Statistical Challenges in Modern Astronomy*, ed. E. Feigelson & G. J. Babu (New York: Springer-Verlag), p. 307
- Nousek, J. A. & Shue, D. R. 1989, *Astrophys. J.* **342**, 1207
- Oort, J. 1950, *Bull. Astron. Netherlands* **11**, 91
- Owens, A. *et al.* 1993, in *AIP Conf. Proc. No. 280, Compton Gamma-Ray Observatory*, ed. M. Friedlander, N. Gehrels & D. J. Macomb (New York: AIP Press), p. 798
- Pacini, F. & Ruderman, M. 1974, *Nature* **251**, 399
- Paczynski, B. 1986, *Astrophys. J.* **308**, L43
- . 1990, *Astrophys. J.* **348**, 485
- Paczynski, B. & Rhoads, J. E. 1993, **418**, L5
- Palmer, D. M. 1993, *Astrophys. J.* **417**, L25
- Palmer, D. M., *et al.* 1994, *Astrophys. J.* **433**, L77
- Pedersen, H. 1994, *Astron. Astrophys.* **291**, L17
- Peebles, P. J. E. 1973, *Astrophys. J.* **308**, L43
- Pelaez, F., *et al.* 1994, *Astrophys. J. Suppl. Ser.* **92**, 651
- Petrosian, V. 1981, *Astrophys. J.* **251**, 727
- Piran, T. & Shemi, A. 1992, *Astrophys. J.* **403**, L67
- Press, W. H., Flannery, B. P., Teukolsky, S. A. & Vetterling, W. T. 1986, *Numerical Recipes, The Art of Scientific Computing* (Cambridge: Cambridge University Press), p. 165
- Quashnock, J. M. & Lamb, D. Q. 1993, *Mon. Not. Roy. Astron. Soc.* **265**, 59p
- . 1994, in *AIP Conf. Proc. No. 307, Gamma-Ray Bursts*, ed. G. J. Fishman, J. J. Brainerd & K. Hurley (New York: AIP Press), p. 107
- Ramana Murthy, P. V. & Wolfendale, A. W. 1993, *Gamma-Ray Astronomy—Second Edition*

- (Cambridge: Cambridge University Press), p. 43
- Rappaport, S. A. & Joss, P. C. 1985, *Nature* **314**, 242
- Rees, M. J. & Mézáros, P. 1992, *Mon. Not. Roy. Astron. Soc.* **258**, 41p
- Ricker, G. R., Vanderspek, R. K. & Ajhar, E. A. 1986, *Adv. Space Res.* **6**(4), 75
- Ricker, G. R., *et al.* 1992, in *Gamma-Ray Bursts Observations, Analyses and Theories*, ed. C. Ho, R. I. Epstein & E. E. Fenimore (Cambridge: Cambridge University Press), p. 288
- Roland, J. Frossati, G. & Teyssier, R. 1994, *Astron. Astrophys.* **290**, 364
- Ryan, J. M., *et al.* 1979, *J. Geophys. Res.* **84**, 5279
- . 1994a, *IAU Circ.* 5950
- . 1994b, *Astrophys. J.* **422**, L67
- Schaefer, B. E. 1981, *Nature* **294**, 722
- . 1986, *Adv. Space Res.* **6**(4), 47
- . 1990, *Astrophys. J.* **364**, 590
- . 1992, in *Gamma-Ray Bursts Observations, Analyses and Theories*, ed. C. Ho, R. I. Epstein & E. E. Fenimore (Cambridge: Cambridge University Press), p. 107
- . 1994, in *AIP Conf. Proc. No. 307, Gamma-Ray Bursts*, ed. G. J. Fishman, J. J. Brainerd & K. Hurley (New York: AIP Press), p. 382
- Schaefer, B. E. & Cline, T. L. 1985, *Astrophys. J.* **289**, 490
- Schaefer, B. E., *et al.* 1987, *Astrophys. J.* **313**, 226
- . 1989, *Astrophys. J.* **340**, 455
- . 1992, *Astrophys. J.* **393**, L51
- . 1993, *Astrophys. J.* **404**, 673
- . 1994a, in *AIP Conf. Proc. No. 307, Gamma-Ray Bursts*, ed. G. J. Fishman, J. J. Brainerd & K. Hurley (New York: AIP Press), p. 280
- . 1994b, *Astrophys. J. Suppl. Ser.* **92**, 285
- . 1994c, *Astrophys. J.* **422**, L71
- Schmidt, W. K. H. 1978, *Nature*, **271**, 525
- Schnee, R., *et al.* 1994, in *AIP Conf. Proc. No. 307, Gamma-Ray Bursts*, ed. G. J. Fishman, J. J.

- Brainerd & K. Hurley (New York: AIP Press), p. 481
- Schneid, E., *et al.* 1992a, in *AIP Conf. Proc. No. 265, Gamma-Ray Bursts*, ed. W. S. Paciasas & G. J. Fishman (New York: AIP Press), p. 38
- . 1992b, *Astron. Astrophys.* **255**, L13
- Schönfelder, V., Hirner, A. & Schneider, K. 1973, *Nucl. Instr. Meth.* **107**, 385
- Schönfelder, V., *et al.* 1984, *IEEE Trans. Nucl. Sci.* **NS-31**, 766
- . 1993, *Astrophys. J. Suppl. Ser.* **86**, 657
- Scott, D. & Tout, C. A. 1989, *Mon. Not. Roy. Astron. Soc.* **241**, 109
- Shapiro, S. L., Lightman, A. P. & Eardley, D. M. 1976, *Astrophys. J.* **204**, 187
- Share, G. H., *et al.* 1986, *Adv. Space Res.* **6**(4), 15
- . 1994, in *AIP Conf. Proc. No. 307, Gamma-Ray Bursts*, ed. G. J. Fishman, J. J. Brainerd & K. Hurley (New York: AIP Press), p. 283
- Shemi, A. & Piran, T. 1990, *Astrophys. J.* **365**, L55
- Smith, I. A. & Epstein, R. I. 1993, *Astrophys. J.* **410**, 315
- Smith, I. A. & Lamb, D. Q. 1993, *Astrophys. J.* **410**, L23
- Sommer, M., *et al.* 1994a, *Astrophys. J.* **422**, L63
- . 1994b, *Bull. Am. Astron. Soc.* **26**, No. 2, 873
- Stecker, F. W., 1971, *Cosmic Gamma Rays*, (Washington DC: NASA SP-249), p. 78
- Strohmayer, T. E., Fenimore, E. E. & Miralles, J. A. 1994, *Astrophys. J.* **432**, 665
- Strong, I. B. & Klebesadel, R. W. 1976, *Sci. Am.* **235**(4), 66
- Strong, A. W., *et al.* 1992, in *Data Analysis in Astronomy IV*, ed. V. diGesù, *et al.* (New York: Plenum Press), p. 251
- Sunyaev, R. A. & Titarchuk, L. G. 1980, *Astron. Astrophys.* **86**, 121
- Thompson, D., *et al.* 1983, *Astrophys. J. Suppl. Ser.* **86**, 629
- Tremaine, S. & Zytkov, A. N. 1986, *Astrophys. J.* **301**, 155
- Varendorff, M. G., *et al.* 1992, in *AIP Conf. Proc. No. 265, Gamma-Ray Bursts*, ed. W. S. Paciasas & G. J. Fishman (New York: AIP Press), p. 77
- Verba, F. J., Hartmann, D. H. & Jennings, M. C. 1992, in *Gamma-Ray Bursts Observations*,

- Analyses and Theories*, ed. C. Ho, R. I. Epstein & E. E. Fenimore (Cambridge: Cambridge University Press), p. 138
- Verba, F. J., *et al.* 1994, in *AIP Conf. Proc. No. 307, Gamma-Ray Bursts*, ed. G. J. Fishman, J. J. Brainerd & K. Hurley (New York: AIP Press), p. 443
- Vedrenne, G. 1991, *Ann. N.Y. Acad. Sci.* **647**, 556
- Wang, V. C. & Lingenfelter, R. E. 1993, *Astrophys. J.* **416**, L13
- White, R. S. 1993, *Astrophys. Space Sci.* **208**, 301
- . 1994, in *AIP Conf. Proc. No. 307, Gamma-Ray Bursts*, ed. G. J. Fishman, J. J. Brainerd & K. Hurley (New York: AIP Press), p. 620
- Whitmire, D. P., Whitman, P. G. & Matese, J. J. 1994, *Bull. Am. Astron. Soc.* **26**, No. 2, 882
- Wickramasinghe, W. A. D. T., *et al.* 1993, *Astrophys. J.* **411**, L55
- Wijers, R. A. M. J. & Paczynski, B. 1994, *Astrophys. J.* **437**, L107
- Winkler, C., *et al.* 1986, *Adv. Space Res.* **6**(4), 113
- . 1995, *Astron. Astrophys.* in press
- Woods, E. & Loeb, A. 1994, *Astrophys. J.* **425**, L63
- Woosley, S. E., 1984, in *AIP Conf. Proc. No. 115, High Energy Transients in Astrophysics*, ed. S. E. Woosley (New York: AIP Press), p. 485
- . 1993, *Astrophys. J.* **405**, 273
- Woosley, S. E. & Baron, E. 1992, *Astrophys. J.* **391**, 228
- Woosley, S. E. & Taam, R. E. 1976, *Nature* **263**, 101
- Woosley, S. E. & Wallace, R. K. 1982, *Astrophys. J.* **258**, 716
- Yoshida, A., *et al.* 1992, in *Gamma-Ray Bursts Observations, Analyses and Theories*, ed. C. Ho, R. I. Epstein & E. E. Fenimore (Cambridge: Cambridge University Press), p. 399
- Zdziarski, A. A. 1984, *Astron. Astrophys.* **134**, 301
- Zdziarski, A. A. & Lamb, D. Q. 1986, *Astrophys. J.* **309**, L79
- Zytkow, A. N. 1990, *Astrophys. J.* **359**, 138